Numerical and experimental exploration of the contour method for residual stress evaluation

Thesis

Faculty of Technology

Department of Materials Engineering

Numerical and Experimental Exploration of the Contour Method for Residual Stress Evaluation

Ying Zhang

January 2004

A THESIS SUBMITTED TO THE DEPARTMENT OF MATERIALS ENGINEERING OF THE OPEN UNIVERSITY FOR THE DEGREE OF DOCTOR OF PHILOSOPHY

Ying Zhang
The Open University

Ph.D. Thesis
January 2004

ABSTRACT

This thesis comprehensively investigates the contour method – a newly-invented destructive technique for residual stress evaluation – in terms of its principle and application.

The principle of the contour method is based on a variation of Bueckner's elastic superposition theory. A two-dimensional map of residual stress profile normal to a plane of interest can be determined in a simple, cheap and time-efficient manner. In practice, residual stress evaluation using the contour method involves the experimental measurement of the displacement formed by the stress release following a cut on the surface at issue, and then numerical calculation of the residual stress based on the experimentally measured displacement. The whole process of the contour-method measurement was simulated using a finite element method and the simulated result confirms the correctness of the novel technique.

A number of different applications have been explored using the contour method to measure a cross-sectional residual stress distribution: a hole cold expansion EN8 steel plate, a hole cold expansion 7475-T7351 aluminium alloy plate, a MIG 2024-T351 aluminium alloy welded plate and a VPPA 2024-T351 aluminium alloy welded plate. Favourably good outcomes were obtained from each case. The most impressive comparison of the contour-method result was made on the VPPA 2024-T351 weld with neutron and synchrotron X-ray diffraction measurements, showing an extremely good match with deviation approximately 9 % on average.

This work has proved that the contour method is a powerful novel technique to determine a cross-sectional residual stress profile with accuracy in many engineering components, and has great prospects to find application elsewhere.

ACKNOWLEDGEMENTS

I would like to express my sincere gratitude to my internal supervisors, Prof. Lyndon Edwards and Dr. Michael Edward Fitzpatrick, for their invaluable guidance and advice throughout this work. I also thank The Open University for financial support of the project.

I particularly thank Dr. Michael Bruce Prime, who is the pioneer of the contour method, for his generous help allowing me to use his measured data when I started this project, and continual advice in dealing with some tricky experiments and analysis, so that I am able to succeed in exploring this fantastic new world of the contour method.

I should thank Jim Moffatt for help with the tension-compression test, Peter Ledgard and Tim Gough for their excellent technical assistance in cutting and preparation of specimens, Stan Hiller for help with the surface treatment and making wonderful photos of the specimens. Many thanks should be given to Ian Norman and Gordon Imlach for kind help when needed in experiments. Deep appreciation should be also given to Rehana Malik and Jennifer Seabrook for their handy help in many other aspects. I should also thank all the colleagues in my department and particularly in my research group, for helpful discussion of diffraction measurements and sharing other useful information.

My deepest thanks and regards should be credited to my dear parents and brothers for their constant encouragement throughout my PhD study. I also should thank my husband and only daughter for their understanding and putting up with our long separation. Especially, I should thank my mother-in-law who takes responsibility to look after my daughter. Without their love and support I could not complete my PhD. In particular, I have to mention my dear six-year-old daughter. It is her who gave me strength to overcome any difficulty occurring in the course of my PhD study. I know that she is too young to understand how important is the role she has been playing during this period. I love her most in this world and this never changes even though she loves me "slightly". She keeps confirming this "slightly" every time I ask. But I never stop fancying that she might change her attitude someday. A difficult decision has to be made in some circumstances and I never regret the choice. I believe that my daughter will eventually be able to understand me, with time, of course. I also believe that she must be very proud of her mother some day in future. I entirely delicate this thesis to them.

Ying Zhang

January 2004

PREFACE

This thesis is submitted for the degree of Doctor of Philosophy of The Open University. The work described in this thesis was performed in the Department of Materials Engineering, Faculty of Technology, between October 2000 and September 2003, under the co-supervision of Prof. L. Edwards and Dr. M. E. Fitzpatrick. It is entirely the work of the author except where clearly referenced. None of this work has been submitted for a degree or other qualification at this or any other university. The views and opinions represented in this thesis are solely those of the author, not The Open University. Some of the work has been published in academic journals and conference proceedings in the following.

- Published in Journal

1. Y. Zhang, M. E. Fitzpatrick, L. Edwards, *Measurement of the Residual Stresses around a Cold Expanded Hole in an EN8 Steel Plate using the Contour Method*, Materials Science Forum, Vols. 404-407, pp. 527-534, 2002.

- Presented in Conference and Published in Conference Proceedings

1. Y. Zhang, L. Edwards, M. E. Fitzpatrick, *Finite Element Simulation of Hole Cold Expansion Process in EN8 Steel Plates*, Proceedings of Sixteenth ABAQUS UK User Group Conference, Warrington, UK, 12-13 Nov. 2002.

2. Y. Zhang, M. E. Fitzpatrick, L. Edwards, *Measurement of the Residual Stresses around a Cold Expanded Hole in an EN8 Steel Plate using the Contour Method*, Proceedings of the 6th European Conference on Residual Stresses (ECRS6), Vols. 404-407, pp. 527-534,Coimbra, Portugal, 10-12 July 2002.

TABLE OF CONTENTS

LIST OF NOTATIONS

Symbol	Definition
Roman Notations	
2D	Two dimensional
3D	Three dimensional
a	Inner radius; hole radius
a_m	Mandrel radius
A	Current cross-sectional area
A_0	Original cross-sectional area
b	Fourier coefficient; outer radius
$[B]$	Strain-displacement matrix
CMM	Co-ordinate measuring machine
CNC	Computer numerically controlled
CPU	Central processing unit
d	Lattice spacing of a stressed crystal
d_0	Lattice spacing of an unstressed crystal
$[D]$	Material matrix
$[D^{ep}]$	Material matrix relating elastic-plastic strains
DOF	Degree of freedom
e	Engineering strain
e_i	Residual
E	Elastic modulus
E_s	Secant modulus
EDM	Electric discharge machining
$E(Y_i)$	Expectation
f	Mathematical function; Fourier coefficient
$f(X_i;\beta)$	Subpopulation means
$f(X;\beta)$	Deterministic part
$\{f\}$	Nodal force vector of an element
$\{F\}$	Global nodal force vector

$\{F^{nr}\}$	Internal force vector (sum of element stresses).
FE	Finite element
FEA	Finite element analysis
FTI	Fatigue Technology Inc
G	Shear modulus
$\{hkl\}$	Miller indices describing a family of crystalline planes
I_a	Interference
I_0	Interference ratio
K	Bulk modulus; acoustoelactic constant
$[k]$	Stiffness matrix of an element
$[K]$	Global stiffness matrix
$[K^T]$	Tangent stiffness matrix
l	Current gauge length
L	Left part
L	Interval of length; measured length
l_0	Original gauge length
Δl	Change in gauge length under load
n	Integer; strain hardening exponent
$[N]$	Shape function matrix
p	Polynomial coefficients; internal pressure
p_p	Pressure on the boundary between elastic domain and plastic domain
P	Applied load
Q	Plastic potential
r	Radius
r_p	Radius at the boundary between elastic domain and plastic domain
R	Right part
R	Level of plastic anisotropy
S_1, S_2	X-ray elastic constants
$S(\beta)$	Sum of squared deviations
TOF	Time of flight
u	Radial displacement
$U1$	Measuring accuracy
$U3$	Volumetric accuracy

$\{u\}$	Displacement vector
UTS	Ultimate tensile strength
V	Original volume of material; wave speed in a stressed material
ΔV	Volume change of material
V_0	Wave speed in an unstressed material
X, X_i	Independent variable
Y, Y_i	Dependent variable; smoothed value
y	Estimated value
y_i	Average value of a dependent; i th data value
$\hat{Y}$	Estimated value

Greek Notations

θ	Angle
2θ	Angle between incident beam and diffracted beam for a stressed crystal
$2\theta_0$	Angle between incident beam and diffracted beam for a unstressed crystal
λ	Wavelength of incident monochromatic radiation
$d\lambda$	Plastic multiplier
ϕ, ψ	Angles of a diffracting lattice plane normal (rotation and tilt) relative to a fixed coordinate system.
ε	Strain; stochastic part; true strain
ε_i	Error
ε_m	Average or hydrostatic strain
$\varepsilon_{\phi\psi}$	Strain in the direction defined by angles ϕ and ψ
$\{\varepsilon\}$	Strain vector
$d\varepsilon_{ij}$	Total incremental strain
$d\varepsilon_{ij}^e$	Elastic incremental component
$d\varepsilon_{ij}^p$	Plastic incremental component
ε_x, ε_y, ε_z	Strain tensors in the x-, y-, and z- directions
σ	Stress; standard deviation; true stress; effective stress

σ_0	Engineering stress
σ_e	Equivalent stress
σ_y	Initial yield stress of a material
σ_m	Average or hydrostatic stress
σ_r	Radial stress
σ_θ	Hoop stress
σ_{ij}	stress tensor
$\{\sigma\}$	Stress vector of an element
$\sigma_x, \sigma_y, \sigma_z$	Stress tensors in the x-, y-, and z-directions respectively
$\sigma_1, \sigma_2, \sigma_3$	Principal stresses
σ^2	Constant variance
β	Unknown parameter, Bauschinger parameter
$\hat{\beta}$	Estimated parameter
$\gamma_{yz}, \gamma_{zx}, \gamma_{xy}$	Shear strain tensors
$\gamma_{r\theta}$	Shear strain
$\tau_{yz}, \tau_{zx}, \tau_{xy}$	Shear stress tensors
$\tau_{r\theta}$	Shear stress
υ	Poisson's ratio
$\{\delta\}^e$	Nodal displacement vector of an element
$\{\delta\}$	Global displacement vector
$\{\Delta\delta\}$	Displacement increment
$\Delta\upsilon$	Frequency shift
Π_{ij}	Piezo-spectroscopic tensor
α	Parameter

Superscripts

–	Unloading step
e	Element
el	Elastic component
pl	Plastic component
T	Transposition

Subscripts

1, 2, 3	Principal directions
hkl	Miller indices
i	Integer
ij	Matrix index
m	Integer, mandrel
n	Number of observation
p	Number of independent; elastic-plastic boundary
x, y, z	Directions relevant to Cartesian co-ordinate axis
r	Radial direction
θ	Hoop direction
ϕ, ψ	Angle vectors relative to a fixed coordinate system

TABLE OF FIGURES

1 Introduction

1.1 Background

It is well known that residual (locked-in) stresses are present in almost all manufactured components without and usually prior to the application of any service or other external loads. They can significantly affect engineering properties of structural components, notably fatigue life, dimensional stability, corrosion resistance, etc. Such effects can lead to considerable costs in repair or replacement of damaged components. In a worst situation, they could result in a disastrous accident. However, residual stresses are not always detrimental. In some cases, they are deliberately introduced to enhance fatigue resistance of structures. Hole cold expansion is a typical example, which has been widely used in the aircraft industry for decades, to produce beneficial compressive residual stresses around a hole to improve the fatigue life in fastener joints. Nevertheless, the residual stresses need to be fully characterised if any critical engineering structure is to be used within a safety margin. Nowadays, residual stress analysis is becoming a compulsory stage in the design of structures and in the estimation of their reliability under real service conditions.

A large number of reports on residual stresses have been published during the past decades to understand their effects upon component behaviour. Meanwhile, there is much literature on attempts to address the exploration of a variety of residual stress assessment methods to quantify the residual stresses arising from various causes. However, the complex nature of residual stresses and the multitude of their causes, in combination with the limitations of each measurement technique, constantly challenges the capability and applicability of the current suite of residual stress measurement techniques, as will be described in the following context in Section 1.4. A considerable effort remains to develop efficient and

cost-effective methods of residual stress analysis, despite certain progress having been achieved in the development and improvement of the measurement techniques.

A newly invented contour method (Prime and Gonzales, 2000), first proposed in 2000, is undoubtedly a welcome addition to the existing residual stress measurement families. It enables two-dimensional (2D) mapping of residual stresses on a cross-sectional surface of interest. Up to now (2003), it has been successfully demonstrated on a number of applications, such as welds (Prime et al., 2001), a hole cold expansion plate (Zhang et al., 2002) and forgings (Prime et al., 2003). Nevertheless, there is much room for this novel technique, obviously due to its new features, for further development and exploitation. Hence, the objective of this work is to systematically investigate the potential of the contour method, to explore diverse applications in a variety of fields, and to see if the contour method can be used as a reliable tool for residual stress evaluation.

1.2 Outline of the thesis

The present research mainly focuses on the exploration of a newly-invented residual stress measurement technique – the contour method – for its correctness and applicability. The outline of the thesis is briefly given below.

In Chapter 1, the background of the project is introduced. Then, the general knowledge on residual stresses is presented with a special emphasis on the techniques currently used for residual stress measurement.

Chapter 2 covers three major fields of theories extensively exploited in the present project: data smoothing analysis, theories of elasticity and plasticity, and the finite element method.

In Chapter 3, a literature review of the contour method and its principle are presented. Furthermore, the procedure of how to perform the contour method is given with a special focus on its experimental aspects. Finally, the theoretical principle and some practical issues relevant to experiments are simulated numerically.

Chapter 4 is mainly concerned with the development of an analytical theory of cold expansion problems in a finite plate, enabling comparison of the contour-method result to be made additionally from a theoretical point of view.

From Chapter 5 through to Chapter 7, the major issues are to address the application of the contour method. In Chapter 5, the first application of the contour method is demonstrated on a medium carbon steel (EN8) specimen subjected to 4% hole cold expansion. For validation and comparison purposes, analytical prediction, finite element simulation and X-ray diffraction measurement are performed.

Chapter 6 describes the implementation of the contour method on a 7475-T7351 aluminium alloy specimen with a 4% cold expanded hole with a particular emphasis on the experimental aspects.

Chapter 7 presents results of aluminium alloy welds received as real industrial components: a MIG 2024-T351 weld and a VPPA 2024-T351 weld. Longitudinal cross-sectional residual stress profiles are measured using the contour method for both welds. The comparison of the contour-method outcome with neutron and synchrotron X-ray diffraction measurements is made for the VPPA welded plate, and shows excellent agreement.

Finally, overall conclusions are drawn and future work is given in Chapter 8 based on the comprehensive study of the contour method presented above.

1.3 Residual stresses

1.3.1 Types of residual stresses

Residual stresses are stresses that remain within the bulk of material and are self-equilibrated in a body. In other words, the resultant force and moment that they produce must be zero in a system. Residual stresses may be classified according to the scale over which they are able to be observed, or the technique by which they are measured, or the cause (e.g. thermal or elastic mismatch) (Withers and Bhadshia, 2001). Here, the scale classification is adopted, by which the residual stresses are categorised into three types: type I, type II and type III (Lu et al., 1996; Wang, 1996; Withers and Bhadshia, 2001).

- Residual stresses of type I are macrostresses that are nearly homogeneous across a large range from several grains to many millimetres or even to centimetres and equilibrated within a whole body of a component. The macroscopic stresses can arise from heat treatment, machining, secondary processing and assembly.
- Residual stresses of type II (grain scale) are structural microstresses that are almost homogeneous across a microscopic range of one grain or a partial grain and are equilibrated over a few grains. The microstructural stresses often result from a mismatch in material properties such as coefficients of thermal expansion or elastic modulus between different phases or from phase transformations.
- Residual stresses of type III (atomic scale) are inhomogeneous across a submicroscopic range of several atomic distances within a grain and are equilibrated over a small portion of the grain.

Residual stresses can be present in any type or combination of two or three types in a material or component. In general, type-I stresses are based on the overall properties of bulk materials whereas type-II and type-III stresses are dependent on the microscopic properties of individual grains and/or phases.

1.3.2 Production of residual stresses

Manufacturing processes are the most common causes of residual stresses. Virtually all fabricating processes, for example, casting, welding, machining, moulding, heat treatment, introduce residual stresses into the manufactured components (Smith et al., 2001). It is unlikely that any component will be entirely free from residual stresses induced during manufacturing and processing. Another common cause of residual stress is in-service repair or modification. In some cases, residual stresses may also be induced later in the life of the structure by installation, assembly, occasional overloads, etc. The following are three major causes of residual stresses arising from manufacturing processes (Lu et al., 1996).

- From plastic deformation or forming, including rolling, drawing, extruding, bending, forging, pressing, spinning, shot-peening and laser shock.
- From machining, joining and coating, such as welding, brazing sprayed coating, cladding, electrodeposition, grinding.
- From heat or thermochemical treatment, such as quenching, laser and plasma heat treatment, carburizing, nitriding, case hardening.

1.4 Overview of current residual stress measurement techniques

In view of the importance of residual stresses, a variety of techniques for residual stress measurement have been developed. Some are destructive, while others are semi-destructive and others are non-destructive; some are able to measure 3D stress states whereas others are constrained to only a certain direction of stress; some can detect stress fields within materials yet others are limited to near surfaces. No single technique wins in every aspect. The choice of measurement methods is dependent on the specific application, techniques available and other conditions.

Almost all techniques of residual stress measurement rely on the measurement of deformation or strain in a material under study. With knowledge of the material properties, the measured strain can be converted into a corresponding stress. Destructive or semi-destructive methods normally involve mechanical processes, by which material is removed incrementally, resulting in a variation in strain in the remaining material. This strain change can be then related to the residual stress existing in the removed material. Material removal can introduce additional stresses, so modifying an original stress field. It is hence essential to minimise this effect. In contrast, non-destructive measurements are based on intrinsic properties of the material to enable strain measurement. For instance, variations in interplanar spacing, or velocities of ultrasonic waves, or magnetic properties can be used to determine the corresponding stresses.

In this section, the techniques currently most widely used for residual stress measurement will be briefly presented, including hole drilling, the ring core method, curvature, the Sachs method and the compliance method, which are destructive or semi-destructive, as well as non-destructive methods such as X-ray diffraction, synchrotron X-ray diffraction, neutron diffraction, piezo-spectroscopy, magnetic methods and ultrasonic. Some of these

techniques are summarised in Table 1-1 in terms of penetration, spatial resolution and accuracy.

Table 1-1 Main stress measurement techniques (Withers and Bhadshia, 2001)

	Methods	Penetration depths	Spatial resolution	Accuracy	Comments
Destructive	Curvature (distortion as stresses arise or relax)	10%~50% of thickness	5% of thickness; no lateral resolution	Limited by minimum measurable curvature	Unless used incrementally, stress field not uniquely determined; measures in-plane type I stresses
Semi-destructive	Hole drilling (distortion from stress relaxation)	~120% × hole diameter	50μm depth	±50MPa, limited by reduced sensitivity with increasing depth	Measure in-plane type I stresses
Non-destructive	Laboratory X-ray diffraction (atomic strain gauge)	<50μm (Al); <5μm (Ti); <1mm (with layer removal)	1mm laterally; 20μm depth	±20MPa, limited by non-linearities in $\sin^2\psi$ or surface condition	Non-destructive only as a surface technique; sensitive to surface preparation; peak shifts: type I, volume averaged type II; peak widths: types II, III
	Synchrotron X-rays (atomic strain gauge)	150~50mm (Al)	20μm lateral to incident beam; 1mm parallel to beam	$\pm 10\times10^{-6}$strain, limited by grain sampling statistics	Small gauge volume leads to spotty powder patterns; peak shifts; type I, II, volume averaged type II; peak widths: types II, III
	Neutrons (atomic strain gauge)	200mm (Al); 25mm(Fe); 4mm(Ti)	500μm	$\pm 50\times10^{-6}$strain, limited by counting statistics and reliability of stress free references	Access difficulties; low data acquisition rate; costly; peak shifts: type I, volume averaged type II (widths rather broad)
	Ultrasonics (stress related changes in elastic wave velocity)	>10cm	5mm	10%	Microstructure sensitive; types I, II, III
	Magnetic (variations in magnetic domains with stress)	10mm	1mm	10%	Microstructure sensitive; for magnetic materails only, types I, II, III
	Raman	<1μm	<1μm approx.	$\Delta\lambda\approx0.1\text{cm}^{-1}$ ≡50MPa	Types I, II

1.4.1 Destructive or semi-destructive techniques

Hole drilling

One of the most popular techniques for measuring residual stresses is the hole-drilling strain gauge method. The general principle of the procedure of the method involves drilling a small hole with 1~ 4 mm in diameter to a depth equal to its diameter in the centre of the strain rosette (Lu et al., 1996). The stresses will be relaxed when introducing a hole in the specimen. A specially designed strain gauge rosette is employed to measure the relieved surface strains, allowing a back-calculation of residual stress to be made.

Ring core method

The ring core method (Wolf and Bohm, 1971) is similar in principle to hole drilling except that an annular groove typically 15 ~ 150 mm in internal diameter is drilled outside the strain rosette instead of a hole inside the strain rosette. A typical depth of the annular groove is 25 ~ 150% of its internal diameter (Lu et al., 1996). The strain gauge rosette is placed on the surface of interest of a given component. The strain relaxation is measured as a function of machined depth. The residual stress before ring drilling is calculated based on the measured change in strain with depth.

Curvature

The curvature method is often used for measuring residual stresses within coatings and layers of a component with a simple geometry (Clyne and Gill, 1996). The curvature of the substrate is measured as successive layers of coating are deposited using a variety of methods including laser scanning, video, strain gauges, or profilometry. The corresponding

stress can be derived from the measured change in curvature as a function of deposit thickness.

The Sachs method

The Sachs method (Sachs, 1927) is a destructive method of determining the longitudinal, tangential and radial residual stresses, usually in bars and tubes. However, this method is limited to cylindrical components in which the residual stresses vary in the radial direction but not in the longitudinal and circumferential directions. The technique involves the attachment of a pair of strain gauges in the principal directions (longitudinal and tangential) on the outer surface of the cylinder. A thin annulus is removed from the inside of the cylinder and the resulting changes in length and diameter are measured by the strain gauges on the outside of the cylinder. The corresponding stress is then evaluated from the Sachs equations (Ozdemir, 1993).

Compliance method

The compliance method (Vaidyanathan and Finnie, 1971) involves machining a small slot incrementally to monitor the relaxation of stress using strain gauges attached on the free surface in the vicinity of the slot. The measured strains as a function of depth are then used to calculate the original stress. A fine slot with little stress introduced can be achieved by wire electric discharge machining (Cheng et al., 1994).

1.4.2 Non-destructive techniques

X-ray diffraction

The technique of X-ray diffraction measurement is described here in detail as it will be employed to measure surface residual stresses of a steel plate to be presented in Chapter 5. X-ray diffraction is one of most popular techniques that can be used to measure non-destructively the residual stress near or at surface of a component. It measures lattice deformations of crystalline materials with the lattice spacing of specific planes as gauge lengths. For a material without any residual stress, the lattice parameters are independent of the orientation of the diffracting {hkl} planes relative to the surface of the specimen. If the material is submitted to a stress, the lattice deformation becomes a function of the orientation according to linear elasticity.

The principle of X-ray diffraction measurement is based on Bragg's law, and it states the essential condition which must be met if diffraction is to occur (Cullity, 1956), as illustrated in Fig. 1-1,

$$2d_0 \sin\theta_0 = n\lambda \tag{1.1}$$

where d_0 is the lattice spacing of the unstressed crystal for any given set of hkl planes, $2\theta_0$ is the angle between the incident beam and the diffracted beam on the unstressed crystal, n is an integer and λ is the wavelength of the incident monochromatic beam.

Differentiation of Equation (1.1) leads to the relationship between the strain, ε, in a stressed crystal and the angular displacement of the interference line, as displayed in Fig. 1-2,

$$\varepsilon = \frac{d - d_0}{d_0} = -(\theta - \theta_0)\cot\theta_0 \tag{1.2}$$

where d is the lattice spacing of the stressed crystal, 2θ is the angle between the incident beam and the diffracted beam on the stressed crystal.

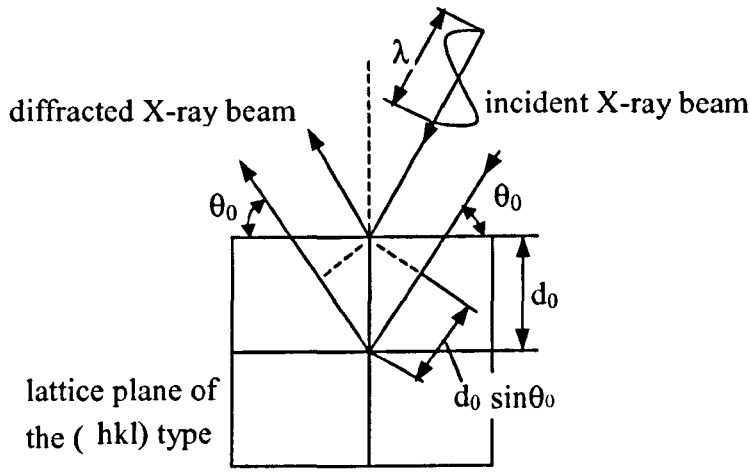

Figure 1-1 Stress-free crystals

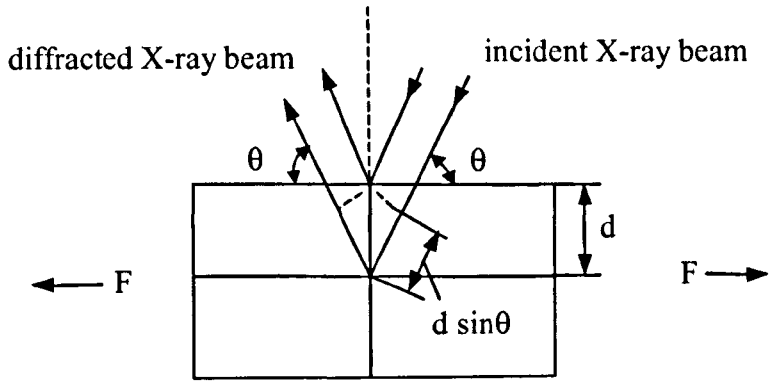

Figure 1-2 Stressed crystals

Rewriting Equation (1.2) in a broad format results in

$$\varepsilon_{\phi\psi} = \frac{d_{\phi\psi} - d_0}{d_0} = -(\theta_{\phi\psi} - \theta_0)\cot\theta_0 \tag{1.3}$$

where, $d_{\phi\psi}$ is the lattice spacing in the measured ϕ-direction and ψ-tilt of the scattering vector, ϕ and ψ are the angles of the diffracting lattice plane normal (rotation and tilt) relative to the fixed coordinate system, as indicated in Fig.1-3.

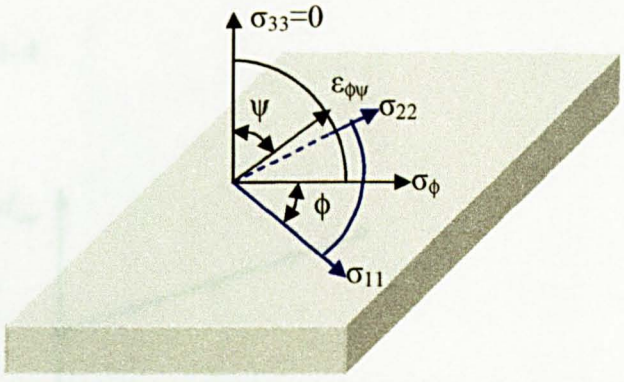

Figure 1-3 Schematic showing diffraction planes parallel to the specimen surface and at an angle $\phi\psi$. Note both σ_{11} and σ_{22} lie in the plane of the specimen surface

The penetration of X-rays into metals is very small. For example, the thickness of the surface layer that X-rays penetrate into steel that contributes two-thirds of the diffracted intensity of Cr Kα, which is the most intense characteristic line of chromium radiation produced from an X-ray tube, in the plane {211}, is approximately 6 μm at $\psi = 0$ and 4 μm at $\psi = 45^0$, varying with ψ tilt (Barrett and Massalski, 1980). As a result, only at or very near the surface, can the strain or stress be readily measured by the X-ray diffraction technique. However, this characteristic has a great advantage of allowing the measured strain to be converted conveniently into the stress by the assumption of plane stress conditions, under which the stress in the irradiated volume normal to the surface is zero, or $\sigma_{33} = 0$. For biaxial stress states, the most common form of equation used for X-ray measurement is in accordance to the classical technique of d versus $\sin^2\psi$ analysis, termed $\sin^2\psi$ technique or simply the ψ method (Noyan and Cohen 1987),

$$\frac{d_{\phi\psi}-d_0}{d_0}=\frac{1+\upsilon}{E}\sigma_\phi \sin^2\psi-\frac{\upsilon(\sigma_{11}+\sigma_{22})}{E} \tag{1.4}$$

where υ and E are Poission's ratio and elastic modulus respectively. σ_ϕ is the stress in the ϕ-direction to be determined on the surface, and σ_{11}, σ_{22} are the in-plane principal stresses. It can be seen from Equation (1.4) that the relationship of $d_{\phi\psi}$ vs. $\sin^2\psi$ is linear, as typically shown in Fig. 1-4.

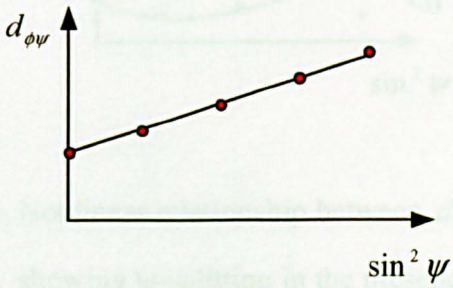

Figure 1-4 Linear relationship between $d_{\phi\psi}$ and $\sin^2\psi$

The σ_ϕ stress can be obtained directly from the slope of a least-squares line fitted to the measured data at multiple $d_{\phi\psi}$ vs. $\sin^2\psi$ tilts, if the elastic constants υ, E and the unstressed lattice spacing d_0 are known. In general, d_0 is not readily available and replaced by the stressed lattice spacing measured at $\psi=0$. Such a replacement is based on the fact that elastic strains introduce at most 0.1% deviation between the unstressed d_0 and the stressed $d_{\phi\psi}$ at any ψ for most materials (Noyan and Cohen 1987). Furthermore, d_0 is a multiplier to the slope and the error induced by the assumption in the stress evaluation will be less than 0.1%, which is negligible in comparison with the error induced by other factors (Noyan and Cohen 1987).

In the presence of shear stresses, $\tau_{13} \neq \tau_{23} \neq 0$, however, the relationship of $d_{\phi\psi}$ and $\sin^2\psi$ exhibits nonlinear behaviour, and ψ-splitting for $\psi > 0$ and $\psi < 0$, as illustrated in Fig. 1-5 (Noyan and Cohen 1987).

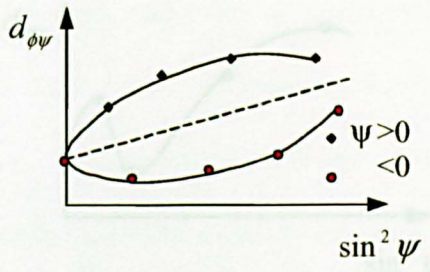

Figure 1-5 Nonlinear relationship between $d_{\phi\psi}$ and $\sin^2\psi$, showing ψ-splitting in the presence of shear stresses

In the case of gradients of the stress in the depth, the plots of $d_{\phi\psi}$ vs. $\sin^2\psi$ will be similar to Fig. 1-6. In such a case, the use of high ψ-points will minimise the errors due to the lower penetration depth.

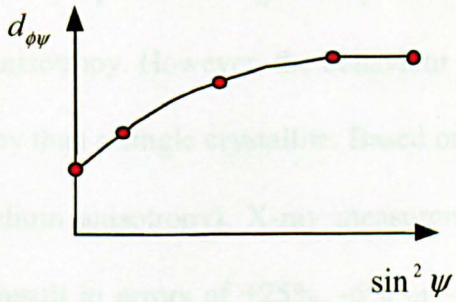

Figure 1-6 Curvature in the $d_{\phi\psi}$ vs. $\sin^2\psi$ plot, as a result of a large stress gradient

Further, an oscillation in the d vs. $\sin^2\psi$ data, illustrated in Fig. 1-7, reveals the presence of an inhomogeneous stress distribution within the irradiated volume for the lattice plane

used in the measurement (Noyan and Cohen 1987). If this effect is observed, the biaxial strain/stress analysis methodology described above may not be valid and a triaxial strain/stress analysis has to be considered.

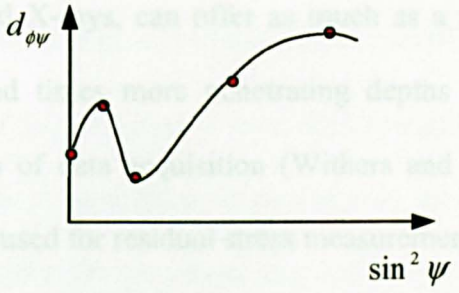

Figure 1-7 Oscillation in the $d_{\phi\psi}$ vs. $\sin^2\psi$ plot, indicating the presence of inhomogeneous stresses due to preferred texture

As we know, X-ray diffraction measures the strain of the diffracting crystallites inside the gauge volume and the stress-strain relationship is related to the X-ray elastic constants, which are dependent on the crystal plane on which the measurement is conducted. The bulk or macroscopic elastic properties are generally different from the values of the crystallites due to elastic anisotropy. However, the behaviour of a crystallite aggregate will show less overall anisotropy than a single crystallite. Based on the investigation of material anisotropy, for α Fe (medium anisotropy), X-ray measurements using {200}, {211} or {222} lattice planes will result in errors of +25%, -6% or –17% for the evaluated stress respectively if bulk elastic constants are adopted instead of X-ray elastic constants (Lu et al., 1996). Apparently, adoption of the plane {211} for X-ray measurement will produce the least error. Nevertheless, for highly textured materials, the X-ray elastic constants $S_1 = (\frac{\upsilon}{E})_{hkl}$ and $S_2/2 = \left(\frac{2(1+\upsilon)}{E}\right)_{hkl} \Big/ 2$ relative to the crystallographic planes

characterised by the Miller indices hkl should be used instead of bulk material elastic constants υ and E, which may be obtained from the literature or experiment.

Synchrotron X-rays

Synchrotron X-rays, or hard X-rays, can offer as much as a million times more intense beams and over a thousand times more penetrating depths than laboratory X-rays in combination with fast rates of data acquisition (Withers and Bhadshia, 2001). To date, three approaches have been used for residual stress measurement at near surface and within materials: traditional $\theta/2\theta$ scanning, high energy 2D diffraction and white beam high energy photons. However, the use of high energies leads to low scattering angles, resulting in an elongated gauge volume and thus poor resolution perpendicular to the scattering vector (Withers et al., 2002).

Neutron diffraction

The greatest advantage of neutrons over laboratory X-rays is that neutrons have much deeper penetration depths typically to many centimetres in engineering materials (Withers and Bhadshia, 2001). With translational and rotational movements of a sample under study, complete 3D strain maps can be achieved, and triaxial stresses are then readily evaluated in accordance with Hooke's law. There are actually two types of neutron diffraction techniques applied for residual stress measurement: conventional $\theta/2\theta$ scanning and time-of-flight (TOF) methods. The former utilizes continuous beams from a reactor source, and the latter uses pulsed beams from a spallation source. However, the weakness of the neutron diffraction technique is in its difficult access to facilities and high cost.

Piezo-spectroscopy

The technique of the piezo-spectroscopy is based on the frequency shift of characteristic luminescence lines (Raman or fluorescence) with variations in hydrostatic stresses, which can be expressed by the following relationship:

$$\Delta \upsilon = \prod_{ij} \sigma_{ij} \tag{1.5}$$

where $\Delta \upsilon$ is the frequency shift, $\prod_{ij}$ is the piezo-spectroscopic tensor and σ_{ij} is the stress tensor. The big advantage of the technique is in its high spatial resolution of less than a few microns with the help of an optical microscope (Muraki et al., 2002). The Raman and fluorescence spectroscopies are the two most important approaches widely used in this field for residual stress measurement. Raman spectroscopy is well suited to measure stresses in carbon fibres, and fluorescence spectroscopy is normally used to study stresses in sapphire, alumina and ceramics (Banerjee et al., 2001).

Magnetic methods

Magnetic methods are based on an interaction between the magnetization and elastic strain in ferromagnetic materials. The Barkhausen noise and magnetostriction methods are two commonly-used magnetic techniques for non-destructive residual stress measurement. The former relies on the abrupt motion of ferromagnetic domain walls, whereas the latter uses the effect of inverse magnetostriction. The magnetic methods are not only sensitive to the stress state, but also to the microstructural state of the component. The measurements therefore must be calibrated individually for different materials (Lu et al., 1996). The methods are fast and portable, but limited to ferromagnetic materials and inherently sensitive to the microstructural characteristics of the material.

Ultrasonic

The ultrasonic speed is changed when an ultrasonic wave passes through a stressed material, and the stress is evaluated based on variations of the wave speed, conceptually represented by the equation below:

$$V = V_0 + K\sigma \tag{1.6}$$

where V is the wave speed in a stressed material, V_0 is the wave speed in an unstressed material, K is the acoustoelactic constant which is dependent on material properties and σ is the stress. The technique offers an averaged stress along an entire ultrasonic path. The material texture and structure can influence the accuracy of the speed measurement (Tanala et al., 1995). The ultrasonic technique generally measures macrostresses both near surface and deep inside materials with the advantages of portability, no ionizing radiations, cheapness and fast implementation (Thompson, 1994).

1.5 References

[1] Banerjee, D., Rho, H., Jackson, H. E. and Singh, R. N. (2001). Characterization of residual stresses in a sapphire-fiber-reinforced glass-matrix composite by micro-fluorescence spectroscopy. Composites Science and Technology, Vol. 61, pp. 1639-1647.

[2] Barrett, C. S. and Massalski, T. B. (1980). Structure of Metals: Crystallographic Methods, Principles and Data. Oxford, Pergamon Press.

[3] Cheng, W., Finnie, I., Gremaud, M., Rosselet, A. and Streit, R. D. (1994). The compliance method for measurement of near surface residual stresses - application and

validation for surface treatment by laser and shot-peening. Journal of Engineering Materials and Technology, Vol. 116, pp. 556-560.

[4] Clyne, T. W. and Gill, S. C. (1996). Residual stresses in thermal spray coatings and their effect on interfacial adhesion: a review of recent work. Journal of Thermal Spray Technology, Vol. 5 (4), pp. 401-418.

[5] Cullity, B. D. (1956). Elements of X-ray diffraction. London, Addison-Wesley Publishing Company, Inc.

[6] Lu, J., James, M. and Roy, G. (1996). Handbook of measurement of residual stresses. Lilburn, Georgia, USA, The Fairmont Press, Inc.

[7] Muraki, N., Matoba, N., Hirano, T. and Yoshikawa, M. (2002). Determination of thermal stress distribution in a model microelectronic device encapsulated with alumina filled epoxy resin using fluorescence spectroscopy. Polymer, Vol. 43, pp. 1277-1285.

[8] Noyan, C. and Cohen , J. B. (1987). Residual Stress. New York, Springer-Verlag.

[9] Ozdemir, A. T. (1993). Residual stresses and fatigue performances at cold expanded fastener holes. PhD Thesis, Materials Discipline, Faculty of Technology, The Open University. Milton Keynes, UK.

[10] Prime, M. B. and Gonzales, A. R. (2000). The contour method: simple 2-D mapping of residual stresses. Proceedings of the sixth International Conference on Residual Stresses, 10-12 July, Oxford, U.K., IOM Communications Ltd, ISBN:1-86125-123-8, pp. 617-624.

[11] Prime, M. B., Hughes, D. J. and Webster, P. J. (2001). Weld application of a new method for cross-sectional residual stress mapping. Proceedings of 2001 SEM Annual Conference on Experimental and Appplied Mechanics, 4-6 June, Portland, OR, pp. 608-611.

[12] Prime, M. B., Newborn, M. A. and Balog, J. A. (2003). Quenching and cold-work residual stresses in aluminum hand forgings: contour method measurement and FEM prediction. Materials Science Forum, Vol. 426-432, pp. 435-440.

[13] Sachs, V. G. (1927). Zeitschrift fur Metalkunde, Vol. (**19**), pp. 352.

[14] Smith, D. J., Farrahi, G. H., Zhu, W. X. and McMahon, C. A. (2001). Obtaining multiaxial residual distributions from limited measurements. Materials Science and Engineering A: Structural Materials: Properties, Microstructure and Processing, Vol. 303 (**1-2**), pp. 281-291.

[15] Tanala, E., Bourse, G., M., F. and De Belleval, J. F. (1995). Determination of near surface residual stresses on welded joints using ultrasonic methods. NDT & E International, Vol. 28 (**2**), pp. 83-88.

[16] Thompson, R. B. (1994). An overview of ultrasonic measurement techniques. Proceedings of the Fourth International Conference on Residual Stress (ICRS-4), 8-10 June, Baltimore, Maryland USA, Society for Experimental Mechanics, Inc., pp. 97-111.

[17] Vaidyanathan, S. and Finnie, I. (1971). Determination of residual stresses from stress intensity factor measurements. Journal of Basic Engineering, Vol. (**93**), pp. 242-246.

[18] Wang, D. Q. (1996). Strain measurement using neutron diffraction. PhD thesis, Department of Materials Engineering, The Open University. Milton Keynes, UK.

[19] Withers, P. J. and Bhadshia, H. K. D. H. (2001). Residual stress: part 1- measurement techniques. Materials Science and Technology, Vol. 17, pp. 355-365.

[20] Withers, P. J., Preuss, M., Webster, P. J., Hughes, D. J. and Korsunsky, A. M. (2002). Residual strain measurement by synchrotron diffraction. Materials Science Forum, Vol. 404-407, pp. 1-12.

[21] Wolf, H. and Bohm, W. (1971). Arch. Eisenhuttenwes, Vol. (**42**), pp. 175.

[22] Zhang, Y., Fitzpatrick, M. E. and Edwards, L. (2002). Measurement of the residual stresses around a cold expanded hole in an EN8 steel plate using the contour method. Materials Science Forum, Vol. 404-407, pp. 527-534.

2 Fundamentals

The fundamentals of data smoothing analysis, theories of elasticity and plasticity, and the finite element method, with a particular emphasis on nonlinear finite element analysis, are introduced here as they will be extensively used in the course of the investigation of the contour method.

The technique of the data smoothing analysis will be employed to smooth the measured data and to remove the experimental error in using the contour method. The concept of the hole cold expansion is strongly associated with the hole cold expansion specimens in which the residual stress profiles will be measured by the contour method in Chapters 5 and 6. As an additional way to evaluate the residual stress distribution induced by the hole cold expansion process, the analytical model is developed on the basis of the theories of elasticity and plasticity, which will be detailed in Chapter 4. The finite element method will be mainly used for geometry modelling, stress calculation, and numerical simulation in Chapters 5, 6 and 7.

2.1 Data smoothing analysis

2.1.1 Introduction of data smoothing analysis

The purpose of smoothing analysis is to eliminate outliers, to reduce randomness, to minimise data measurement errors, and to obtain the underlying pattern and trend of given data. Generally, observed data can be divided into a smooth component and a rough component (Tukey, 1977):

$$\text{DATA} = \text{SMOOTH} + \text{ROUGH},$$

for a parametric smooth, $\text{DATA} = \text{FIT} + \text{RESIDUAL}.$

The SMOOTH or FIT represents the average behaviour or general trends of the data, while the ROUGH or RESIDUAL is the variation of observations about the means. The ROUGH should contain as little fluctuation in level as possible so that the SMOOTH can include as much pattern in the data as it can.

If the observed data is accurate enough, it might be sufficient to get the required values by interpolation. However, in most applications, the observed values are subject to measurement errors. The interpolation method would keep the errors rather than filter out them because it uses the observed values as basic data to interpolate non-observed values. On the contrary, smoothing techniques can more or less filter out the measurement errors and non-measured values can be inferred from the smoothed curve or surface.

A variety of smoothing techniques are reported in the literature of data analysis (Gowar and Baker, 1974; Abraham and Ledolter, 1983; Siegel, 1988; Moore and McCabe, 1989; Ratkowsky, 1989; Harrell, 2001). They differ substantially in methodology, efficiency, applicability, computational demands, mathematical complexity, etc. The classifications of smoothing techniques are also diverse. However, they share the same target of approximating the observed data by providing smoother results than the original observations. In the following context, we roughly divide the data smoothing techniques into three groups: parametric smooth with a special emphasis on linear regression, semi-parametric smooth, and non-parametric smooth. Semi- or non-parametric methods are well suited for the situation where little is known about the trend of the data under study as they allow more flexibility for the functions than typical parametric methods do.

2.1.2 Parametric smooth

Single-equation regression models are one of the most widely used parametric smoothers for fitting observed data. The goal of the regression analysis is to determine the values of parameters for a function that best fits a set of observed data. Statistically, it focuses on the mathematical relationship of a dependent variable Y and p independent (or explanatory, or regressor, or predictor) variables $X_1, X_2, X_3, ..., X_p$, with a set of n observations of X and Y, and also investigates the errors between the observed values Y and the estimated values y from the mathematical function f. In the most general form, the regression model consists of a deterministic part $f(X;\beta)$ and a stochastic part ε:

$$Y_i = f(X_i;\beta) + \varepsilon_i \qquad \text{for } 1 \le i \le n \qquad (2.1)$$

$$\text{where} \quad f(X_i;\beta) = E(Y_i) = y_i \qquad (2.2)$$

$f(X_i;\beta)$ are mathematical functions of the p independent variables X_i and unknown parameters $\beta = (\beta_1, \beta_2, \beta_3, ..., \beta_m)'$, which are estimated from the series of observations Y and X. Mathematically, $E(Y_i)$ or y_i represents the expectation or average value of the dependent Y_i. In other words, the $f(X_i;\beta)$ are subpopulation means describing the FIT part of the statistical model. The errors ε_i are the deviation of an individual observation from its subpopulation mean, which are assumed to be independent and normally distributed with zero mean (otherwise, the errors are not purely random and contain systematic errors) and standard deviation σ.

The key issue of estimating parameters β from the observed values is to choose parameter estimates $\hat{\beta} = (\hat{\beta}_1, ..., \hat{\beta}_m)'$ so that the fitted function $f(X_i;\hat{\beta})$ is close to the observations. The least-squares method is commonly used to estimate parameters, which minimises the sum of the squared deviations that is usually the measurement of the closeness:

$$S(\beta) = \sum_{i=1}^{n} [Y_i - f(X_i; \beta)]^2 \tag{2.3}$$

To make clear the confused concept on linearity and non-linearity in the field of data analysis, several special cases of the general regression models with one or two independent variables are presented in combination with corresponding graphical illustrations in Fig. 2-1.

(a) $Y_i = \beta_0 + \varepsilon_i$ (constant mean model)

(b) $Y_i = \beta_0 + \beta_1 x_i + \varepsilon_i$ (linear regression model with one independent variable)

(c) $Y_i = \beta_0 + \beta_1 x_i + \beta_2 x_i^2 + \varepsilon_i$ (quadratic model with one independent variable)

(d) $Y_i = \beta_0 \exp(\beta_1 x_i) + \varepsilon_i$ (exponential growth model with one independent variable)

(e) $Y_i = \beta_0 + \beta_1 x_{i1} + \beta_2 x_{i2} + \varepsilon_i$ (linear model with two independent variables)

(f) $Y_i = \beta_0 + \beta_1 x_{i1} + \beta_2 x_{i2} + \beta_{11} x_{i1}^2 + \beta_{22} x_{i2}^2 + \beta_{12} x_{i1} x_{i2} + \varepsilon_i$ (quadratic model with two independent variables)

In terms of parameters, all models above except the model (d) are linear in the parameters, which means that the derivatives of $f(X_i; \beta)$ with respect to the parameters in β do not depend on β. In contrast, the model (d) is nonlinear in the parameters, since its derivatives depend on β_0 and β_1. In terms of variables, the models (c), (d), (f) are nonlinear in the independent variables, whereas the models (a), (b) and (e) are linear in the independent variables since the derivatives of $f(X_i; \beta)$ with respect to elements in X_i are constant and do not depend on X_i. However, the model (d) is nonlinear both in the parameters and in the independent variables. It is also found that all the polynomial models are linear in the parameters even though they are non-linear in the independent variables.

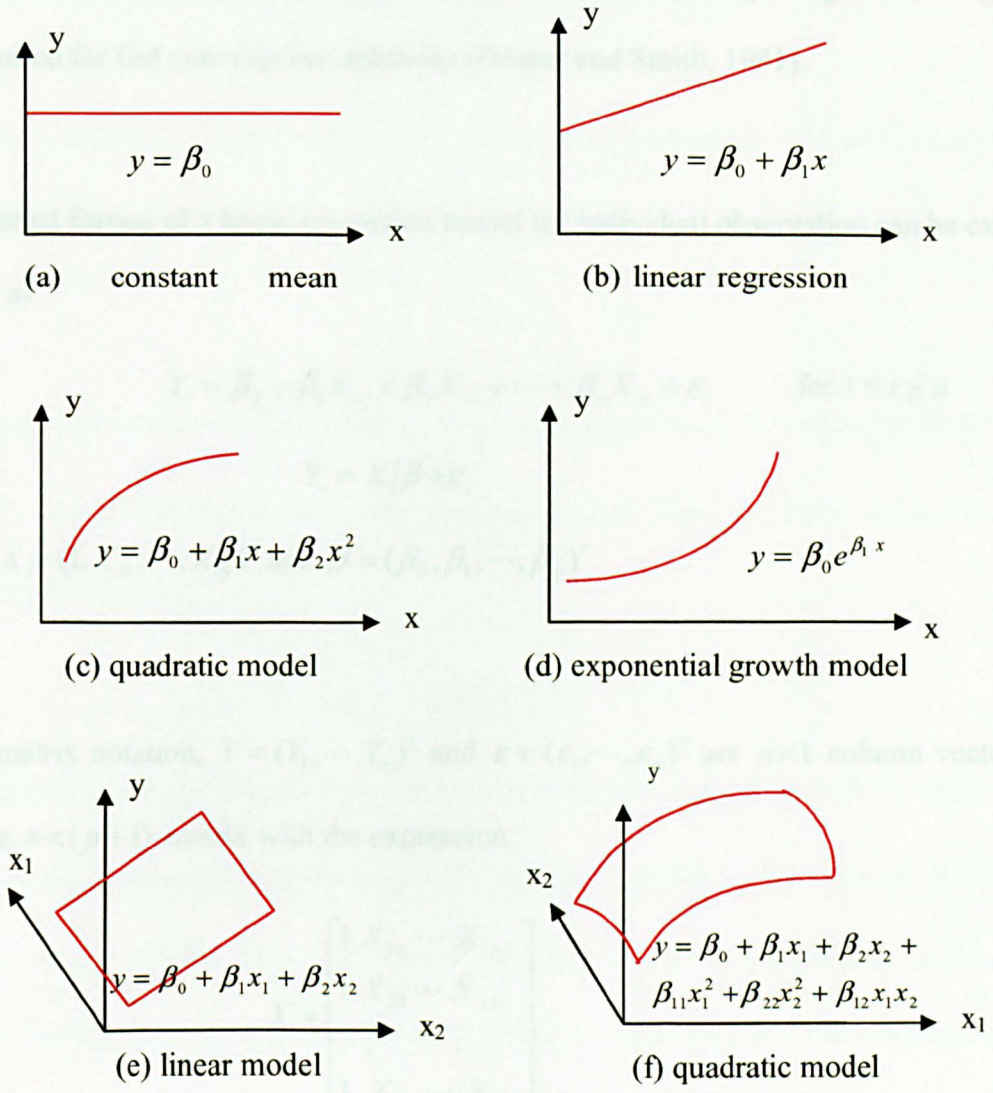

Figure 2-1 Graphical representation of regression models

Only the linear regression model will be presented here because it is the most popular parametric technique to fit scattered data. It is also the basic theory enabling ones to better understand more complex concepts like nonlinear models. Further, many nonlinear relationships, in certain situations, can be approximated, at least locally, by linear models. It is noted that the techniques used in this thesis for data smoothing are not constrained to the linear regression model. In the case of nonlinear regression models, the parameters have to be estimated using iterative techniques, such as linearization, steepest descent and

Marquardt's compromise, to minimize the error sum of squares, and good starting values are required for fast convergence solutions (Draper and Smith, 1981).

The general format of a linear regression model for individual observation can be explicitly written as

$$Y_i = \beta_0 + \beta_1 X_{i1} + \beta_2 X_{i2} + \cdots + \beta_p X_{ip} + \varepsilon_i \qquad \text{for } 1 \le i \le n \qquad (2.4a)$$

or

$$Y_i = X_i'\beta + \varepsilon_i \qquad (2.4b)$$

where $X_i = (1, X_{i1}, \cdots, X_{ip})'$ and $\beta = (\beta_0, \beta_1, \cdots, \beta_p)'$.

In the matrix notation, $Y = (Y_1, \cdots, Y_n)'$ and $\varepsilon = (\varepsilon_1, \cdots, \varepsilon_n)'$ are $n \times 1$ column vectors and X is the $n \times (p+1)$ matrix with the expression:

$$X = \begin{bmatrix} 1 & X_{11} & \cdots & X_{1p} \\ 1 & X_{21} & \cdots & X_{2p} \\ \vdots & \vdots & & \vdots \\ 1 & X_{n1} & \cdots & X_{np} \end{bmatrix}$$

So, the general regression model for $1 \le i \le n$ can be defined as:

$$Y = X\beta + \varepsilon \qquad (2.5)$$

As stated earlier, the ε_i are assumed to be independent and normally distributed with mean 0 and constant variance σ^2. The parameters of the model (2.4) or (2.5) are $\beta = (\beta_0, \beta_1, \cdots, \beta_p)'$ and σ.

The least squares criterion for estimation of $\beta = (\beta_0, \beta_1, \cdots, \beta_p)'$ can be expressed as minimizing

$$S(\beta) = \sum_{i=1}^{n} [Y_i - X_i'\beta)]^2 \tag{2.6}$$

The minimization of $S(\beta)$ leads to the least squares estimator $\hat{\beta}$, which satisfies the $p+1$ equations:

$$\hat{\beta} = (X'X)^{-1} X'Y \tag{2.7}$$

Substitution of the least squares estimate $\hat{\beta}$ in the model (2.5) yields the fitted values $\hat{Y} = X\hat{\beta}$. The differences between the observed values Y and the fitted values are called the residuals and given by

$$e = Y - \hat{Y} = Y - X(X'X)^{-1} X'Y \tag{2.8}$$

The residuals e_i can be thought of as estimates of the errors ε_i. Although the errors ε_i are independent by assumption, the residuals e_i are correlated. Analysis of residuals is essential to the validity of a particular application and to detect failures in the model assumptions because the residuals, e_i correspond to the errors, ε_i. The residuals derived from the least squares regression have two special properties:

- The sum and therefore the mean of the errors are zero.
- The variance of the errors is the smallest.

Perhaps the most widely-used regression techniques are attributed to polynomial fitting and trigonometric fitting. The polynomial regression uses finite parts of a Maclaurin or Taylor series whereas the trigonometric regression is based on the Fourier series. The following examples are presented with explicit equations frequently used in the regression analysis for univariate fitting or regression for curves. They can also be extended to bivariate fitting for surfaces or multivariate fitting.

The univariate polynomial model (one independent variable) can be written explicitly as:

$$p(x) = p_0 + p_1 \cdot x + p_2 \cdot x^2 + ... + p_n \cdot x^n \tag{2.9}$$

where, $p_0, p_1, p_2, ..., p_n$ are polynomial coefficients of function p.

The univariate trigonometric model (one independent variable) can be described explicitly as:

$$f(x) = f_0 + f_1 \cdot \cos x + b_1 \cdot \sin x + f_2 \cdot \cos 2x + b_2 \cdot \sin 2x + ... + f_n \cdot \cos nx + b_n \cdot \sin nx \tag{2.10a}$$

or $$f(x) = f_0 + f_1 \cdot \cos x + f_2 \cdot \cos 2x + ... + f_n \cdot \cos nx \tag{2.10b}$$

or $$f(x) = f_0 + f_1 \cdot \sin x + f_2 \cdot \sin 2x + ... + f_n \cdot \sin nx \tag{2.10c}$$

where, $f_0, f_1, f_2, ..., f_n; b_1, b_2, ..., b_n$ are Fourier coefficients of function f.

If the trigonometric function $f(x)$ is defined on an interval of length L, x will be replaced by $\frac{\pi x}{L}$.

2.1.3 Semi-parametric smooth

The parametric regression analysis tries to accommodate all data points by one single parameter function. A large error will be yielded if the regression model with one equation cannot fit all the data properly. In addition, individual observations can influence remote parts of the curve or surface in unexpected ways (Green and Silverman, 1994). However, a semi-parametric smooth alleviates this kind of problem by conducting local regression. Semi-parametric regression, or local regression, carries out approximation of observed data locally by fitting a parametric function in a small neighbourhood of data, called the span. This local regression is locally parametric, in contrast with the polynomial regression that is globally parametric based on the entire set of data. Only weak assumptions, such as

continuity of the function and its differentiability to some order in the neighbourhood are applied. In parametric regression, the degree of the polynomial controls the complexity of the smooth and the extra complexity can produce significant distortion globally. However, a semi-parametric smooth allows local use of additional complexity and thus better captures complex features such as peaks or valleys. The span defines a window of neighbouring points to be used in the smoothing calculation for each data point. This window moves across the data set as the smoothed response value is calculated for each independent value. A large span increases the smoothness and captures the general trend, but may severely attenuate the more interesting features. The optimal span value depends on the data set and the smoothing method, and usually requires some experimentation to find. For all locally weighted smoothing methods, if the span is less than 1, it is interpreted as the percentage of the total number of data points.

The Lowess and Loess are two most popular semi-parametric smoothers, derived from a locally weighted regression approach (Cleveland, 1979; Cleveland and Devlin, 1988). They both use weighted least squares fitting techniques and are resistant to outliers. For Lowess, the regression is performed based on a linear (first degree) polynomial, whereas for Loess, the regression is conducted according to a quadratic (second degree) polynomial.

A spline smoother (Wahba, 1990) is also an important class of semi-parametric smoothers based on piecewise cubic polynomial fits, where constraints are imposed to assure smoothness between segments at the knots that define segment end points.

2.1.4 Non-parametric smooth

A moving average, one of the non-parametric smooth methods, smoothes data by replacing each data point with the average of the neighbouring data points specified within a span:

$$Y_i = \frac{1}{2N+1}(y_{i+N} + y_{i+N-1} + \ldots + y_{i-N}) \tag{2.11}$$

where Y_i is the smoothed value for the ith data point, N is the number of neighbouring data points on either side of y_i, and $2N+1$ is the span. It is noted that the end points cannot be smoothed for the moving average.

Other non-parametric techniques such as the moving median and other median-based smoothers are often used when outliers become an issue. For example, a moving median of length 3 can be expressed by:

$$Y_i = median\{y_{i-1}, y_i, y_{i+1}\} \tag{2.12}$$

2.1.5 Extrapolation

The raw data provided by experiment normally contain missed or bad values more often occurring at ends due to the difficulties or restrictions arising from measurement or equipment used. The bad values that are far from true have to be removed from the measured data. Thus, extrapolation of the missed and removed data is unavoidable if this situation arises. In general, extrapolation of data is not only difficult but also very dangerous. It sometimes presents unexpected and illogical results, and therefore care should be applied when using the technique of extrapolation. In addition, both the extrapolated data and the calculated results deduced from them need studying further if they are of major interest. Otherwise, they should not be taken seriously or even not be

used for any purposes. The most popular and widely used extrapolation method is linear extrapolation because of the advantages of ease of use and simplicity.

2.1.6 Importance of data smoothing analysis

With the development of the data smoothing analysis enhanced by sophisticated computation techniques, there is a wide variety of smoothing methods including local averaging, running medians, moving averaging, cubic spline, polynomial regression, Loess local regression, mostly available in the commercial software such as MATLAB and MathCad. It is clear that each data smoothing technique has its own characteristics, strengths and weaknesses, and there is no definite winner in all circumstances. Generally speaking, choice of a particular data smoothing method or model primarily depends on the objective of the application, the goal of the data smoothing, data available, degree of accuracy required, degree of complexity desired, and the tolerable cost. In most applications, the smoothing accuracy is the main concern. However, increasing the accuracy usually raises substantially the costs of data acquisition, computer time and labour time. However, the smoothing accuracy or goodness-of-smooth is not the only criteria to judge the goodness of data smoothing, and trade-off between the goodness-of-smooth quantified by the residual sum of squares and the roughness is particularly critical. For example, 'high smoothing accuracy' can be typically obtained from high order polynomial regression. However, use of an overly high order could make the smoothed result follow the noise in the measured data rather than represent the underlying pattern of the data. On the other hand, over-smoothness, for instance, resulting from a too low order of the polynomial regression, may lead to loss of important peak or valley information. One of the important factors for selecting an appropriate smoothing model for a given application is the analysis of the smoothing error, which should carry as little pattern and as much randomness as possible.

Another critical issue worth mentioning is the relationship between parametric and semi- or non-parametric techniques. The resulting data smoothed by semi- or non-parametric techniques should not be fitted further by a parametric model because the act of semi- or non-parametric smoothing invalidates the assumption that the errors are normally distributed. Instead, semi- or non-parametric smoothing should be considered a powerful alternative of data exploration techniques.

2.2 Theories of elasticity and plasticity

Elasticity theory is primarily concerned with the behaviour of material subjected to loads below the yield stress, while plasticity theory mainly deals with the response of material subjected to loads exceeding the yield stress. A thorough understanding of the mechanical behaviour and constitutive relationships between stresses and strains is fundamentally essential for the safe design of all structures.

2.2.1 Features of stress-strain behaviour

Stress-strain curve

A uniaxial tension test is of importance to help understanding of the fundamental behaviour of a material, which changes at several critical points as the load is progressively increased, as displayed in Fig. 2-2. Initially the stress varies linearly with the strain below the proportional limit. On further loading, the relationship between stress and strain is no longer linear but the material is still elastic. The maximum stress without producing permanent deformation is the yield point. Below the yield point, any deformation that

occurs during loading will disappear upon removal of the load. There is usually little difference between the yield point and the proportional limit. After the yield point, the stress increases with further strain and strain hardening or work hardening occurs. This is due to the effect of the material being able to withstand a greater load despite the uniform reduction in a cross-sectional area. When the level of the stress reaches the ultimate tensile strength (UTS), the rate of strain hardening is unable to keep pace with the rate of reduction in the cross-section area and necking or local straining starts leading to fracture. The portion of the stress-strain curve below the yield point is the elastic portion, and beyond is the plastic portion. Thus, proportional limit, yield point and strain hardening can be readily derived from the results of the uniaxial stress-strain curve.

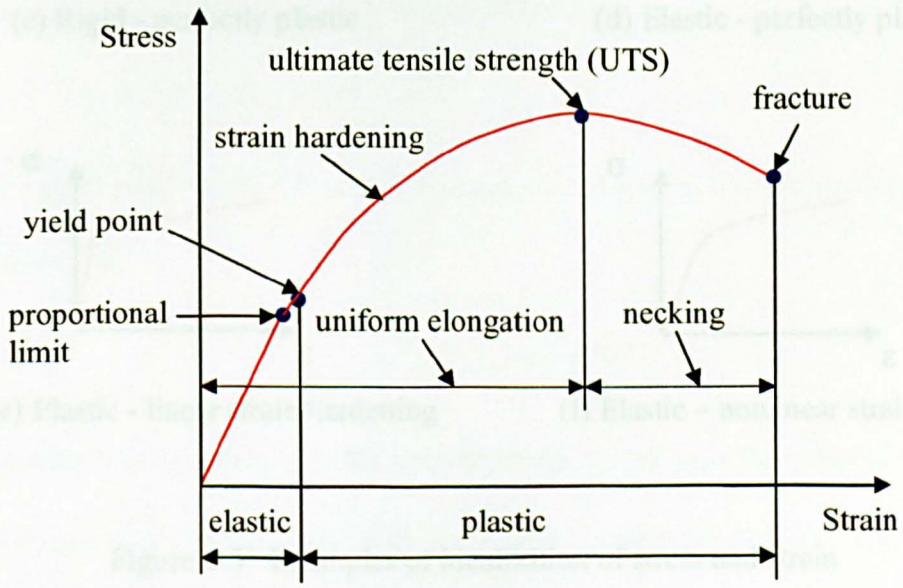

Figure 2-2 Typical stress-strain curve for a mild steel

Fig. 2-3 illustrates several typical idealized stress-strain curves (Shames and Cozzarelli, 1997). In each case, the objective is to describe the dominant features of the stress-strain relationships.

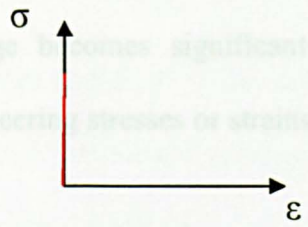

(a) Rigid

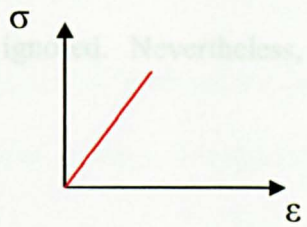

(b) Linear elastic

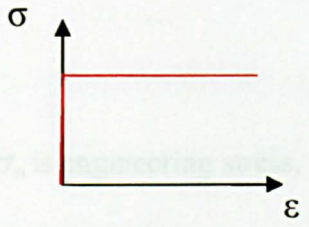

(c) Rigid - perfectly plastic

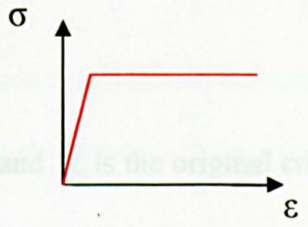

(d) Elastic - perfectly plastic

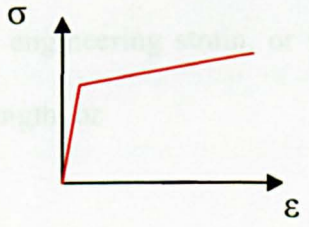

(e) Elastic - linear strain hardening

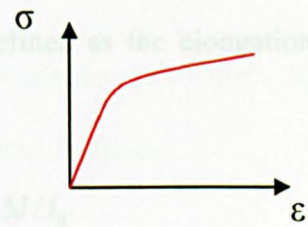

(f) Elastic – nonlinear strain hardening

Figure 2-3 Examples of idealisation of stress and strain relationships (Shames and Cozzarelli, 1997)

Engineering stress and true stress

A uniaxial stress-strain curve is usually supplied either in the form of engineering stress versus engineering strain, or true stress versus true, or log, strain. However, the engineering stress-strain curve does not give a true indication of the deformation

characteristics of a material because it is based entirely on the original dimensions of the specimen that varies continuously during loading (Dieter, 1976). In the plastic range, this change becomes significant and should not be ignored. Nevertheless, the true and engineering stresses or strains are convertible.

Engineering stress and strain are normally related to an original geometry of a specimen. Engineering stress, or nominal stress, is defined to be the force per unit of the original cross-sectional area, or

$$\sigma_0 = P / A_0 \tag{2.13}$$

where σ_0 is engineering stress, P is the applied load, and A_0 is the original cross-sectional area of the specimen normal to P in a simple tensile test.

Similarly, engineering strain, or nominal strain, is defined as the elongation per unit of original length, or

$$e = (l - l_0)/l_0 = \Delta l / l_0 \tag{2.14}$$

where e is engineering strain, l is the current gauge length, l_0 is the original gauge length prior to application of the load, and Δl is the change in gauge length under load.

To derive the relationship between the true and engineering stresses or strains, it is assumed that material is incompressible by neglecting the very small changes in volume that occur during a tensile test. This assumption that the volume of the materials remains constant throughout the loading is experimentally well verified, thus

$$Al = A_0 l_0 \tag{2.15}$$

where A is the current cross-sectional area.

The true stress σ is the actual stress based on the actual area corresponding at every instant to the current value of load and can be expressed in terms of engineering stress and engineering strain by

$$\sigma = \frac{P}{A} = \frac{P}{A_0} \cdot \frac{l}{l_0} = \sigma_0 \cdot \frac{l_0 + \Delta l}{l_0} = \sigma_0 (1 + e) \tag{2.16}$$

Similarly, the true strain, or logarithmic strain, ε, is associated with an instantaneous value of gauge length, which changes with increase in the applied load and is defined in terms of engineering strain as:

$$\varepsilon = \int_{l_0}^{l} \frac{dl}{l} = \ln \frac{l}{l_0} = \ln \frac{l_0 + \Delta l}{l_0} = \ln(e + 1) \tag{2.17}$$

In general, engineering stress-strain data is almost sufficient for small strain analyses while a true stress-strain curve is expected for large strain plastic analyses.

Anisotropy and the Bauschinger effect

There are two notable phenomena of material behaviour commonly encountered in the tension-compression testing of metals — anisotropy and the Bauschinger effect. Plastic deformation occurs when a metal is loaded over its yield stress. The crystallographic directions in each grain of the metal are gradually rotated towards a common axis dictated by the loading, thus creating a preferred orientation. In particular, the grains initially orientated at random (isotropy) are rendered anisotropic when plastically deformed. This implies that the yield stress and ductility of the metal may vary in different directions.

If a material is plastically deformed and unloaded, and then reloaded in the reverse direction until yield, it is found that the yield stress in the reloading or reversed direction is much less than the yield stress in the original direction. This phenomenon is the Bauschinger effect and has been observed in polycrystalline metals as well as single crystals (Khan and Huang, 1995). This is the consequence of the anisotropy of the dislocation introduced by the previous loading.

2.2.2 Elasticity theory

Elasticity theory offers a mathematical relationship of stress and strain that describes the elastic response of materials below the yield stress. The linear relationship between stress and strain in the elastic range for homogeneous and isotropic engineering materials has been well established experimentally, which obeys the generalized Hooke's law and is expressed as (Timoshenko and Goodier, 1970):

$$\begin{aligned}
\varepsilon_x &= \frac{1}{E}\left[\sigma_x - \upsilon(\sigma_y + \sigma_z)\right] \\
\varepsilon_y &= \frac{1}{E}\left[\sigma_y - \upsilon(\sigma_x + \sigma_z)\right] \\
\varepsilon_z &= \frac{1}{E}\left[\sigma_z - \upsilon(\sigma_x + \sigma_y)\right] \\
\gamma_{yz} &= \frac{\tau_{yz}}{2G} \\
\gamma_{zx} &= \frac{\tau_{zx}}{2G} \\
\gamma_{xy} &= \frac{\tau_{xy}}{2G} \\
G &= \frac{E}{2(1+\upsilon)}
\end{aligned} \tag{2.18}$$

where, ε_x, ε_y, ε_z are the strain tensors in x-, y-, and z- directions; $\sigma_x, \sigma_y, \sigma_z$ are the stress tensors in x-, y-, and z-directions respectively; $\gamma_{yz}, \gamma_{zx}, \gamma_{xy}$ are shear strain tensors and

$\tau_{yz}, \tau_{zx}, \tau_{xy}$ are shear stress tensors, where by convention, for the mixed indices, the first index indicates direction and the second index defines the normal of the plane in which they acts; E is Young's modulus; G is shear modulus; υ is Poisson's ratio.

However, it would be physically meaningful to distinguish between strains only related to a change in shape and those only related to a change in volume. The relations above can be written in the form (Johnson and Mellor, 1962):

$$\begin{aligned}
\varepsilon_x &= \frac{1}{2G}(\sigma_x - \sigma_m) + \frac{(1-2\upsilon)}{E}\sigma_m \\
\varepsilon_y &= \frac{1}{2G}(\sigma_y - \sigma_m) + \frac{(1-2\upsilon)}{E}\sigma_m \\
\varepsilon_z &= \frac{1}{2G}(\sigma_z - \sigma_m) + \frac{(1-2\upsilon)}{E}\sigma_m \\
\gamma_{yz} &= \frac{\tau_{yz}}{2G} \\
\gamma_{zx} &= \frac{\tau_{zx}}{2G} \\
\gamma_{xy} &= \frac{\tau_{xy}}{2G}
\end{aligned} \tag{2.19}$$

$$\begin{aligned}
\sigma_m &= \frac{\sigma_x + \sigma_y + \sigma_z}{3} \\
\varepsilon_m &= \frac{\varepsilon_x + \varepsilon_y + \varepsilon_z}{3} = \frac{\sigma_m}{3K}
\end{aligned} \tag{2.20}$$

where, σ_m, ε_m are the average or hydrostatic stress and strain; $(\sigma_x - \sigma_m)$, $(\sigma_y - \sigma_m)$ and $(\sigma_z - \sigma_m)$ are reduced or deviatoric stresses and written in the form σ_x', σ_y' and σ_z' respectively. In response to the hydrostatic load, the material will change its volume. This behaviour is described by the bulk modulus, K, which is technically defined as the ratio of hydrostatic stress to the relative volume change that is related to the three strains:

$$K = \frac{\sigma_m}{\Delta V / V} = \frac{\sigma_m}{\varepsilon_x + \varepsilon_y + \varepsilon_z} = \frac{E}{3(1-2\upsilon)} \tag{2.21}$$

where, ΔV is the volume change of the material and V is the original volume of the material.

The complete elastic stress-strain relations may be written in the following format using a double suffix notation (Johnson and Mellor, 1962),

$$\begin{aligned} \varepsilon_{ij} &= \frac{\sigma'_{ij}}{2G} + \frac{(1-2\upsilon)}{E}\delta_{ij}\sigma_m \\ \sigma_m &= \frac{1}{3}\sigma_{ij} \end{aligned} \tag{2.22}$$

The delta symbol, δ_{ij}, is equal to unity when $i = j$ and to zero when $i \neq j$.

2.2.3 Plasticity theory

Plasticity theory deals with the mathematical relationship of stress and strain that primarily characterizes the plastic response of materials over the yield stress. It consists of three basic sub-theories: yield criterion, flow rule and hardening rule.

Yield criterion

The yield criterion is a single-valued (scalar) measure of the stress state to determine the initiation of yielding by comparison with the yield stress normally obtained from a uniaxial test. For multi-stress states, it is described as a function of the individual components of stresses, $f(\sigma)$, which can be interpreted as an equivalent stress, σ_e:

$$\sigma_e = f(\sigma) \tag{2.23}$$

where σ are the stress states at any point in a solid. When the equivalent stress reaches the initial yield stress of a material, σ_y,

$$\sigma_e = \sigma_y \tag{2.24}$$

yielding starts and the material will develop plastic strains. Otherwise, the material is elastic and the stresses will develop based on the elastic stress-strain relationship. The stress state and the yield criterion can determine when plastic straining will develop.

A commonly-used yield criterion is the Von Mises yield criterion which physically implies that yielding will occur whenever the internal energy of distortion (equivalent stress) arrives at the yield stress of the material. The Von Mises equivalent stress is defined below in terms of principal stresses $\sigma_1, \sigma_2, \sigma_3$:

$$\sigma_e = \sqrt{\tfrac{1}{2}[(\sigma_1 - \sigma_2)^2 + (\sigma_2 - \sigma_3)^2 + (\sigma_1 - \sigma_3)^2]} \tag{2.25}$$

An alternative yielding criterion is the Tresca yield criterion which physically means that yielding will occur whenever the maximum shear stress reaches the yielding stress of the material, which is indicated below in terms of principal stresses $\sigma_1, \sigma_2, \sigma_3$:

$$\sigma_e = \max\{|\sigma_1 - \sigma_2|, |\sigma_1 - \sigma_3|, |\sigma_2 - \sigma_3|\} \tag{2.26}$$

Previous research has showed that the Von Mises criterion has a general better agreement with experiments performed on ductile materials than the Tresca criterion (Calladine, 2000).

Flow rule

The plastic flow rule determines the direction of plastic straining when yielding occurs. After yielding, the total incremental strain, $d\varepsilon_{ij}$, consists of two parts: an elastic incremental component, $d\varepsilon_{ij}^{e}$ and a plastic incremental component, $d\varepsilon_{ij}^{p}$:

$$d\varepsilon_{ij} = d\varepsilon_{ij}^{e} + d\varepsilon_{ij}^{p} \tag{2.27}$$

The $d\varepsilon_{ij}^{e}$ is given by the relationship of the generalized Hooke's law as follows:

$$de_{ij}^{e} = \frac{d\sigma_{ij}^{'}}{2G} + \frac{(1-2\upsilon)}{E}\delta_{ij}d\sigma_{m} \tag{2.28}$$

The $d\varepsilon_{ij}^{p}$ is governed by the flow rule as (Cook et al., 1989):

$$d\varepsilon_{ij}^{p} = d\lambda\frac{\partial Q}{\partial \sigma_{ij}} \tag{2.29}$$

where $d\lambda$ is the plastic multiplier (scalar) that represents the magnitude of the plastic strain increment vector and varies throughout the loading path. Q is the plastic potential that is a function of the stresses. If Q is the yield function, the flow rule is associative and the plastic strains develop in a direction normal to the yield surface. The associated flow rule is normally used for ductile materials, whereas a non-associated rule is better suited to soil and granular materials (Cook et al., 1989).

Hardening rule

The hardening rule describes how the initial yield criterion changes with progressive plastic straining, and how the yield surface is modified during plastic flow. Moreover, it determines when the material will yield again if the loading is continuing or if the loading

is reversed. Two basic hardening rules are commonly applied: isotropic hardening and kinematic hardening.

- **Isotropic hardening**

Isotropic hardening implies that a yield locus expands in size without change in shape, and the yield locus is uniquely defined by the final plastic state of stress regardless of the actual strain path (Hill, 1950). This suggests that the material remains isotropic without the Bauschinger effect throughout the plastic deformation (Chakrabarty, 2000). For the Von Mises yield criterion, the yield locus increases uniformly in all directions with plastic flow, as shown in Fig. 2-4. The subsequent yield in compression is equal to the highest equivalent stress attained during the tension phase for a uniaxial tensile and compressive cycle, as displayed in Fig. 2-5. Isotropic hardening is normally used for large strain or proportional (non-cyclic) loading simulations (ANSYS, 2000).

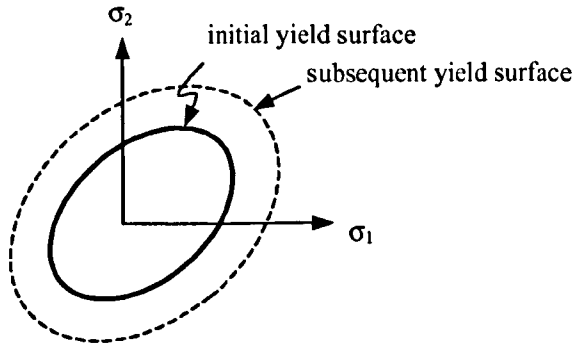

Figure 2-4 Isotropic hardening

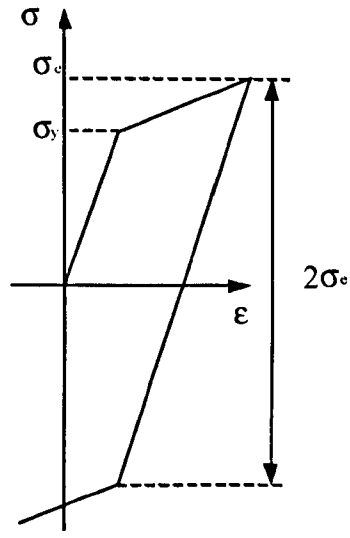

Figure 2-5 One-dimensional illustration of isotropic hardening

- **Kinematic hardening**

Kinematic hardening assumes that the yield locus remains constant in both size and shape and translates in the direction of yielding, as illustrated in Fig. 2-6. The subsequent yield in compression is decreased by the amount that the yield stress in tension is increased, so that a $2\sigma_y$ difference always exists between the respective yields for a uniaxial tensile and compressive cycle, as indicated in Fig. 2-7. This is the phenomenon of the Bauschinger effect, observed in most metals. The kinematic hardening rule implies that an initially isotropic material will no longer be isotropic after yielding. So it can predict the development of anisotropy and the Bauschinger effect (Chakrabarty, 2000). The kinematic hardening model is generally used for small strain and cyclically loaded applications where the Bauschinger effect may be significant, and is not appropriate for large strain cases (ANSYS, 2000).

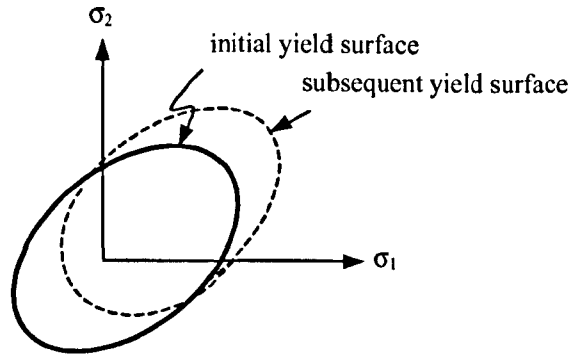

Figure 2-6 Kinematic hardening

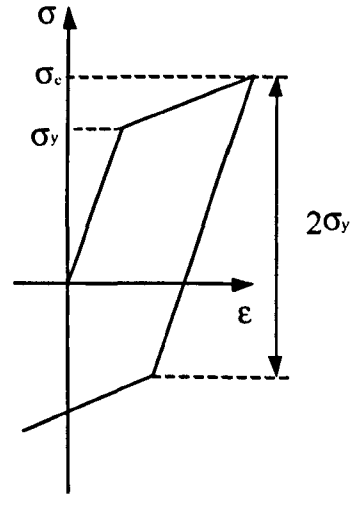

Figure 2-7 One-dimensional illustration of kinematic hardening

A more complicated hardening model extended from the concept of kinematic hardening is combined or mixed hardening that claims that the yield locus expands in size along with translation.

2.3 Finite element method

The finite element (FE) method is a computer-based numerical technique which allows engineering behaviour to be approximated in a discrete manner where analytical methods are difficult or impossible to deal with. It is now a well-established technique for analysing

the behaviour of structures subjected to a variety of static or dynamic loads. It can be used to calculate deflection, stress, vibration, buckling behaviours and many other phenomena. The technique involves a discretisation procedure where a finite number of elements are assembled to describe the initial shape of a complex solid. These elements are represented by a number of nodes for which nodal displacements or nodal forces can be applied to simulate external loads. Equations relating nodal displacements to nodal forces are defined for each of these elements which can then be solved using a number of numerical techniques. In this way, a continuum, supposed to have infinite degrees of freedom (DOFs), is discretised into an approximated system with finite DOFs.

It should be kept in mind that the finite element method is an efficient and powerful technique to solve complicated mathematical models that are difficult to solve with satisfaction by other approaches such as classical theoretical analysis. It cannot provide more information than the mathematical model itself (Bathe, 1996). However, the theoretical model is always associated with the issue how to solve the model efficiently by the finite element method.

2.3.1 FE linear analysis

FE linear analysis offers solutions to linear systems with a constant coefficient matrix. It is an important and basic procedure, always performed preceding non-linear analysis. In general, three main assumptions are applied in the FE linear analysis (Bathe, 1996). Firstly, the displacements or deformations are presumed to be infinitesimally small because all integrations are based on the original shapes of the elements. Secondly, the material under consideration is linearly elastic. This assumption leads to a constant stress-strain matrix. Finally, the boundary conditions should remain unchanged in the course of application of

the loads to the element assemblage. Otherwise, it will not produce constant constraint relationships. The standard formulation for the finite element analysis (FEA) is the displacement method based on the principle of virtual displacements (work).

Imagine a point within an element. The displacement $\{u\}$ of the point as a function of nodal displacement of the element $\{\delta\}^e$ can be expressed as:

$$\{u\} = [N]\{\delta\}^e \tag{2.30}$$

where $[N]$ is the shape function matrix associated with the element. The compatibility between the nodal displacement and the strain within the element is given by:

$$\{\varepsilon\} = [B]\{\delta\}^e \tag{2.31}$$

where $[B]$ is the strain-displacement matrix containing the derivatives of $[N]$ and the strain vector $\{\varepsilon\}$. Finally, the constitutive law allows the stresses to be related to the strains through the material matrix $[D]$ as:

$$\{\sigma\} = [D]\{\varepsilon\} \tag{2.32}$$

Based on the principal of virtual work, the relationship of nodal force $\{f\}$ and nodal displacement $\{\delta\}^e$ can be connected by the stiffness matrix of the element $[k]$ as follows:

$$\{f\} = [k]\{\delta\}^e \tag{2.33}$$

where $[k]$ is given by:

$$[k] = \iiint [B]^T [D][B]\, dx\, dy\, dz \tag{2.34}$$

Once the individual stiffness matrices of each element have been obtained, they are assembled into a global stiffness matrix, $[K]$, associated with the nodal forces and the nodal displacements of the overall structure,

$$\{F\}=[K]\{\delta\} \tag{2.35}$$

where, $\{F\}$is the global force vector and $\{\delta\}$ is the global displacement vector. A large number of calculations and data processing arise when computing the element stiffness matrices and assembling them into the global stiffness matrix. However, the element stiffness matrix and the global stiffness matrix are both symmetric for linear problems. This characteristic makes it possible for assembly of the global stiffness matrix to save a great amount of computer memory and thus to reduce substantially the computing time required for a solution. This is achieved by numbering nodes of the discrete model in an optimal manner. Most commercial FE codes provide an automatic procedure that minimises the wave front of the global stiffness matrix by reordering the element numbers and checking the element connectivity. A Gaussian elimination technique is usually employed to solve a set of simultaneous equations.

2.3.2 FE non-linear analysis

For many structural stress analyses, a linear FEA provides an acceptable and cheap solution to the problem of loaded deformable structures within the linear elastic range of the material. Beyond the elastic range, however, the material behaviour becomes non-linear and is characterised by irreversible plastic deformation. The nonlinear behaviour is mainly described by a yield criterion determining the stress level at which plastic strains commence and a relationship between stresses and strains indicating the post-yielding behaviour.

The procedure of an elastic-plastic FE solution is essentially based on the linear elastic FEA procedure. Since the nonlinear stress-strain relation is path-dependent, an incremental

sequence needs to be considered. So, the incremental stress is related with the incremental strain through the elastic-plastic material matrix, $[D^{ep}]$:

$$\{d\sigma\} = [D^{ep}]\{d\varepsilon\} \tag{2.36}$$

and will be calculated at any step of the incremental process. As a result, the global stiffness matrix $[K]$ in Equation (2.35) will be continuously varying as a function of applied load. This response cannot be achieved by directly solving the set of linear equations. An iterative series of linear approximations with corrections have to be relied on. A Newton-Raphson method is a most frequently used iterative process to iterate equations by:

$$\{F\} - \{F^{nr}\} = [K^T]\{\Delta\delta\} \tag{2.37}$$

where:

$[K^T]$ = Tangent stiffness matrix

$\{\Delta\delta\}$ = Displacement increment

$\{F^{nr}\}$ = Internal force vector (sum of element stresses)

Fig. 2-8 illustrates the typical iteration process of the Newton-Raphson method.

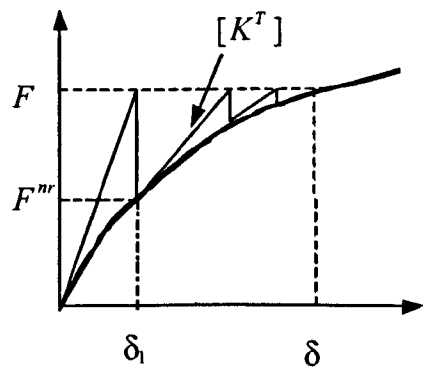

Figure 2-8 Illustration of Newton-Raphson iteration method

The difference between external and internal forces, $\{F\}-\{F^{nr}\}$, is a measure of the force imbalance in the structure, called the force residual. The goal is to make the force residual becomes acceptably small by iterating the nonlinear equation until the solution is converged. It should be noted that one iteration is as expensive as a single linear static analysis. However, the Newton-Raphson method cannot guarantee all solutions to converge under all circumstances and special strategies are needed to achieve desired convergence (ANSYS, 2000).

There are a number of techniques available for solving non-linear problems in many commercial FE codes. The most common methods are sparse, preconditioned conjugate gradient (PCG) and frontal solvers (ANSYS, 2000).

1. The sparse solver is based on a direct elimination technique similar to the frontal solver, as opposed to iterative methods. It takes advantage of the fact that the stiffness matrix $[K]$ is normally sparse and banded to reduce memory demands by storing non-zero terms only. It is relatively robust and efficient, and is usually used for situations where the matrix is ill-conditioned, or unsymmetric (for example, contact with friction) or has a wide range of element stiffness in the model. It is also very suitable for dealing with the models made up of beam and shell elements, or beams, shell and solid elements. Due to these great advantages, the sparse method has become a default solver in some commercial software such as ABAQUS and ANSYS.

2. The PCG solver is an iterative solver that solves Equation (2.35) by guessing a solution of $\{\delta\}$ and then updates it using a preconditioning matrix. It is most efficient but least

robust. It has a potential capability of solving a 3D model with a relatively large number of DOFs, i.e., more than 100,000 DOFs.

3. The frontal solver is a direct elimination solver which actually triangulates the stiffness matrix, $[K]$, and then back-substitutes for the displacement vector, $\{\delta\}$. This process is time-consuming and least efficient, but most robust. It is used when robustness is required or memory is limited.

It is noted, however, that the above information provided should be considered as general guidelines only, as they are largely dependent on the chosen software that may be constantly updated by existing computation techniques.

FE nonlinearities

Structural nonlinearities can be categorised into three main groups: geometric nonlinearity, material nonlinearity and status-changing nonlinearity. It is not uncommon that these non-linear behaviours may occur in combinations of two or three simultaneously.

- **Geometric nonlinearity**

Geometric nonlinearity arises when the deformation in a loaded structure becomes significant (problem-dependent) and the geometry change can no longer be neglected. Large strains (typically more than a few percent), large deflections (typically more than one or two degrees) and stress stiffening are typical examples of geometric nonlinearity. In these cases, the overall stiffness of a structure largely depends on the orientation and

stiffness of its individual elements. In a sense, large displacement effects may improve the accuracy of a solution, but at the expense of running an iterative nonlinear solution.

- **Material nonlinearity**

Many factors relevant to material properties can change a structure's stiffness and consequently cause nonlinear structural behaviour. For instance, nonlinear stress-strain relationships such as plasticity and hyperelasticity cause nonlinearity by changing structural stiffness at different levels of load or temperature. As another example, the nonlinearities induced by creep or viscoplasticity can be related to time, rate, temperature or stress.

- **Status-changing nonlinearity**

A change of status that causes an abrupt stiffness change is another common cause of nonlinear behaviour. For example,

- A cable changes stress status suddenly from slack to taut.
- Two parts come into contact , i.e., impact or rolling processes.
- Material is removed by machining or added by welding.

Contact is a status-changing nonlinearity. In the common physical sense, surfaces in contact have the following characteristics:

- They do not interpenetrate.
- They can transmit compressive normal forces and tangential friction forces.
- They often do not transmit tensile normal forces. They are therefore free to separate and move away from each other.

Contact has a strong nonlinearity because both the normal and tangential stiffness at contact surfaces change significantly with changing contact status. Large, sudden changes in stiffness often cause severe convergence difficulties.

Nonlinear FE solution issues

Some of the issues that are of importance in nonlinear FE solutions are worth addressing: convergence, expense versus accuracy and verification. Nevertheless, a through understanding of physical phenomena under study combined with FEA experience will help to solve the problems efficiently.

- **Convergence**

Convergence has been regarded as the biggest challenge for nonlinear problems since overcoming convergence is never straightforward and extremely problem-dependent. A classical technique of trial-and-error is still an effective way to obtain convergence. As a general rule, sudden changes to any aspect of a structure will cause convergence difficulties, for instance, a sudden stiffness change or/and a sudden load change. For better convergence performance, it would be helpful to break sudden changes down into a series of many small increments by using ramped loading or/and small steps. It should be noted that the more load increments, the more iterations and computation time will be required whenever convergence difficulty occurs.

- **Expense versus accuracy**

The trade-off between expense and accuracy is a common issue for nonlinear FEA. Fine meshes with many details can achieve a high accuracy of solution, but demand more computing time and system resources. Nonlinearities add a great deal of difficulties to the optimization of accuracy and expense. More load increments often improve the accuracy, but also generally increase the expense.

- **Verification**

Verification of the outcomes obtained from FEA is essential, particularly for a nonlinear analysis. However, nonlinear results are generally more difficult to verify due to the increased complexity incurred by nonlinearities. Checks of mesh density, mesh distortion, material models and boundary conditions are necessary for verification. In addition, actual testing of components under real conditions, reasonable interpretation of results based on the good understanding of the problem at issue, careful observation of post-processing, and sensitivity studies are also important for verification of FEA results.

2.4 References

[1] Abraham, B. and Ledolter, J. (1983). Statistical Methods for Forecasting. New York, John Wiley & Sons.

[2] ANSYS (2000). Basic Structural Nonlinearities (Training Manual for Release 5.6), ANSYS, Inc.

[3] Bathe, K. J. (1996). Finite element procedures. New Jersey, Prentice-Hall, Inc.

[4] Calladine, C. R. (2000). Plasticity for engineers: theory and applications. Chichester, Horwood Publishing Limited.

[5] Chakrabarty, J. (2000). Applied plasticity. New York, Springer-Verlag New York, Inc.

[6] Cleveland, W. S. (1979). Robust locally weighted regression and smoothing scatterplots. Journal of the American Statistical Association, Vol. 74 (**368**), pp. 829-836.

[7] Cleveland, W. S. and Devlin, S. J. (1988). Locally weighted regression: an approach to regression analysis by local fitting. Journal of the American Statistical Association, Vol. 83 (**403**), pp. 596-610.

[8] Cook, R. D., Malkus, D. S. and Plesha, M. E. (1989). Concepts and applications of finite element analysis. New York, John Wiley & Sons, Inc.

[9] Dieter, G. E. (1976). Mechanical Metallurgy. New York, London, Paris, McGraw-Hill, Inc.

[10] Draper, N. R. and Smith, H. (1981). Applied Regression Analysis. New York, John Wiley & Sons, Inc.

[11] Gowar, N. W. and Baker, J. E. (1974). Fourier Series, Chatto & Windus and Collins.

[12] Green, P. J. and Silverman, B. W. (1994). Nonparametric regression and generalized linear models. London, Chapman & Hall.

[13] Harrell, F. E. (2001). Regression modeling strategies: with applications to linear models, logistic regression, and survival analysis. New York, 2001 Springer-Verlag New York, Inc.

[14] Hill, R. (1950). The mathematical theory of plasticity. London, Oxford University Press.

[15] Johnson, W. and Mellor, P. B. (1962). Plasticity for mechanical engineers. London, D. Van Nostrand Company Ltd.

[16] Khan, A. S. and Huang, S. (1995). Continuum theory of plasticity. New York, John Wiley & Sons, Inc.

[17] Moore, D. S. and McCabe, G. P. (1989). Introduction to the Practice of Statistics. New York, Oxford, W. H. Freeman and Company.

[18] Ratkowsky, D. A. (1989). Handbook of Nonlinear Regression Models (volume 107). New York and Basel, Marcel Dekker, Inc.

[19] Shames, I. H. and Cozzarelli, F. A. (1997). Elastic and inelastic stress analysis, Taylor & Francis Ltd.

[20] Siegel, A. F. (1988). Statistics and Data Analysis, an Introduction. New York, John Wiley & Sons.

[21] Timoshenko, S. P. and Goodier, J. N. (1970). Theory of Elasticity. New York, McGraw-Hill Book Company.

[22] Tukey, P. W. (1977). Exploratory data analysis. Reading,MA, Addison-Wesley Publishing Co.

[23] Wahba, G. (1990). Spline Models for Observational Data. Philadelphia, SIAM.

3 Exploration of the contour method

The general aspects of residual stress and its measurement methodologies, as well as some aspects of the fundamental theories to be used subsequently, have been presented in the previous chapters. They have laid a foundation for further investigating the novel technique of the contour method, which will be focused on from this chapter forward.

In this chapter, a brief literature review of the contour method and its principle are introduced. The procedure of how to perform the contour method is then presented with a special emphasis on the experimental issues such as specimen cutting and contour measurement. The validation of the principle of the contour method is performed by finite element simulation. In addition, other important simulations arising from aspects of the implementation of the contour method are conducted and some useful conclusions inferred from the simulations are given.

3.1 Introduction of the contour method

The contour method, first presented in 2000 (Prime and Gonzales, 2000), is a newly-invented relaxation method of enabling a 2D residual stress map to be made experimentally and numerically on a plane of interest. The method was published in detail in 2001, where the contour method was numerically verified by finite element simulation and experimentally validated on a bent steel beam having a known residual stress distribution (Prime, 2001). The potential of the contour method was later demonstrated on a 12-pass TIG BS4360 steel weld to measure a complex 2D stress variation across the weld section (Prime et al., 2001). The result obtained from the contour method was in excellent quantitative agreement with the outcome measured by a completely different technique – non-destructive neutron diffraction. A high stress component, over the initial yield stress of

the material, was measured in this case. The contour method was also successfully used for measuring the residual stress induced by impact in a high-strength low-alloy steel (HSLA-100) with thickness up to 51 mm (Prime and Martineau, 2002). The comparison with the explicit FE simulation of the impact process indicated a good match. Meanwhile, an as-received HSLA-100 quenched plate was also measured using the contour method, showing a typical quenching residual stress distribution. The latest application of the contour method was a 7075 aluminium alloy hand forging, in which three cuts were performed in orthogonal directions to obtain three directions of the stress tensor (Prime et al., 2003). The measured stresses were in good agreement with the FE predicted outcomes.

The contour method offers several improvements over conventional relaxation methods of measuring residual stresses. Firstly, instead of tedious material removal layer by layer, a specimen needs only one flat cut along the plane of interest. Furthermore, the deformation or displacement or contour (the terms of the deformation, displacement and contour are interchangeable in terms of the contour method throughout this thesis) resulting from the relaxation of residual stresses is measured directly on the cut surface under study rather than on a pre-existing free surface. There is no need for complex analytical inversion due to the geometrical disagreement between the location of stress release and the place of stress to be determined. The measured deformation is uniquely associated with the original residual stress that can be calculated by finite element analysis. It should be pointed out, however, that only the residual stress normal to the cut plane can be determined because only the deformation normal to the cut plane is measured. However, different direction stresses can be measured by multiple cuts along the planes of interest.

3.1.1 Principle of the contour method

The theory of the contour method is based on a variation of Bueckner's elastic superposition principle (Bueckner, 1958). Fig. 3-1 illustrates the principle as Step A = Step B + Step C in a 2D view for simplicity and clarity, which also applies to 3D cases.

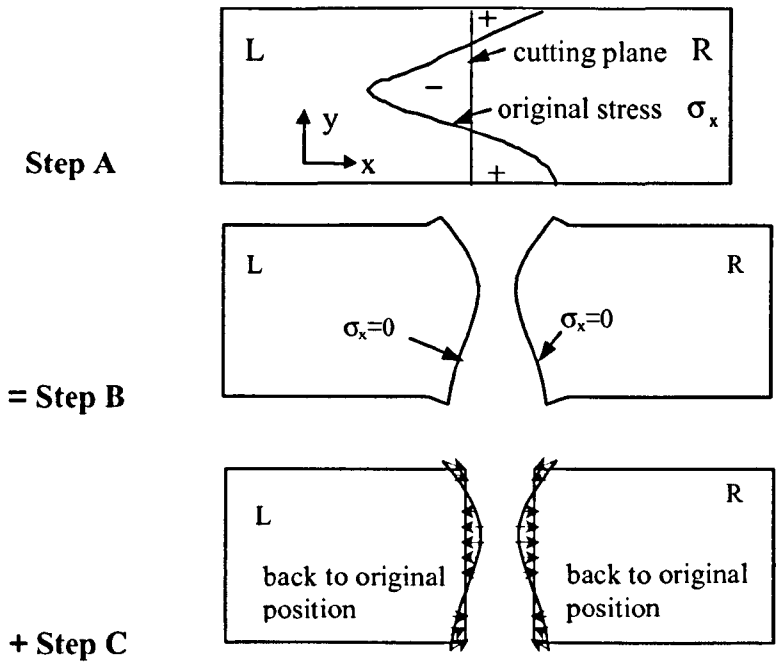

Figure 3-1 Illustration of Bueckner's superposition principle as applied to the contour method

In Step A, a solid part as a whole comprised of two parts: a left part L and a right part R, contains original residual stresses: one normal stress (σ_x) and two shear stresses (τ_{xy}, τ_{xz}) across the plane of interest to be cut. It is noted that only the σ_x stress is shown in Fig. 3-1 as it is of interest to be determined by the contour method. In Step B, the entire part is cut into two: the part L and the part R. The cut surfaces are deformed as the residual stresses are fully released, resulting in zero normal stress, $\sigma_x = 0$. The deformations on both sides are measured at this step. In Step C, the deformed surface is 'forced' back to the original position. This is achieved by applying the deformation measured in the step B in an

opposite direction to an unstressed half part as a boundary condition to calculate the corresponding stress. Superposing the stress in Step B upon the calculated stress in Step C gives the original stress of σ_x in the cutting plane in Step A, based on the elastic superposition principle. The calculated stress in Step C equals the original stress of σ_x due to the zero stress (fully released) normal to the cut plane in Step B.

According to Prime's interpretation of Bueckner's superposition principle (Prime, 2001), the original stresses σ_x, τ_{xy} and τ_{xz} in the cutting plane determine uniquely the deformation after cutting. The transverse stresses σ_y, σ_z, τ_{yz} and other stresses away from the cutting plane will not contribute any deformation on the cut plane. It is inferred that the correct original stresses σ_x, τ_{xy} and τ_{xz} would be determined if the 3D deformation on the cut plane could be measured exactly across the cut plane. In reality, however, only the deformation normal to the cut surface can be measured without difficulty, and this measured deformation will determine uniquely the σ_x stress normal to the cut plane. It should be noted that the x-direction deformation measured on the cut plane of each part also includes a contribution from release of the shear stresses τ_{xy} and τ_{xz} if there are any. Implementation of single side measurement will result in errors caused by the influence of the shear stresses on the cut plane. Averaging the measured displacements of both sides properly will cancel out this deviation and give a correct original stress of σ_x (Prime, 2001). This conclusion will be confirmed by the following FE simulation.

There are three assumptions implicit in the contour method (Prime, 2001). Firstly, relaxation of a residual stress is elastic when a specimen is cut. Secondly, the cutting does not significantly modify the original residual stress and hence the deformation released after cutting. These two assumptions are common to the conventional relaxation methods

of residual stress measurement. The third assumption is unique for the contour method and requires that the cutting should be flat along the plane of interest.

3.1.2 Application of the contour method

Application of the contour method primarily involves four steps: specimen cutting, contour measuring, data analysis and stress analysis, which will be discussed subsequently in detail.

Specimen cutting

Specimen cutting is the first and thus the most critical step in implementing the contour method, as the subsequent procedures such as contour measurement, data analysis and stress analysis are all reliant on the quality of the cutting. The ideal cutting should (1) not introduce any extra stress, (2) make a perfectly flat cut, and (3) not move any material. It is almost impossible to completely meet all three requirements, particularly (3). However, efforts are made to minimize errors induced from each of these factors. Wire electric discharge machining (EDM) has been identified as an especially suitable method of cutting for the contour method (Prime, 2001) as it uses electrical discharges (sparks) instead of hard cutting tools to remove material. There is no physical contact between the wire and the part being machined and hence no cutting force is present. In addition, possible thermal stresses due to high temperature during wire cutting can be minimised by submerging the specimen and clamps into a cycling liquid in the EDM tank. However, there must be a re-cast layer, although modern EDM equipment is designed to minimize this feature. Preventing a specimen from any movement during cutting by proper clamping is critical to achieve flat cutting. Making a constant width of cut is also important to guarantee flat cutting. This is strongly related to the type of cutting wire chosen, material to be cut and

EDM operating parameters. It is reported that bare brass wire cuts 21Cr6Ni9Mn austenitic stainless steel fairly flatly, whereas zinc-coated wire can cause curvature on the edges of a specimen (Prime, 2001). Finally, minimum material removal can be achieved by choosing the cutting wire as thin as possible, say ϕ0.1 mm.

The equipment used for specimen cutting in this project is a FANUC ROBOCUT α-O*i*B CNC (computer numerically controlled) wire electric discharge machine, located in our department workshop ,as illustrated in Fig. 3-2. The closer view of the clamps and the cut specimen can be seen in Fig. 3-3, in which half the cut piece was removed from the front for clearer view. EDM has greatly altered the tooling and manufacturing industry, resulting in dramatic improvements in accuracy and quality. This process uses a thin running wire as an electrode that goes through a specimen, and the wire is precisely monitored by a CNC system. A specimen is placed on the XY table also controlled by the CNC unit.

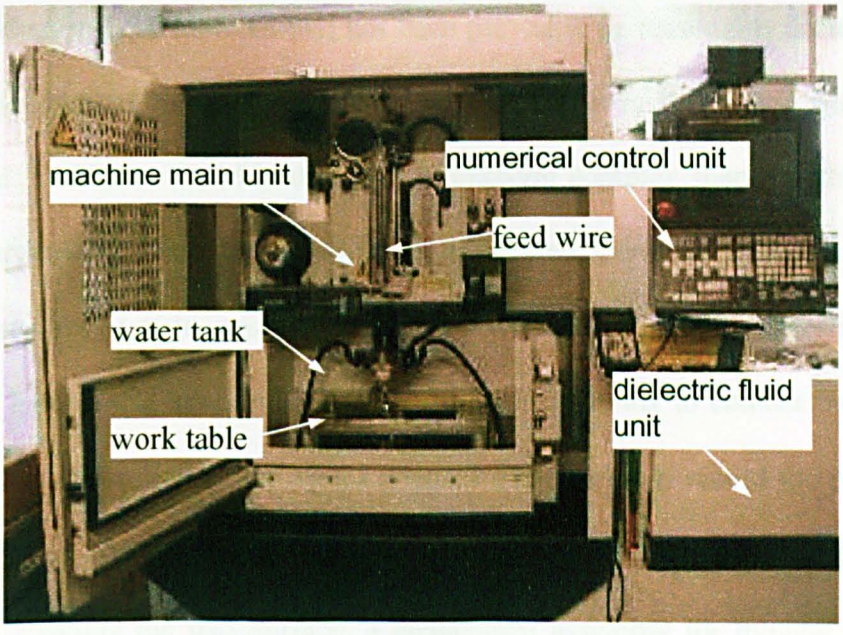

Figure 3-2 Overview of ROBOCUT CNC wire electric discharge machine

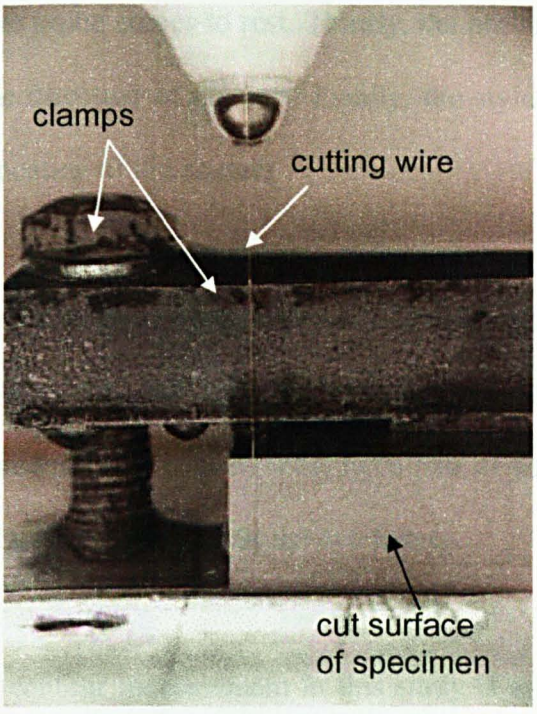

Figure 3-3 Closer view of clamps and cut surface, in which half the cut piece was removed from the front for clearer view.

Contour measuring

Following specimen cutting, the contour needs to be measured for both cut surfaces. A co-ordinate measuring machine (CMM) has been proved to be reasonably accurate for surface profile measurement by many applications (Prime, 2001; Prime and Martineau, 2002; Zhang et al., 2002). A CMM is designed to measure complex shapes with high precision and is particularly used to measure manufactured parts to determine if tolerance specifications are met. It uses a ruby-tipped stylus as a sensor for detecting a specimen surface. A mechanical assembly moves the sensor or stylus to contact the surface to be measured. The deflection of the stylus triggers a computer to record the position of each contact point. A CMM typically consists of a workspace in which specimens are fixed, a sensor for detecting the part surface, a mechanical assembly for moving the part sensor around the workspace, and a computer for calculating the part dimensions based on the sensor measurement. Generally, a single cycle of CMM measurement consists of four steps. Firstly, a CMM moves a sensor to the vicinity of a part geometry that is to be

measured. Secondly, the probe comes to rest. Thirdly, the probe is reaccelerated to a small constant velocity in the direction of the part. Finally, the stylus contacts the part and the computer records the location of the contact.

The detailed procedure for contour measurement by CMM is graphically illustrated in Fig. 3-4. After a specimen is cut into half, each cut surface will be measured based on a datum that can be specified randomly by convenience. Each pair of points to be averaged should be measured, ideally at a mirror position in the two halves.

The machine used for contour measurement in this study is a Mitutoyo Crystal Plus 574 CMM equipped with a thermal compensation system located in an air-conditioned laboratory, as illustrated in Fig. 3-5. It has a probe mounted at the end of the Z-axis spindle. It is motor-driven in all three axial directions: x-direction from left to right, y-direction from front to back and z-direction from down to up, vertically perpendicular to the other two, when viewing from the front of the machine. The probe displacement is detected by high-accuracy linear encoders, which are installed on each axis. The co-ordinate data at each measured point are output to the data processing system for 2D or 3D measurement/analysis of geometry and contours. It also ensures high measuring accuracy over a wide temperature range with the temperature compensation capability. The resolution of the Mitutoyo CMM is 0.1 μm and the estimated uncertainty of measurement for a $\phi 30$ mm calibration masterball is +/- 0.5 μm with a confidence level of approximately 95%. The linear positioning accuracy $U1$ on each of three X, Y and Y axes for Mitutoyo Crystal Plus 574 CMM is given by the manufacturer with the following equation:

$$U1 = 2.9 + 3L/1000 \tag{3.1}$$

where L is the measured length in millimetres and the accuracy $U1$ is in micrometers.

The volumetric positioning accuracy $U3$ in micrometers, which ensures a machine centre to position precisely in a 3D volume in X, Y and Z axes, is defined below for Mitutoyo Crystal Plus 574 CMM:

$$U3 = 2.9 + 4L/1000 \tag{3.2}$$

The volume accuracy becomes significant when 3D contoured surfaces are of interest.

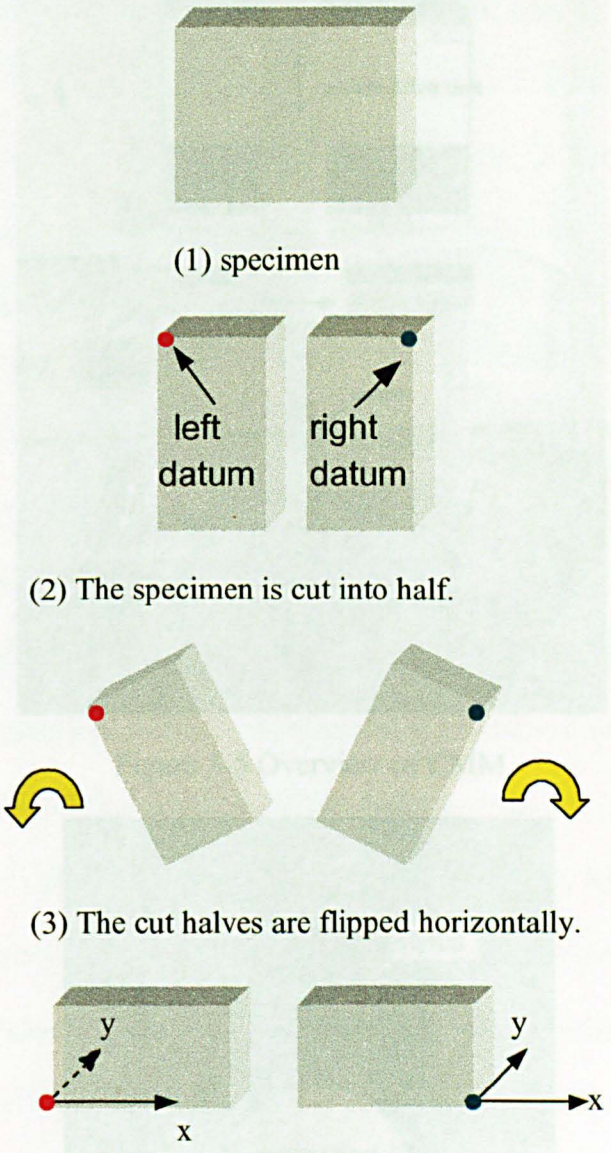

(1) specimen

(2) The specimen is cut into half.

(3) The cut halves are flipped horizontally.

(4) The coordinates used in CMM measurement.

Figure 3-4 One example of CMM measurement method

It should be noted that calibration should be performed prior to each specimen measurement. The calibration master ball designed for the Mitutoyo CMM is 30 mm in

diameter, as shown in Fig. 3-6. The Mitutoyo CMM can be equipped with different sizes of stylus, for instantce, 1 mm, 2 mm or 3 mm in diameter. The larger the stylus, the less effect it has on the surface finish of the specimen since the contact point is spread over a larger area of the feature being measured.

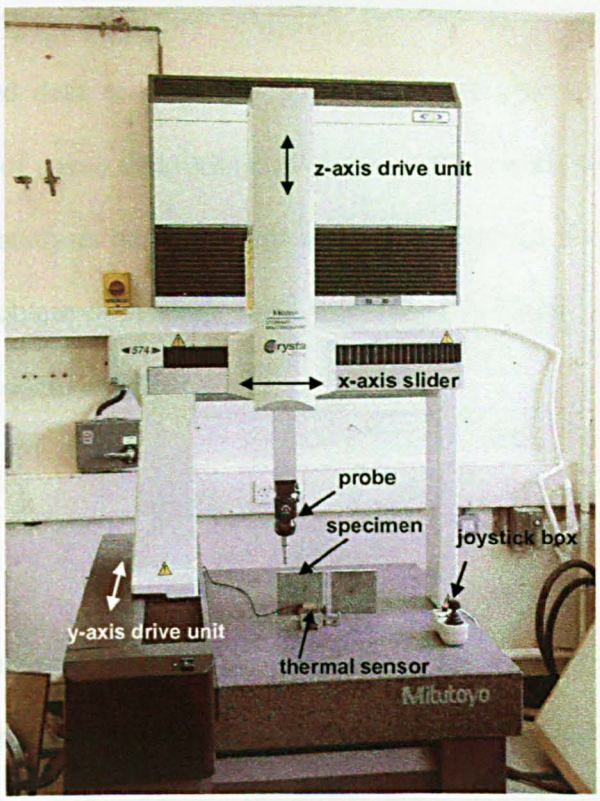

Figure 3-5 Overview of CMM

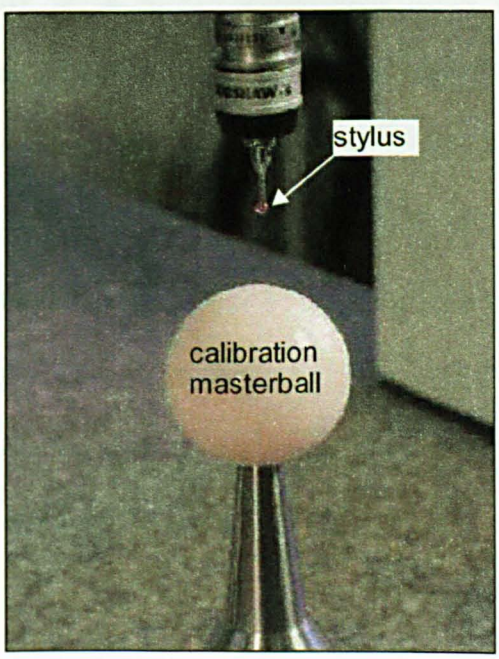

Figure 3-6 CMM calibration before specimen measurement

Data analysis

The very first step of the data analysis is to average each pair of measured contours of corresponding points, which should be at the mirror positions from the two cut planes. It is unavoidable that the measured contours contain an error from the cutting and the CMM measurement. Further, stress evaluation magnifies the error involved in the measured data. Smoothing of measured data to minimise the error in the data is, therefore, crucial to achieve high accuracy of stress determination in the contour method. The general theory of the data smoothing analysis has been presented in Chapter 2. However, the smoothing technique is very problem-dependent, and will be described specifically for each application in the subsequent chapters.

Stress analysis

Finite element modelling and analysis are employed to calculate the original stress based on the smoothed data that will be input to a FE model in an opposite sign as displacement boundaries. The basic principle of finite element method has been introduced in Chapter 2 and will not be necessarily given here. Nevertheless, there are several points worth mentioning. Firstly, only one of two cut parts needs modelling. In addition, FE solution is simply linear as the process of the residual stress relief is assumed to be elastic. Furthermore, the cut plane in the FE model can be simplified to a flat surface instead of a deformed surface. This simplification makes FE modelling much easy, and gives little difference, because the deformation is relatively small compared to the large size of a geometric model. The appropriateness of this geometry simplification will be studied and confirmed in the following context of simulation.

3.2 Finite element simulation of the contour method

In this section, finite element simulation will be utilised to validate the principle applied to the contour method.

3.2.1 Simulation

Validation of the contour method by FE simulation is designed to involve two relevant simulations: the first to model Step A and Step B, and the second for Step C. The first simulation or cutting simulation consists of the introduction of known initial residual stresses into a specimen (Step A), followed by specimen cutting at the plane of interest to relax the residual stresses (Step B). The released displacement is acquired through post-processing of the FE solution. The second simulation or contour simulation, which simulates the process of implementation of the contour method, includes application of the displacement obtained from the first simulation to the plane at issue of an unstressed model as boundary conditions, and then conduction of linear FE analysis to calculate the corresponding original stresses. Only one of the cut pieces needs modelling for the contour simulation, as stated earlier.

The geometrical model used for this study is a solid plate, 40 mm wide, 100 mm long and 5 mm thick, as shown in Fig. 3-7. The material is assumed to be isotropic amd elastic, with 200 GPa Young's modulus and 0.3 Poisson's ratio, typical for steel.

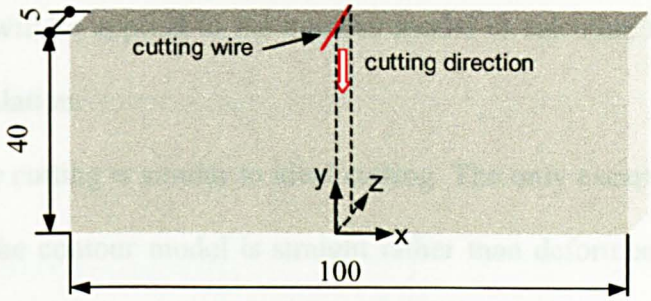

Figure 3-7 3D geometrical model for study of the contour method

The mesh of all FE models is characterised by approximately uniform 1 mm space with 8-node biquadratic plane stress quadrilateral elements (CPS8) for 2D models or with 20-node quadratic brick, reduced integration elements (C3D20R) for 3D models. ABAQUS/CAE 6.2 and ABAQUS/Standard 6.2 were used for the modelling and FEA.

In the 2D simulations, five different situations for specified purposes were taken into account: 1) 2D ideal cutting, 2) 2D ideal contour cutting, 3) 2D symmetrical cutting, 4) 2D unsymmetrical shear cutting, and 5) 2D symmetrical shear cutting, which are explained in detail as follows. It should be noted that each situation covers two associated simulations: cutting simulation and contour simulation.

1. 2D ideal cutting assumes that no material is removed during cutting and no shear stress is present at the plane under study. The plane in the contour model, to which the measured displacement will be applied, is deformed instead of straight. This is an ideal situation obeying Bueckner's elastic superposition theory without any simplification of the geometry. Only half the geometry in Fig. 3-7 will be modelled owing to this symmetrical feature. Simulation of the cutting is achieved simply by releasing the constraint of the boundary plane of interest, and thus there is no material removed in this case. The displacements released from the plane are acquired through post-

processing and will be applied to the contour model to calculate the original stress in the contour simulation.

2. 2D ideal contour cutting is similar to ideal cutting. The only exception is that the plane under study in the contour model is straight rather than deformed. The motivation of the modelling is to examine what impact this geometric simplification may have on the result. The methodology of the pair of simulations is the same as the ideal cutting.
3. 2D symmetrical cutting means that the cutting takes place at the location where there is no shear stress and no shear stress gradient. In addition, the stresses normal to the cut planes are equal on the both cut sides. The whole geometry in Fig. 3-7 is modelled and the cutting is conducted in the middle length for the cutting simulation. The cut slot is presumed to be 1 mm. The significant difference of the 2D symmetrical cutting from the 2D ideal contour cutting lies in its involvement of material removal during cutting.
4. 2D unsymmetrical shear cutting implies that the cutting is performed at a plane 15 mm from the centre, containing a high shear stress, but a small shear stress gradient and a small σ_x stress gradient. The cut width is 1 mm.
5. 2D symmetrical shear cutting presumes that the cutting is performed in the middle of the specimen where the plane bears a high shear stress and a high shear stress gradient that is deliberately exaggerated and achieved by widening the cut slot to 10 mm instead of 1 mm. The stresses normal to the cut planes are equal on both the cut surfaces. The main purpose of the simulation is to study the influence of the shear stress gradient in the two cut planes on the result.

Two common situations will be demonstrated using 3D FE models: cutting at a place with zero or little shear stress (3D cutting without shear stress) and cutting at a place with high shear stress (3D cutting with shear stress). The cut width is assumed to be 1 mm for both situations. In fact, the actual condition is much better than this assumption because the cutting slot removed by wire electric discharge machining is normally less than 0.5 mm. It

is noted that all simulations except the ideal cutting simulation simplify the cut plane to a flat surface as the contour method usually does.

3.2.2 Results and discussion

As stated earlier, the contour method determines one stress direction profile with one cut. Hence, only the σ_x stress profile normal to the cut plane is obtained and presented for all 2D and 3D simulations.

2D ideal cutting

In the contour simulation, the originally deformed surface is modelled so that the contour method principles can be examined under ideal conditions. Only half the geometry is modelled owing to the symmetrical features of the overall system, as seen in Fig. 3-8, where the deformation magnification is 376 for all three figures of Fig. 3-8 (a), Fig. 3-8 (b) and Fig. 3-8 (c). Fig. 3-8 (a) represents a part containing an original stress distribution; Fig. 3-8 (b) displays the deformation after the left boundary is fully released; and Fig. 3-8 (c) shows the deformed surface back to the original position after applying the deformation in an opposite direction on the left plane in Fig. 3.8 (b).

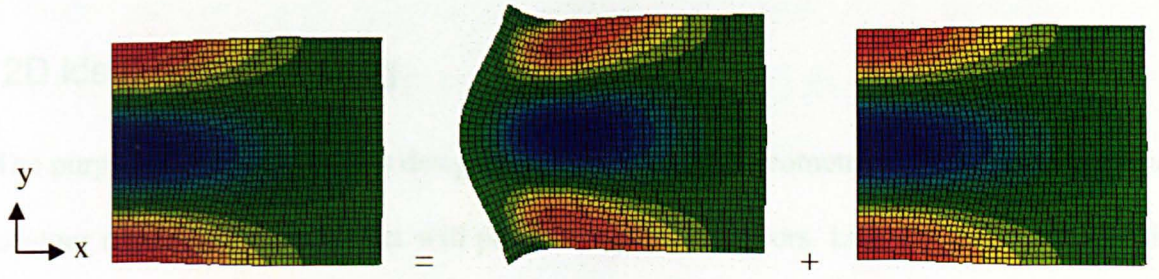

(a) original stress (b) release of stress (c) back to original position and original stress,

Figure 3-8 Ideal cutting: FE illustration of the contour method principle (deformation magnification: 376)

When forcing the x-direction displacement back to its initial location, the y-direction position automatically returns to its initial location because of the effect of Poisson's ratio. As expected, the stress distribution calculated from the contour simulation matches exactly the original, as seen in Fig. 3-9. There is no error involved in this case. This pair of simulations has perfectly validated the Bueckner's elastic superposition principle that the contour method relies on.

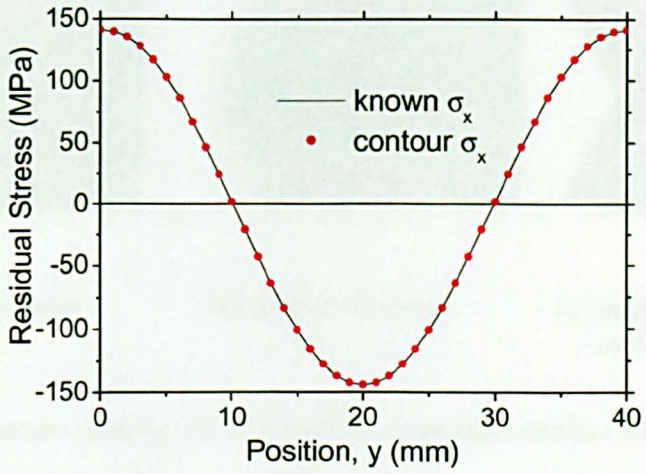

Figure 3-9 Results of ideal cutting (perfect match, no error)

2D ideal contour cutting

The purpose of this situation is designed to examine if the geometrical simplification of the contour model described earlier will produce significant errors. Like the ideal cutting, this situation presumes no material removed and no shear stress present at the plane of interest (the left boundary in Fig. 3-10). Unlike the ideal cutting, it uses a flat surface instead of the deformed surface in the contour model. Again, only half the geometry is modelled as seen in Fig. 3-10, where the deformation magnification is 376 for all three figures of Fig. 3-10 (a), Fig. 3-10 (b) and Fig. 3-10 (c). Fig. 3-10 (a) represents a plate containing an original

stress profile; Fig. 3-10 (b) displays the resulting deformation after the left plane is relaxed; and Fig. 3-10 (c) shows the result when applying the contour method. A significant difference is identified in the contour model that the plane under study becomes curved in Fig. 3-10 (c) (exaggerated) instead of straight as in Fig. 3-8 (c). It is certainly the consequence of the use of an initially straight plane in the contour model to represent the deformed plane.

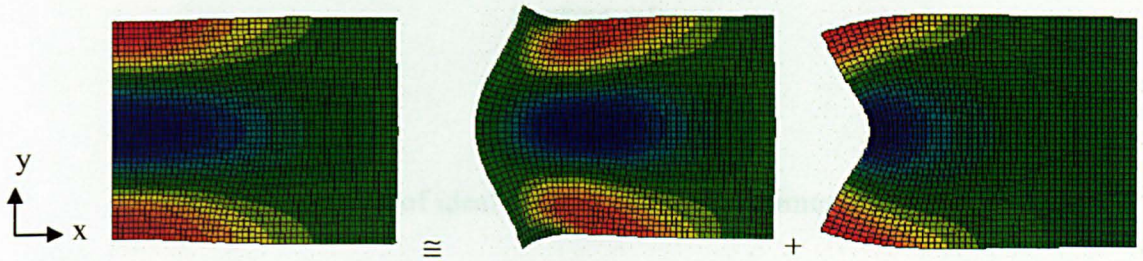

(a) original stress (b) release of stress (c) applying the contour method

Figure 3-10 Ideal contour cutting: FE illustration of implementation of the contour method (deformation magnification: 376)

However, as seen in Fig. 3-11, the residual stress distribution obtained from the contour method is in such good agreement with the known stress that one can not see visually any diversion between them. Nevertheless, careful examination of the numerical values acquired from post-processing of FEA indicates a maximum absolute error of 0.985 MPa with 0.7% relative error occurring at the end points. This small deviation is purely attributed to the use of the geometry simplification in the contour model and can be ignored without introduction of significant errors in the result. This is because the geometrical deformation induced by the relief of residual stresses at the left boundary is so tiny in comparison with the large size of the whole model that it has little impact on the result. This simulation has validated the adaptability of the simplification used in the contour method, which will be reconfirmed by the subsequent modelling.

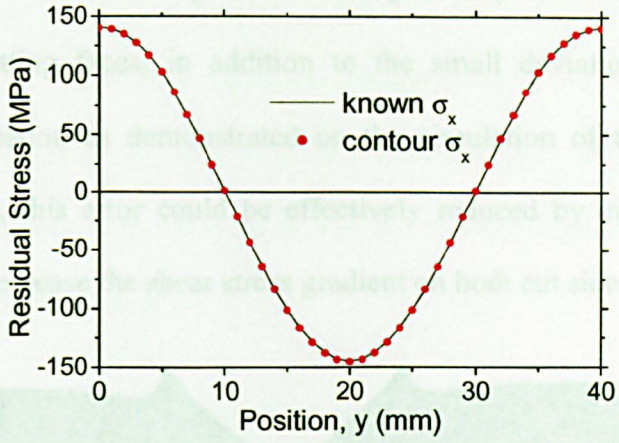

Figure 3-11 Results of ideal contour cutting (maximum error = 0.7%)

2D symmetrical cutting

The symmetrical cutting is performed in the middle plane, as seen in Fig. 3-7, bearing a σ_x stress ideally without shear stress $\tau_{xy,}$, which is difficult to create for the current model. However, the shear stresses at both cutting planes are very small, less than 1.09 MPa in magnitude and the maximum shear stress gradient is 2.18 MPa between the cutting planes 1mm apart.

Fig. 3-12 illustrates the post-cutting deformations of the two cut halves. It can be seen that the deformations from both sides are identical. It is inferred that use of the displacement from either side or an average in the contour model will give the same result in this particular case.

Fig. 3-13 shows the comparison between the known initial stress acquired from the cutting simulation and the calculated stress obtained from the contour simulation. The comparison

illustrates a good agreement between them, with a maximum error of 3.807 MPa and 2.7 % relative error in this case. This slight difference primarily stems from the τ_{xy} gradient between the two cutting faces, in addition to the small deviation introduced by the geometrical simplification as demonstrated on the simulation of the 2D ideal contour cutting. Nevertheless, this error could be effectively reduced by minimising the cutting width in practice to decrease the shear stress gradient on both cut sides.

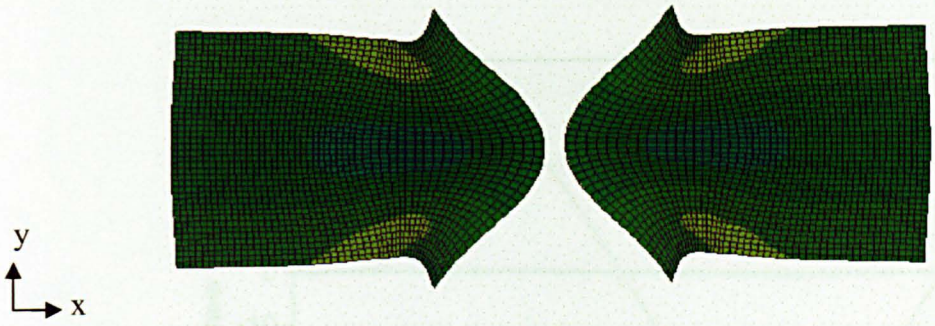

(a) left cut part (b) right cut part

Figure 3-12 Deformation after symmetrical cut (deformation magnification: 735)

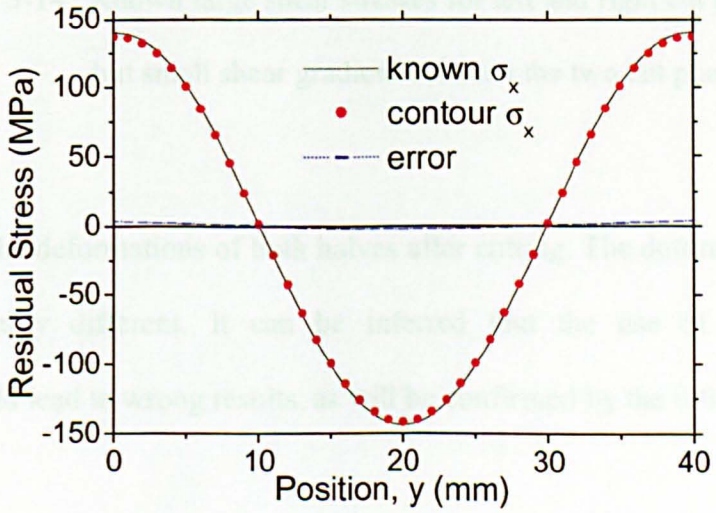

Figure 3-13 Results of symmetrical cutting (maximum error = 2.7%)

2D unsymmetrical shear cutting

This simulates cutting being conducted at a plane bearing a comparatively large shear stress, with a maximum 29.6 MPa shear stress in magnitude on the left plane, 30.5 MPa on the right plane, but little shear gradient with the maximum 0.851 MPa between the two cut plane 1mm apart in this case, as depicted in Fig. 3-14. There also exists a small σ_x stress gradient between the cut surfaces.

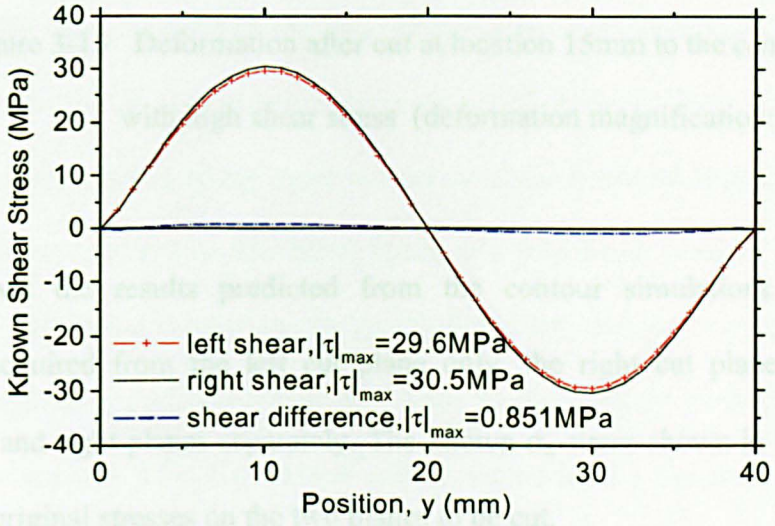

Figure 3-14 Known large shear stresses for left and right cut planes, but small shear gradient between the two cut planes

Fig. 3-15 shows the deformations of both halves after cutting. The deformations from both sides are noticeably different. It can be inferred that the use of only one side's displacement could lead to wrong results, as will be confirmed by the following outcomes.

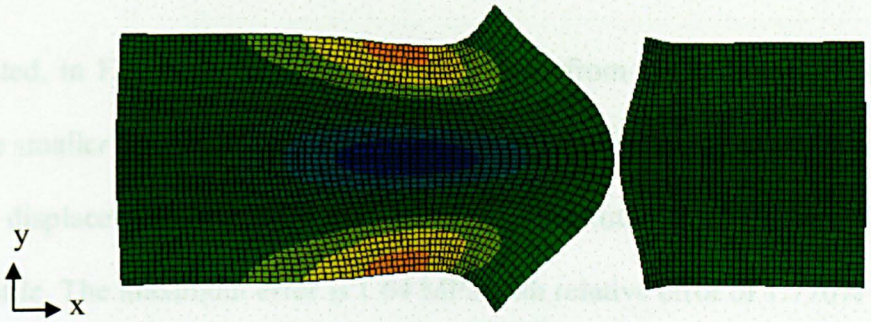

(a) left cut part (b) right cut part

Figure 3-15 Deformation after cut at location 15mm to the centre with high shear stress (deformation magnification: 643)

Fig. 3-16 shows the results predicted from the contour simulations by using the displacement acquired from the left cut plane only, the right cut plane only, and the average of left and right planes separately. The known σ_x stress shown in Fig. 3-16 is the average of the original stresses on the two planes to be cut.

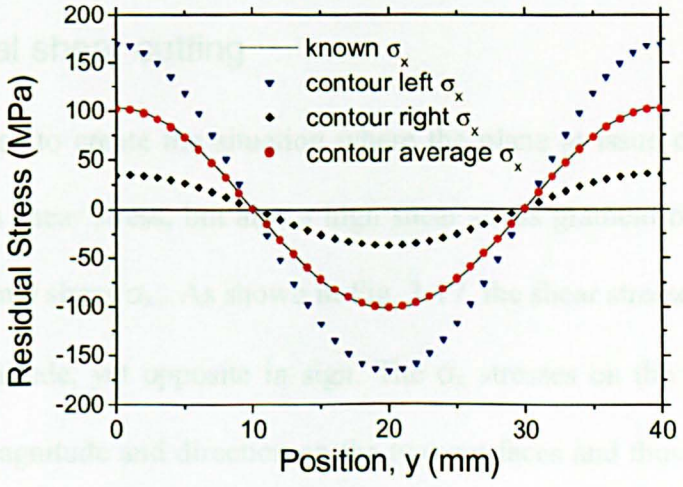

Figure 3-16 Results of unsymmetrical cutting (maximum error for average = 1.776%)

As expected, in Fig. 3-16 the greater displacement from the left part results in a greater stress; the smaller displacement from the right part gives a smaller stress in magnitude. The averaged displacement of both halves leads to a quantitative agreement with the known stress profile. The maximum error is 1.64 MPa with relative error of 1.776% in this case.

It is found from the last two situations that 2D symmetrical cutting where there is a small shear stress (1.09 MPa) and relatively large shear stress difference (2.18 MPa) between two cut planes results in a maximum error of 3.807 MPa (2.7%). Whereas, the 2D unsymmetrical shear cutting where there is a larger shear stress of maximum 30MPa and smaller shear stress gradient (0.851 MPa) leads to a maximum error of only 1.64 MPa (1.776%). It appears that it is the shear stress difference between the two cut planes, not the shear stress magnitude, that contributes the error in the contour method if the average displacement is applied. This conclusion will be supported by the next simulation: 2D symmetrical shear cutting.

2D symmetrical shear cutting

This simulation tries to create the situation where the plane at issue contains not only a comparatively high shear stress, but also a high shear stress gradient on both cut sides in addition to the normal stress σ_x. As shown in Fig. 3-17, the shear stresses on both sides are equivalent in magnitude, yet opposite in sign. The σ_x stresses on the two cut planes are identical in both magnitude and direction on the two cut faces and thus there is no normal stress gradient. It should be mentioned that the cutting width is 10 mm in this exceptional simulation so as to yield a greater shear stress difference. This simulation is mainly designed to study the influence of the shear stress gradient between the two cut surfaces on the accuracy of the contour method.

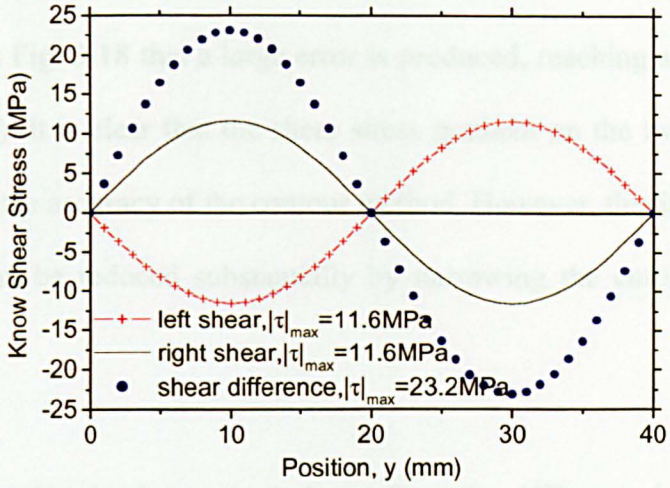

Figure 3-17 Known shear stress profiles for left side, right side and difference between the two sides

Like the case of symmetrical cutting, the deformations from both cut sides are identical but not displayed here, similar to Fig. 3-12 in shape (not in magnitude, though). Thus, use of either side's displacement or an average in the contour model should give identical outcomes. Fig. 3-18 presents the result under the situation of symmetrical shear cutting.

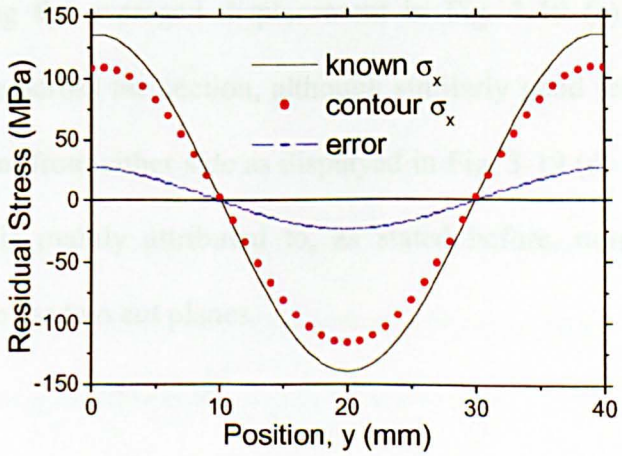

Figure 3-18 Results of symmetrical shear cutting (maximum error = 19.8%)

It can be seen from Fig. 3-18 that a large error is produced, reaching a maximum value of 26.76 MPa (19.8%). It is clear that the shear stress gradient on the two cut surfaces does significantly affect the accuracy of the contour method. However, this inaccuracy with a 10 mm cutting slot can be reduced substantially by narrowing the cutting width, as stated earlier.

It is also found that the absolute error induced from the difference between the two cut planes in normal stress and shear stress is proportional to the magnitude of the normal stress to be determined, as seen in both Fig. 3-13 and Fig. 3-18.

3D cutting without shear stress

The 3D cutting without shear stress assumes the cutting is performed at the plane of interest bearing a σ_x normal stress and little shear stress. However, there still exists a small normal stress gradient as seen in Fig. 3-19 (a) and (b) between the left cutting plane and the right cutting plane due to the presence of the 1 mm cutting slot. There is also a small amount of shear stress gradient, not shown here. It can be seen from Fig. 3-19 that the contour method using the averaged displacement in Fig. 3-19 (c) gives an acceptably accurate stress profile across the section, although similarly good results can be achieved using the displacement from either side as displayed in Fig. 3-19 (d) and (e) in this special case. The variation is mainly attributed to, as stated before, normal and shear stress differences existing in the two cut planes.

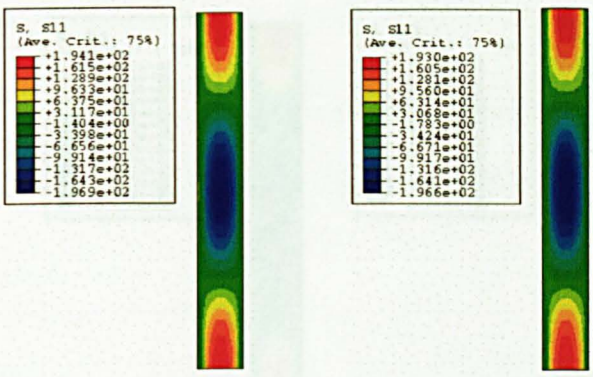

(a) known σ_x left (b) known σ_x right

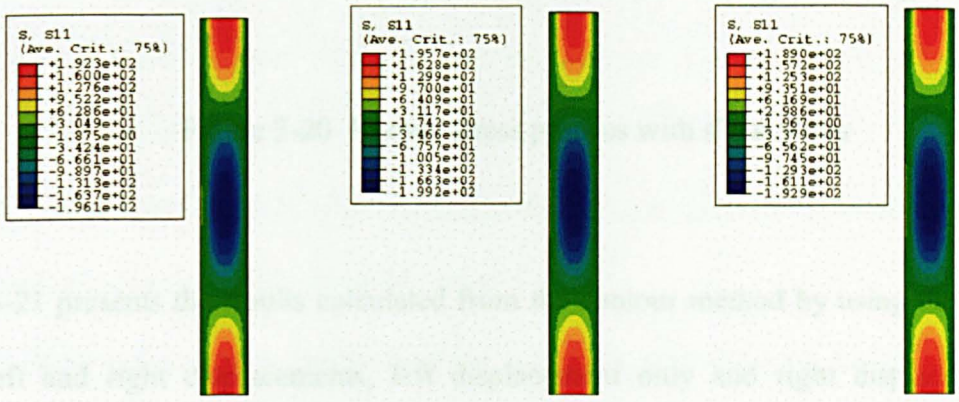

(c) contour average (correct) (d) contour left (correct) (e) contour right (correct)

Figure 3-19 2D through-thickness stress profile without shear stress. Note that they look similar, but values are slightly different (see the values in the figures)

3D cutting with shear stress

The present simulation demonstrates the situation where the cutting is carried out at the plane possessing a certain amount of σ_x normal stress and shear stresses, τ_{xy} and τ_{xz}, as illustrated in Fig. 3-20, in which only one plane is shown. Again, there are also small normal and shear stress gradients in the two cut planes.

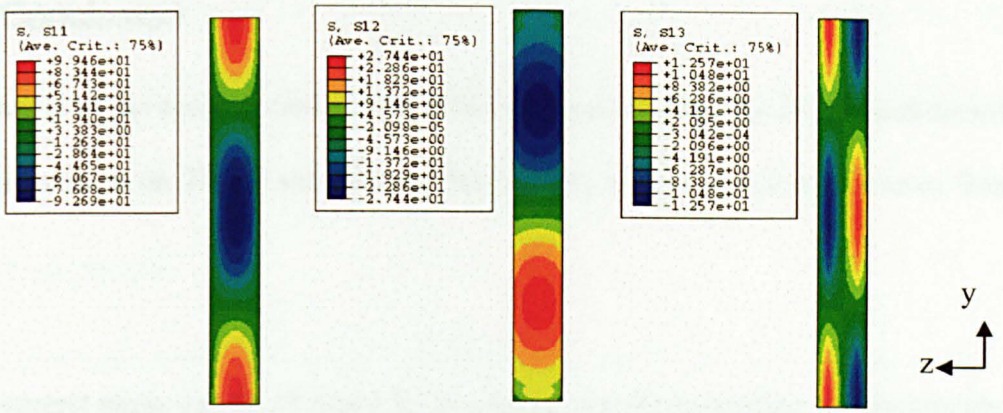

(a) known σ_x (b) known τ_{xy} (c) known τ_{xz}

Figure 3-20 Known stress profiles with shear stress

Fig. 3-21 presents the results calculated from the contour method by using the average of the left and right displacements, left displacement only and right displacement only. Clearly, only applying the averaged displacement gives the desired original stress distribution, as presented in Fig. 3-21 (a). Again, the tiny deviation primarily stems from, as stated earlier, both normal and shear stress gradients present in the two cut planes spaced 1 mm apart.

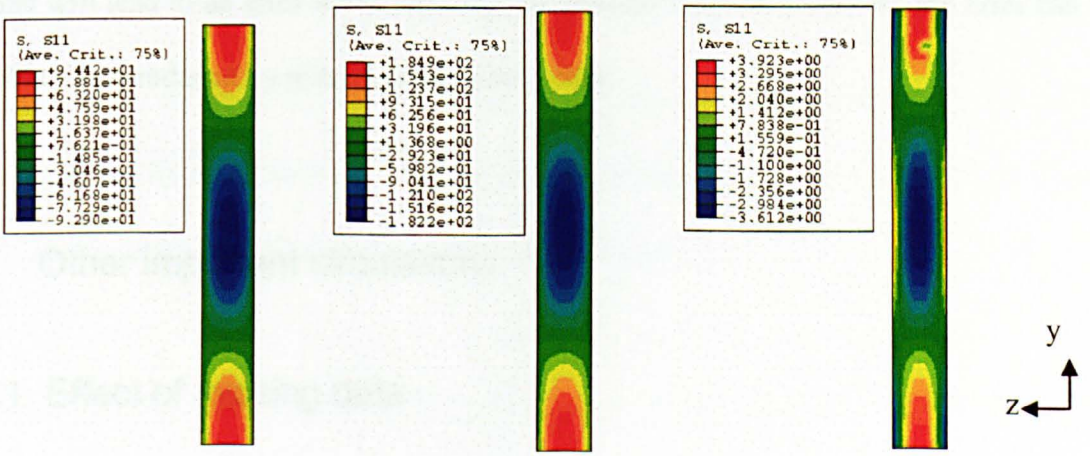

(a) contour average (correct) (b) contour left (incorrect) (c) contour right (incorrect)

Figure 3-21 Stress profiles calculated by the contour method

3.2.3 Conclusion

The principle of the contour method has been examined in detail by 2D FE simulations and also demonstrated on 3D FE simulations. Several key conclusions can be drawn from this study.

- The correct stress can be obtained by averaging two corresponding displacements from the two cut planes regardless of the conditions present, although use of the displacement from either of the two cut surfaces can give acceptable accuracy under a condition where there is no or little shear stress on the plane at issue.
- The geometrical simplification applied in the contour method is reasonable to obtain an original stress field with negligible error.
- The inaccuracy in the contour method is largely dependent on the difference of the stress states of both normal and shear stresses between the two cut planes. The bigger the stress difference is, the greater the error will be introduced.
- The error is proportional to the magnitude of the stress to be determined.
- In practice, material removal inevitably produces a stress gradient in the two cut planes that will lead to an error when applying the contour method. However, the error can be effectively reduced by minimising the cut width.

3.3 Other important simulations

3.3.1 Effect of missing data

It is not uncommon that some of the measured data are missing or bad, particularly at the edges of surfaces, partly due to the limitation of the measurement equipment used. This is especially true when measuring displacements of a surface using a co-ordinate measuring machine. To deal with this kind of problem, two cases are considered here: the first case

presumes that the model is narrowed to the region having valid data; the second case assumes that the missed data at the edge are equal to the values closest to the valid data.

- Narrow model

The half geometry used in this study is 50 mm long and 40 mm wide as seen in Fig. 3-22, in which the left plane is of interest. It is assumed that 2 mm of data are missing at two sides of the left plane. So the initial width of the model is correspondingly reduced to 36 mm from the initial 40 mm, as illustrated in Fig. 3-22.

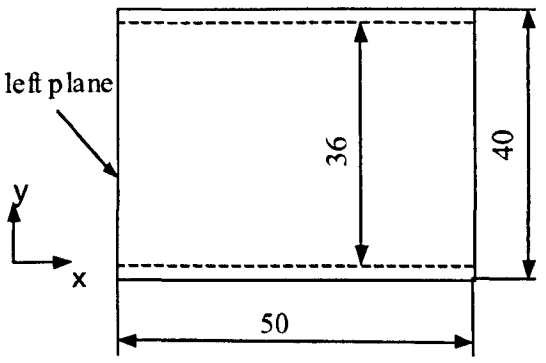

Figure 3-22 Geometrical model

Fig. 3-33 shows the initial displacement distribution, illustrated by the solid line, on the left plane to be applied by the contour method. However, only the data within the 36 mm width in the middle, represented by the dots, is used for this case.

Fig. 3-24 illustrates the influence of the narrow model on the calculated stress profile at the left boundary, and the known stress profile. It can be seen that the use of the narrowed model to deal with the missed data will globally affect the stress distribution, particularly at the sides where the width is reduced. This can be explained by a physical phenomenon that the originally balanced stress distribution along the plane will change if a portion of

the stress at the ends is removed. This imbalance consequently leads to stress redistribution along the plane. This simulation suggests that using the actual geometry is necessary even though complete data on the surface at issue are not available for some reasons.

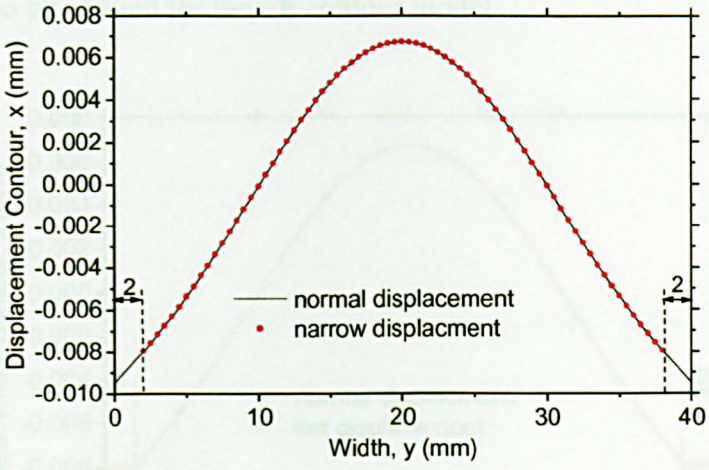

Figure 3-23 Narrow displacement

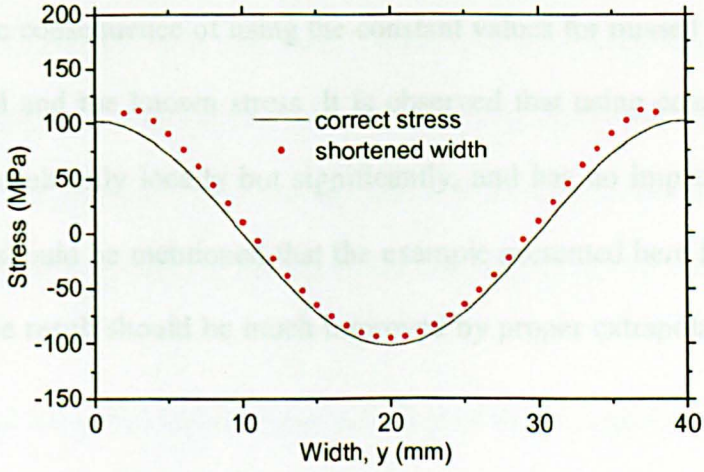

Figure 3-24 Stress profiles for the narrowed model and the whole model

- Flat displacement

In this case, the missed data 2 mm long at each side of the left plane are replaced by constant values, equivalent to the nearest valid values, as shown in Fig. 3-25 in dots. In Fig. 3-25, the solid line represents the original displacement profile and the dotted line is the displacement to be applied for the FE contour model.

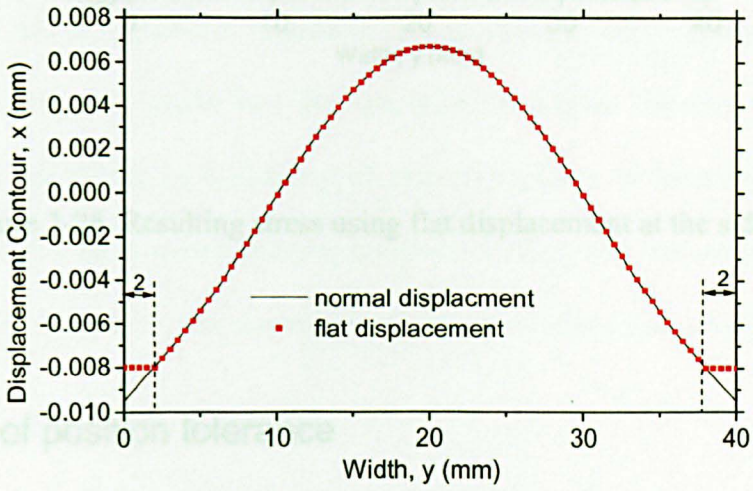

Figure 3-25 Flat displacement at both sides

Fig. 3-26 gives the consequence of using the constant values for missed data at the ends in the contour model and the known stress. It is observed that using constant values at the ends affects the result only locally but significantly, and has no impact on the stress far from the ends. It should be mentioned that the example presented here is almost the worst case. In reality, the result should be much improved by proper extrapolation of the missed data.

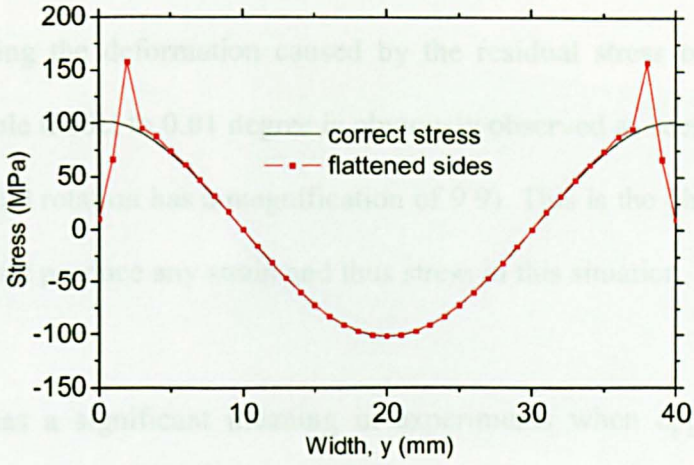

Figure 3-26 Resulting stress using flat displacement at the sides

3.3.2 Effect of position tolerance

In applying the contour method, the plane under study needs cutting and then measuring. In practice, the cutting plane is not perfectly parallel to the reference plane due to the presence of the machining tolerance. In addition, the surface contour measurement does not always share the same reference plane as the cutting. Under any circumstance, there must be position tolerances with the plane of interest, whenever cutting or measuring. Therefore, the measured deformations must include the displacements induced by this position tolerance, resulting in an untrue deformation measurement. The following study will examine if this inconsistency produces errors when applying the contour method.

It is presumed that the additional displacement is introduced by cutting and/or measuring with an angle of 0.01 degree to the plane under study in addition to the deformation relaxed by the residual stress, as illustrated in Fig. 3-27 (a). This combined effect is shown in Fig. 3-27 (b) and included in the measurement data. Again, a half 2D model is used, 50 mm in length and 40 mm in width. The combined displacement is applied on the left plane

under study in the contour model. Performing the FEA yields the exact same outcome as the case when using the deformation caused by the residual stress only. However, the rotation of the whole model to 0.01 degree is obviously observed as seen in Fig. 3-28 (It is noted that this visual rotation has a magnification of 9.9). This is the phenomenon of rigid rotation that does not produce any strain and thus stress in this situation.

This simulation has a significant meaning in experiments when applying the contour method. It eliminates the doubt that the specimen cutting or contour measuring could introduce errors due to the inconsistency of reference planes or location tolerance. This brings such convenience to experiments as specimen cutting and surface measuring can be conducted without too much consideration and restriction of position tolerance.

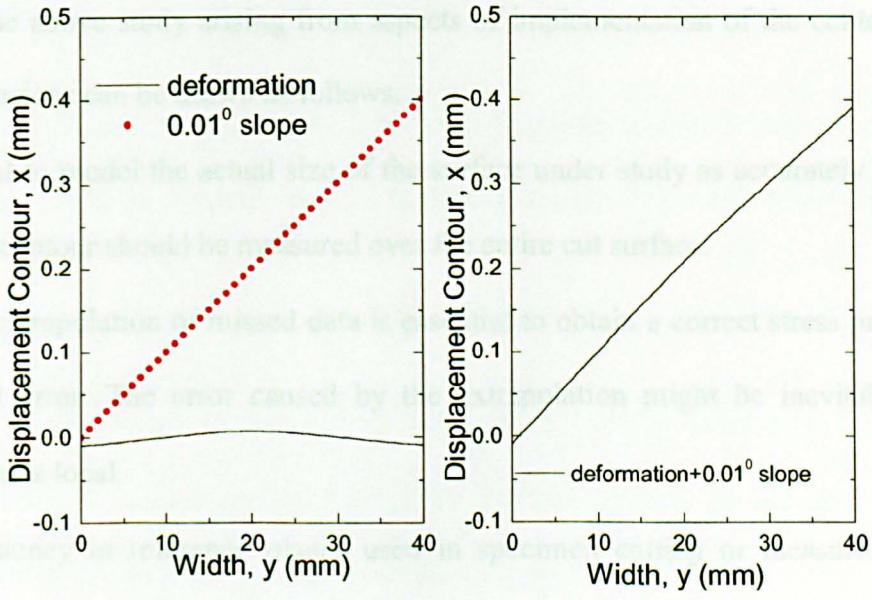

(a) deformation and 0.01° slope (b) combined displacement

Figure 3-27 Displacement with slope (0.01 degree)

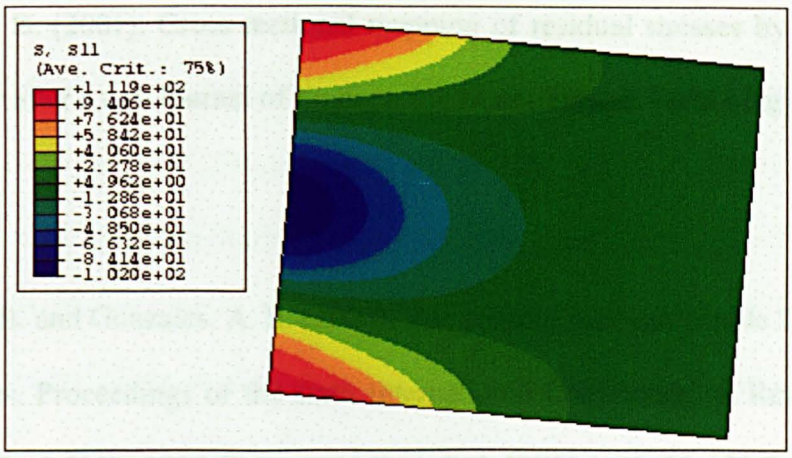

Figure 3-28 FE result applied with combined displacement (deformation scale factor: 9.9)

3.3.3 Conclusion

Based on the above study arising from aspects of implementation of the contour method, some conclusions can be drawn as follows.

- It is vital to model the actual size of the surface under study as accurately as possible, and the contour should be measured over the entire cut surface.
- Proper extrapolation of missed data is essential to obtain a correct stress profile with a minimal error. The error caused by the extrapolation might be inevitable, but the influence is local.
- Inconsistency in reference planes used in specimen cutting or measuring does not introduce any errors to the result.

3.4 References

[1] Bueckner, H. F. (1958). The propagation of cracks and the energy of elastic deformation. Transaction of the ASME, Vol. 80, pp. 1225-1230.

[2] Prime, M. B. (2001). Cross-sectional mapping of residual stresses by measuring the surface contour after a cut. Journal of Engineering Materials and Technology, Vol. 123, pp. 162-168.

[3] Prime, M. B. and Gonzales, A. R. (2000). The contour method: simple 2-D mapping of residual stresses. Proceedings of the sixth International Conference on Residual Stresses, 10-12 July, Oxford, U.K., IOM Communications Ltd, ISBN:1-86125-123-8, pp. 617-624.

[4] Prime, M. B., Hughes, D. J. and Webster, P. J. (2001). Weld application of a new method for cross-sectional residual stress mapping. Proceedings of 2001 SEM Annual Conference on Experimental and Appplied Mechanics, 4-6 June, Portland, OR, pp. 608-611.

[5] Prime, M. B. and Martineau, R. L. (2002). Mapping residudal stresses after foreign object damage using the contour method. Materials Science Forum, Vol. 404-407, pp. 521-526.

[6] Prime, M. B., Newborn, M. A. and Balog, J. A. (2003). Quenching and cold-work residual stresses in aluminum hand forgings: contour method measurement and FEM prediction. Materials Science Forum, Vol. 426-432, pp. 435-440.

[7] Zhang, Y., Fitzpatrick, M. E. and Edwards, L. (2002). Measurement of the residual stresses around a cold expanded hole in an EN8 steel plate using the contour method. Materials Science Forum, Vol. 404-407, pp. 527-534.

4 Hole cold expansion and theoretical analysis

Hole cold expansion is a well-known mechanical process to introduce beneficial compressive residual stresses into structural components for fatigue enhancement (Reid, 1996). It has been investigated theoretically, experimentally and numerically, leading to a large number of published reports. It is advantageous to use this well-understood process to validate the novel technique of the contour method. Analytical prediction is the cheapest and quickest way to model the residual stress field induced by the hole cold expansion. To achieve this, an analytical model suitable for a finite plate has been extended and explicitly established based on existing analytical models and methodologies.

4.1 Introduction to hole cold expansion

It is useful to introduce this popular process of hole cold expansion prior to establishment of the theoretical model. The concept of the split-sleeve method for hole cold expansion was pioneered by the Boeing Company in the late 1960s for the purpose of protecting fastener holes in aircraft structures from the initiation and the growth of cracks. Later it was further developed as a lubricated split sleeve method by Fatigue Technology Inc. (FTI). It has been proved that a mandrel, in conjunction with a split sleeve, is a particularly effective tool to extend the fatigue life of components containing fastener holes (Reid, 1996). Nowadays, the technique of FTI split sleeve cold expansion has been broadly used in all kinds of metallic fastener joints for improvement of fatigue resistance without penalty of weight.

The FTI split sleeve cold expansion involves positioning a longitudinally-split sleeve inside a hole to be expanded, and then pulling an oversized tapered mandrel through the hole. It means that the maximum diameter of the mandrel combined with the split-sleeve is

greater than the initial diameter of the hole. Thus, upon removal of the mandrel, the action of the elastic spring-back of the material lying beyond the zone of plastic deformation induced by the process creates a compressive residual stress field in the vicinity of the hole. This resulting effect will retard crack initiation and propagation from the hole under fatigue loads. Fig. 4-1 illustrates a typical residual stress profile resulting from the hole cold expansion process.

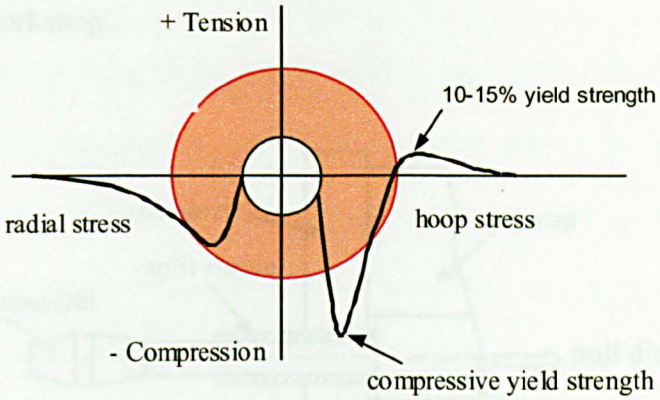

Figure 4-1 Typical cold expansion residual stress profile (Reid, 1996)

Typically, a compressive stress zone covers about one hole diameter from the hole edge and the absolute maximum value of the compressive hoop stress is approximately equivalent to the compressive yield stress of the material under study.

A standard FTI tooling assembly (Champoux and Landy, 1984) generally consists of a pre-lubricated stainless steel split sleeve, a tapered mandrel, a hydraulic puller unit, and a mandrel. The split sleeve is designed to be disposable, with the aim of ensuring proper radial expansion of the hole and avoiding damage to the hole. In general, the expansion or interference ratio, defined as the interference between the mandrel coupled with the sleeve and the hole, divided by the initial radius of the hole, is nominally 4% for aluminium alloys and mild steels and 5.5% for high strength metals (Stefanescu, 2001). The final procedure

of the hole cold expansion process normally involves reaming the expanded hole to a desirable diameter with a good quality internal surface.

The FTI tool set used for our study is specifically comprised of an HP-20 (S/N 561) mandrel with a maximum diameter of 8.58 mm, a CBS-10-3-N-16F self-lubricated split sleeve with a thickness of 0.25 mm and a puller unit, as illustrated in Fig. 4-2. All hole cold expansion specimens examined in the subsequent chapters were processed by this tool set in our department workshop.

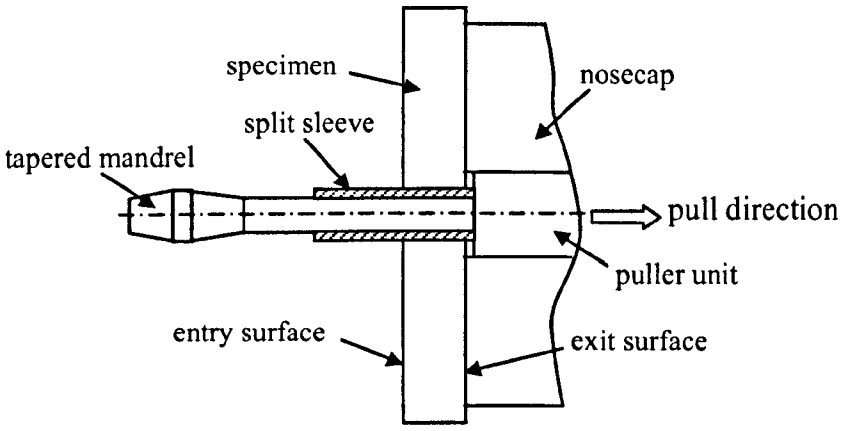

Figure 4-2 Schematic illustration of the FTI assembly used in our study

Due to the presence of the split in the split-sleeve, as seen in Fig. 4-3 (a), a pip at the split location during the expansion process can be observed as illustrated in Fig. 4-3 (b).

However, the pip can be removed by reaming if necessary to reach the desired diameter. The presence of the pip suggests that the hole is not uniformly expanded by the split-sleeve tool system, thus resulting in a non-uniform stress distribution.

(a) Used split-sleeve (b) Pip caused by the split sleeve

Figure 4-3 Used split-sleeve and an expanded hole showing the pip

For convenience, the following terms will be used throughout the thesis for cold expansion issues. The surface of the specimen where the mandrel enters the hole during the cold expansion is referred to as the mandrel entrance surface or entry surface or inlet surface. The surface of the specimen where the mandrel leaves the hole is called the mandrel exit surface or exit surface or outlet surface. The region at the edge of the hole subjected to a non-uniform radial expansion due to the split of the sleeve is termed the pip, as shown in Fig. 4-3 (b). The split of the sleeve, and as a result the pip, are always located on the longitudinal direction of the specimens in this study.

4.2 Theoretical analysis of hole cold expansion in a finite plate

With the popularity of the cold expansion process in industry, various methods such as analytical prediction (Nadai, 1943; Hsu and Forman, 1975; Rich and Impellizzeri, 1977; Guo, 1993; Ball, 1995), experimental measurement (Cook and Holdway, 1993; O'Brien, 1993; Ozdemir and Edwards, 1996; Webster et al., 2000; Stefanescu et al., 2002; Zhang et al., 2002b) and numerical simulation (Forgues et al., 1993; Poussard et al., 1995; Pavier et al., 1997; Pavier et al., 1998; Kang et al., 2002; Zhang et al., 2002a) have been developed and reported to quantify this mechanical effect. However, analytical prediction still remains attractive owing to its low demand for computation resources, quick generation of

results and ease of performing parametric studies which is particularly significant at the design stage for any engineering project.

Analytical studies of the cold expansion process have been initiated since the 1940s. The solutions differ substantially in their assumptions: yield criterion (Von Mises or Tresca), stress state (plane stress or plane strain), material model (elastic perfectly-plastic or elastic nonlinear-strain-hardening), and unloading (elastic or/with reverse yielding). The analytical complexity primarily depends on the level of model assumptions, particularly on the treatment of unloading and material behaviour. Several reviews of these analytical studies have been presented by Sharpe (Sharpe, 1978), Poolsuk and Sharpe (Poolsuk and Sharpe, 1978), Mann et al. (Mann and Jost, 1983), Ozdemir (Ozdemir, 1993), Poussard et al. (Poussard et al., 1995), Ball (Ball, 1995) and more recently by Pavier et al. (Pavier et al., 1997). Five analytical models relevant to the current model are summarized in Table 1.

In studying the development of an analytical model describing cold working effects, Nadai (1943) firstly considered a tube of elastic-plastic strain hardening material, to be fitted into a plate with the assumptions of elastic perfectly-plastic material, plane stress conditions and using the Von Mises yield criterion. Later, Hsu and Forman (1975) published a solution using a technique developed by Budiansky (Budiansky, 1971) based on the J_2 deformation theory of plasticity. A more complicated non-linear material relationship called a modified Ramberg-Osgood model was implemented. However, these treatments on the unloading step were very cursory, by assuming elastic unloading. The results obviously could not predict the effect of reverse yielding and the development of a reverse-yielded zone around a hole. As indicated by Sharpe (1978) in his study, the Nadai and Hsu-Forman theories did not agree well with the result measured experimentally from an indentation technique, although they both presented similar trends. Gradually, reverse yielding was realized to be potentially important to achieve a correct prediction of the cold

expansion process, and further investigation of the plasticity action during unloading and the Bauschinger effect were carried out by others. As an example, Rich and Impellizzeri (1977) took reverse yielding on unloading into account, although the treatment of the reverse zone and reverse yielding was approximate. Nevertheless, their solution coupled with plain strain conditions predicted the reverse-yielded location reasonably well for thicker plates (Poolsuk and Sharpe, 1978). Later, Hsu and Forman's work was expanded by Guo (1993) to account for non-linear response during both loading and unloading, with a special emphasis on the boundary effect of a finite plate instead of an infinite plate. However, the solution of how to deal with the unloading step was not explicitly presented, although a suggestion was given. Again, based on the Budiansky technique and the modified Ramberg-Osgood model, Ball (1995) advanced Hsu and Forman's solution by giving an explicit solution addressing elastic-nonlinear plastic unloading, but his model was limited to infinite plate conditions. However, the model for finite plates is closer to the real condition than the model for infinite plates. It is therefore the motivation to complete Guo's work by including the explicit solutions of unloading based on Ball's methodology for dealing with the unloading step in an infinite plate.

In this chapter, a complete closed-form solution for the hole cold expansion process is explicitly presented, which attempts to deal with the situation where hole cold expansion is performed in a finite size plate, with consideration of boundary effects, elastic-nonlinear plastic loading and unloading, plane stress conditions and using the Von Mises yield criterion. An elastically deformable mandrel and the cold expansion ratio are also explicitly incorporated into the solution.

Table 1 Five Analytical Models

References	Yield criterion	Plane condition	Material model	Unloading	Mandrel or insert	Specimen
(Nadai, 1943)	Von Mises	Plane stress	Elastic-perfectly plastic	Elastic	Elastically-plastically deformable tube	Thin, infinite plate
(Hsu and Forman, 1975)	Von Mises	Plane stress	Elastic-nonlinear strain hardening	Elastic	Not included	Thin, infinite plate
(Rich and Impellizzeri, 1977)	Von Mises	Plane strain	Elastic–perfectly plastic	Elastic unloading with approximation for reverse yielding	Elastically deformable mandrel	Thick, finite plate
(Guo, 1993)	Von Mises	Plane stress	Elastic-nonlinear strain hardening	Elastic-nonlinear strain hardening with Bauschinger effect	Elastically deformable bolt	Thin, finite plate
(Ball, 1995)	Von Mises	Plane stress	Elastic-nonlinear strain hardening	Elastic-nonlinear strain hardening with Bauschinger effect	Elastically deformable mandrel	Thin, infinite plate

4.2.1 Description of the problem

It is assumed that a hole in a finite plate with inner radius of a and outer radius of b is subjected to an internal pressure of p, as illustrated in Fig. 4-4. A cylindrical co-ordinate system with the origin at the hole centre is suggested by the axial symmetry of the structural system. The boundary conditions for this case are defined as:

$$\sigma_r = 0 \quad at \ r = b \tag{4.1a}$$

$$\sigma_r = -p \quad at \ r = a \tag{4.1b}$$

where σ_r is the radial stress, and r is the radius at any point between a and b.

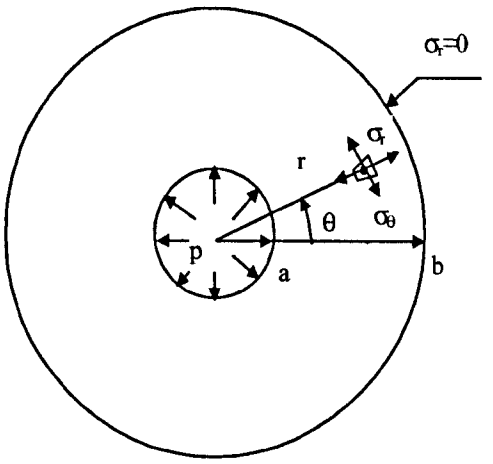

Figure 4-4 Finite plate with a circular hole subjected to pressure, p

The modified Ramberg-Osgood model (Budiansky, 1971), instead of the Ramberg-Osgood law (Mangasarian, 1960), is assumed for the problem:

$$\varepsilon = \begin{cases} \dfrac{\sigma}{E} & for\ |\sigma| \le \sigma_y \\ \dfrac{\sigma}{E}\left|\dfrac{\sigma}{\sigma_y}\right|^{n-1} & for\ |\sigma| \ge \sigma_y \end{cases} \tag{4.2}$$

where ε is the true strain, σ is the true stress, E is the elastic modulus, σ_y is the initial yield stress and n is the strain hardening exponent, as shown in Fig. 4-5.

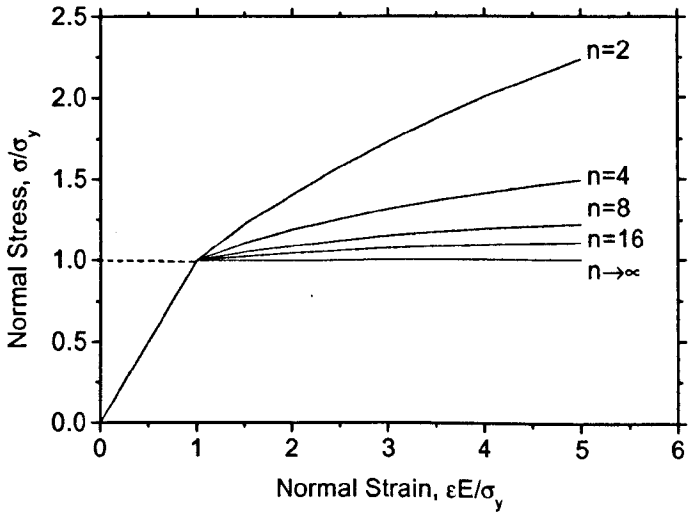

Figure 4-5 Relationship of stress and strain with strain hardening exponent, n

4.2.2 Constitutive equations

In this section, the constitutive equations will be formulated to describe the relationships of stresses and strains in the plate subjected to elastic-plastic deformation. The stress states of interest in the plate are assumed to be of small strain, two-dimensional, axially symmetric and in plane stress condition where the stress normal to the surface is zero. The shear stress $\tau_{r\theta}$ and the shear strain $\gamma_{r\theta}$ are also zero owing to the symmetry. The radial and hoop stresses, σ_r and σ_θ, must meet the stress equilibrium equation as follows:

$$\frac{d\sigma_r}{dr}+\frac{\sigma_r-\sigma_\theta}{r}=0 \tag{4.3}$$

Similarly, the corresponding strains, ε_r and ε_θ, should satisfy the compatibility equation in the following:

$$\frac{d\varepsilon_\theta}{dr}+\frac{\varepsilon_\theta-\varepsilon_r}{r}=0 \tag{4.4}$$

Further, the strains are related to the radial displacement, u, by the following equations:

$$\varepsilon_r=\frac{du}{dr} \tag{4.5a}$$

$$\varepsilon_\theta=\frac{u}{r} \tag{4.5b}$$

The total strains are defined as the sum of elastic components denoted by el and plastic components denoted by pl:

$$\varepsilon_r=\varepsilon_r^{el}+\varepsilon_r^{pl} \tag{4.6a}$$

$$\varepsilon_\theta=\varepsilon_\theta^{el}+\varepsilon_\theta^{pl} \tag{4.6b}$$

The relationships of the elastic strains and the stresses are based on the Hooke's law:

$$\varepsilon_r^{el}=\frac{1}{E}(\sigma_r-\upsilon\sigma_\theta) \tag{4.7a}$$

$$\varepsilon_\theta^{el}=\frac{1}{E}(\sigma_\theta-\upsilon\sigma_r) \tag{4.7b}$$

where E is the Young's modulus and υ is the Poisson's ratio.

The relationships of the plastic strains and the stresses, considering the anisotropy of the material, are (Hsu and Forman, 1975):

$$\varepsilon_r^{pl} = \left(\frac{1}{E_s} - \frac{1}{E}\right)\left(\sigma_r - \frac{R}{1+R}\sigma_\theta\right) \tag{4.8a}$$

$$\varepsilon_\theta^{pl} = \left(\frac{1}{E_s} - \frac{1}{E}\right)\left(\sigma_\theta - \frac{R}{1+R}\sigma_r\right) \tag{4.8b}$$

In Equations (4.8), the level of plastic anisotropy is described by R, defined as the ratio of the true in-plane transverse plastic strain to the true through-thickness plastic strain, where $R=1$ results in isotropic behaviour. R is normally measured in a tensile test specimen after a certain amount of straining in the uniform elongation region, and there is a standard test method for R detailed in ASTM E 517. E_s is the secant modulus at the point σ, ε on the uniaxial stress-strain curve and obtained from Equation (4.2):

$$\frac{1}{E_s} = \frac{\varepsilon}{\sigma} = \frac{1}{E}\left|\frac{\sigma}{\sigma_y}\right|^{n-1} \tag{4.9}$$

As υ has no effect on the solution of the stresses and $\upsilon = R/(1+R)$ is chosen (Hsu and Forman, 1975; Guo, 1993), leading to the relationships of the total strains and the stresses from Equations (4.6), (4.7), (4.8) as follows:

$$\varepsilon_r = \frac{1}{E_s}\left(\sigma_r - \frac{R}{1+R}\sigma_\theta\right) \tag{4.10a}$$

$$\varepsilon_\theta = \frac{1}{E_s}\left(\sigma_\theta - \frac{R}{1+R}\sigma_r\right) \tag{4.10b}$$

However, once the stresses are solved, the actual strains can be derived from Equations (4.6) and (4.7) using the true Poisson's ratio υ (Hsu and Forman, 1975).

4.2.3 Elastic-plastic analysis of radial expansion (loading)

The first analytical step of the hole cold expansion process is to apply a uniform radial pressure, p, on the hole edge, as depicted in Fig. 4-4. If the plate only experiences elastic deformation, the elastic solutions (Timoshenko and Goodier, 1970) are simply as follows:

$$\sigma_r = -\frac{(b^2/r^2)-1}{(b^2/a^2)-1}p \tag{4.11a}$$

$$\sigma_\theta = \frac{(b^2/r^2)+1}{(b^2/a^2)-1}p \tag{4.11b}$$

On the other hand, if the plate has to undergo elastic-plastic deformation, the solutions in the elastic domain ($r_p \le r \le b$), as shown in Fig. 4-6, are:

$$\sigma_r = -\frac{(b^2/r^2)-1}{(b^2/a^2)-1}p_p \tag{4.12a}$$

$$\sigma_\theta = \frac{(b^2/r^2)+1}{(b^2/a^2)-1}p_p \tag{4.12b}$$

where, p_p is the pressure on the boundary between the elastic domain and plastic domain, at $r = r_p$.

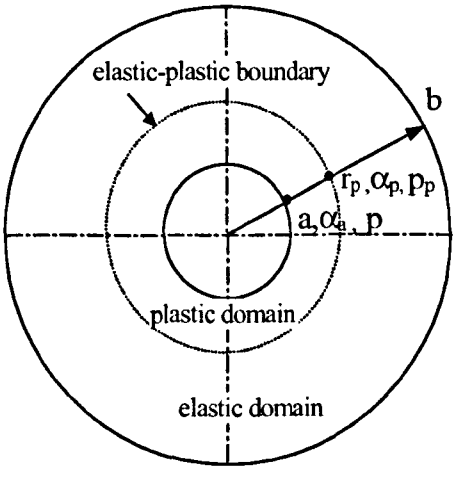

Figure 4-6 Plate subjected to elastic-plastic deformation

In the plastic domain ($a \le r \le r_p$), the effective stress σ is defined as:

$$\sigma = \left(\sigma_r^2 + \sigma_\theta^2 - \frac{2R}{1+R} \sigma_r \sigma_\theta \right)^{0.5} \tag{4.13}$$

and the yielding criterion is:

$$\sigma = \sigma_y \tag{4.14}$$

The elastic solutions of Equations (4.12) at $r = r_p$ should satisfy Equations (4.13) and (4.14) as well owing to the continuity of the stresses on the elastic-plastic boundary. Combining Equations (4.12), (4.13) and (4.14) leads to:

$$p_p = \sigma_y \left(\frac{b^2}{a^2} - 1 \right) \left[2\frac{b^4}{r_p^4} + 2 + \frac{2R}{1+R} \left(\frac{b^4}{r_p^4} - 1 \right) \right]^{-0.5} \tag{4.15}$$

The critical pressure at which yielding begins is available from Equation (4.15) by letting $r_p = a$, and assuming $R = 1$:

$$p_y = \sigma_y \frac{b^2/a^2 - 1}{\sqrt{3b^4/a^4 + 1}} \tag{4.15a}$$

If the plate is infinite, the critical pressure in Equation (4.15a) when $b \to \infty$ becomes:

$$p_y = \frac{\sigma_y}{\sqrt{3}} \tag{4.15b}$$

The final elastic solutions are obtained by substituting Equation (4.15) into Equations (4.12) in the elastic domain:

$$\sigma_r = -\sigma_y \left(\frac{b^2}{r^2} - 1 \right) \left[2\frac{b^4}{r_p^4} + 2 + \frac{2R}{1+R} \left(\frac{b^4}{r_p^4} - 1 \right) \right]^{-0.5} \tag{4.16a}$$

$$\sigma_\theta = \sigma_y \left(\frac{b^2}{r^2} + 1 \right) \left[2\frac{b^4}{r_p^4} + 2 + \frac{2R}{1+R} \left(\frac{b^4}{r_p^4} - 1 \right) \right]^{-0.5} \tag{4.16b}$$

which satisfies Equation (4.13) identically.

In the plastic domain, Budiansky solutions in terms of the parameter, α, which varies monotonically between the values at the hole edge and the elastic-plastic boundary (Ball, 1995), are used:

$$\sigma_r = \sigma\sqrt{\frac{1+R}{2}}\left(\cos\alpha - \frac{1}{\sqrt{1+2R}}\sin\alpha\right) \tag{4.17a}$$

$$\sigma_\theta = \sigma\sqrt{\frac{1+R}{2}}\left(\cos\alpha + \frac{1}{\sqrt{1+2R}}\sin\alpha\right) \tag{4.17b}$$

Combining Equations (4.16) and (4.17) results in equations under the conditions of $\alpha = \alpha_p$ at $r = r_p$ and $\sigma = \sigma_y$:

$$\sin\alpha_p = \sqrt{1+2R}\left(\frac{b}{r_p}\right)^2\left[(1+2R)\left(\frac{b}{r_p}\right)^4 + 1\right]^{-0.5} \tag{4.18a}$$

$$\cos\alpha_p = \left[(1+2R)\left(\frac{b}{r_p}\right)^4 + 1\right]^{-0.5} \tag{4.18b}$$

where, $0 < \alpha_p \le \pi/2$.

Combining Equations (4.3), (4.4), (4.9), (4.10), (4.17) and then differentiating the resulting equation in terms of the effective stress, σ, and the parameter α, yields (Guo, 1993):

$$\frac{1}{\sigma}d\sigma = \frac{2(1+R)\sin\alpha}{(n+1+2R)\cos\alpha + (n-1)\sqrt{1+2R}\sin a}d\alpha \tag{4.19}$$

Then integrating Equation (4.19) with $\sigma = \sigma_y$ at $\alpha = \alpha_p$ gives:

$$\int_{\sigma_y}^{\sigma}\frac{1}{\sigma}d\sigma = \int_{\alpha_p}^{\alpha}\frac{2(1+R)\sin\alpha}{(n+1+2R)\cos\alpha + (n-1)\sqrt{1+2R}\sin\alpha}d\alpha \tag{4.20}$$

Performing the integration of Equation (4.20) produces:

$$\frac{\sigma}{\sigma_y} = \left(\frac{a_1\sin\alpha_p + a_2\cos\alpha_p}{a_1\sin\alpha + a_2\cos\alpha}\right)^{\mu}\exp\left(\frac{2\,a_1(1+R)(\alpha-\alpha_p)}{a_1^{\,2} + a_2^{\,2}}\right) \tag{4.21}$$

where

$$a_1 = (n-1)\sqrt{1+2R}$$

$$a_2 = n+1+2R$$

$$\mu = \frac{2\,a_2(1+R)}{a_1^{\,2} + a_2^{\,2}}$$

Letting $\alpha = \alpha_a$ at $r = a$ in Equation (4.17a) and (4.21), the relationship between p, α_a, α_p can be obtained from Equations (4.17a), (4.21) and (4.1b) in the following:

$$p = \sigma_y \sqrt{\frac{1+R}{2}} \left(\frac{\sin \alpha_a}{\sqrt{1+2R}} - \cos \alpha_a \right) \left(\frac{a_1 \sin \alpha_p + a_2 \cos \alpha_p}{a_1 \sin \alpha_a + a_2 \cos \alpha_a} \right)^{\mu} \exp \left[\frac{2a_1 (1+R)(\alpha_a - \alpha_p)}{a_1^2 + a_2^2} \right] \quad (4.22)$$

Combining Equations (4.3) and (4.17), with the aid of Equation (4.21) and integrating the resulting equation from $\alpha = \alpha_a$ at $r = a$ lead to:

$$\frac{r}{a} = \sqrt{\frac{\sin \alpha_a}{\sin \alpha}} \left(\frac{a_1 \sin \alpha + a_2 \cos \alpha}{a_1 \sin \alpha_a + a_2 \cos \alpha_a} \right)^{\gamma} \exp \left[\frac{(n^2 - 1)\sqrt{1+2R}(\alpha_a - \alpha)}{2(n^2 + 1 + 2R)} \right] \quad (4.23)$$

where

$$\gamma = \frac{n(1+R)}{n^2 + 1 + 2R}$$

The relationship between r_p, α_a, α_p can be obtained from Equation (4.23) at $r = r_p, \alpha = \alpha_p$:

$$\frac{r_p}{a} = \sqrt{\frac{\sin \alpha_a}{\sin \alpha_p}} \left(\frac{a_1 \sin \alpha_p + a_2 \cos \alpha_p}{a_1 \sin \alpha_a + a_2 \cos \alpha_a} \right)^{\gamma} \exp \left[\frac{(n^2 - 1)\sqrt{1+2R}(\alpha_a - \alpha_p)}{2(n^2 + 1 + 2R)} \right] \quad (4.24)$$

The maximum of α can be acquired from Equation (4.24) when $b \to \infty, p \to \infty, r_p \to \infty$:

$$\alpha_{\max} = \tan^{-1} \left[\frac{n+1+2R}{(1-n)\sqrt{1+2R}} \right] \quad (4.25)$$

Thus, r_p, α_a, α_p can be readily solved from Equations (4.24), (4.22) and (4.18), with $\alpha_p < \alpha_a < \alpha_{\max}$.

With r_p, α_a, α_p being known, the radial and hoop stresses at any point in the plastic domain can be obtained from Equations (4.23), (4.21) and (4.17). Similarly, the radial and hoop stresses at any point in the elastic domain can be obtained from Equations (4.16).

In general cases of cold expansion problems, it is the interference, I_a, defined as here the difference between the mandrel radius a_m, and the hole radius a, rather than the internal pressure p, which are known. It is therefore necessary to establish the relationship between the expansion interference and the pressure on the hole edge. Cold expansion processes normally involve radial expansion of the hole and radial contraction of the mandrel. Therefore, the interference I_a should equal the difference between the radial displacement of the plate, $u_p(r)$, and the radial displacement of the mandrel, $u_m(r)$, at $r = a$:

$$I_a = a_m - a = u_p(a) - u_m(a) \tag{4.26}$$

It is assumed that the mandrel is subjected to elastic deformation only. So, the radial displacement of the mandrel at the hole edge is:

$$u_m(a) = -\frac{a_m p}{E_m}(1-\upsilon_m) \tag{4.27}$$

where E_m, υ_m are the Young's modulus and Poisson's ratio of the mandrel respectively.

The radial displacement of the plate at the hole edge, $u_p(a)$, is available from Equation (4.5b) at $r = a$:

$$u_p(a) = a\,\varepsilon_\theta(a) \tag{4.28}$$

If the plate experiences only elastic deformation, the radial displacement of the plate at $r = a$ is derived from Equations (4.7b) and (4.16):

$$u_p(a) = \frac{a\sigma_y}{E}\left[\frac{b^2}{a^2}+1+\upsilon\left(\frac{b^2}{a^2}-1\right)\right]\left[2\frac{b^4}{r_p^4}+2+\frac{2R}{1+R}\left(\frac{b^4}{r_p^4}-1\right)\right]^{-0.5} \tag{4.28a}$$

If the plate undergoes plastic deformation, the total strain has to be accounted for by combining Equations (4.6b) together with (4.7b), (4.8b), (4.17), (4.21) and setting $\alpha = \alpha_a$, the radial displacement of the plate at $r = a$ is:

$$u_p(a)=\frac{a\sigma_y}{E}\sqrt{\frac{1+R}{2}}\left[(1-\lambda)\cos\alpha_a+\frac{1+\lambda}{\sqrt{1+2R}}\sin\alpha_a\right]$$
$$\left\{\left(\frac{a_1\sin\alpha_p+a_2\cos\alpha_p}{a_1\sin\alpha_a+a_2\cos\alpha_a}\right)^{\mu}\exp\left[\frac{2a_1(1+R)(\alpha_a-\alpha_p)}{a_1^{\,2}+a_2^{\,2}}\right]\right\}^{n} \tag{4.28b}$$

where

$$\lambda=\frac{R}{1+R}-\left(\frac{R}{1+R}-\upsilon\right)\left[\left(\frac{a_1\sin\alpha_p+a_2\cos\alpha_p}{a_1\sin\alpha_a+a_2\cos\alpha_a}\right)^{\mu}\exp\left(\frac{2a_1(1+R)(\alpha_a-\alpha_p)}{a_1^{\,2}+a_2^{\,2}}\right)\right]^{(1-n)}$$

Finally, the relationship between p and I_a can be obtained by substituting Equations (4.28) and (4.27) into (4.26).

Often in reality, in place of the interference, I_a, the interference ratio is used, I_0, which is defined as the ratio of the interference to the hole radius:

$$I_0=\frac{I_a}{a}=\frac{a_m-a}{a} \tag{4.29}$$

So far, all the relationships between relevant parameters during the loading process have been established.

4.2.4 Elastic-plastic analysis of unloading

As mentioned earlier, Hsu and Forman simply gave an elastic treatment of the unloading step and thus reverse yielding was not accounted for. Ball presented explicitly the treatment of elastic-plastic unloading, but with the restriction to the condition of an infinite plate. Guo took the elastic-plastic unloading into account for a finite plate; but, the closed-formed equations on the unloading step were not presented in the literature. However, some issues are still thought to need addressing and clarifying, particularly in the use of the reverse yield criterion and the understanding of the unloading process.

The following is an explicit treatment of elastic-plastic unloading in a finite plate, where reverse yielding is considered. It is noted that all solutions relevant to the unloading step are denoted by '–'. For points not yielding during the loading cycle, the reverse yield stress of σ_y^- is determined by (Guo, 1993):

$$\sigma_y^- = \sigma + \sigma_y \tag{4.30}$$

For points which undergo plastic deformation during the loading, the reverse yield stress is defined as (Ball, 1995):

$$\sigma_y^- = (1+\beta)\sigma_y + (1-\beta)\sigma \tag{4.31}$$

where β is the Bauschinger parameter defined such that $\beta = 0$ implies isotropic hardening, $\beta = 1$ results in kinematic hardening, and β between 0 to 1 means combined hardening.

In a manner similar to the loading step, the relationship between the pressure, p, parameter α_a^- at $r = a$, and parameter α_p^- at $r = r_p^-$, during the unloading step is:

$$p = \sigma_y^- \sqrt{\frac{1+R}{2}} \left(\frac{\sin\alpha_a^-}{\sqrt{1+2R}} - \cos\alpha_a^- \right) \left(\frac{a_1 \sin\alpha_p^- + a_2 \cos\alpha_p^-}{a_1 \sin\alpha_a^- + a_2 \cos\alpha_a^-} \right)^{\mu} \exp\left[\frac{2a_1(1+R)(\alpha_a^- - \alpha_p^-)}{a_1^{\,2} + a_2^{\,2}} \right] \tag{4.32}$$

The reverse-yielded boundary, r_p^-, is found:

$$\frac{r_p^-}{a} = \sqrt{\frac{\sin\alpha_a^-}{\sin\alpha_p^-}} \left(\frac{a_1 \sin\alpha_p^- + a_2 \cos\alpha_p^-}{a_1 \sin\alpha_a^- + a_2 \cos\alpha_a^-} \right)^{\gamma} \exp\left[\frac{(n^2-1)\sqrt{1+2R}(\alpha_a^- - \alpha_p^-)}{2(n^2+1+2R)} \right] \tag{4.33}$$

For the points at $a \le r \le r_p^-$, the unloading is elastic-plastic, and the corresponding radial and hoop stresses are:

$$\sigma_r^- = -\sigma^- \sqrt{\frac{1+R}{2}} \left(\cos\alpha^- - \frac{1}{\sqrt{1+2R}} \sin\alpha^- \right) \tag{4.34a}$$

$$\sigma_\theta^- = -\sigma^- \sqrt{\frac{1+R}{2}} \left(\cos\alpha^- + \frac{1}{\sqrt{1+2R}} \sin\alpha^- \right) \tag{4.34b}$$

The effective stress, σ^-, for the unloading step is:

$$\frac{\sigma^-}{\sigma_y^-}=\left(\frac{a_1\sin\alpha_p^-+a_2\cos\alpha_p^-}{a_1\sin\alpha^-+a_2\cos\alpha^-}\right)^{\mu}\exp\left[\frac{2a_1(1+R)(\alpha^--\alpha_p^-)}{a_1^{\,2}+a_2^{\,2}}\right] \tag{4.35}$$

where the reverse yield stress, σ_y^-,relies upon Equation (4.31).

The relationship between r and α^- is:

$$\frac{r}{a}=\sqrt{\frac{\sin\alpha_a^-}{\sin\alpha^-}}\left(\frac{a_1\sin\alpha^-+a_2\cos\alpha^-}{a_1\sin\alpha_a^-+a_2\cos\alpha_a^-}\right)^{\gamma}\exp\left[\frac{(n^2-1)\sqrt{1+2R}(\alpha_a^--\alpha^-)}{2(n^2+1+2R)}\right] \tag{4.36}$$

For the points at $r_p^- \le r \le r_p$, the unloading is elastic but the reverse yield criterion is based on Equation (4.31). The corresponding radial and hoop stresses are:

$$\sigma_r^-=\left[(1+\beta)\sigma_y+(1-\beta)\sigma\right]\left(\frac{b^2}{r^2}-1\right)\left\{2\left(\frac{b}{r_p^-}\right)^4+2+\frac{2R}{1+R}\left[\left(\frac{b}{r_p^-}\right)^4-1\right]\right\}^{-0.5} \tag{4.37a}$$

$$\sigma_\theta^-=-\left[(1+\beta)\sigma_y+(1-\beta)\sigma\right]\left(\frac{b^2}{r^2}+1\right)\left\{2\left(\frac{b}{r_p^-}\right)^4+2+\frac{2R}{1+R}\left[\left(\frac{b}{r_p^-}\right)^4-1\right]\right\}^{-0.5} \tag{4.37b}$$

For the points at $r \ge r_p$, the unloading is elastic and the reverse yield criterion is dependent on Equation (4.30). The corresponding radial and hoop stresses are:

$$\sigma_r^-=\left(\sigma+\sigma_y\right)\left(\frac{b^2}{r^2}-1\right)\left\{2\left(\frac{b}{r_p^-}\right)^4+2+\frac{2R}{1+R}\left[\left(\frac{b}{r_p^-}\right)^4-1\right]\right\}^{-0.5} \tag{4.38a}$$

$$\sigma_\theta^-=-\left(\sigma+\sigma_y\right)\left(\frac{b^2}{r^2}+1\right)\left\{2\left(\frac{b}{r_p^-}\right)^4+2+\frac{2R}{1+R}\left[\left(\frac{b}{r_p^-}\right)^4-1\right]\right\}^{-0.5} \tag{4.38b}$$

Finally, the residual radial and hoop stresses after the loading and unloading are:

$$\Delta\sigma_r=\sigma_r+\sigma_r^- \tag{4.39a}$$

$$\Delta\sigma_\theta=\sigma_\theta+\sigma_\theta^- \tag{4.39b}$$

To this end, the entire analysis of the cold expansion process on loading and unloading is now complete.

4.2.5 Parametric study

A parametric study can be performed with ease as the equations given above are all in explicitly closed forms. The variations of hoop and radial stresses with respect to interference ratio and plate size, Bauschinger parameter and hardening exponent are examined, as shown in Figs. 4-7 and 4-8 respectively, so that the consequent trend of a stress profile affected by each parameter can be observed.

As seen in Fig. 4-7 (a), the compressive stresses generally tend to increase as the interference ratio increases. However, the hoop compressive stress following reverse yielding does not always increase as the expansion level grows, although the reverse-yielded zone increases correspondingly. The reverse yielding stress remains nearly constant when the interference ratio rises from 3% to 4%, and is slightly reduced from 4% to 5%. This phenomenon suggests that there must exist an optimal interference ratio to reach a maximum compressive stress for a given sized plate and material. By contrast, there is a rapid change in the location of the elastic-plastic boundary and an increase in the maximum residual tensile stress.

It can be seen from Fig. 4-7 (b) that the plate size does affect the stress distributions. The compressive hoop stress following reverse yielding increases as the plate increases in size; on the contrary, the tensile hoop stress drops with an increase of plate size. It is also interesting to find that the stress at the hole edge and the reverse-yielded zone are almost unchanged as the plate varies in dimensions. On the other hand, the elastic-plastic zone size decreases when increasing plate size.

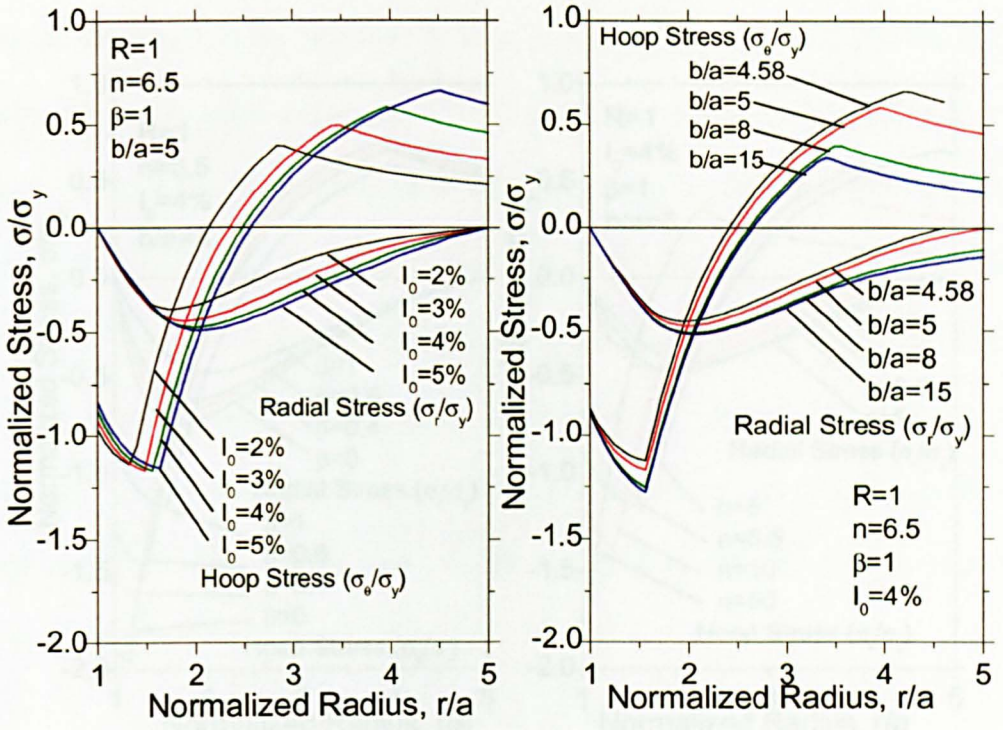

Figure 4-7 Effect of (a) interference ratio, I_a (b) Plate radius ratio, b/a on the residual stress field

It can be seen in Fig. 4-8 (a) that the Bauschinger parameter has a pronounced influence on the magnitude of the compressive stress following reverse yielding, and also on the reverse-yielded area. The hoop stress after reverse yielding increases dramatically, while the reverse-yielded zone decreases as the Bauschinger parameter changes from kinematic hardening ($\beta = 1$) to isotropic hardening ($\beta = 0$). Nevertheless, it has no impact on the elastic-plastic boundary.

It can be seen in Fig. 4-8 (b) that the material hardening behaviour strongly affects almost every aspect of the residual stress distribution. The compressive hoop stress increases noticeably in magnitude whereas the reverse-yielded location, elastic-plastic boundary and

tensile hoop stress decrease noticeably when the hardening exponent increases from 5 up to 50.

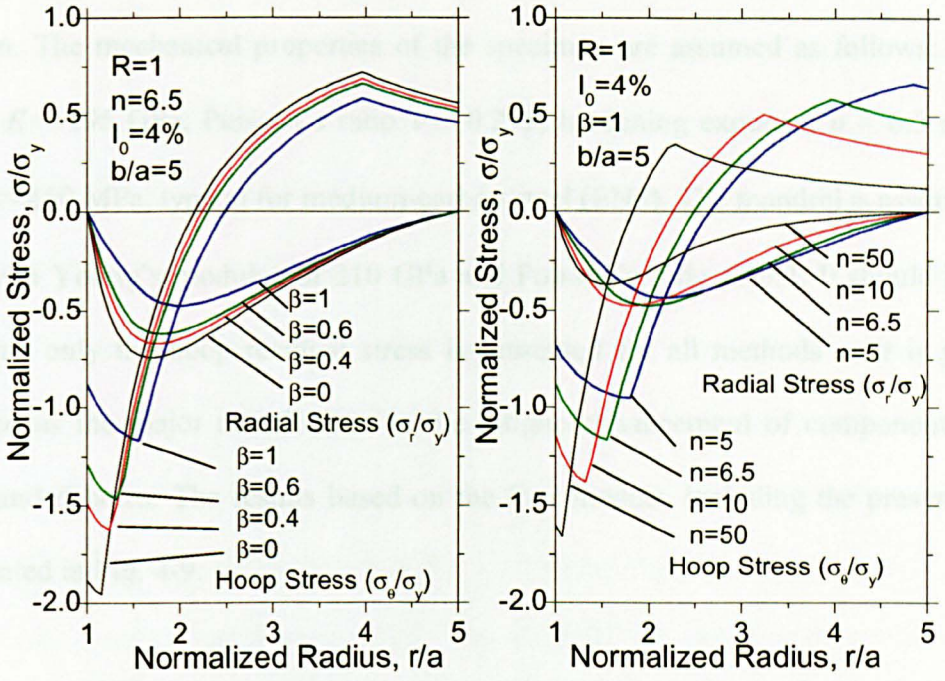

Figure 4-8 Effect of (a) Bauschinger parameter, β (b) Hardening exponent, n on the residual stress field

4.2.6 Discussion

The parametric examination offers useful overall insight into what role each parameter plays in determining the final residual stress profile. It is helpful for design engineers to better understand fundamentals behind the problem for a given condition. It is also important to examine the present solution by comparing it with other well-established analytical methods. Three closed form solutions, proposed by Hsu and Forman (Hsu and Forman, 1975), Rich and Impellizzeri (Rich and Impellizzeri, 1977), Ball (Ball, 1995), are used for the comparison study. They are deliberately chosen as being typically representative of analytical predictions applied for varied situations from simply elastic unloading to complex reverse yielding.

A specimen (plate) used for the current comparison study is defined with an outside diameter of 40 mm and an initial 8.73 mm diameter hole followed by 4% hole cold expansion. The mechanical properties of the specimen are assumed as follows: Young's modulus E = 195 GPa, Poisson's ratio ν = 0.295, hardening exponent n = 6.5 and yield stress σ_y = 450 MPa, typical for medium-carbon steel (EN8). The mandrel is assumed to be elastic, with Young's modulus of 210 GPa and Poisson's ratio of 0.3. It should be stated clearly that only the hoop residual stress is presented for all methods as it is generally recognised as the major contribution to the fatigue enhancement of components having cold expanded holes. The results based on the four models, including the present model, are presented in Fig. 4-9.

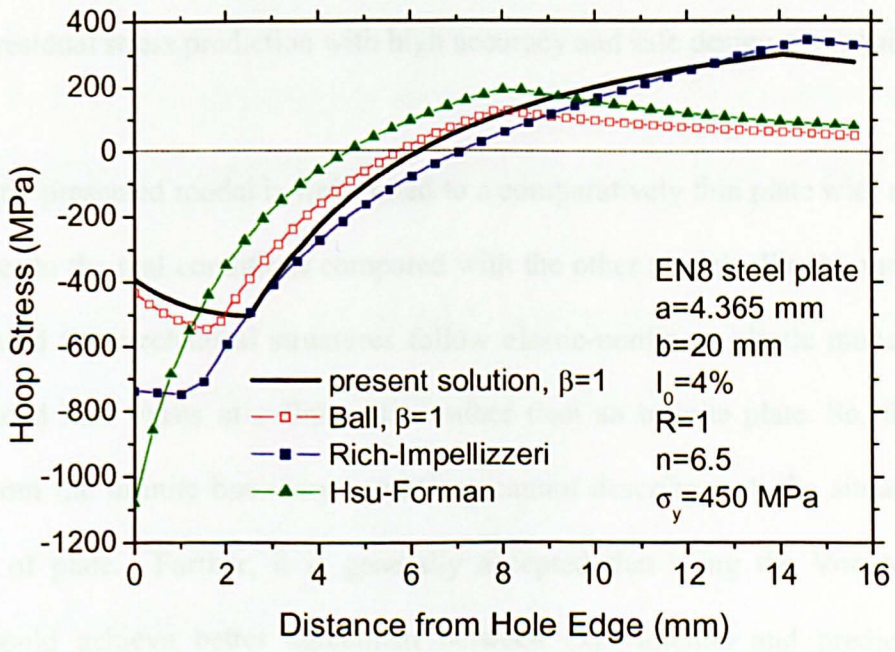

Figure 4-9 Comparison between four analytical predictions

Careful observation of Fig. 4-9 leads to the following findings. Firstly, the Hsu and Forman solution clearly did not account for any reverse yielding, as it uses only elastic

unloading. Next, significant reverse yielding was predicted by Ball, Rich-Impellizzeri and the present solution, even though Rich and Impellizzeri only gave only a rough elastic-plastic treatment of unloading. A slight difference in reverse-yielded zone and compressive residual stress field was found between the present model and Ball's solution. This difference is certainly due to the consequence of the boundary effect of the limited size of the plate. It is also found that using a plate that is finite in the model has a considerable influence on both the stress field and on the location of the elastic-plastic zone boundary, with both the present method and the Rich-Impellizzeri solution showing similar results. The boundary conditions of an infinite plate used in the Hsu-Forman and Ball solutions appear to underestimate these values considerably, at least in this case. The exact determination of the elastic-plastic boundary is very important in the design and spacing of hole locations (Poolsuk and Sharpe, 1978). The effect of the plate size should be taken into account if residual stress prediction with high accuracy and safe design are required.

The currently presented model is well suited to a comparatively thin plate with a finite size and is closer to the real conditions compared with the other models. Firstly, most metallic materials used for mechanical structures follow elastic-nonlinear plastic models. Next, a cold-expanded hole exists in a finite plate rather than an infinite plate. So, the solution deduced from the infinite boundary conditions cannot describe well the situation with a finite size of plate. Further, it is generally accepted that using the Von Mises yield criterion could achieve better agreement between experimental and predicted results (Stacey and Webster, 1988; Calladine, 2000). Furthermore, a certain amount of constraint in the through-thickness direction is applied during hole cold expansion and significant deformation can be observed experimentally which suggests that the assumption of plane strain is inappropriate; plane stress solutions are better representative of this kind of problem (Ball, 1995). Lastly, the cold expansion process inevitably involves the action of a mandrel that is deformable rather than rigid, as was accounted for in the present paper.

In summary, the closed-form elastic-plastic solution for predicting the residual stress distribution around a cold-expanded hole in a finite plate has been explicitly presented. A parametric study of the effects of interference ratio, plate size, Bauschinger parameter and hardening exponent on the final residual stress profile has been conducted and presented. Comparison is made with three other published analytical solutions and shows that the present prediction can better describe the effect of the hole cold expansion action. It provides a cheap, easy, quick and reasonably accurate solution for assessment of residual stresses in hole cold expansion plates.

4.3 References

[1] Ball, D. L. (1995). Elastic-plastic stress analysis of cold expanded fastener holes. Fatigue and Fracture of Engineering Materials and Structures, Vol. 18 (**1**), pp. 47-63.

[2] Budiansky, B. (1971). An exact solution to an elastic-plastic stress concentration problem. Prikladnaya Matematika i Physik, Vol. 35 (**1**), pp. 40-48.

[3] Calladine, C. R. (2000). Plasticity for engineers: theory and applications. Chichester, Horwood Publishing Limited.

[4] Champoux, R. L. and Landy, M. A. (1984). Cold expansion of fastener and other holes using the split sleeve systems (Cx) and countersink cold expansion nosecap (CsCx). FTI Engineering Process Specification FTI 8101B, Fatigue Technology Inc. Vol., pp.

[5] Cook, R. and Holdway, P. (1993). Residual stresses induced by hole cold expansion. Proceedings of Computer Methods and Experimental Measurements for Surface Treatment Effects, Computational Mechanics Publications, pp. 91-100.

[6] Forgues, S. A., Bernard, M. and Bui-Quoc, T. (1993). 3-D axisymmetric numerical analysis and experimental study of the fastener hole cold working process. Proceedings of Computer Methods and Experimental Measurements for Surface Treatment Effects, Computational Mechanics Publications, pp. 61-70.

[7] Guo, W. (1993). Elastic-plastic analysis of a finite sheet with a cold-worked hole. Engineering Fracture Mechanics, Vol. 45 (**6**), pp. 857-864.

[8] Hsu, Y. C. and Forman, R. G. (1975). Elastic-plastic analysis of an infinite sheet having a circular hole under pressure. Transactions of the ASME, Journal of Applied Mechanics, Vol. 42, pp. 347-352.

[9] Kang, J., Johnson, W. S. and Clark, D. A. (2002). Three-dimensional finite element analysis of the cold expansion of fastener holes in two aluminum alloys. Transactions of the ASME, Journal of Engineering Materials and Technology, Vol. 124, pp. 140-145.

[10] Mangasarian, O. L. (1960). Stress in the plastic range around a normally loaded circular hole in an infinite sheet. Transactions of the ASME, Journal of Applied Mechanics, Vol. 27 (**Series E**), pp. 65-73.

[11] Mann, J. Y. and Jost, G. S. (1983). Stress fields associated with interference fitted and cold-expanded holes. Metals Forum, Vol. 6 (**1**), pp. 43-53.

[12] Nadai, A. (1943). Theory of the expanding of boiler and condenser tube joints through rolling. Transactions of the ASME, Vol. 65, pp. 865-880.

[13] O'Brien, E. W. (1993). Four dimensional strain analysis in some thick aircraft alloys with large holes cold expanded for fatigue enhancement. Proceedings of Computer Methods and Experimental Measurements for Surface Treatment Effects, Computational Mechanics Publications, pp. 71-80.

[14] Ozdemir, A. T. (1993). Residual stresses and fatigue performances at cold expanded fastener holes. PhD Thesis, Materials Discipline, Faculty of Technology, The Open University. Milton Keynes, UK.

[15] Ozdemir, A. T. and Edwards, L. (1996). Measurement of the three-dimensional residual stress distribution around split-sleeve cold-expanded holes. Journal of Strain Analysis, Vol. 31 (**6**), pp. 413-421.

[16] Pavier, M. J., Poussard, C. G. C. and Smith, D. J. (1997). A finite element simulation of the cold working process for fastener holes. Journal of Strain Analysis, Vol. 32 (**4**), pp. 287-300.

[17] Pavier, M. J., Poussard, C. G. C. and Smith, D. J. (1998). Finite element modelling of the interaction of residual stress with mechanical load for a crack emanating from a cold worked fastener hole. Journal of Strain Analysis, Vol. 33 (**4**), pp. 275-289.

[18] Poolsuk, S. and Sharpe, W. N., Jr. (1978). Measurement of the elastic-plastic boundary around coldworked fastener holes. Transactions of the ASME, Journal of Applied Mechanics, Vol. 45, pp. 515-520.

[19] Poussard, C., Pavier, M. J. and Smith, D. J. (1995). Analytical and finite element predictions of residual stresses in cold worked fastener holes. Journal of Strain Analysis, Vol. 30 (**4**), pp. 291-304.

[20] Reid, L. (1996). Enhanced repair durability with cold expansion techniques. Proceedings of the Forty-first International SAMPE Symposium and Exhibition, 24-28 March, pp. 951-961.

[21] Rich, D. L. and Impellizzeri, L. F. (1977). Fatigue analysis of cold-worked and interference fit fastener holes. In Cyclic Stress-Strain and Plastic Deformation Aspects of Fatigue Crack Growth, ASTM STP 637 (American Society for Testing and Materials, Philadelphia, Pennsylvania), Vol., pp. 153-175.

[22] Sharpe, W. N., Jr. (1978). Residual strains around coldworked fastener holes. Transactions of the ASME, Engineering Materials and Technology, Vol. 100, pp. 310-312.

[23] Stacey, A. and Webster, G. A. (1988). Determination of residual stress distributions in autofrettaged tubing. International Journal of Pressure Vessels and Piping, Vol. 31, pp. 205-220.

[24] Stefanescu, D. (2001). Effect of load history on residual stresses developed at cold expanded fastener holes. PhD thesis, Department of Materials Engineering. Milton Keynes, UK, The Open University.

[25] Stefanescu, D., Edwards, L. and Fitzpatrick, M. E. (2002). X-ray diffraction measurement of the residual stresses surrounding a cold expanded hole. Materials Science Forum, Vol. 404-407, pp. 185-190.

[26] Timoshenko, S. P. and Goodier, J. N. (1970). Theory of Elasticity. New York, McGraw-Hill Book Company.

[27] Webster, P. J., Mills, G., Browne, P. A., Hughes, D. J. and Holden, T. M. (2000). Residual stress around a cold-expanded hole. Proceedings of the Sixth International Conference on Residual Stresses (ICRS-6), 10-12 July, Oxford, UK, IOM Communications Ltd, ISBN:1-86125-123-8, pp. 125-132.

[28] Zhang, Y., Edwards, L. and Fitzpatrick, M. E. (2002a). Finite element simulation of hole cold expansion process in EN8 steel plates. Proceedings of the Sixteenth ABAQUS UK User Group Conference, 12-13 Nov., Warrington, UK, pp.

[29] Zhang, Y., Fitzpatrick, M. E. and Edwards, L. (2002b). Measurement of the residual stresses around a cold expanded hole in an EN8 steel plate using the contour method. Materials Science Forum, Vol. 404-407, pp. 527-534.

Appendix A - Form of Tender: EQUIPMENT *(All prices to be subject to VAT as applicable)*

- **Full specification details to be provided with tender documents.**

	Bradford B1/03	Durham 393 (CFMB03)	Exeter Physic (E4)	Glasgow Caledon GCU2	Hull ESRU SEM1	KCL D	Leeds NANO 3	Leeds NANO 1	Leeds NANO 2
Basic Equipment Cost Breakdown:									
•									
•									
•									
Total Cost Basic Equipment =									
Less Discount(s): 1. Collaborative Agreement. 2. Equipment trade–in where requested. • Others (please state) 3.									
Net Cost of Basic Equipment = (1A)									
Cost of Attachments/ Accessories Requested									
•									
•									
•									
Total Cost of all attachments/ accessories requested =									
Less Discount(s): 1. Collaborative Agreement. 2. Equipment trade–in where requested. • Others (please state) 3.									
Net Cost of Attachments/ Accessories Requested = (1B)									
Training as specified =(1C)									
NET PRICE PAYABLE FOR EQUIPMENT (1A +1B+1C) = (A)									

	Leicester 468 (/18)	Leicester 466(/13)	Leicester 466 heating stage	Leicester 466 Manipulators	LJM SRIF2/ BIOMED/ SEM (110)	Reading UOR/ SRIF2 /04
Basic Equipment Cost Breakdown:						
•						
•						
•						
Total Cost Basic Equipment =						
Less Discount(s): 1. Collaborative Agreement. 2. Equipment trade–in where requested. • Others (please state) 3.						
Net Cost of Basic Equipment = (1A)						
Cost of Attachments/ Accessories Requested						
•						
•						
•						
Total Cost of all attachments/ accessories requested =						
Less Discount(s): 1. Collaborative Agreement. 2. Equipment trade–in where requested. • Others (please state) 3.						
Net Cost of Attachments/ Accessories Requested = (1B)						
Training as specified =(1C)						
NET PRICE PAYABLE FOR EQUIPMENT (1A +1B+1C) = (A)						

	Southampton SU Micro FEGSEM	Southampton (12d) BIU/SEM	Stirling A01	Surrey UNIS 1 /FIB	Surrey UNIS 1 /ESEM
Basic Equipment Cost Breakdown:					
•					
•					
•					
Total Cost Basic Equipment =					
Less Discount(s): 1. Collaborative Agreement. 2. Equipment trade-in where requested. • Others (please state) 3.					
Net Cost of Basic Equipment = (1A)					
Cost of Attachments/ Accessories Requested					
•					
•					
•					
Total Cost of all attachments/ accessories requested =					
Less Discount(s): 1. Collaborative Agreement. 2. Equipment trade-in where requested. • Others (please state) 3.					
Net Cost of Attachments/ Accessories Requested = (1B)					
Training as specified =(1C)					
NET PRICE PAYABLE FOR EQUIPMENT (1A +1B+1C) = (A)					

Appendix B - Form of Tender: WARRANTY, MAINTENANCE & AFTER SALES SUPPORT
(All prices to be subject to VAT as applicable)

- ***PLEASE COMPLETE APPENDIX B FOR EACH UNIVERSITY/ PIECE OF EQUIPMENT AS APPROPRIATE***

WARRANTY

- Purchasing University's require as a minimum a one-year on-site warranty (parts, labour including software), unless otherwise stated in the equipment specification.
- **Please detail below the type and cost of service support that can be offered to cover a 5 year period** (unless otherwise stated in the equipment specification)**, clearly stating guaranteed response times, what will be provided and which costs are not included.**

Q1. Are these options yearly renewable?
Q2. Reductions for multiple equipment cover?

MAINTENANCE	Year 1	Year 2	Year 3	Year 4	Year 5	**Total Cost**
a) **As specified in equipment specification**	£	£	£	£	£	**£ (= B) (for full period stated in spec)**
Other Options (please specify):						
b)	£	£	£	£	£	**£**
c)	£	£	£	£	£	**£**
d)	£	£	£	£	£	**£**
e)	£	£	£	£	£	**£**

SUPPORT

- Please give details of the nearest support facility to purchasing University.

Address: _____

Telephone: _____

E-mail: _____

Contact: _____

Number of miles/ minutes from purchasing University: _____

- Please give details of Engineers.

Number of Engineers:_____

Relevant Qualifications:

_____

_____

• Do you intend sub-contracting the :	
a) site survey	YES /NO
b) installation	YES /NO
c) maintenance	YES /NO
d) repair facility	YES /NO
e) other (please state)	YES /NO
If 'Yes', give full details (including address/ telephone number of contractor(s)	
a)	
b)	
c)	
d)	
e)	

• What are the maximum and minimum response times for a call-out to site?	_____Hrs max _____Hrs min
• During the warranty period, after what time period, a machine being out of service and under repair on or off site, would you provide a free of charge replacement?	YES/NO
• Do you have an escalation period/procedure? Please provide details: _____	YES/NO
• What is the anticipated long-term availabity of spare parts?	_____Years
• How long will you guarantee to hold spare parts?	_____Years
• Please provide details if software included in the package will be upgraded free of charge during the warranty period. Details: _____	YES/NO
• Will all operating manuals be provided free of charge? If not, please provide details of charges here: _____	YES/NO £

• Please give details and costs of major spare parts. Item(s): 1. . 2. . 3. . 4. . 5. .	£
• Describe the power supply and other infrastructure requirements for the equipment.	

Appendix C - Form of Tender: SUMMARY OF TENDERER'S SUBMISSION *(All prices to be subject to VAT as applicable)*

- **Added Value Proposition:**

For each Institution, information must be supplied on proposed mutual benefits that would bring added value through a partnership/ scientific collaborative agreement with the respective Institution purchasing the equipment. *For example, collaboration on future research & development projects, sponsorship of seminars, reduced purchase price and future upgrade programmes.* An estimated financial value **must** be attributed to all collaborative aspects in addition to any expectations that the supplier might have as regards the commitment required by that particular Institution (staff, access, intellectual input, financial).

	Bradford B1/03	Durham 393(CFMB03)	Exeter Physics (E4)	Glasgow Caledon GCU2	Hull ESRU SEM1	KCL D	Leeds NANO 3	Leeds NANO 1	Leeds NANO 2
Equipment (A)									
Maintenance (B)									
Total Cost (A+B) = C									
	Leicester 468 (/18)	Leicester 466(/13)	Leicester 466 heating stage	Leicester 466 Manipulators	LJM BIOMED /SEM (110)	Reading UOR/ SRIF2/04			
Equipment (A)									
Maintenance (B)									
Total Cost (A+B) = C									
	Southampton SU Micro FEGSEM	Southampton (12d) / BIU/SEM	Stirling A01	Surrey UNIS 1 /FIB	Surrey UNIS 1 /ESEM				
Equipment (A)									
Maintenance (B)									
Total Cost (A+B) = C									

- **Please detail additional discount structure for the purchase of 2 or more installations**
- **DELIVERY SCHEDULE TO BE ATTACHED showing:** lead times for each instrument offered assuming orders placed in July 2004. Schedule should include at least: Receipt of purchase order to delivery, installation to hand over.

5 Residual stresses in a hole cold expanded EN8 steel plate

As described in Chapter 4, hole cold expansion is a widespread method of improving the fatigue resistance of fastener holes as the compressive hoop stresses created by the technique retard both crack initiation and propagation (Fitzpatrick and Edwards, 1998). In order to include the benefits from cold expansion in design calculations, a number of techniques have been studied and developed to quantity the effect in recent decades, making the problem ideal for evaluating the usefulness and potential of the newly-developed contour method. For that purpose, a steel specimen subjected to 4% hole cold expansion was fabricated and a cross-sectional hoop stress profile was measured using the contour method. Other methods, such as analytical prediction, finite element simulation and X-ray diffraction measurement were also performed to validate the novel technique of the contour method.

5.1 Material and specimen

5.1.1 Material

The material used for the hole cold expansion specimen is medium carbon steel BS 970 080M40 (1983) widely used in industry, in which "080" means a plain carbon steel containing a mean manganese content (Mn) of 0.80%; M represents the requirement of meeting a mechanical property; "40" denotes a mean carbon content (C) of 0.40%. Its previously used name of EN8 (1955) is still retained because of its wide acceptance, long history and familiarity to people. The EN8 material was supplied in the form of hot rolled and cold drawn flat bar with a cross-section of 50 mm by 12.5 mm, meeting the

specification of British Standard 970 080M40 (EN8). Its nominal chemical composition and mechanical properties are given in Table 5-1 and Table 5-2 respectively.

Table 5-1 Nominal chemical composition of BS 970 080M40 (by weight)

Element	C	Si	Mn	S	P
Min.	0.36	0.10	0.60	-	-
Max.	0.44	0.40	1.00	0.05	0.05

Table 5-2 Nominal mechanical properties of BS 970 080M40

Name	Tensile strength	0.2% proof stress	Elongation after fracture
Units	MPa	MPa	%
Min.	660	495	7

As a prerequisite for the subsequent experimental, numerical and analytical studies, a tension-compression test of EN8 steel was conducted to obtain actual material elastic constants, strain-hardening characteristics and a true stress-strain curve. The cross-sectional diameter was carefully chosen to balance the strength between the specimen and the Woods metal grip that fixed the specimen into the test system. On the one hand, the specimen should be strong enough to avoid premature buckling in compression or premature necking in tension. On the other hand, the applied force should not exceed the maximum capacity of 25 kN that the Woods metal grip is capable of bearing. The 5 mm in diameter was finalised for the specimen to meet both strength requirements. The M12 $\times$1.75 threaded-ends were designed to match the dimensions of the fixture of the test system, and the 20 mm uniform region was determined to accommodate the 17 mm long

extensometer. Finally, the test specimen was manufactured from a 50 mm × 12.5 mm flat blank, with its logitudinal axis along the rolling direcion, as shown in Fig. 5-1, which conforms to the standard of ASTM E 606.

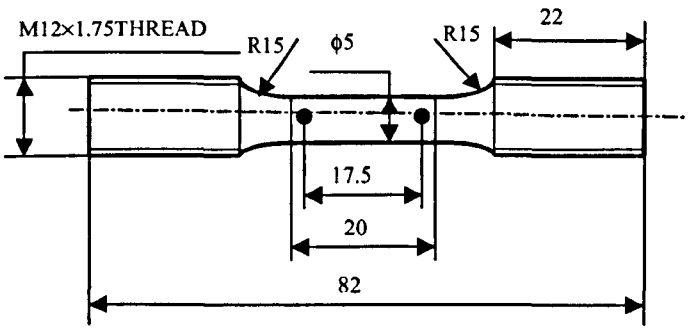

Figure 5-1 Round section specimen for tension-compression test (unit: mm)

Prior to the tension-compression test, a uniaxial tension test was taken to acquire the general trend and limits of the mechanical characteristics of the EN8, in which the ultimate tensile strength was found to be about 797 MPa with an elongation of 5.1%.

For the tension-compression test, the threaded ends of the specimen were connected to an Instron servo-hydraulic test machine, as illustrated in Fig. 5-2. In the middle of the specimen, a side extensometer with a gauge length of 17 mm was placed to monitor the strain response of the material at a strain rate of 6.7×10^{-5} s^{-1}, which is the lowest rate to obtain a stable tension-compression curve based on the performance of the test machine used in our department.

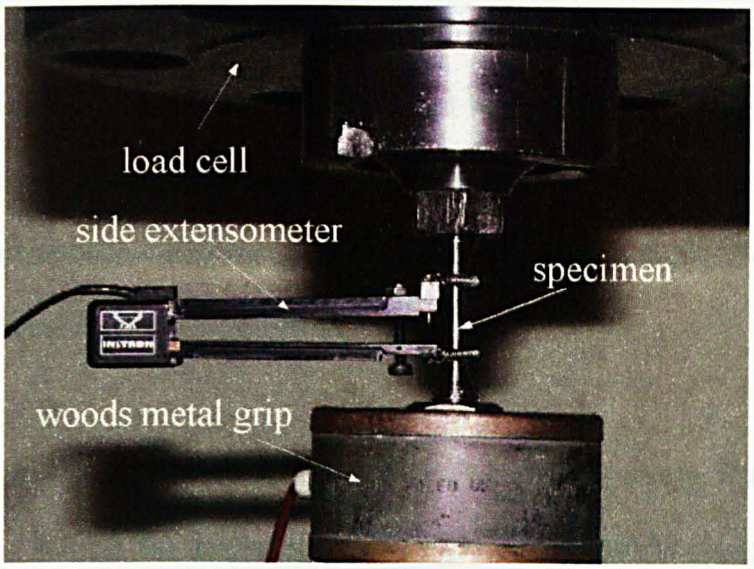

Figure 5-2 Set-up for tension-compression test

The uniaxial responses of the true stress versus the true strain measured are depicted in the following figures, coupled with the fitting curve for loading and the kinematic, isotropic, mixed hardening curves on unloading. Two sets of tension-compression test data are presented in Fig. 5-3 (a) and (b) respectively, one with a maximum loading strain of 0.026 and the other with a maximum strain approximate to 0.051. It is noted that the change of the true stress corresponding to the true strain is presumably equal in tension and in compression. Further, the mechanical properties at issue are assumed to be homogenous, isotropic and elastic-plastic.

The fitting curve for the monotonous elastic-plastic characteristics of the EN8 material is represented by the modified Ramberg-Osgood model (Budiansky, 1971) as follows:

$$\varepsilon = \begin{cases} \dfrac{\sigma}{E} & \text{for } |\sigma| \le \sigma_0 \\ \dfrac{\sigma}{E}\left|\dfrac{\sigma}{\sigma_0}\right|^{n-1} & \text{for } |\sigma| \ge \sigma_0 \end{cases} \tag{5.1}$$

where ε is the true strain, σ is the true stress, E is the elastic modulus, σ_0 is the yield stress and n is the strain hardening exponent. The yield stress was determined based on 0.2% strain offset, and the elastic modulus was calculated on the basis of linear least squares estimation. The mixed hardening curve for the unloading portion in Fig. 5-3 is the result of averaging the kinematic and isotropic hardening curves.

It can be seen from Fig. 5-3 that the EN8 material does exhibit a strong Bauschinger effect, like most steels. Neither the kinematic hardening rule nor the isotropic hardening rule describes exactly the actual EN8 hardening characteristics. Nevertheless, both hardening models bound the Bauschinger effect of the EN8, which falls almost in the middle of the kinematic and isotropic hardening curves, very close to the mixed hardening curve shown in Fig. 5-3. In summary, the measured EN8 mechanical properties are detailed in Table 5-3.

Table 5-3 Measured mechanical properties of EN8 (080M40)

0.2% yield stress $\sigma_{0.2\%}$ (MPa)	Elastic modulus E (GPa)	Poisson's ratio μ	Strain hardening Exponent, n
450	195	0.295	6.5

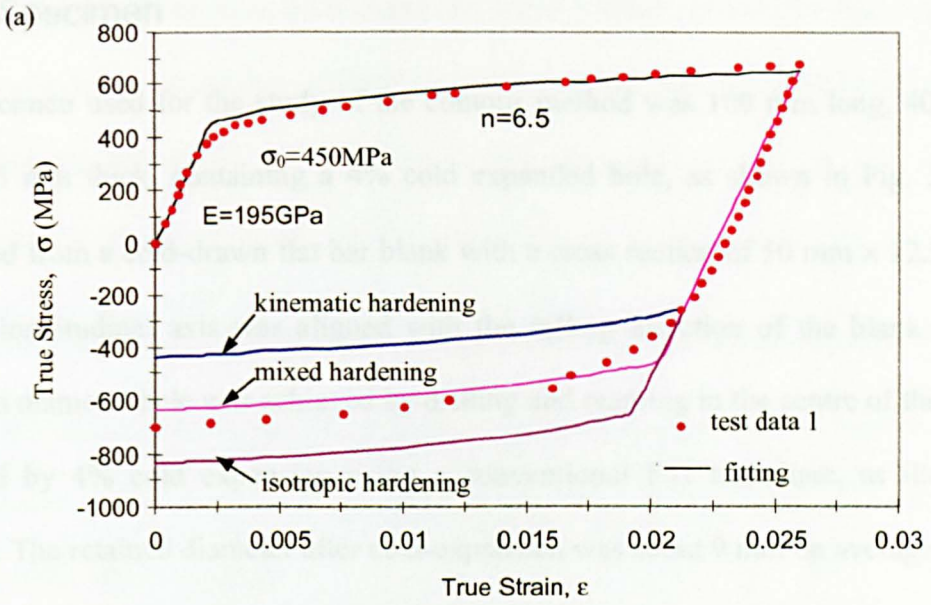

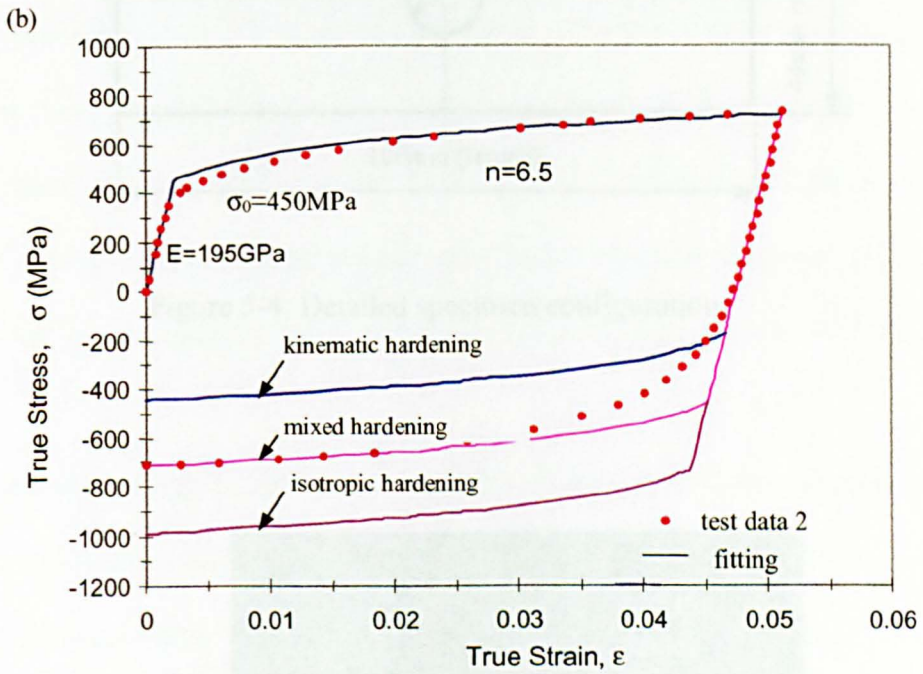

Figure 5-3 Response of true stress vs. true strain for tension and compression test

(a) test data 1 with max. strain=0.026 (b) test data 2 with max. strain=0.051

5.1.2 Specimen

The specimen used for the study of the contour method was 100 mm long, 40 mm wide and 12.5 mm thick, containing a 4% cold expanded hole, as shown in Fig. 5.4. It was machined from a cold-drawn flat bar blank with a cross section of 50 mm × 12.5 mm such that its longitudinal axis was aligned with the rolling direction of the blank. An initial 8.73 mm diameter hole was achieved by drilling and reaming in the centre of the specimen followed by 4% cold expansion using a conventional FTI technique, as illustrated in Fig. 5-5. The retained diameter after cold-expansion was about 9 mm on average.

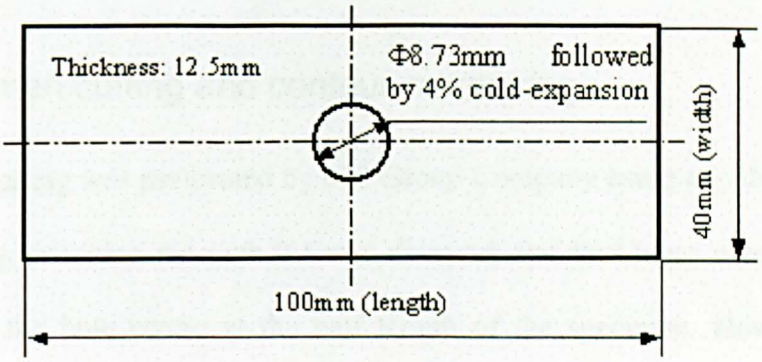

Figure 5-4 Detailed specimen configuration

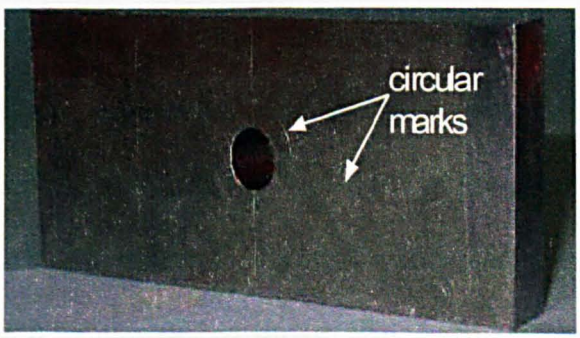

Figure 5-5 Hole cold expanded EN8 steel plate

As seen in Fig. 5-5, annular marks on the exit surface of the specimen were observed. This is due to the constraint action of the FTI tool set against the movement of the specimen during hole expansion.

5.2 Measurement of residual stresses using the contour method

Application of the contour method basically consists of four procedures: specimen cutting, surface contour measurement, data analysis and finite element analysis, which will be detailed in the following context.

5.2.1 Specimen cutting and contour measuring

The specimen cutting was performed by 600 Group Company using a FANUC Alpha 1 iA electric discharge machine fed with 0.1 mm diameter standard brass wire. The specimen was cut across the hole centre at the half length of the specimen. However, complete details of the cutting process are not known. The cut slot was measured to be about 0.22 mm after the cut and the expected accuracy given by the company was +/- 5 μm.

After specimen cutting, the deformation profile of the cut surfaces was measured using a Mitutoyo Crystal Plus 574 CMM fitted with a 1 mm-diameter Renishaw probe, located in an air conditioned room in our department. The thermal compensation system was also activated during measurement to record the variation in temperature and correct the measurement automatically. The measurements were performed sequentially on the two cut surfaces with a uniform 0.25 mm-spaced square grid. Each cut surface was divided by the hole edge into two patches, and each patch, with an area of 12.5 mm by 15.5 mm, resulted in 3213 points, giving in total 6426 points on each surface. The datum plane and datum point referred to by the points to be measured can be specified randomly by

convenience. It is important to note that the measurement methodology should guarantee each pair of data to be averaged ideally in a mirror position, as explained in Chapter 3. In addition, the specimen should be held steadily during measuring to avoid any movement and achieve correct measurement of each point. Fig. 5-6 illustrates the scheme of the specimen clamping for the contour measurement using the CMM.

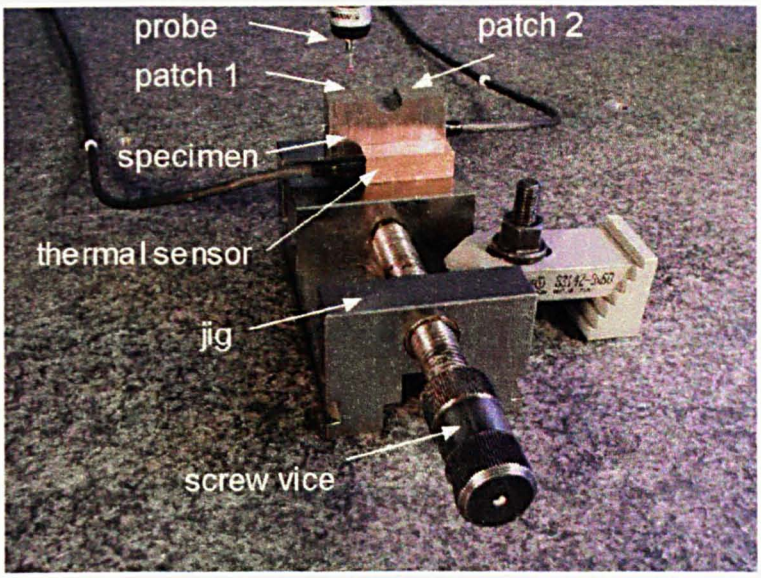

Figure 5-6 General view of the specimen clamping for contour measurement

Firstly, the fixing jig was tightly clamped to the CMM table, on which there are several female threads able to be used. Then the specimen was placed between the two holding blocks of the jig set and tightened in the screw vice. Two thermal sensors were connected to the specimen to monitor the change in temperature during measuring. The measurement started from the front left corner and continued back and forth, advancing from left to right.

5.2.2 Data analysis

Initially, trial FE calculations showed that the calculated stresses were highly sensitive to the error in the measured displacements and magnified the error a great deal. Smoothing of measured data to remove 'noise' in the data is thus imperative so that a high accuracy of stress evaluation can be achieved. In addition, some data at the edges of the specimen were "bad" due to imperfection of the specimen manufacturing and specimen cutting, or limitation of measurement using the CMM. These data must be removed and need extrapolating for replacement of the removed data. A commercial code, MATLAB R12, was employed to perform the data analysis.

Fig. 5-7 shows the raw data measured by CMM on the left cut plane and the right cut plane respectively before average. It can be seen that some measurements are out of the surface, and obviously they can't be used for any purpose. The measured displacements of the two cut surfaces need to be averaged for further analysis. As stated earlier, each pair of points to be averaged should be ideally in a mirror position, which can be achieved by proper arrangement of the measurement. The 'bad' data should be deleted from the data. Fig. 5-8 displays three-dimensionally the averaged and measured data of the two patches separated by the cold expanded hole after removal of the bad data at the edges. The general view of deformation on the surface can be seen. The place in the neighbourhood of the hole has a higher value, suggesting the compressive stress. By contrast, the lower value indicates the tensile stress, which is in the far-field of the hole. The peak-to-valley amplitude for the left patch was approximately 53 μm, and 36 μm for the right patch.

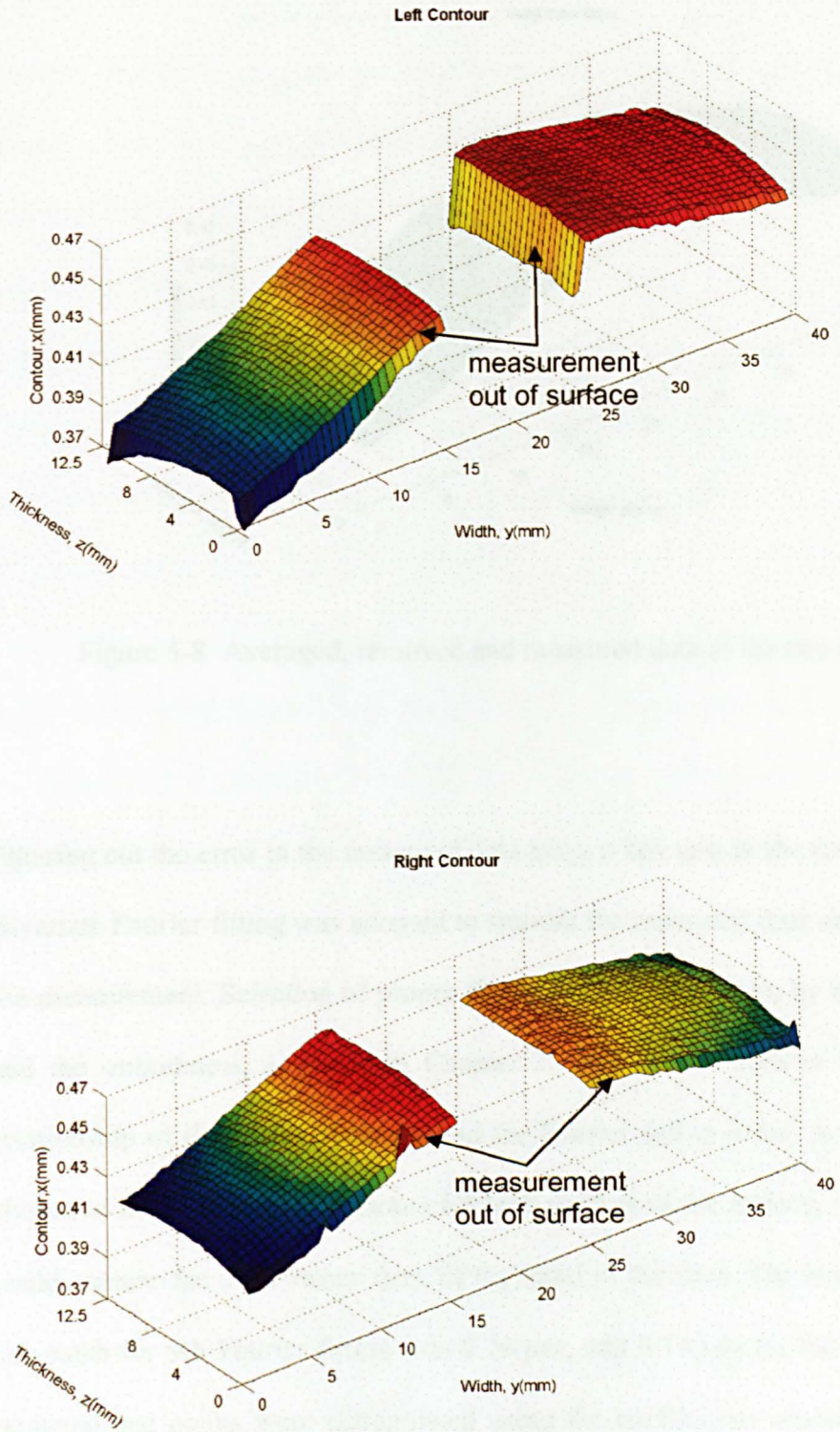

Figure 5-7 Measured data of two sides by CMM

Top: contour of the left plane; bottom: contour of the right plane

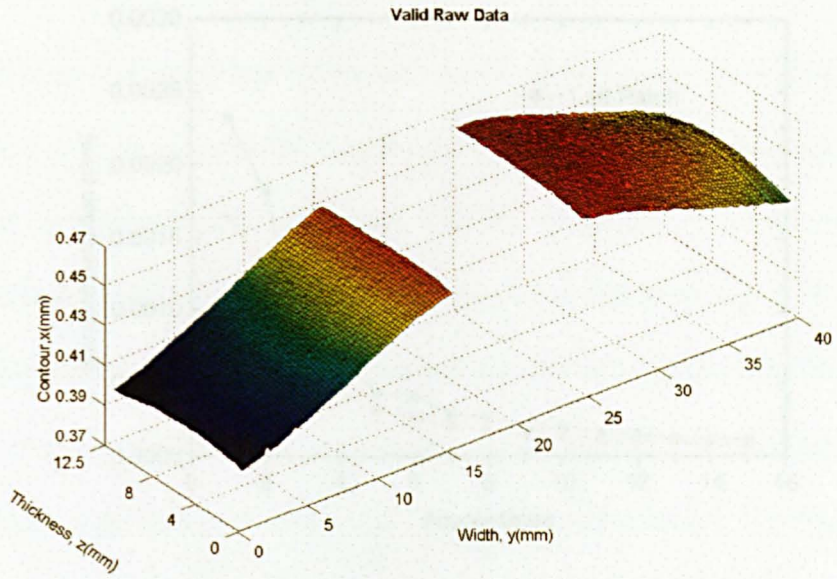

Figure 5-8 Averaged, removed and measured data of the two patches

Filtering out the error in the measured data plays a key role in the data smoothing analysis. Bivariate Fourier fitting was adopted to smooth the measured data and remove the noise in the measurement. Selection of proper fitting order is important, by balancing the accuracy and the smoothness, as stated in Chapter 2. This can be seen in Fig. 5-9, showing the relationship of the fitting accuracy and the Fourier fitting order. A 9th Fourier order was chosen to fit the measured contours for both patches of the surface, as an overly high order could capture the error rather than fit the trend of the data. The standard deviation of the left patch for 9th Fourier fitting was 0.20 μm, and 0.14 μm for the right patch. Then, the removed bad points were extrapolated using the coefficients available from the bivariate Fourier fitting of the valid data. Finally, the smoothed and extrapolated data are shown in Fig. 5-10.

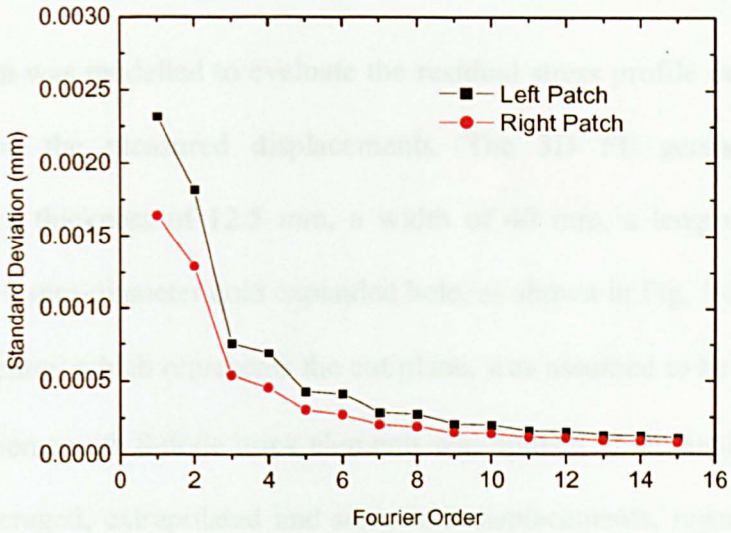

Figure 5-9 Relationship of standard deviation and order for Fourier fitting

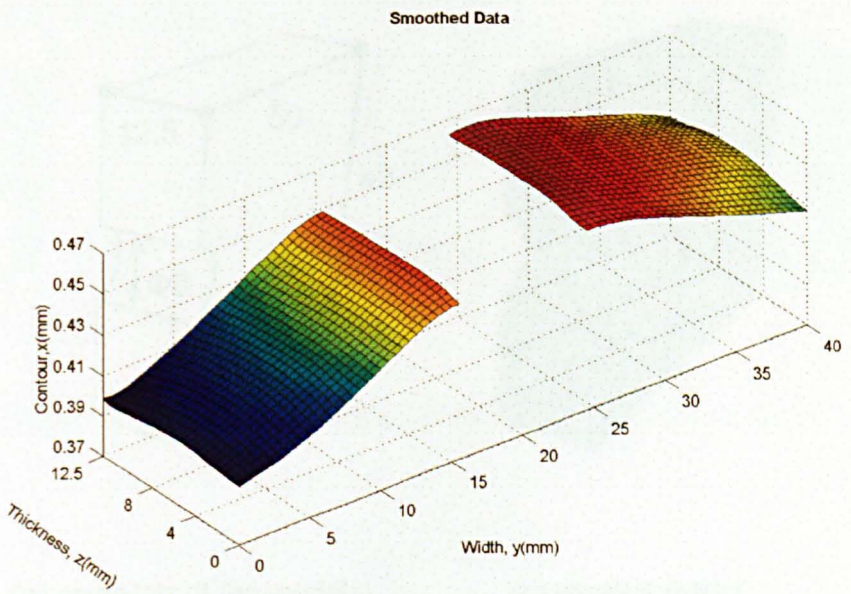

Figure 5-10 Averaged, extrapolated and smoothed data of the two patches

5.2.3 Finite element analysis

Half the specimen was modelled to evaluate the residual stress profile on the cut plane of interest based on the measured displacements. The 3D FE geometry model was characterised by a thickness of 12.5 mm, a width of 40 mm, a length of 50 mm (half specimen), and a 9 mm-diameter cold expanded hole, as shown in Fig. 5-11 (a). The plane across the hole centre, which represents the cut plane, was assumed to be flat. A 0.5 mm × 0.5 mm mesh scheme with 8-node brick elements was applied to the model as seen in Fig. 5-11 (b). The averaged, extrapolated and smoothed displacements, regarded as boundary conditions, were carefully arranged to fit the meshed nodes of the cut plane on the FE model. The elastic constants of the EN8 material were 195 GPa for Young's modulus and 0.295 for Poisson's ratio as measured in our laboratory, and given in Table 5-3. A commercial FE code, ABAQUS 6.3, was employed to conduct the geometry modelling and the linear FE solution.

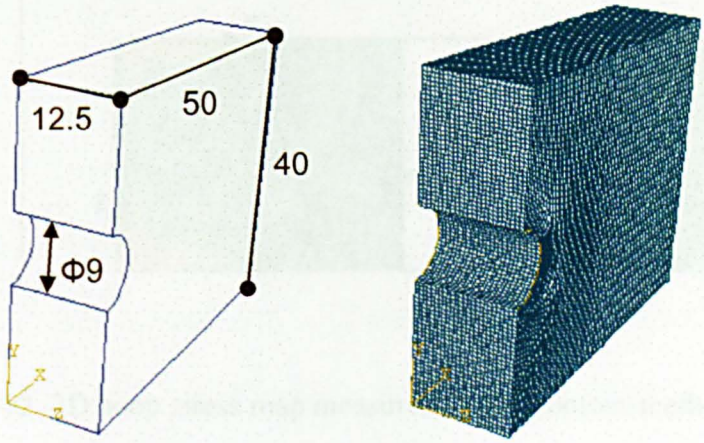

(a) geometry of the model (b) meshed model

Figure 5-11 3D FE model used in the contour method

5.2.4 Result and discussion

A through-thickness hoop stress profile across the cold expanded hole was obtained from the FEA, as illustrated in Fig. 5-12, and the well-known hoop stress distribution for the cold expansion problem can be seen. The stress near the hole is compressive and the stress far from the hole is tensile. It is also found that the stress distributions at the two sides of the hole are not symmetrical. This is partly because the split of the split-sleeve was not placed exactly at the longitudinal direction of the plate. In addition, it is likely that the pulling force exerted manually was not precisely along the hole axis. Any deviation of the pulling force from the central axis of the hole will probably produce an asymmetry of the stress profile around the hole more or less. It is felt from Fig. 5-12 that the tensile stresses around the four corners seems to be overestimated, and this is likely attributed to irregular cutting near the corners. However, the detail of the cutting was not clear, and thus the cutting-induced error cannot be estimated in this case.

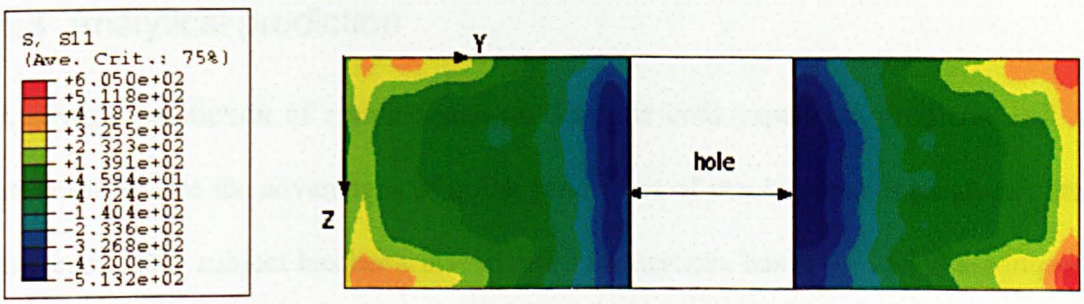

Figure 5-12 2D hoop stress map measured by the contour method

The hoop stresses with respect to the distance from the hole centre at the specified thicknesses from the entry surface are plotted in Fig. 5-13. It can be seen that reverse yielding in the vicinity of the hole was measured by the contour method. The stress at the entry surface is less compressive than the stress at the exit surface; and the stress at the middle of the thickness is most compressive.

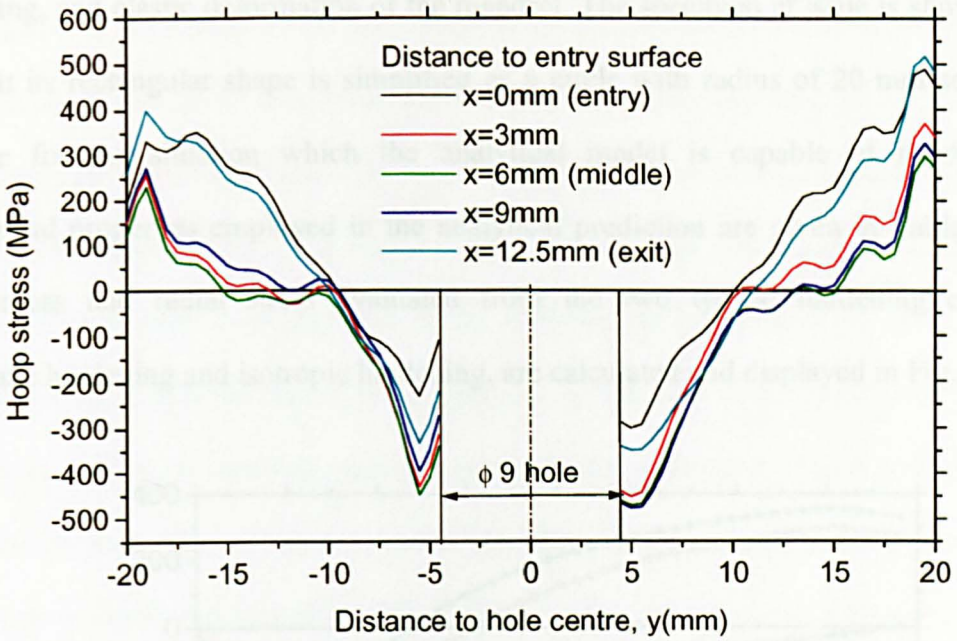

Figure 5-13 Hoop stresses at specified thickness locations

5.3 Analytical prediction

Analytical prediction of residual stresses for hole cold expansion problems still remains attractive due to the advantages of quick generation of results, ease of parameter study and low cost. This subject has been investigated for decades based on varied assumptions that are substantially different, as described in Chapter 4. The closed form equations given in Chapter 4 consist of two analytical steps: a loading step in which a certain amount of uniform radial expansion is applied to the hole edge, and an unloading step in which equations are developed in the exact same manner as the first step except the yielding criterion. The analytical model presented in Chapter 4 will be used to evaluate the residual stress profile resulting from the hole cold expansion process because it is generally more representative of the actual conditions applied in the current specimen under study. The assumptions implemented in the model primarily include plane stress conditions, the Von

Mises yield criterion, finite size boundary conditions, elastic-nonlinear plastic loading and unloading, and elastic deformation of the mandrel. The specimen at issue is shown in Fig. 5-5, but its rectangular shape is simplified as a circle with radius of 20 mm so that it is suitable for the situation which the analytical model is capable of handling. The mechanical properties employed in the analytical prediction are given in Table 5-3. The hoop stress and radial stress evaluated from the two typical hardening conditions, kinematic hardening and isotropic hardening, are calculated and displayed in Fig. 5-14.

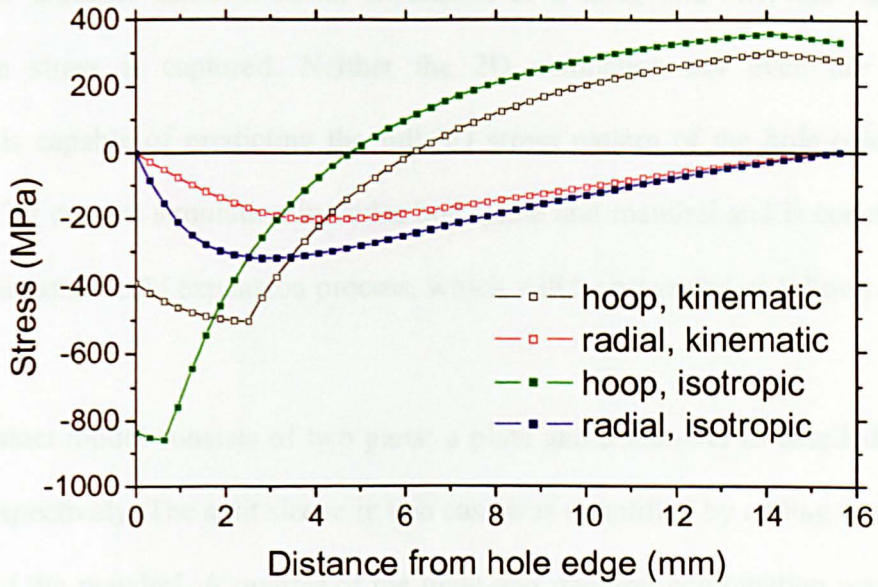

Figure 5-14 Hoop and radial stress profiles predicted by the analytical model

It is clear that the hardening conditions have a significant impact on the stress profiles, particularly on the reverse yielding stress. The isotropic hardening predicts much more compressive stresses than the kinematic hardening does. For instance, the maximum hoop compressive stress reaches 859 MPa for the isotropic hardening condition, but only 504 MPa for the kinematic hardening condition. The radial stresses are always compressive throughout, and equal to zero at the two edges, as would be expected.

5.4 Finite element simulation

A complete FE simulation of the hole cold expansion process for the EN8 plate, including 2D simulation, simple 3D simulation and complex 3D contact simulation, has been carried out to evaluate the residual stress profiles resulting from the process (Zhang et al., 2002). The 2D simulation of the hole cold expansion process is simplified to uniform radial expansion of a hole to a specified level, and inevitably leads to an identical stress distribution through thickness. The 3D simple simulation of the hole cold expansion process also assumes uniform radial expansion of a hole, and only the half-thickness variation in stress is captured. Neither the 2D simulation nor even the simple 3D simulation is capable of predicting the full 3D stress pattern of the hole cold expansion process. A 3D contact simulation includes both plate and mandrel and is considered to be closest to the actual cold expansion process, which will be presented as follows.

The 3D contact model consists of two parts: a plate and a mandrel as detailed in Fig. 5-4 and 5-15 respectively. The split sleeve in this case was simplified by adding its thickness to the radius of the mandrel. A quarter of the plate and mandrel combination was simulated, taking advantage of the symmetry of the system and thus saving a huge amount of memory and CPU time. The mesh was characterized by 3D 8-node linear brick elements with reduced integration and hourglass control. The mandrel was initially positioned just in touch with the plate surface, as illustrated in Fig. 5-16. A 5 mm blend radius at the intersection of the taper portion and cylinder portion of the mandrel was selected for a smoother geometry transition to overcome the convergence difficulty incurred during the movement of the mandrel though the hole. In addition, friction between mandrel and hole edge was attempted, but failed, due to poor convergence and extensive CPU time needed.

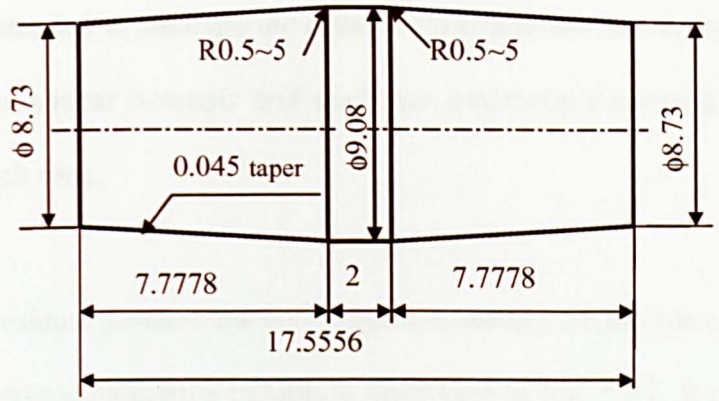

Figure 5-15 Mandrel configuration details used for the 3D contact model

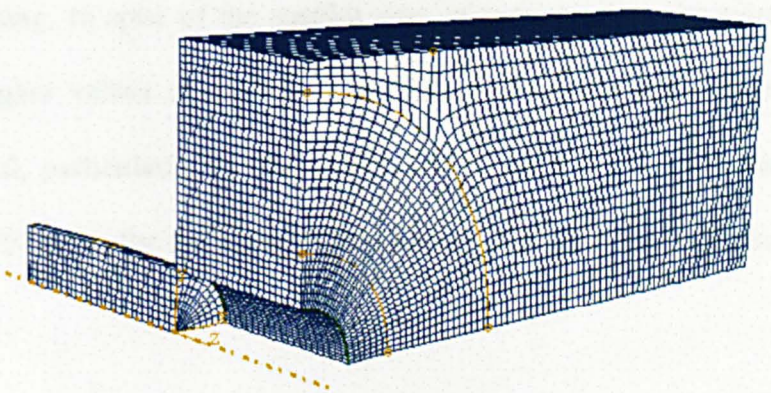

Figure 5-16 Initial position of the plate and the mandrel

Simulation of the cold expansion process was achieved by applying a displacement as a boundary condition to the mandrel front face step by step, which models the movement of the mandrel along its central axis. The displacement is renewed in every single load step so as to pull the mandrel through the hole. The 16 load steps were designed to withdraw the mandrel out of the hole with a total displacement of 31 mm. Another two load steps were additionally implemented to release the constraint on the exit surface of the plate, and the constraint on the plate short edge, which were applied as initial boundary conditions

beforehand and intended to simulate the actual cold expansion action as performed in our workshop. Both nonlinear isotropic and nonlinear kinematic hardening rules were taken into account in each case.

A plot of hoop residual stresses on the transverse surface of the plate predicted by the kinematic and isotropic hardening models is illustrated in Fig. 5-17. It is obvious that the 3D contact simulation is capable of predicting the variation in hoop stresses through the thickness of the plate. Stresses are compressive in the near field of the hole and tensile in the far field of the hole. The location of the most compression predicted by the kinematic hardening is further away from the hole than the most compressive place obtained from the isotropic hardening. In spite of the smaller area of compression, the isotropic hardening model gives higher values of compressive stress and tensile stress than the kinematic hardening model, particularly for the compressive stress. The maximum compressive stress reaches 758 MPa for the isotropic hardening, but only 466 MPa for the kinematic hardening.

However, clear details can be found from a line plot of the hoop stresses as a function of distance from the hole edge at the entry, middle and exit surfaces, as shown in Fig. 5-18. It can be seen that the most compressive stress occurs around the middle plane. Furthermore, the level of the compression in the neighbourhood of the hole is higher at the exit surface than at the entry surface. Additionally, much higher compressive hoop stresses are observed, especially at the middle plane, when predicted by isotropic hardening in comparison with kinematic hardening.

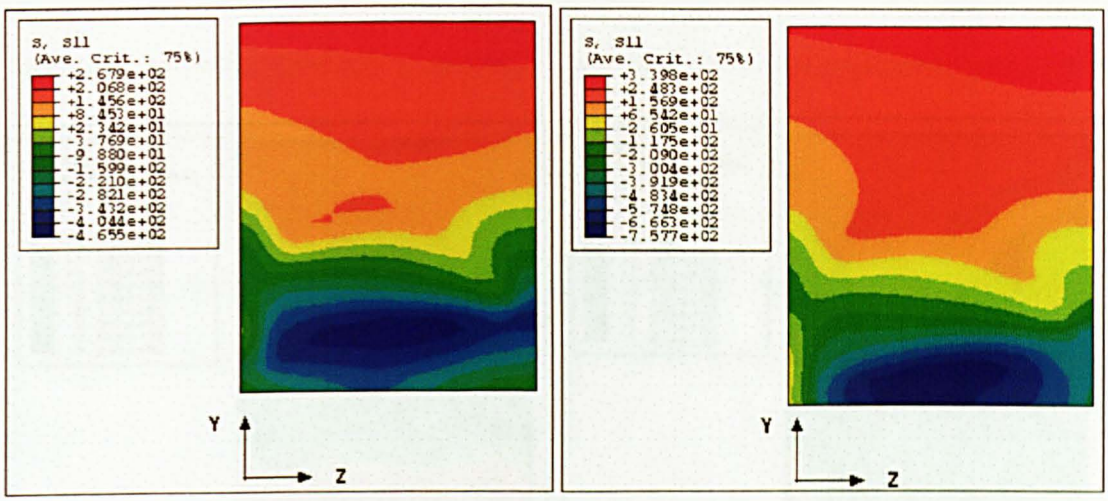

(a) kinematic hardening (b) isotropic hardening

Figure 5-17 Contour plot of hoop stresses predicted by 3D contact FEA

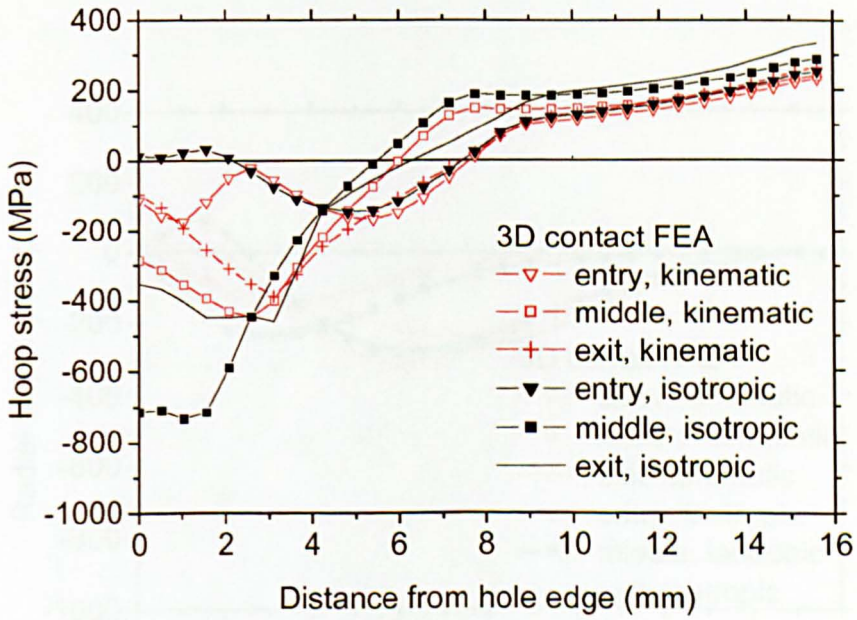

Figure 5-18 Line plot of hoop stresses (using kinematic and isotropic hadening)

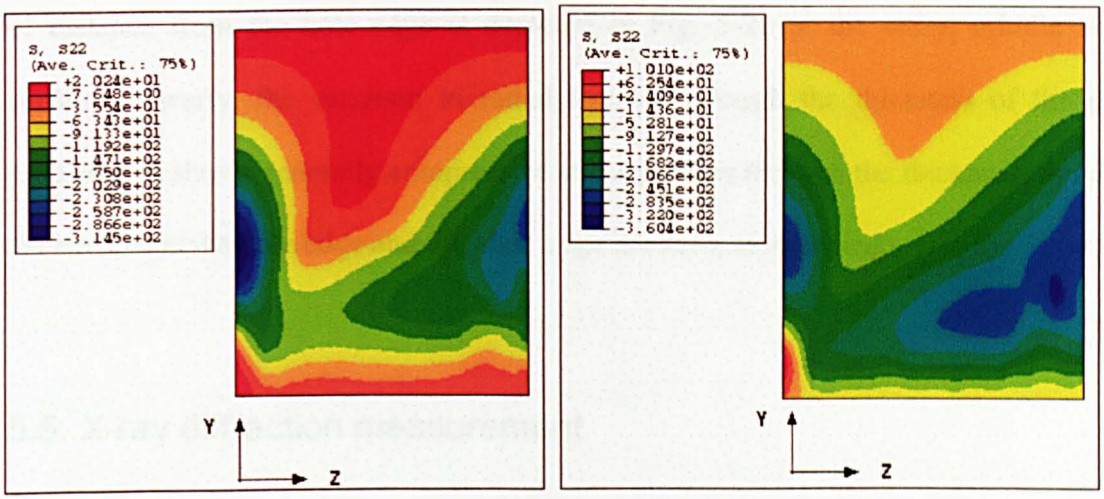

(a) kinematic hardening (b) isotropic hardening

Figure 5-19 Contour plot of radial stresses predicted by 3D contact FEA

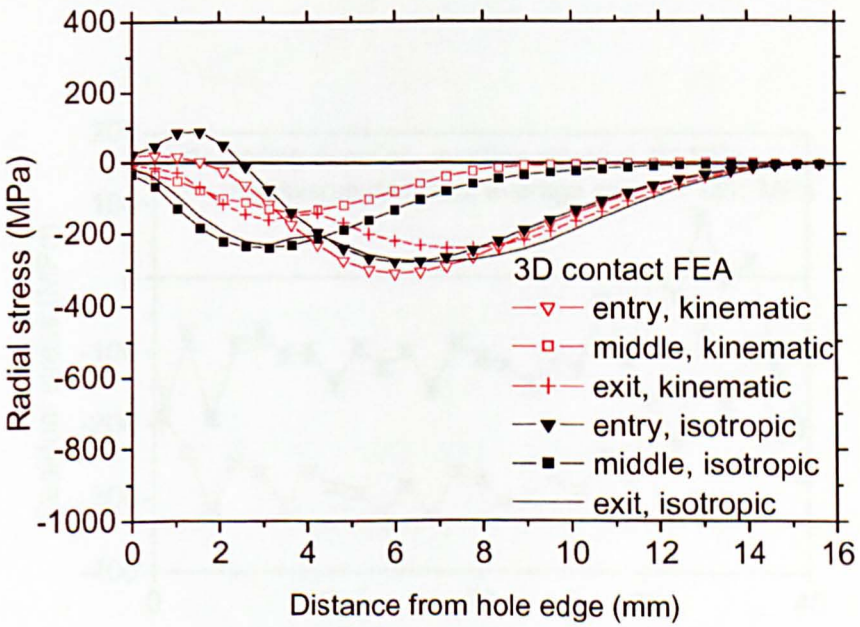

Figure 5-20 Line plot of radial stresses (using kinematic and isotropic hardening)

Similarly, the contour plot of the radial residual stresses predicted by the kinematic and isotropic hardening models is displayed in Fig. 5-19, and the line plot of them as a function of distance from the hole edge is depicted in Fig. 5-20 at the entry, middle and exit surfaces. Clearly, the variation in radial stresses through the thickness of the plate is predicted. It shows generally compressive stress profiles through the thickness. In addition, the stresses at the hole edge and the plate edge are zero, as expected.

5.5 X-ray diffraction measurement

The initial X-ray measurement of the specimen prior to hole cold expansion showed there were highly compressive residual stresses on the surfaces as illustrated in Fig. 5-21. The average compressive stress in the rolling direction was approximately 94 MPa, and 251 MPa in the transverse direction. This high compressive residual stress is mainly attributed to the mechanical grinding of the surface during specimen machining. However, the stressed near surface layer can be eliminated by chemical etching using acid dissolution.

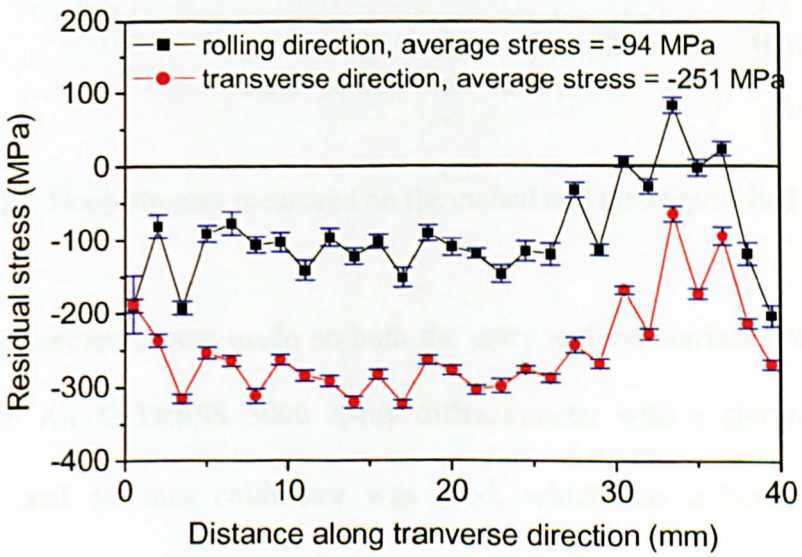

Figure 5-21 Surface stresses prior to cold expansion

In order to facilitate good quality of X-ray diffraction, the sample was electrolytically polished by means of a mixture of phosphoric acid, sulphuric acid and distilled water, with a volume ratio 2:1:1. The current was controlled at around 3 mA/mm^2 to minimise surface pitting. A thickness of about 0.1 mm on each side was eventually removed including the chemically etched layer. A study on the effect of the etching and electropolishing processes was also performed and indicated that the stress measured on the etched surface was underestimated by up to 200 MPa in tension far from the hole edge and 50 MPa in compression near the hole edge, in comparison with the stress measured on the electropolished surface, as detailed in Fig. 5-22. It is mainly because the pitting or porosity resulting from etching process makes X-ray diffraction imperfect.

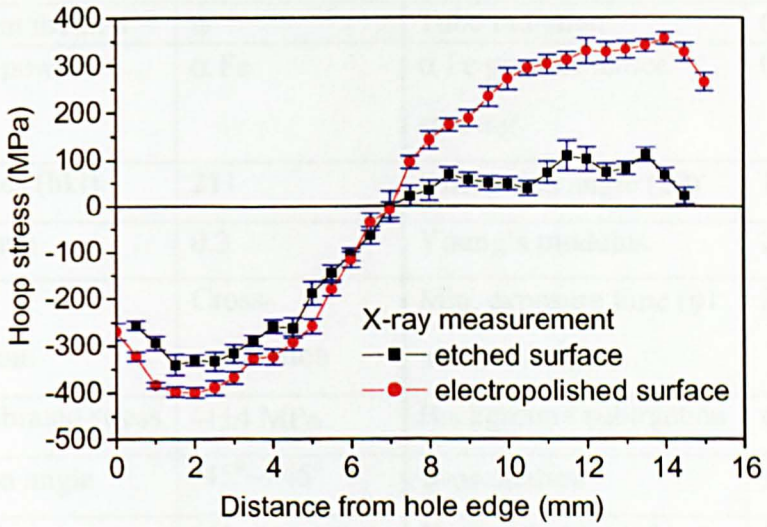

Figure 5-22 Hoop stresses measured on the etched and electropolished surfaces

The X-ray measurements were made on both the entry and exit surfaces of the hole cold expanded plate. An XSTRESS 3000 X-ray diffractometer with a chromium (Cr K-α) radiation tube and ϕ1 mm collimator was used, which has a better resolution of measurement than ϕ2 mm and ϕ3 mm collimators. Lattice spacings on the {211} diffracting planes at an angle of ~156.4° were measured by the ψ-method with a total of twelve ψ-tilts (six positive and six negative tilts) between -45° and +45°. A measurement,

with additional ψ-oscillations of ±2° around each specified ψ-tilt, was conducted and showed no benefit to the measured results. Stress evaluation was based on a Young's modulus of 211 GPa and Possion's ratio of 0.3 given by the X-ray analysis software used for the {211} plane, which are slightly different with the values of bulk materials measured, together with the plane stress assumption due to the shallow penetration depth of X-rays in metallic materials. The X-ray measurement parameters for the EN8 (Fe ferrite) specimen using chromium radiation (wavelength ~ 2.289 Å) are summarised in Table 5-4 below.

Table 5-4 X-ray diffraction parameters for EN8 steel

Measurement method	ψ	Tube radiation	Cr K-α
Calibration powder material	α Fe	α Fe powder lattice spacing	0.28662 nm
Miller indices (hkl)	211	Diffraction angle (2θ)	156.4°
Poisson's ratio	0.3	Young's modulus	211 GPa
Peak shift determination	Cross-correlation	Min. exposure time (ϕ1 mm collimator)	20 s
Typical calibrated stress	-4±4 MPa	Background subtraction	constant
ψ inclination angle	-45°~+45°	ψ-oscillation	±0°
ψ tilt number: negative/positive	6/6	Typical Calibrated distance	10 mm
ϕ angles	0°, 90°	ϕ-oscillation /number	±0°/0
X-ray operating voltage	30 kV	Time for single point measurement	8 min.
X-ray operating current	7 mA		

Fig. 5-23 illustrates the X-ray measurement result with twelve ψ-tilts for one point. The left half of the window displays the relationship of measured lattice plane d vs. $\sin^2\psi$

with six negative tilts and six positive tilts respectively. The linearity of d vs. $\sin^2\psi$ is clearly presented in this example. Below the graph are the evaluated stress and the error in MPa. The error is calculated by averaging the values of the error bars of two lines (based on the negative tilts and positive tilts separately). The right half of the window lists a table of twelve results containing tilt angle (psi), peak shifts of the two detectors (A and B) in pixels (shift A, shift B), lattice spacing (d(nm)), full width at half-maximum intensity (fwhm) in degrees, and the average intensity (Im) of the maximum intensities of the two detectors.

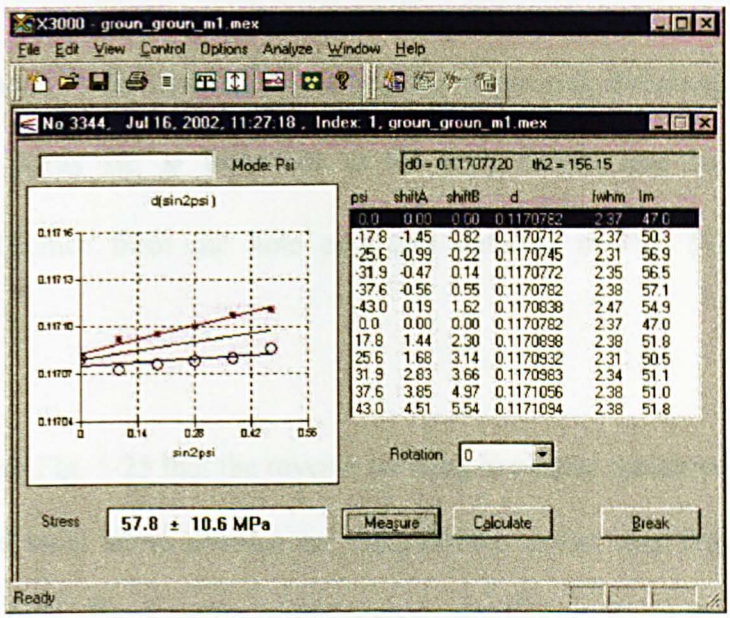

Figure 5-23 An example of an X-ray measurement result

Fig. 5-24 shows typical intensity profiles captured from the two detectors before background subtraction. The location or shift of the peak is determined using the global peak shift method of cross-correlation (Lu et al., 1996), which employs the whole information from the intensity profiles.

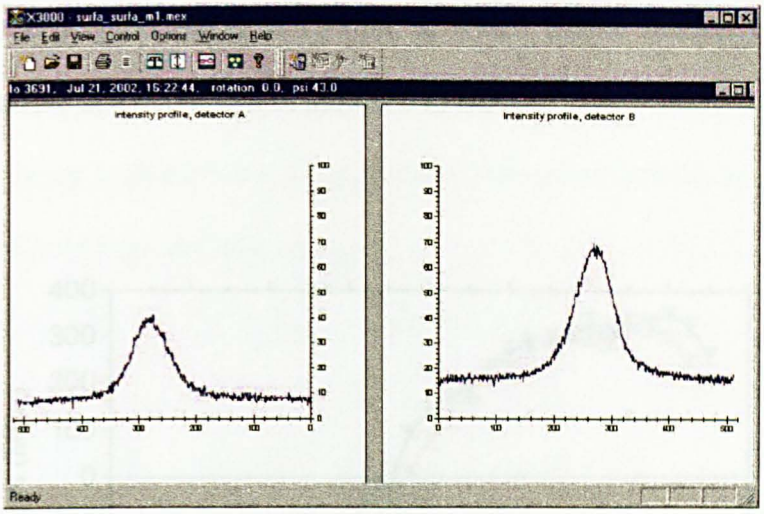

Figure 5-24 Intensity curves received from the two detectors before background subtraction

The hoop and radial stress distributions along the transverse direction of the specimen, measured by the X-ray $\sin^2\psi$ technique, at the entry surface and the exit surface with respect to the distance from the hole edge are detailed in Fig. 5-25 and Fig. 5-26 respectively.

It can be seen from Fig. 5-25 that the reverse yielding is clearly measured at both entry and exit surfaces, and hoop stress profiles are compressive in the near field of the hole and tensile in the far field. The location of the reverse yielding on the entry surface is around 4 mm from the hole edge with maximum compressive hoop stress of ~310 MPa. The position of the reverse yielding on the exit surface is approximately 2 mm with maximum compressive hoop stress up to 400 MPa. In comparison, the exit surface has a smaller area of reverse yielding, but higher compressive stress than the entry surface. It is interesting to find that the stress profiles for both surfaces coincide almost from the distance of 4 mm to the hole edge onward, which is nearly the location of the reverse yielding on the entry surface. The division between the compressive and tensile stress fields for the two surfaces is about 7.2 mm from the hole edge where the hoop stresses are zero. The elastic-plastic

boundary is in the neighbourhood of 13 mm, at which tensile stresses on both surfaces simultaneously arrive at a maximum of almost 340 MPa.

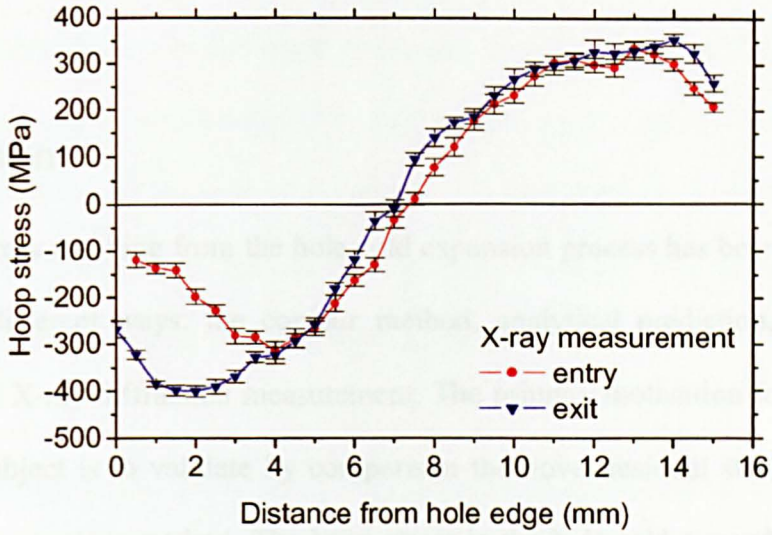

Figure 5-25 Hoop stress profiles at entry and exit surfaces

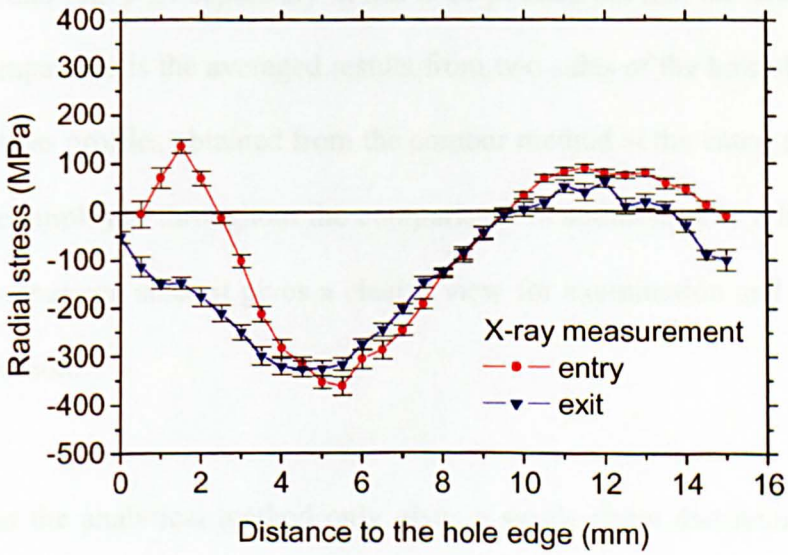

Figure 5-26 Radial stress profiles at entry and exit surfaces

It can be seen in Fig. 5-26 that the radial stresses at the entry and exit surfaces are not always compressive. The most compressive radial stresses, around 350 MPa, occur in the vicinity of 4.5 mm for both surfaces. The tensile stress at the entry face is observed in the near-field and far-field from the hole edge.

5.6 Discussion

The residual stress resulting from the hole cold expansion process has been investigated in a number of different ways: the contour method, analytical prediction, finite element simulation, and X-ray diffraction measurement. The primary motivation for the variety of study of the subject is to validate by comparison the novel residual stress measurement technique — the contour method. The hoop stress in the hole cold expanded plate is used for the validation study because it is generally considered as the dominant factor that contributes to the crack initiation and crack propagation at fastener holes. The comparisons between the contour method and three other techniques: analytical prediction, finite element simulation, X-ray measurement, in terms of hoop stress field, are illustrated in Fig. 5-27, Fig. 5-28 and Fig. 5-29 separately. It has to be pointed out that the hoop stress profile used for the compassion is the averaged results from two sides of the hole shown in Fig. 5-13. The hoop stress profiles obtained from the contour method at the entry, middle and exit surfaces will be employed throughout the comparison. In addition, only a line plot will be used for the comparison since it gives a clearer view for examination and discloses more accurate information.

It is known that the analytical method only gives a single stress distribution through the thickness as it relies upon two-dimensional conditions. As seen in Fig. 5-27, general trend agreement between the two methods is reached. The hoop stress evaluated by the analytical prediction with the kinematic hardening assumption is in good agreement with the tensile

stresses at the entry and exit surfaces, and close to the compressive stress at the middle surface, as determined by the contour method. On the other hand, deviation from both techniques is also indicated. One of the error sources is obviously attributed to the assumptions used in the analytical model that inherently cannot account for three-dimensional stress states. On the other hand, the cutting-induced error in the contour-method measurement is questionable. The data smoothing and extrapolation also add the error. Based on the tension-compression test of EN8 steel, neither kinematic nor isotropic hardening models exactly characterises the hardening response. The kinematic hardening assumption used in the analytical model contributes an additional error.

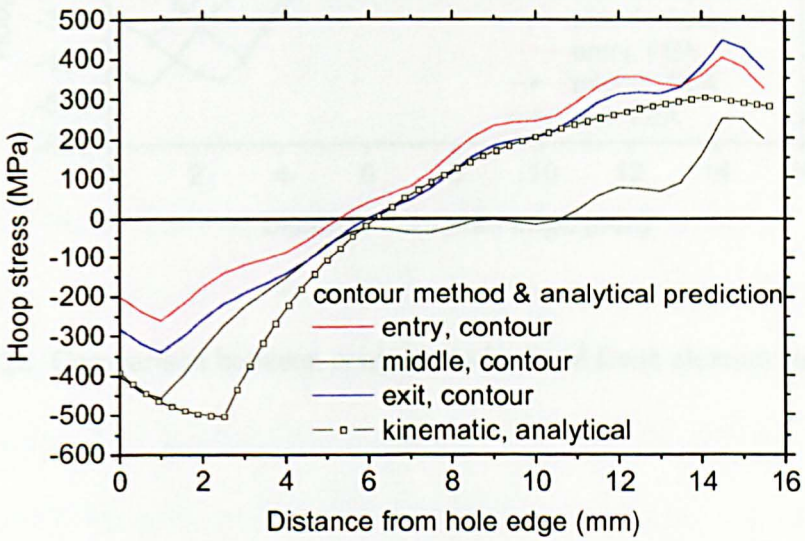

Figure 5-27 Comparison between contour method and analytical prediction

The hoop stress fields at the entry, middle and exit surfaces predicted by the 3D contact finite element simulation in combination with the kinematic hardening assumption are displayed in Fig. 5-28. A general agreement in hoop stresses obtained from both techniques can be seen. The tensile stress predicted by the FEA is in between the tensile stresses at the surfaces and at the middle measured by the contour method. The magnitudes

of compressive stresses also have a general agreement. Nevertheless, the predicted and measured reverse yielding locations appear divergent. The errors, as mentioned above, are attributed to a variety of factors: cutting flatness, data reduction, and the hardening assumption used in the FE simulation.

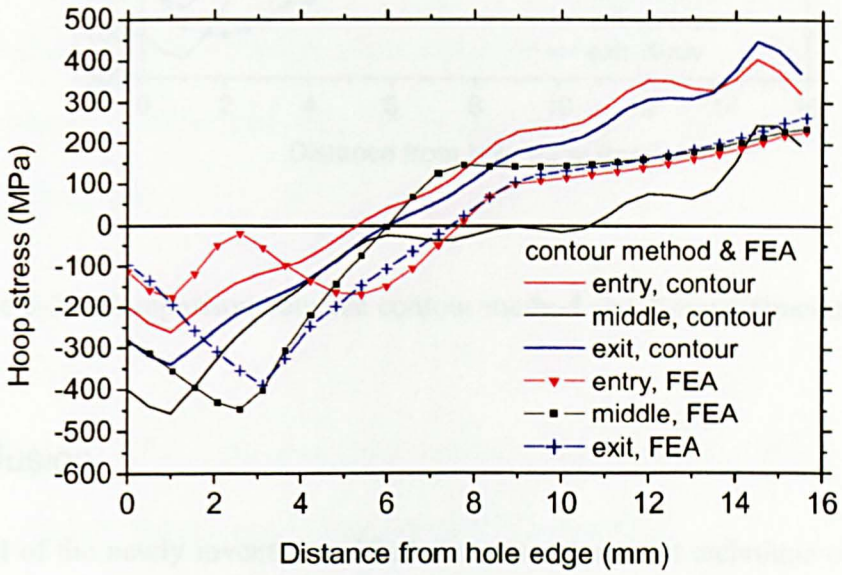

Figure 5-28 Comparison between contour method and finite element simulation

X-ray diffraction is known to enable surface stresses to be evaluated, and therefore the hoop stresses at the entry and the exit surfaces were measured, as depicted in Fig. 5-29. Similar to the previous comparisons, a generally good agreement is obtained, and a better match is observed for the tensile stresses at or near the surfaces, excluding the region near the edge. However, deviations for the compressive stresses are clearly indicated, and generally recognised as arising from the cutting error.

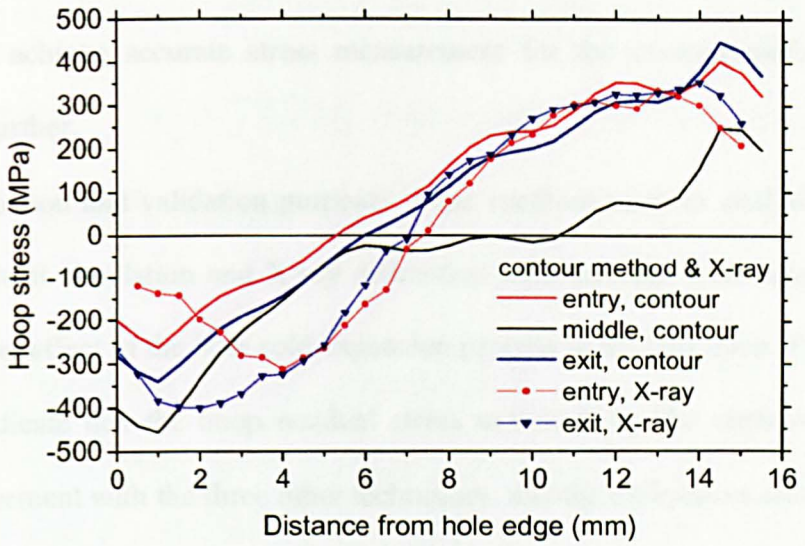

Figure 5-29 Comparison between contour method and X-ray diffraction

5.7 Conclusion

The potential of the newly invented residual stress measurement technique of the contour method has been explored on an EN8 steel plate subjected to 4% hole cold expansion. Although the contour method only enables the determination of the residual hoop stress with one cut, it provides sufficient information for the prediction of crack initiation and growth for the cold expansion problem. The following conclusions can be drawn based on the series of studies above.

- The measurement of a cross-sectional hoop stress profile in the hole cold expanded EN8 steel plate has been performed using the contour method. The result shows the expected variation of compression near the hole and tension in the far-field, and correctly identifies the stress difference through thickness.
- The peak-to-valley amplitude of measured contours is ~ 45 μm and the standard deviation of Fourier fitting is ~ 0.2 μm. It is felt that the cutting is not quite flat, particularly in the vicinity of edges and possibly near the hole as well. The detailed information about wire EDM of the EN8 specimen are little known, and the cutting-

induced error, thus, cannot be given here. However, the flat cutting is found to be critical to achieve accurate stress measurement for the contour method and needs studying further.

- For comparison and validation purposes, other methods such as analytical prediction, finite element simulation and X-ray diffraction measurement were also conducted to evaluate the effect of the hole cold expansion process in the specimen. The comparison studies indicate that the hoop residual stress measured by the contour method is in broad agreement with the three other techniques, and the differences among them were given in Section 5.6.

5.8 References

[1] Budiansky, B. (1971). An exact solution to an elastic-plastic stress concentration problem. Prikladnaya Matematika i Physik, Vol. 35 (**1**), pp. 40-48.

[2] Fitzpatrick, M. E. and Edwards, L. (1998). Fatigue Crack/Residual Stress Field Interactions and Their Implications for Damage-Tolerant Design. Journal of Materials Engineering and Performance, Vol. 7 (**2**), pp. 190-198.

[3] Lu, J., James, M. and Roy, G. (1996). Handbook of measurement of residual stresses. Lilburn, Georgia, USA, The Fairmont Press, Inc.

[4] Zhang, Y., Edwards, L. and Fitzpatrick, M. E. (2002). Finite element simulation of hole cold expansion process in EN8 steel plates. Proceedings of the Sixteenth ABAQUS UK User Group Conference, 12-13 Nov., Warrington, UK.

6 Determination of residual stresses in hole cold expanded 7475-T7351 aluminium alloy plates using the contour method

In this chapter, the contour method is demonstrated on a 7475-T7351 aluminium alloy subjected to 4% hole cold expansion. The experimental aspects of the contour method will be focused on with a particular emphasis on the analysis of the effects of the cutting orientation and the presence of the hole.

6.1 Material and specimen details

6.1.1 Material

The 7475-T7351 aluminium alloy belongs to the Al-Zn-Mg-Cu (Cu containing) 7000 series alloys having high strength, and is widely used in aircraft structures, typically in fuselage and wing skins. The T7351 treatment involves solution treatment at 470°C, water quenching and controlled stretching from ~2% followed by artificial ageing in two stages: first at 121°C for 25 h and secondly at 163°C for a period of 24-30 h. The nominal chemical components of 7475-T7351 aluminium alloy are give in Table 6-1 (ASM, 1979).

Table 6-1 Chemical components of 7475-T7351 aluminium alloy (Wt%)

Cr	Cu	Fe	Mg	Mn	Si	Ti	Zn	Al
0.18-0.25	1.2-1.9	<0.12	1.9-2.6	<0.06	<0.1	<0.06	5.2-6.2	Bal

The mechanical properties of the 7475-T7351 aluminium alloy are listed in Table 6-2 (MIL-HDBK-5H, 1998).

Table 6-2 Mechanical properties of 7475-T7351 aluminium alloy

Name	Units	Value
Ultimate tensile strength in L-dir.	MPa	483
Ultimate tensile strength in LT-dir.	MPa	490
Ultimate tensile strength in ST-dir.	MPa	455
Tensile yield strength in L-dir.	MPa	406.8
Tensile yield strength in LT-dir.	MPa	413.7
Tensile yield strength in ST-dir.	MPa	372.3
Compressive yield strength in L-dir.	MPa	399.9
Compressive yield strength in LT-dir.	MPa	420.6
Compressive yield strength in ST-dir.	MPa	427.5
Ultimate shear strength, L-LY plane	MPa	283
Tensile elastic modulus in L-dir.	MPa	71000
Compressive elastic modulus in L-dir.	MPa	73100
Shear modulus (inplane: L-LT)	MPa	26890
Poisson ration (inplane :L-LT)		0.33

6.1.2 Specimen

The specimen under study was 100 mm long, 40 mm wide and 16 mm thick, containing a 4% cold expanded hole, and its longitudinal axis was aligned with the rolling direction of the blank, as illustrated in Fig. 6-1. An initial nominal 8.73 mm diamter hole was achieved by drilling and reaming in the centre of the specimen followed by 4% cold expansion using a conventional FTI technique. Annular marks and plastic deformation on the exit surface of

the specimen due to the constraint action of the FTI tool set against the movement of the specimen during hole expanding were visually observed, but are not shown here.

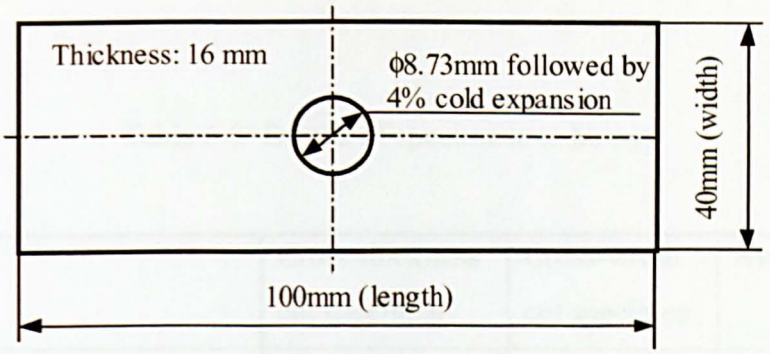

Figure 6-1 Configuration of specimen with 4% hole cold expansion

Two hole cold expansion specimens were prepared and designed to be cut across the thickness and the width respectively to examine the effect of the cutting orientation and the hole on the cutting flatness, as illustrated in Fig. 6-2.

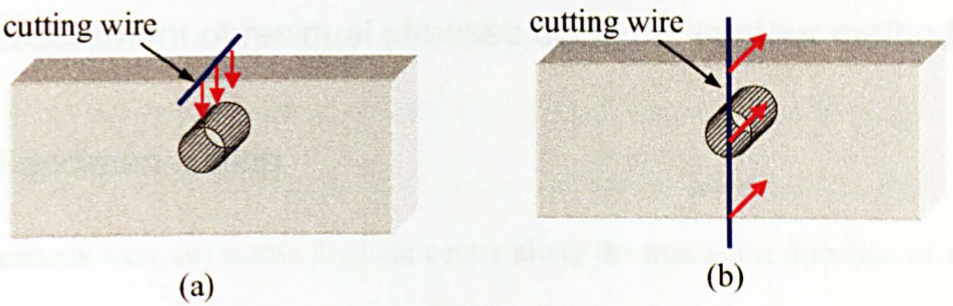

Figure 6-2 Schematic illustration of cutting orientation
(a) cross-thickness cut (b) cross-width cut

The detailed information of the specimens before and after cold expansion is given in Table 6-3. The two specimens have a slight difference in expansion ratio, in spite of the same dimension of initial holes, suggesting the possibility of difference in magnitude of stress. This is probably owing to the variation in thickness of the disposable split-sleeve

used individually in expansion of the two specimens. It is deduced, on the basis of the retained expansion ratio, that the specimen to be cut crossing the thickness would contain higher stress values than the specimen to be cut crossing the width.

Table 6-3 Details of specimens to be cut

	Cross-thickness cut specimen	Cross-width cut specimen	Average
Initial hole diameter	8.726 mm	8.726 mm	8.726 mm
Post-expansion diameter	8.945 mm	8.933 mm	8.939 mm
Max. nominal mandrel diameter (including sleeve)	9.08 mm	9.08 mm	9.08 mm
Retained expansion	62%	58%	60%
Spring back	38%	42%	40%

6.2 Measurement of residual stresses using the contour method

6.2.1 Specimen cutting

Two specimens were cut across the hole centre along the transverse direction of the plate, at the middle length, respectively, one of which was sectioned across the thickness and the other across the width. As discussed in Chapter 5, flat cutting is critical for the contour method to achieve a high accuracy of stress measurement. There are a couple of ways worth mentioning to achieve this. Firstly, steady clamping of the specimen to avoid its movement is important to keep cutting straight. In addition, selection of correct parameters for the wire EDM is vital to make a flat surface. Nowadays, modern computerised wire EDM tends to offer more flexible operations for surface machining. However, this flexibility increases the complexity of the proper selection of operation parameters and

requires more experiments. Other factors such as material properties and specimen geometry also have an influence on the choice of cutting parameters. It is felt that the presence of the hole in the specimen and cutting orientation may affect the cutting quality. To prove this, two additional specimens having a plain hole without cold expansion were cut in two different directions: across the thickness and across the width respectively, corresponding to the hole cold expanded plates. A FANUC ROBOCUT α-O*i*B wire electric discharge machine located in our workshop was used for all cuttings, fed with ϕ0.1 mm bare brass wire. A specially designed jig was used to clamp the specimen tightly. The specimen together with the fixing jig were submerged in a circulating deionized liquid tank during the cutting.

6.2.2 Contour measuring

After specimen cutting, the deformation profile of the cut surfaces was measured using a Mitutoyo Crystal Plus 574 CMM fitted with a 1 mm-diameter Renishaw probe, located at an air conditioned room in our department. The measurements were performed sequentially on the two cut surfaces with a uniform 0.25 mm-spaced square grid. Each cut surface was divided by the hole into two patches, and each patch with an area of 16 mm by 15.5 mm resulted in 4095 points, giving in total 8190 points at each surface. Fig. 6-3 illustrates the scheme of the specimen clamping for specimen measurement using the CMM, similar to the EN8 plate in Chapter 5.

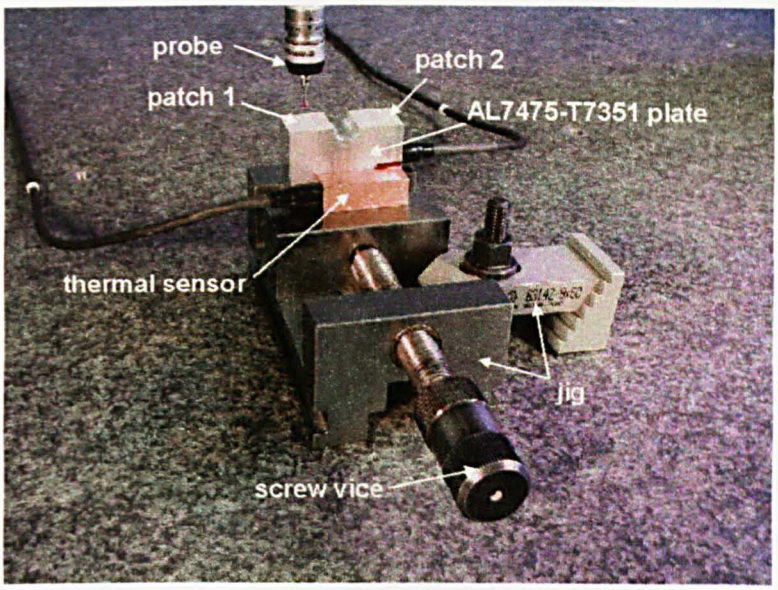

Figure 6-3 Set-up for CMM contour measurement

6.2.3 Data analysis

As discussed earlier, data smoothing to minimise the noise arising from the experimental procedures of specimen cutting and contour measurement is vital to achieve a desirable accuracy of stress measurement, as the calculated stress from FEA magnifies the noise greatly. Other data processes, such as removal of bad data at or near the edges and extrapolation of the removed data, are also important. Again, the commercial code MATLAB R12 was employed to perform the data analysis.

Firstly, the measured displacements of the two corresponding cut surfaces should be averaged. Then, the averaged data can be plotted three-dimensionally to examine the overall look of the measured data. Some of the measured data at the edges, where the probe may fall out of the surface during CMM measuring, must be removed, as the case for dealing with the EN8 specimen described in Chapter 5. Fig. 6-4 displays the averaged, removed and measured data of the specimen cut across the thickness, and Fig. 6-5 for the specimen cut across the width.

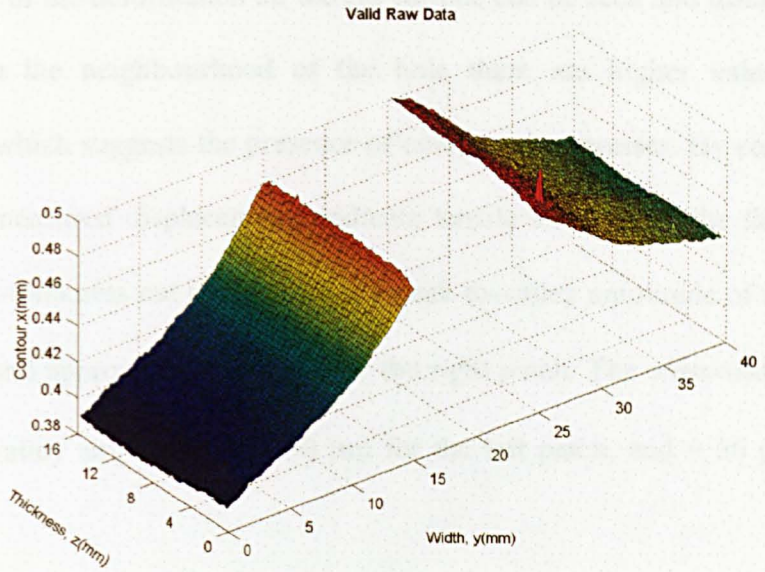

Figure 6-4 Averaged, removed and raw data for cross-thickness cut

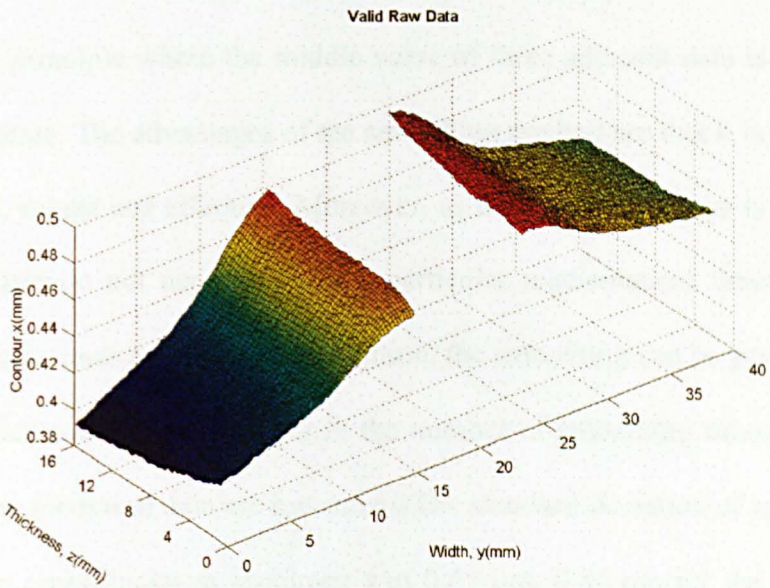

Figure 6-5 Averaged, removed and raw data for cross-width cut

A general view of the deformation on the cut surface can be seen and discloses very useful information. In the neighbourhood of the hole there are higher values of measured displacements which suggests the presence of compressive stresses. By contrast, the lower values of the measured displacements indicate tensile stresses, in the far-field from the hole. The cross-thickness cut specimen has a peak-to-valley amplitude of about 98 μm for the left patch, and approximately 68 μm for the right patch. The cross-width cut specimen has a peak-to-valley amplitude of ~ 90 μm for the left patch, and ~ 56 μm for the right patch.

The scheme of data smoothing or fitting can vary depending on the data profile and availability of fitting functions. The bivariate Fourier fitting used in the EN8 steel specimen described in Chapter 5 is also applicable to the 7475-T7351 aluminium alloy specimen. Here, we will explore a more flexible technique to smooth scattered measurements: bivariate running average, one of the non-parametric smooth techniques. It is based on the principle where the middle value of three adjacent data is replaced by the average of the three. The advantages of the smoothing method are that it is simple, flexible, straightforward, robust and effective. Moreover, as the running average is non-parametric, the measured data do not necessarily fit a particular mathematical function and can be smoothed as many times as required. In addition, the smoothing can be performed in either dimension of data and can be different in the number of smoothing times. However, it is desirable that the measured data are less noisy. The standard deviation of smoothing for the left patch of the cross-thickness specimen was 0.69 μm, 0.84 μm for the right patch, and 0.77 μm for average of both patches. The standard deviation of smoothing for the left patch of the cross-width specimen was 0.62 μm, 0.79 μm for the right patch, and 0.71 μm for average of both patches. In addition, the measurement error was ~ 3 μm for all specimens. The information about the contour measurement and the smoothing accuracy of two

specimens were detailed in Table 6-4. Extrapolation of the removed data is in accordance with the spline function available in MATLAB. Fig. 6-6 shows the smoothed and extrapolated data for the cross-thickness cut specimen, and Fig. 6-7 for the cross-width cut specimen.

Table 6-4 Details of contour measurements for hole cold expanded specimens

	Cross-thickness cut specimen		Cross-width cut specimen	
Unit (μm)	Left patch	Right patch	Left patch	Right patch
Peak-to-valley	98	68	90	56
Average of peak-to-valley of two patches	83		73	
Smoothing error	0.69	0.84	0.62	0.79
Average of smoothing error of two patches	0.77		0.71	
Measurement error	3.05		3.05	

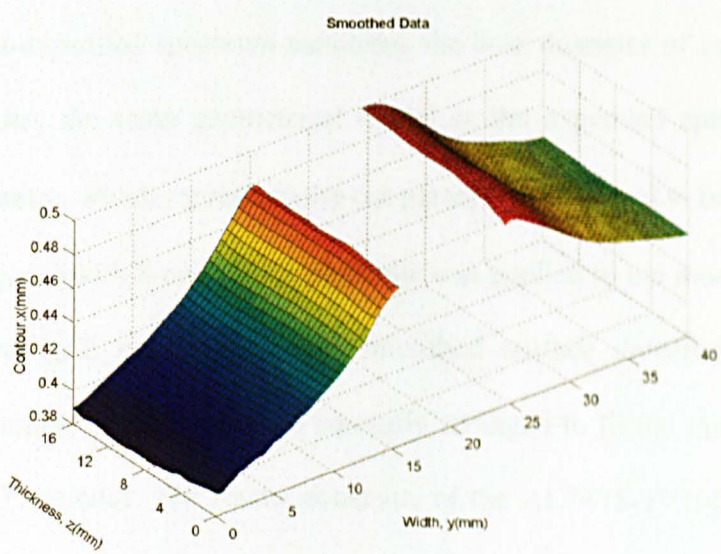

Figure 6-6 Averaged, extrapolated and smoothed data for cross-thickness cut

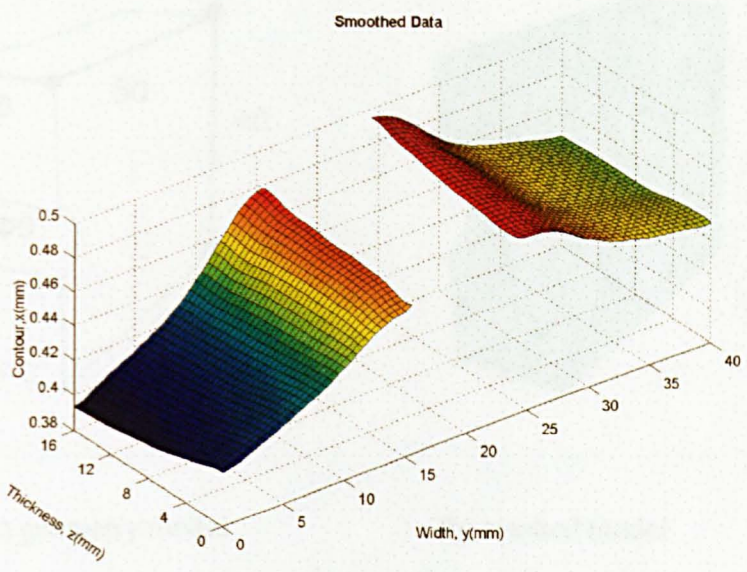

Figure 6-7 Averaged, extrapolated and smoothed data for cross-width cut

6.2.4 Finite element analysis

Half the specimen was modelled to analyse the residual stress profile on the cut plane of interest based on the measured deformation. The 3D FE model of the expanded specimen was characterised by a thickness of 16 mm, a width of 40 mm, a length of 50 mm (half specimen), and a 9 mm-diameter cold expanded hole, as shown in Fig. 6-8 (a). The 3D FE model of the non-expanded specimen simplifies the hole diameter of exactly 8.73 mm to 9 mm and thus has the same geometrical model as the expanded specimen. The plane across the hole centre, which represents the cut plane, was assumed to be flat. A 0.5 mm × 0.5 mm mesh scheme with 8-node brick elements was applied to the model, as seen in Fig. 6-8 (b). The averaged, extrapolated and smoothed surface deformation, regarded as displacement boundary conditions, were carefully arranged to fit the meshed nodes of the cut plane on the FE model. The elastic constants of the AL7475-T7351 material were 71 GPa for Young's modulus and 0.33 for Poisson's ratio, as given in Table 6-2. ABAQUS 6.3 was employed to conduct the geometry modelling and the linear FE solution.

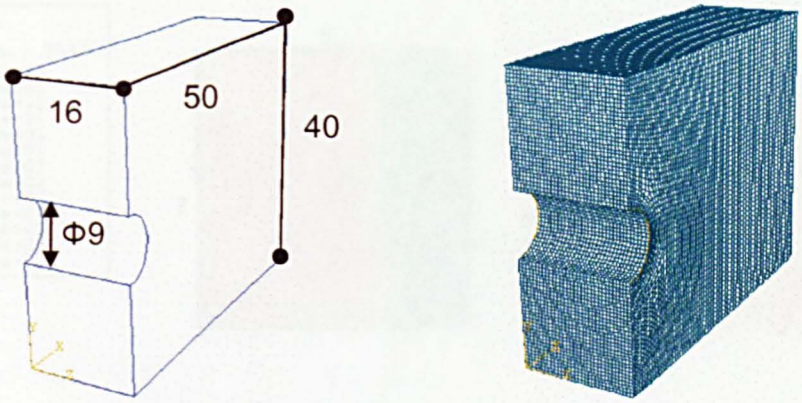

(a) geometry model (b) meshed model

Figure 6-8 FE model used in the contour method

6.2.5 Results and discussion

Through-thickness hoop stress profiles as a result of the hole cold expansion process were obtained, as illustrated in Fig. 6-9 for the cross-thickness cut specimen, and Fig. 6-10 for the cross-width cut specimen. The well-known hoop stress distribution for the cold expansion problem is clearly indicated for both types of cuttings. The stress near the hole is compressive and the stress far from the hole is tensile. The variation in hoop stress through the entire surface is also identified.

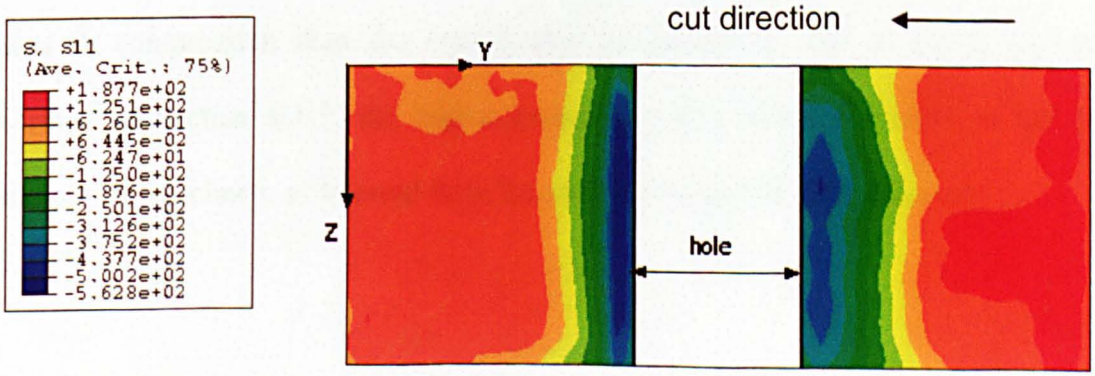

Figure 6-9 Contour plot of hoop stress profile for the cross-thickness cut specimen

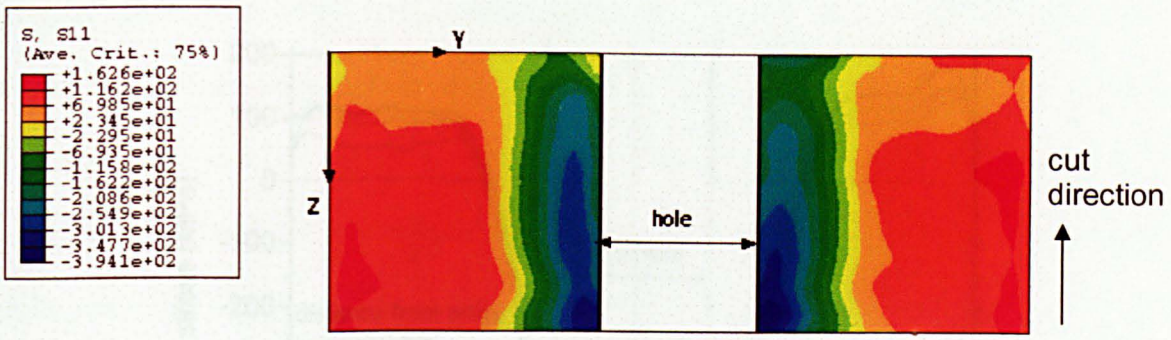

Figure 6-10 Contour plot of hoop stress profile for the cross-width cut specimen

A line plot of the hoop stress profile with respect to the distance from the hole centre at specified thicknesses from the entry surface gives clear illustration and more detail. The stresses at the entry and exit surfaces are not plotted here since they are derived from the extrapolated displacements and may not be correct. It can be seen from Fig. 6-11 and Fig. 6-12 that reverse yielding in the vicinity of the hole was measured by the contour method for both types of cut specimens. The through-thickness variation in hoop stresses is also clearly indicated. It is interesting to find that the boundary between compression and tension measured for both specimens are in excellent agreement, approximately 9.5 mm from the hole centre. The tensile stresses are also in a fairly good agreement, varying around 90 MPa. On the other hand, deviation of the reverse-yielded stresses in magnitude is observed between the two specimens. The cross-thickness cut specimen shows higher values in compression than the cross-width cut specimen. This is partly due to, as described in Section 6.1.2, the higher expansion level actually applied to the cross-thickness cut specimen, as inferred from the retained expansion ratio measured.

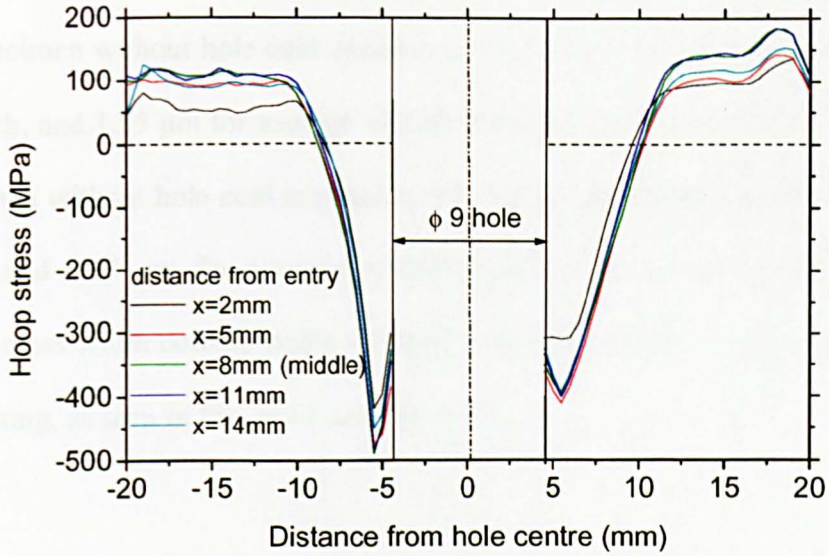

Figure 6-11 Line plot of hoop stress profile for the cross-thickness cut specimen

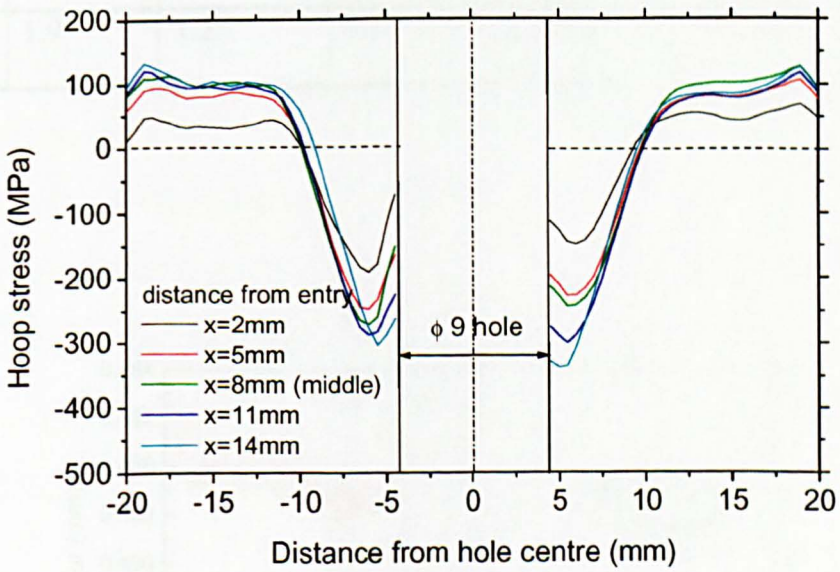

Figure 6-12 Line plot of hoop stress profile for the cross-width cut specimen

Apart from the difference in expansion ratio, the cutting-induced error needs identifying, and a cutting orientation may associate with the cutting flatness. To characterise the error, the plain hole specimens without cold expansion were used. As said earlier, the two plain hole specimens were cut crossing the thickness and width separately, in the exact fashion

as their counterparts of the hole-expanded specimens. The surface flatness of the cross-thickness specimen without hole cold expansion was 1.9 μm for the left patch, 1.2 μm for the right patch, and 1.55 μm for average of both patches. The surface flatness of the cross-width specimen without hole cold expansion was 1.2 μm for the left patch, 1.3 μm for the right patch, and 1.25 μm for average of both patches, as detailed in Table 6-5. This suggests the cross-width cutting yields a flatter, thus better quality, surface than the cross-thickness cutting, as seen in Fig. 6-13 and Fig. 6-14.

Table 6-5 Cut flatness of plain hole specimens

Unit (μm)	Cross-thickness cut			Cross-width cut		
	Left patch	Right patch	Average of two patches	Left patch	Right patch	Average of two patches
Cut flatness	1.9	1.2	1.55	1.2	1.3	1.25

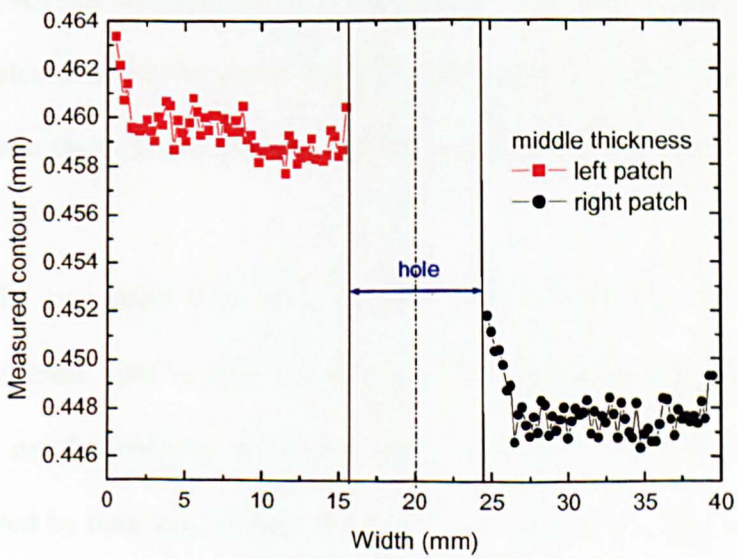

Figure 6-13 Measured contour at the mid-thickness for cross-thickness cutting

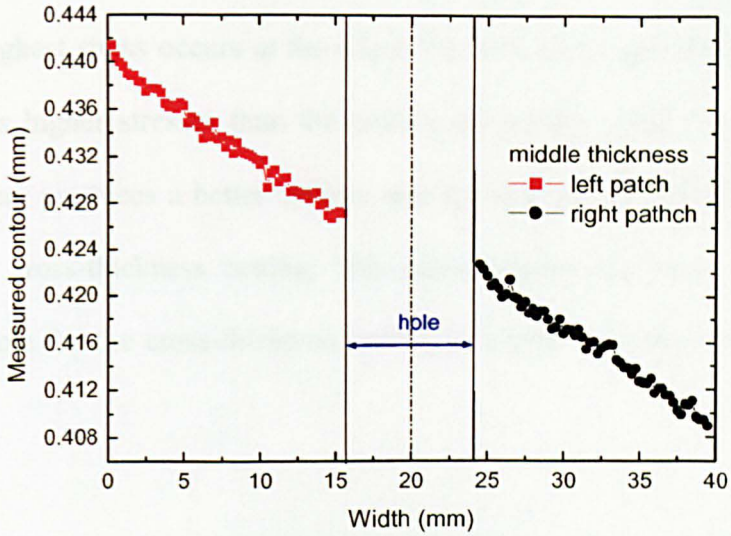

Figure 6-14 Measured contour at the mid-thickness for cross-width cutting

Fig. 6-13 illustrates the contour measured at the mid-thickness of the cross-thickness cut specimen and Fig. 6-14 shows the contour measured at the mid-thickness of the cross-width cut specimen. It can been seen from Fig. 6-13 and Fig. 6-14, the cross-width cutting indeed produced a much flatter plane than the cross-thickness cutting. It is, therefore, inferred that the stress evaluated for the cross-width specimen should be more accurate than the stress calculated for the cross-thickness specimen. It is also found that the worst surfaces appear near the hole and the edge for the cross-thickness cutting.

The errors for the two plain hole specimens are depicted in Fig. 6-15 for the cross-thickness cut specimen, and in Fig. 6-16 for the cross-width cut specimen. They were evaluated based on the contour measurements on the cut surfaces of the plain hole specimens followed by data smoothing, respectively. It can be seen that a dramatic change in stress occurs at an area of approximately 3 mm away from the edges including the hole edges for both cutting situations. The stress profile induced by the cutting is not constant,

and varies over the entire surface, particularly within the area 3 mm from the edges. It is found that the highest stress occurs at the edges for both cases and the cutting across the thickness induces higher stresses than the cutting across the width. In other words, the cross-width cutting produces a better surface quality, and hence a higher accuracy in the results, than the cross-thickness cutting. This phenomenon can partly explain why the stress near the hole for the cross-thickness cutting is higher than the stress for the cross-width cutting.

The errors averaged over the whole surfaces for both specimens are plotted along the width in Fig. 6-17 for clear view. The standard deviation of the cross-thickness cutting was 17 MPa in average, and 4 MPa for the cross-width cutting

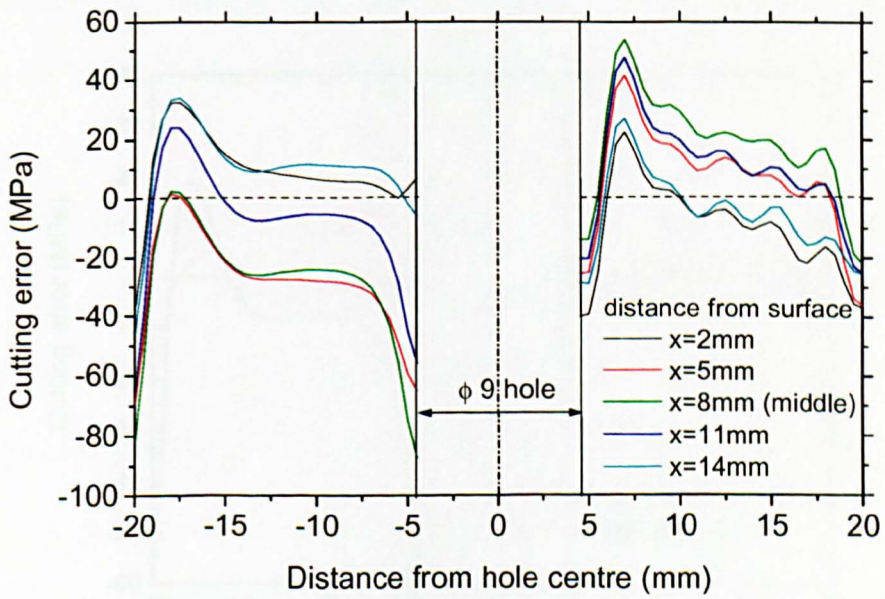

Figure 6-15 Cutting error for the cross-thickness cut

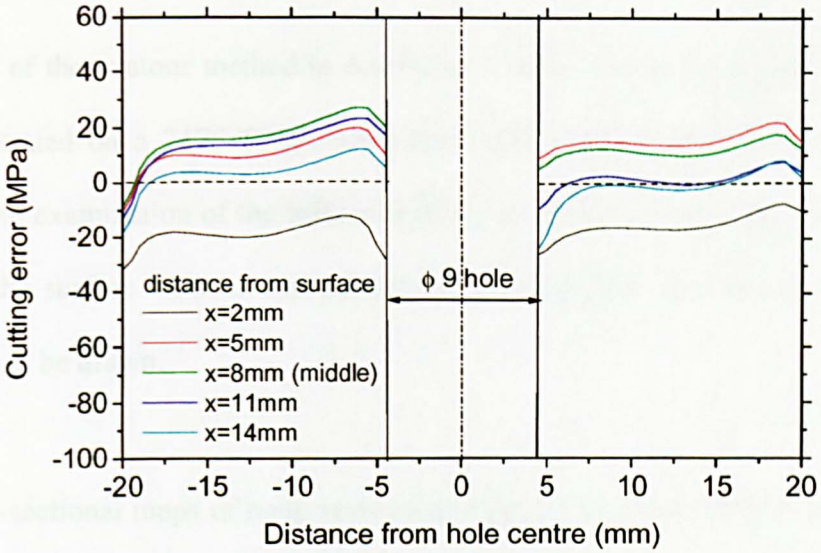

Figure 6-16 Cutting error for the cross-width cut

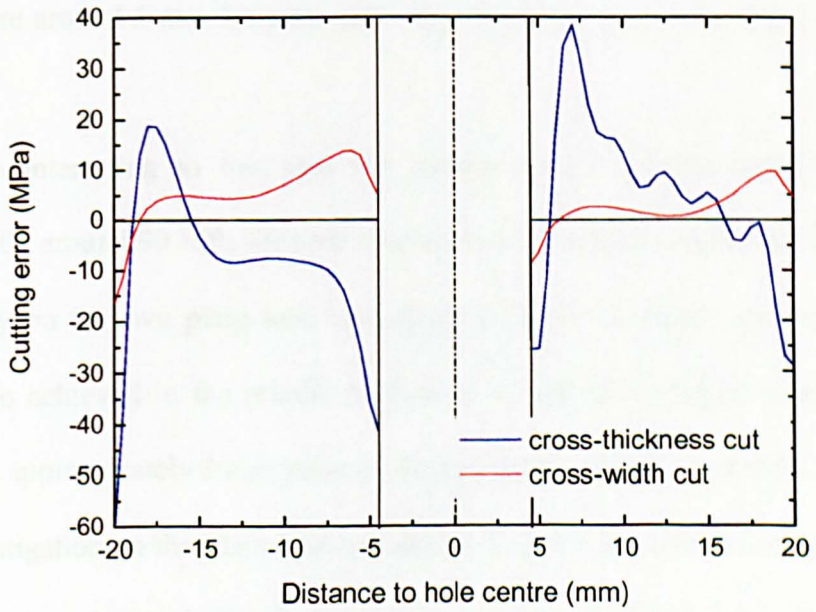

Figure 6-17 Cutting errors for cross-thickness cut and cross-width cut

6.3 Conclusion

The potential of the contour method to determine a cross-sectional hoop stress profile has been demonstrated on a 7475-T7351 aluminium alloy plate subjected to 4% hole cold expansion. The examination of the influence of the cutting orientation and the presence of the hole on the surface flatness was performed on plain hole specimens. The following conclusions can be drawn.

- 2D cross-sectional maps of hoop residual stresses on the two 4% hole cold expansion 7475-T7351 aluminium alloy specimens with 16 mm thickness were obtained using the contour method. The results indeed show the well-known hoop stress distribution for the issue of hole cold expansion: compressive near the hole and tensile far from the hole. Reverse yielding is also observed on both specimens.
- The boundary positions between tension and compression measured by the contour method are around 5 mm from the hole edge for both specimens and on both sides of the hole.
- It is also interesting to find that the tensile stresses are measured to be almost consistently around 90 MPa for both specimens and on both sides of the hole.
- The study on the two plain hole specimens without expansion shows that accurate results are achieved in the middle portion of a material, whereas inaccuracy occurs within an approximately 3 mm range from an edge including a hole edge.
- The investigation on the plain hole specimens in terms of cutting orientation indicates that the cutting direction does have an impact on the cutting flatness. The cross-width cutting produces a better surface, and hence a more accurate result than the cross-thickness cutting. The averaged error for the cross-thickness cutting was ~17 MPa and ~ 4 MPa for the cross-width cutting. It should be aware that the error near the edge and the hole is much bigger than these values.

- The deformation of the 7475-T7351 aluminium alloy subjected to 4% hole cold expansion was up to ~80 μm and the smoothing error was ~ 0.7 μm; whereas the cutting flatness was approximately 1.5 μm. It is apparent that cutting flatness plays a critical role in achieving a high accuracy of stress evaluation using the contour method.
- Owing to the significant error that occurs in the vicinity of the expanded hole where the stress magnitude is particularly of interest, it appears that the hole cold expansion specimen is not ideal for the application of the contour method. However, this error can be effectively reduced by correction for the expanded specimen using its non-expanded counterpart. It is certainly true that the correction would be more accurate if each pair of counterparts could be cut simultaneously under the same conditions.

6.4 References

[1] ASM (1979). Properties and selection: Nonferrous alloys and pure metals, Metals Handbook, Nine edition ,Volume 2. Ohio, USA, American Society for Metals.

[2] MIL-HDBK-5H (1998). Military Handbook: Metallic Materials and Elements for Aerospace Vehicle Structures.

7 2D map of longitudinal residual stresses in MIG 2024-T351 and VPPA 2024-T351 aluminium alloy welds using the contour method

With the rapid development and improvement of welding techniques, driven by the need for low cost and weight saving, there is a potential trend to replace rivets and fasteners with welds in connection of structural components, especially in joining of aircraft components (Mendez, 2000). 2024-T351 aluminium alloy is the principal damage tolerant material widely used in a commercial aircraft and there is considerable interest in the development of high quality welding procedures for this alloy. Metal inert gas (MIG) welding and variable polarity plasma arc (VPPA) welding are two recently developed welding techniques applied for 2024-T351 aluminium alloy as alternatives to mechanical fastening. However, the residual stress field induced by the welding process needs to be fully characterised if a welded part is to be used in safety critical structures. In particular, good knowledge of the residual stress profile in welds will benefit the optimisation of the welding processing parameters.

It has been recognised that residual stresses in welds are difficult to measure using diffraction techniques such as X-ray, synchrotron and neutron diffraction measurements, as there are limitations due to microstructural gradients, dissimilar material combinations, and thick sections (Prime et al., 2002). It is aimed in the present work to investigate the capability and potential of the contour method on two types of welds: MIG Al2024-T351 weld and VPPA Al2024-T351 weld to obtain a full 2D map of the longitudinal (parallel to the weld seam) residual stresses across the thickness.

7.1 Material and welding

7.1.1 Material

2024-T351 aluminium alloy has gained widespread applications in rivets, truck wheels, and aircraft wings, particularly in lower wing skin panels due to its excellent damage tolerant characteristics. 2024-T351 is a heat treatable Al-Cu-Mg alloy, and the supplied plate is usually subjected to solution treatment and stress relief by stretching to ~2% permanent set followed by natural ageing. The nominal chemical composition of 2024-T351 is given in Table 7-1 (ASM, 1979).

Table 7-1 Chemical composition of 2024-T351 (Wt%)

Si	Fe	Cu	Mn	Mg	Cr	Zn	Ti	Others	Al
<0.05	<0.5	3.8-4.9	0.3-0.9	1.2-1.8	<0.1	<0.25	<0.15	<0.05	Bal

The typical mechanical properties of 2024-T351 are listed in Table 7-2 (ASM, 1979).

Table 7-2 Typical mechanical properties of 2024-T351

Name	Unit	Value
Young's modulus for tension	GPa	72.4
Young's modulus for compression	GPa	73.8
Shear modulus	GPa	28
Poisson's ratio		0.33
Tensile stress	MPa	470
Yield stress (0.2% offset)	MPa	325
Elongation to failure	%	20
Density	Mg/m^3	2.77

7.1.2 Welding

The two specimens under study with 2024-T351 aluminium alloy material were welded separately using two newly developed welding techniques: metal inert gas (MIG) welding and variable polarity plasma arc (VPPA) welding, by Cranfield University, UK.

Gas metal arc welding (GMAW) is frequently referred to as metal inert gas (MIG) welding. A large amount of heat is produced when the arc is formed between the electrode and the part. An inert gas or a shielding gas flowing from a gas nozzle surrounds the electrode and protects the molten metal in the weld pool from the adverse influence of oxygen and nitrogen present in the air. This process is one of the most popular welding processes because of its flexible features and minimal cost. The weakness of MIG welding is the relatively large size of the heat source compared with other processes, for example, VPPA, accordingly resulting in poor mechanical properties in the welds (Mendez, 2000). However, it still remains used in less important components, mainly owing to its low cost.

The VPPA welding process was originally designed for space applications and commercialised by Hobart Brothers. The external fuel tank of the space shuttle was one of the early examples for the VPPA technique to weld relatively thick parts of aluminium alloy in the aerospace industry. It has two typical features: variable polarity (VP) and a plasma arc (PA). The concentrated heat of VPPA provides significantly less distortion.

7.2 2D map of longitudinal residual stresses in a MIG 2024-T351 aluminium alloy weld

In this section, a series of investigations using the contour method were performed to determine a cross-sectional longitudinal residual stress in a MIG 2024-T351 aluminium alloy welded plate. The contour method, as stated earlier, consists mainly of four

procedures: specimen cutting, contour measurement, data reduction and finite element analysis, which will be presented in the following context in some detail.

7.2.1 Weld cutting

The specimen at issue was made from 2024-T351 aluminium alloy welded by the MIG technique along the rolling orientation of the parent plate. The "as received" specimen was supplied 187 mm long, 118 mm wide and 12 mm thick, as illustrated in Fig. 7-1. The weld seam, exaggerated dimensionally in Fig. 7-1 for clarity, was located in the middle length (187 mm) of the welded plate. It was featured with two identical longitudinal lips generated by the multipass double-V MIG welding across the width on the both top and bottom surfaces, approximately 14 mm long and 1.2 mm higher outwards the base metal. Angular distortion of the plate, commonly present in welds, was not significantly observed and the surface of the plate was not machined.

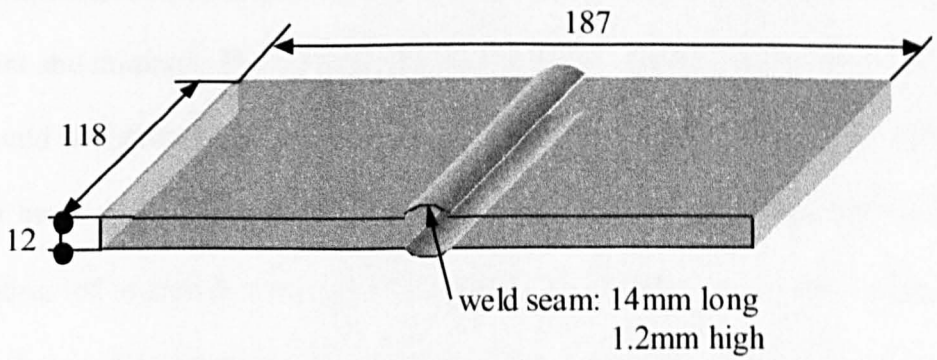

Figure 7-1 Schematic configuration of MIG 2024-T351 weld

The cutting was performed through the thickness progressively along the transverse direction of the weld, across the middle width (118 mm) of the welded plate, as schematically illustrated in Fig. 7-2. It should be recalled that the contour method only enables the stress normal to the cut plane to be evaluated, as described in Chapter 3. Such a

cutting orientation was arranged in order to obtain the longitudinal residual stress in the weld, which is generally considered as the dominant stress in welds.

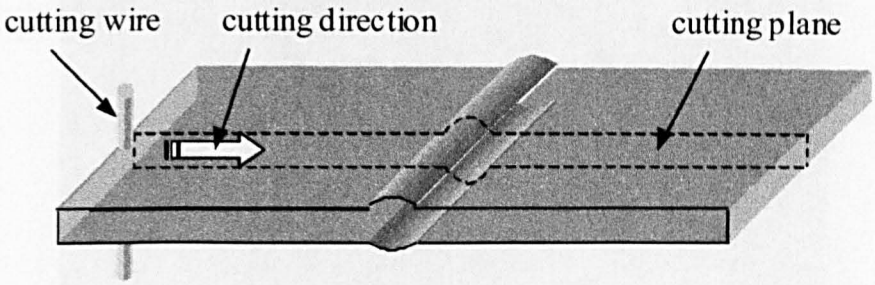

Figure 7-2 Schematic illustration of cutting orientation

A FANUC ROBOCUT wire electric discharge machine located in our department workshop was employed to conduct the cutting. The objective of the cutting is to cut the specimen into half in such a way that the cutting should be straight, and the cut gap should be constant and minimal. The welded plate was tightly clamped by customised jigs on both sides around the cutting path to prevent the plate from movement during cutting. The ϕ0.1 mm brass wire, the smallest size available, was used to section the specimen for minimisation of material removal. The specimen together with the fixing jig was submerged in a circulating deionized liquid tank during the cutting. It took about 50 minutes for the wire EDM to complete the cutting. The wire broke during cutting at about 40 mm distance from the start, and cutting was then restarted from the broken point until the cutting was finished. Fig. 7-3 shows the overall view of wire cutting and clamping of the MIG 2024 weld performed, where one half of the specimen has been removed for a clear view.

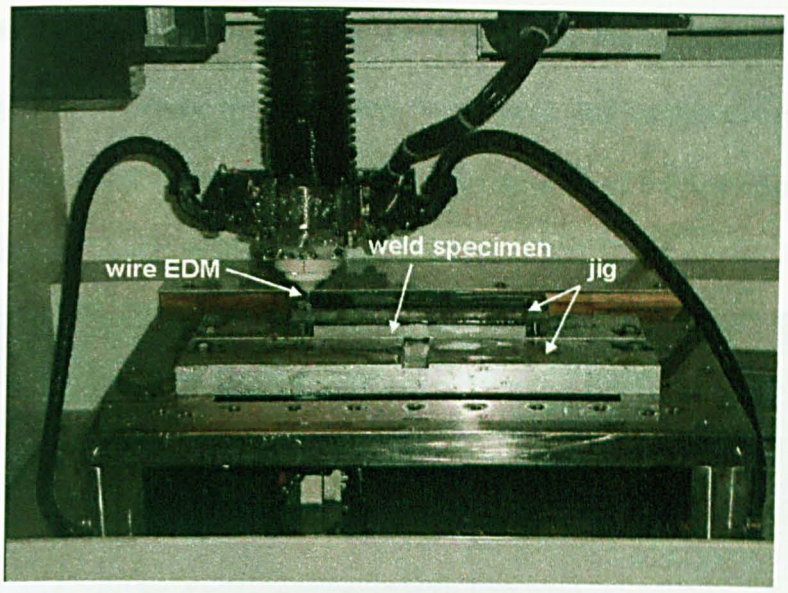

Figure 7-3 Overall view of wire cutting and clamping of the MIG 2024 weld (half the cut specimen was removed)

7.2.2 Contour measurement

After cutting, the residual stress on the cut plane releases, forming a unique shape and thus the cut surface is no longer flat. This unique shape of deformation corresponds to a unique pre-existing residual stress profile. The deformation was experimentally measured using a Mitutoyo Crystal Plus 574 CMM fitted with a 1 mm-diameter Renishaw probe. The thermal compensation system was also activated to record the variation in temperature during measurement and to correct the measurement automatically. The measurement points were designed in such a fashion that 0.5 mm increments along both length (187 mm) and thickness (12 mm) orientations of the cut surface resulted in 375 points in the length and 25 points in the width respectively, with a total of 9,375 points. The contour measurement was repeated in exactly the same manner on the second half of the specimen. Again, the datum plane and datum point referred by each point to be measured can be specified randomly by convenience. It is important to note that the measurement methodology should guarantee each pair of data to be averaged to be measured ideally in a

mirror position, as explained in Chapter 3. In addition, the specimen should be held steadily during measurement to avoid any movement and achieve each point to be measured in a right location. Fig. 7-4 illustrates the scheme of the specimen clamping for CMM measurement, similar to the EN8 plate in Chapter 5.

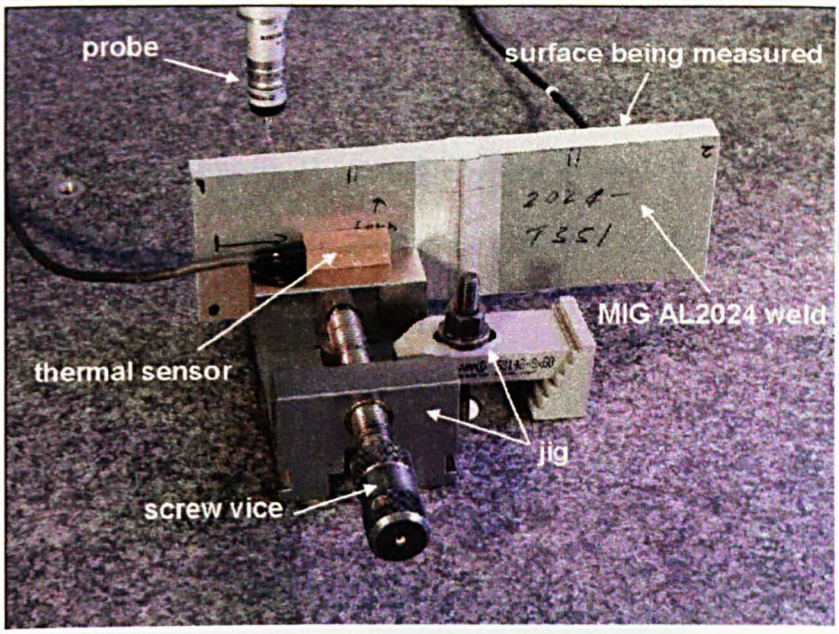

Figure 7-4 Set-up for CMM contour measurement (MIG 2024-T351 weld)

7.2.3 Data reduction

After weld cutting and contour measurement, analysis of the measured data should be conducted, such as averaging the measured displacements for the two corresponding cut surfaces, examination of the overall look of the measured data, or removal of bad data, similar procedures to dealing with the EN8 steel plate and the 7475 aluminium alloy plate. Fig. 7-5 shows the displacement contours measured using the CMM for the left plane, right plane, and average of two planes representative of the cross-sectional displacement on the cut plane. Fig. 7-6 displays the valid data of an averaged, removed and measured contour, which cover from 0.5 mm to 186 mm out of the 187 mm length and from 0.5 mm to 11.5 mm out of the 12 mm thickness. An overall profile of deformation can be globally

observed and reveals very useful information. It can be seen that the measured contour looks smooth even without performing any noise filtering in the measured data, suggesting very good surface finish from the cutting and accurate contour measurement. The lower portion of the shape in the middle indicates the stress field is tensile. Further away from the middle must be the field of a compressive stress, as the whole stress profile on the sectioned surface should be balanced. The peak-to-valley amplitude of the displacement was measured to be approximately 213 μm. It also can be viewed that the place where the wire was broken occurs at around 40 mm away from the cutting-start, as mentioned in Section 7.2.1.

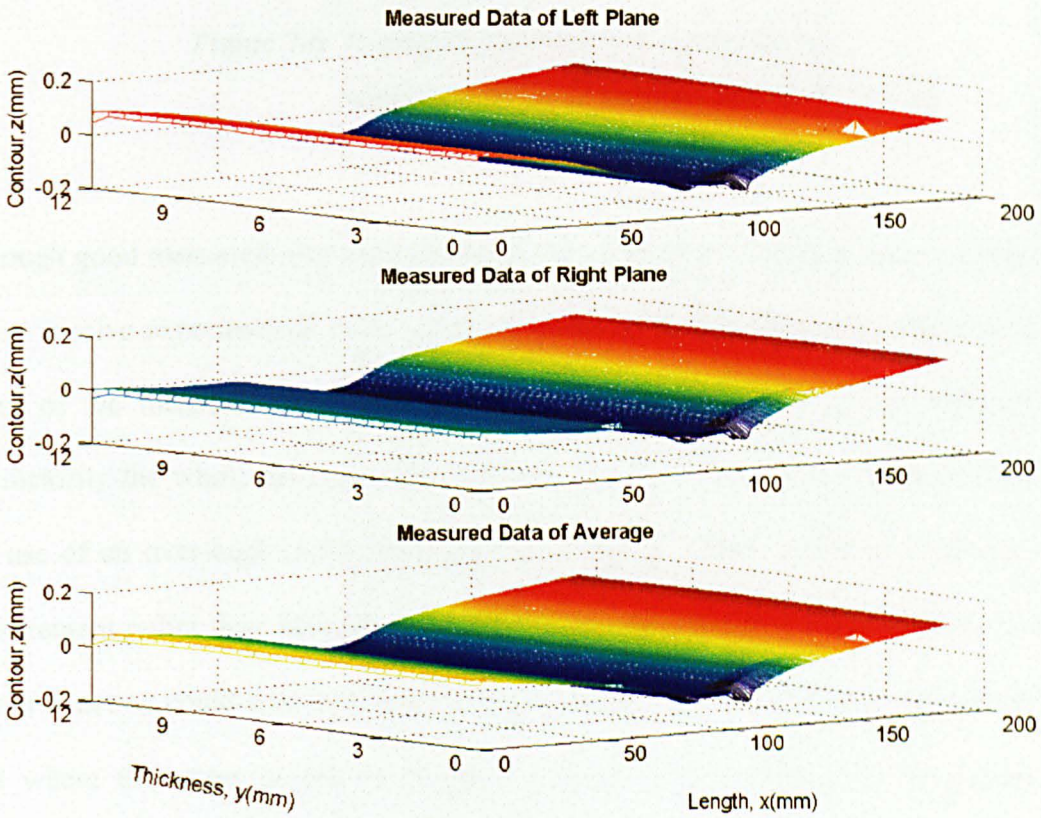

Figure 7-5 Measured data for the left plane (top), right plane (middle) and average of two planes (bottom)

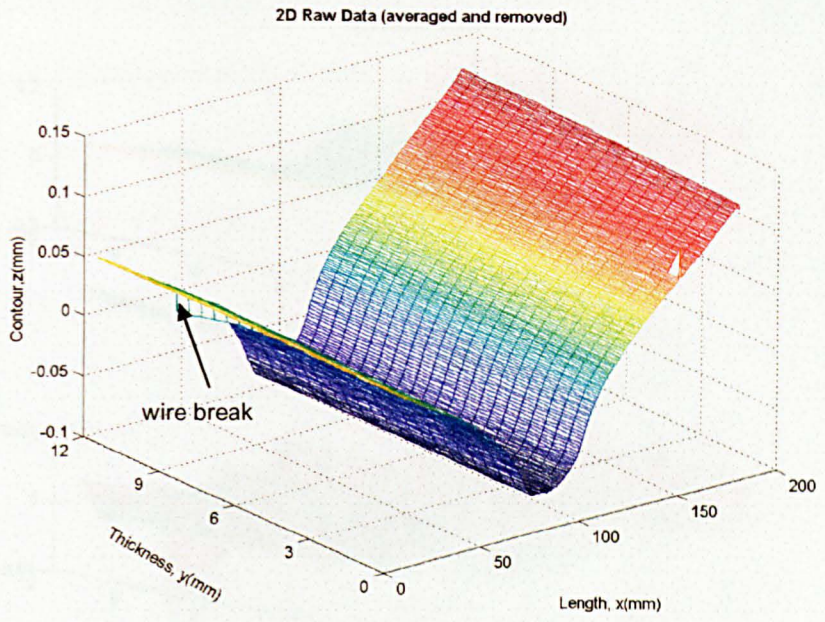

Figure 7-6 Averaged, removed and measured data
with the wire-break location able to be viewed

Although good measured data were obtained, data reduction is still necessary as they more or less involve experimental errors during cutting and measurement. The bivariate Fourier fitting of the measured data was first tried. It was found that it was difficult to fit satisfactorily the whole data by a Fourier function except using an extremely high order. The use of an over-high order, however, may result in fitting the error contained in the measurement rather than filtering it out. On the contrary, use of a comparatively low order Fourier function could lead to a high error, particularly in the vicinity of the middle of the weld where the stress profile is of greatest engineering concern. As an example, the difference or error between the measured data and the smoothed data after bivarite Fourier fitting with an order of 10 shows a strong pattern, especially in the middle part of the weld length. This is illustrated in Fig. 7-7 (bottom) and suggests inappropriate fitting, even though a smooth profile for the surface is achieved as seen in Fig. 7-7 (top).

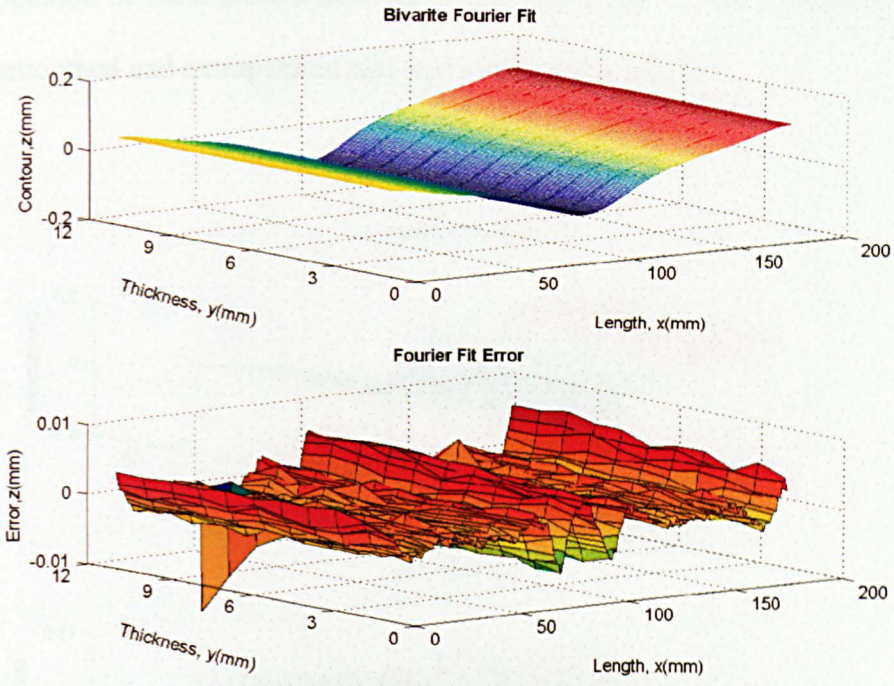

Figure 7-7 Bivariate Fourier fit with order of 10. Top: smoothed contour; bottom: smoothed error with a strong pattern in the middle

It seems that use of a single mathematical function to fit the data in this case is not appropriate. A non-parametric smooth, as mentioned in Chapter 6, may be more suitable since the measured data do not necessarily match a particular mathematical function. The concept of the running average, a non-parametric smooth function, was employed to smooth the measured data, in which the middle value is replaced by the average of the two adjacent data points. This smoothing technique, slightly different from the smoother used for the 7475 plate described in Chapter 6, is intended, in an efficient manner, to filter out the abrupt values arising from cutting faults due to wire breaking. The averaged and smoothed data together with the smoothed error are displayed in Fig. 7-8. The standard deviation of the data smoothing was 0.70 μm. It can be seen from the error plot in Fig. 7-8 (bottom) that the error distributes randomly and has no specific pattern anywhere. It indicates that a good smooth scheme has been applied. The measurement error was 3.08

μm. Extrapolation of the removed data was conducted using a spline function. Finally, the averaged, smoothed and extrapolated data are illustrated in Fig. 7-9.

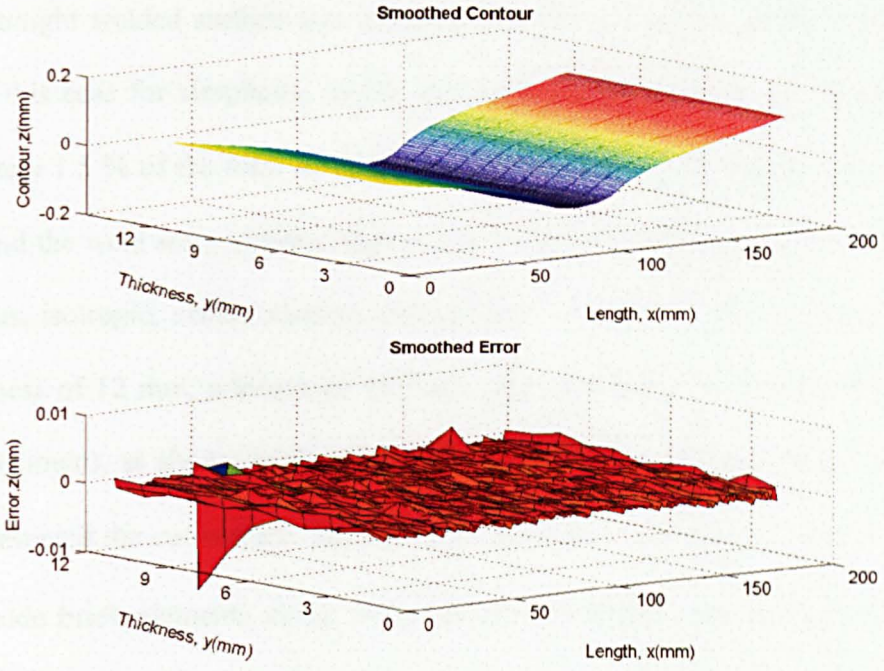

Figure 7-8 Smoothed contour on the top with smoothed error on the bottom

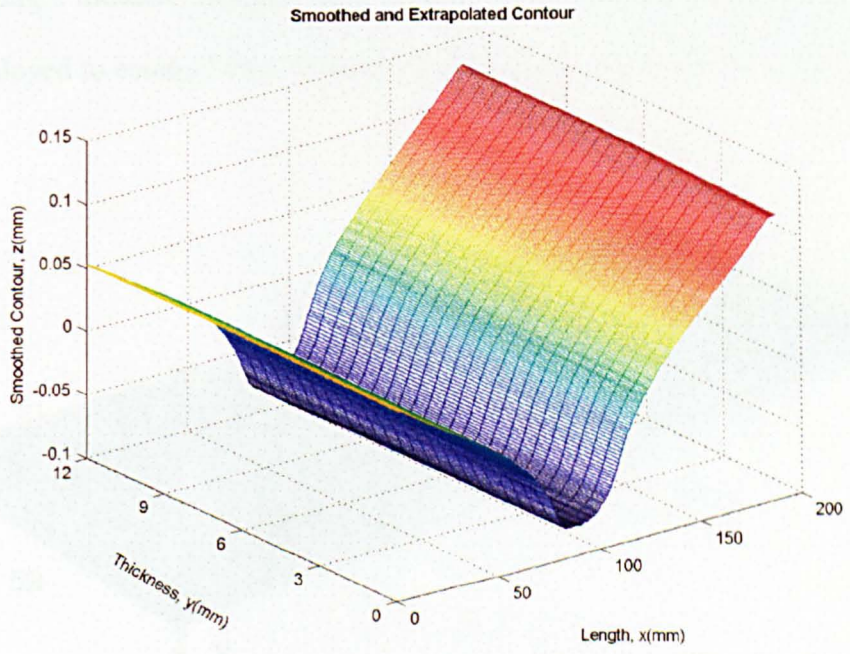

Figure 7-9 Averaged, smoothed and extrapolated contour

7.2.4 Finite element analysis

One of the two cut pieces, which was half the original specimen, was modelled to analyse the residual stress profile on the cut plane of interest based on the measured deformation. A perfectly straight welded surface was assumed. In addition, the lip of the weld seam was ignored in this case for simplicity, as the area of the weld lip was very small, taking up approximately 1.5 % of the total surface under study. This could lead to evaluation of the stress around the weld seam slightly higher. The weld was considered as a single part with homogenous, isotropic, elastic material throughout. The 3D FE model was characterised by a thickness of 12 mm, a length of 187 mm, and a width of 59 mm (half width of the original specimen), as shown in Fig. 7-10. The plane on the XY-axis plane where $z = 0$, which represented the cut surface, was assumed to be flat. A 1 mm × 1 mm mesh scheme having 8-node brick elements along with reduced integration and hourglass control was applied to the model. The averaged, extrapolated and smoothed deformation, regarded as displacement boundary conditions, were carefully arranged to fit the meshed nodes of the cut plane on the FE model. The elastic constants of the Al2024-T351 material were 72.4 GPa for Young's modulus and 0.33 for Poisson's ratio as given in Table 7-2. ABAQUS 6.3 was employed to conduct the geometry modelling and the linear FE solution.

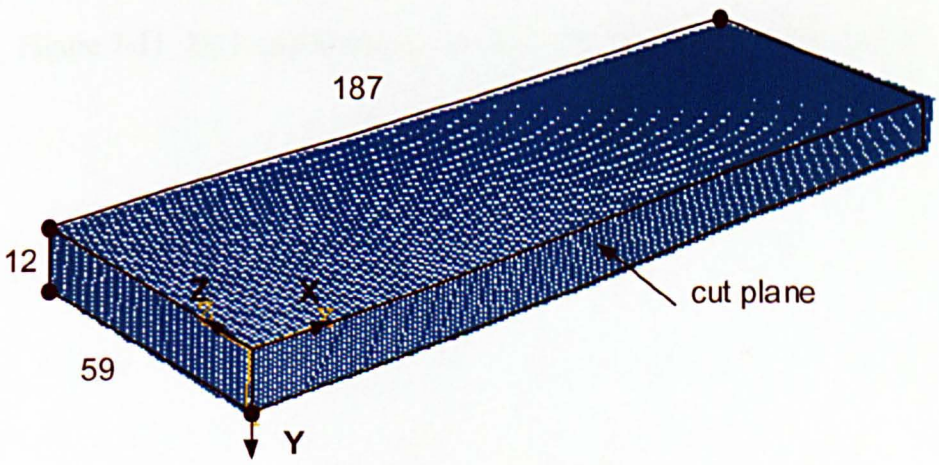

Figure 7-10 Meshed FE model used in the contour method

7.2.5 Results and discussion

A longitudinal residual stress profile through the thickness of the MIG 2024-T351 aluminium alloy welded plate was obtained using the contour method as shown in Fig. 7-11, in which the thickness of the plate is magnified by 2 for clear illustration. A typical stress distribution for the weld is illustrated. Tensile stresses are in the middle portion of the weld, where the heat affected zone and fusion zone are dominant, and further away from the middle are compressive stresses. The maximum tensile stress reaches 175 MPa and the highest compressive stress is 72 MPa. A double-V shaped profile of the longitudinal stress in the middle area of the weld was measured, as shown in Fig. 7-11. A line plot of the longitudinal residual stresses at multiple specified thickness locations in the weld is depicted in Fig. 7-12 for more detailed examination.

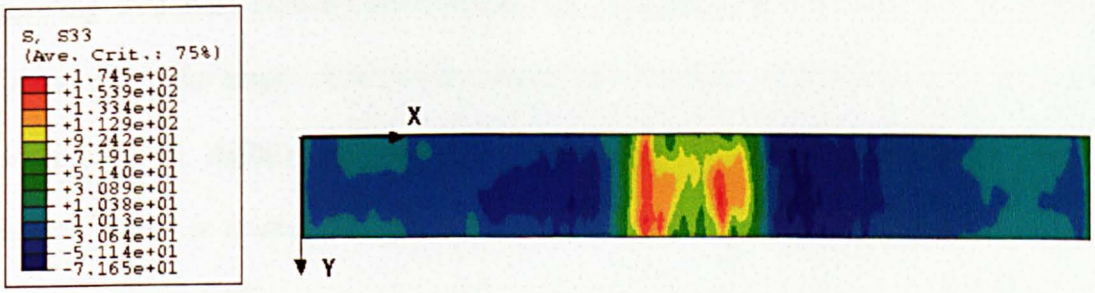

Figure 7-11 2D longitudinal stress map of MIG weld (x = 187 mm, y = 12 mm)

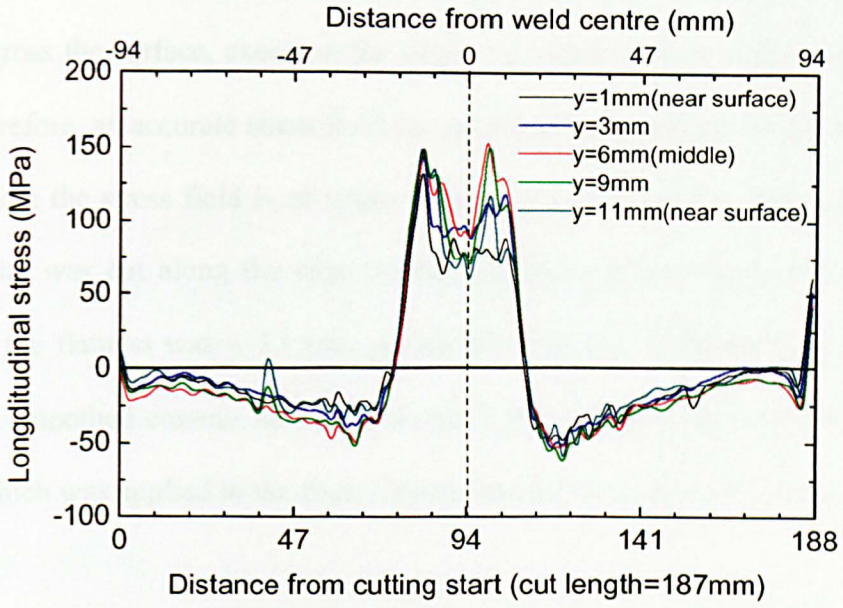

Figure 7-12 Line plot of 2D longitudinal residual stress profile at specified thicknesses through the MIG weld

As can be seen in Fig. 7-12, the longitudinal stress profile varies slightly across-thickness, suggesting an almost uniform distribution of through-thickness stresses. On the contrary, the stress along the length of the weld changes substantially, and presents a double-peaked stress profile. A slightly unsymmetrical stress distribution around the weld centre is indicated. There is overall balance between the tension and the compression across the sectional surface as this is the consequence of conditions imposed on the FE model. The tensile stresses through-section converge almost at the location 74 mm and at 110 mm from the left edge respectively. Further away from the middle area of between 74 mm and 110 mm are the compressive stresses that gradually approach zero in the vicinity of both edges. A sharp change in stress at the two edges, particularly at the right edge, is found. This is primarily attributed to the cutting error at edges and the extrapolation of the removed data at the edges. Nevertheless, it can be seen that the influence is only local, about 3 mm long at both edges, a similar finding to the specimen of hole cold expansion. In addition, the stress in the neighbourhood of the edge is generally small and far from the region of engineering interest. The welded plate has a constant thickness and continuous

material throughout the cutting. This feature benefits wire EDM to produce a good quality of cutting across the surface, except at the edges for around 3 mm at the cutting start and the end. Therefore, an accurate stress field can be achieved especially in the middle part of the weld where the stress field is of major interest. To examine a cutting flatness, 1 mm sliced material was cut along the edge of the specimen. It was found that the standard deviation of the flatness was ~ 3.1 μm, giving the error of ~ 20 MPa in stress evaluated based on the smoothed contour measured on the 1 mm slice cut from the free edge of the specimen, which was applied to the finite element model to calculate the stress.

The variation in the magnitude of the tensile stress is significant and the detail of the variation around the weld centre is plotted in Fig. 7-13. It is found that the tensile stress in the middle thickness is slightly higher than the tensile stress close to the surface. In addition, the stress in the weld centre, where the fusion zone is dominant, is lower than the stress in its neighbouring region.

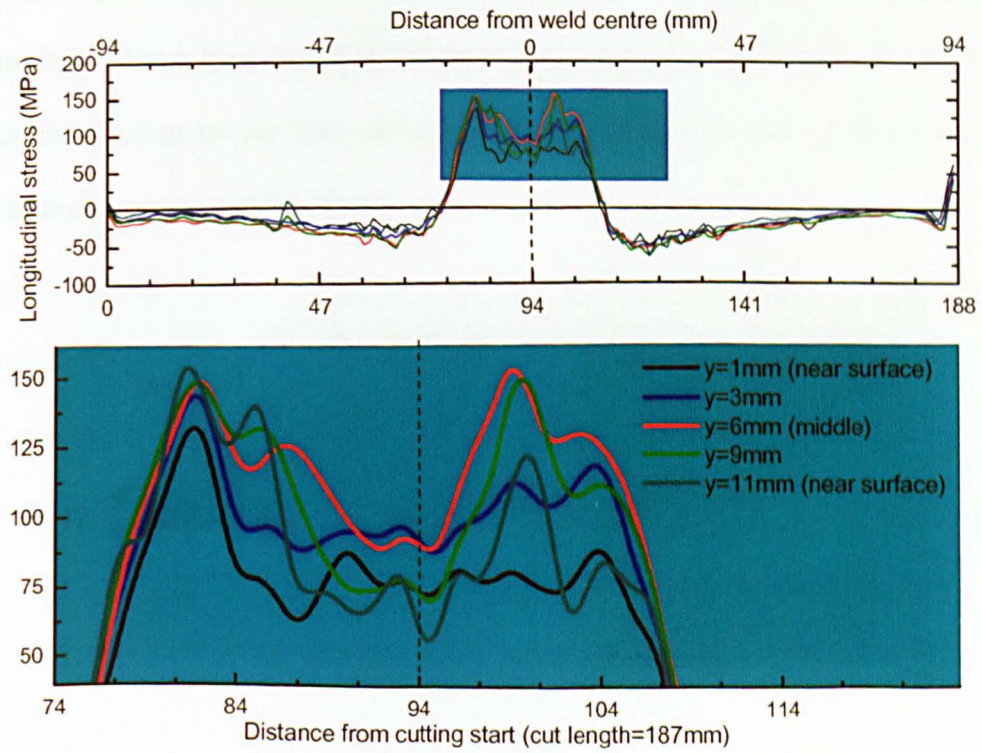

Figure 7-13 Detail of stress profile around the weld centre

7.3 2D map of longitudinal residual stresses in a VPPA 2024-T351 aluminium alloy weld

In this section, the contour method will be applied to measure a longitudinal cross-sectional residual stress field in a VPPA 2024-T351 aluminium alloy welded plate. The result is then compared with the data measured non-destructively on the same specimen by neutron and synchrotron X-ray diffraction.

7.3.1 Weld cutting

The specimen under study was made from 2024-T351 aluminium alloy welded by the VPPA technique along the rolling orientation of the parent plate. The "as received" specimen was supplied 278 mm long, 240 mm wide and 12 mm thick, as illustrated in Fig. 7-14. The weld seam, exaggerated dimensionally in Fig. 7-14 for clarity, was located in the middle length (278 mm) of the welded plate. It was featured with two slightly different longitudinal lips induced by the VPPA welding across the width on the surfaces, approximately 14 mm long on the top surface, 8 mm long on the bottom, and 1 mm higher outwards the base metal for both surfaces. Angular distortion was not observed and the surface of the plate was not machined.

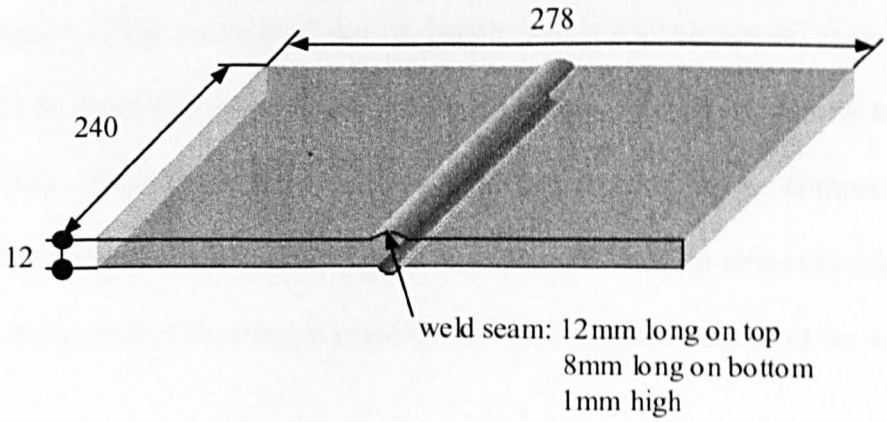

Figure 7-14 Schematic configuration of the VPPA 2024-T351 weld

The cutting was performed through the thickness along the transverse direction of the welding, across the middle width (240 mm) of the welded plate, as illustrated in Fig. 7-15.

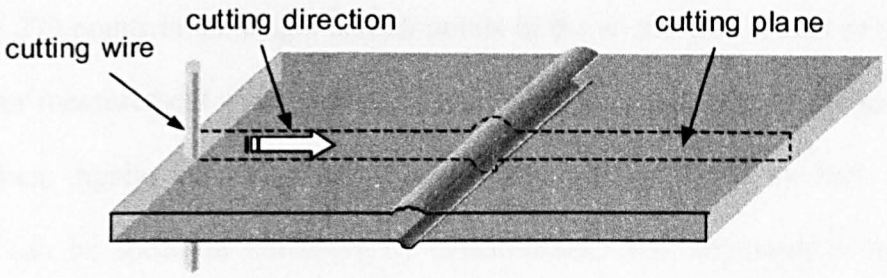

Figure 7-15 Schematic illustration of wire EDM cutting orientation

The ϕ0.1 mm brass wire was used to section the specimen for minimisation of material removal. It took about 2 h for the wire EDM to complete the cutting. The wire broke during cutting at about 195 mm distance from the start. The cutting could not continue from the stopped location because the cut gap was closed due to the relief of the compressive stress there. A second cut had to be started from the opposite side, and unfortunately the wire broke again in the vicinity of the first break point. A third cut was repeated from the opposite edge with great care. However, the third cut still could not cut off the remainder of the material, 2 mm in length, which was broken off manually in the end. It should be noted that such a third cut is not advisable because it is likely to re-cut the surface that was already exposed by the second cutting. In addition, the compressive stress field at that area increases the possibility of re-cutting the surface since the release of the compressive stress makes the cut gap possibly smaller than the diameter of the wire.

7.3.2 Contour measurement

The measurement points were designed in such a fashion that a 1 mm increment along the length (278 mm) and a 0.5 mm increment along the thickness (12 mm) of the cut surface resulted in 279 points in the length and 25 points in the width, with a total of 6,975 points. The contour measurement was repeated in exactly the same manner on the second half of the specimen. Again, the datum plane and datum point referred by each point to be measured can be specified randomly by convenience. It is important to note that the measurement methodology should guarantee each pair of data to be averaged to be measured ideally in a mirror position, as explained in Chapter 3. In addition, the specimen should be held steadily during measurement to avoid any movement and achieve each point to be measured in the right location. Fig. 7-16 illustrates the scheme of the specimen clamping for CMM measurement, similar to the previously presented specimens.

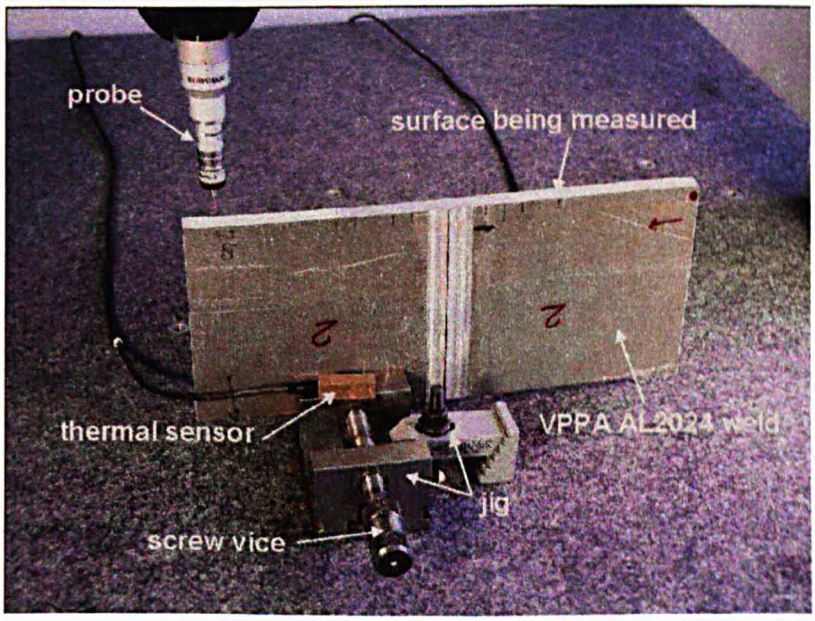

Figure 7-16 Set-up for CMM contour measurement (VPPA 2024-T351 weld)

7.3.3 Data reduction

Fig. 7-17 shows the displacement contours measured by the CMM for the left plane (top), right plane (middle) and average of two planes (bottom). Fig. 7-18 displays the detail of

the averaged and measured contour representative of the cross-sectional deformation on the cut plane. An overall profile of deformation can be observed. In particular, unusually high peaks are clearly observed and indicate the presence of the uncut material, approximately 2 mm long. It also shows the area with abnormally low values where the CMM probe has fallen out of the surface, at the edges. This is because the weld edge is not perfectly straight, and slight angular distortions caused by the welding and small variations in plate thickness are present. Those data are not true and should be deleted from the measured data. Fig. 7-19 displays the averaged, removed and measured data or the valid data, which include the length from 0 mm to 277 mm out of the 278 mm and the thickness from 0.5 mm to 11 mm out of the 12 mm. The overall shape is very similar to the displacement profile of the MIG 2024-T351 weld shown in Fig. 7-6, but not as smooth as the surface of the MIG weld, in particular on the far right of the weld. This is almost certainly due to the repeated cutting on that area, as stated in Section 7.3.1. Detailed observation of Fig. 7-19 after removal of obvious bad data confirms that the third cutting indeed re-cuts the surface that was already cut by the second. This can be viewed from the sudden shallow area about 30 mm long adjacent to the location where the surface was not cut. These data, however, were not deleted because the amount of the material removed by the repeat cutting is not substantial and will not affect the result elsewhere too much, only locally, as demonstrated in Section 3.3.1. In addition, extrapolation of the deleted data is dangerous, and sometimes it is out of control. So, the stress derived in the range of 192 mm to 278 mm from the left edge, about 86 mm long, is unreliable because of the repeated cutting. Again, the lower portion of the shape in the middle suggests a tensile stress field. Further away from the middle must be a field of compressive stress, as the whole stress profile on the sectioned surface should be balanced. The peak-to-valley amplitude of the displacement was measured to be approximately 185 μm.

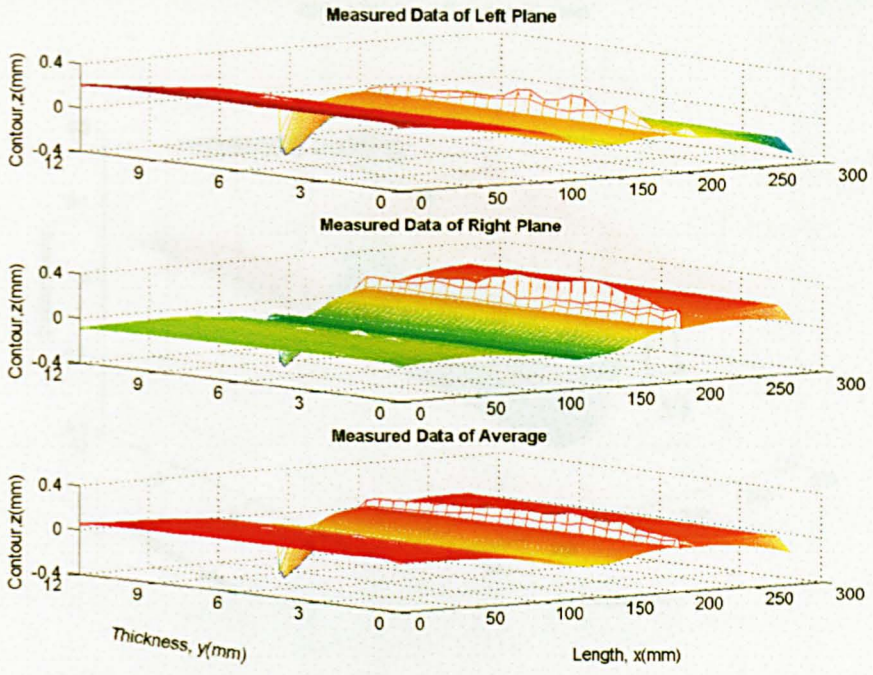

Figure 7-17 Measured data for the left plane (top), right plane (middle) and average of two planes (bottom)

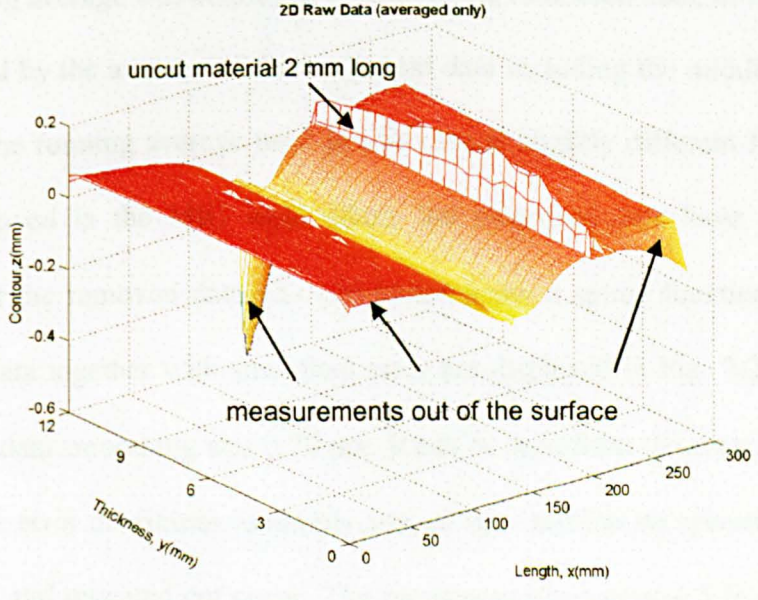

Figure 7-18 Detail of the averaged and measured contour, showing the uncut surface 2 mm long and the measurement out of the surface

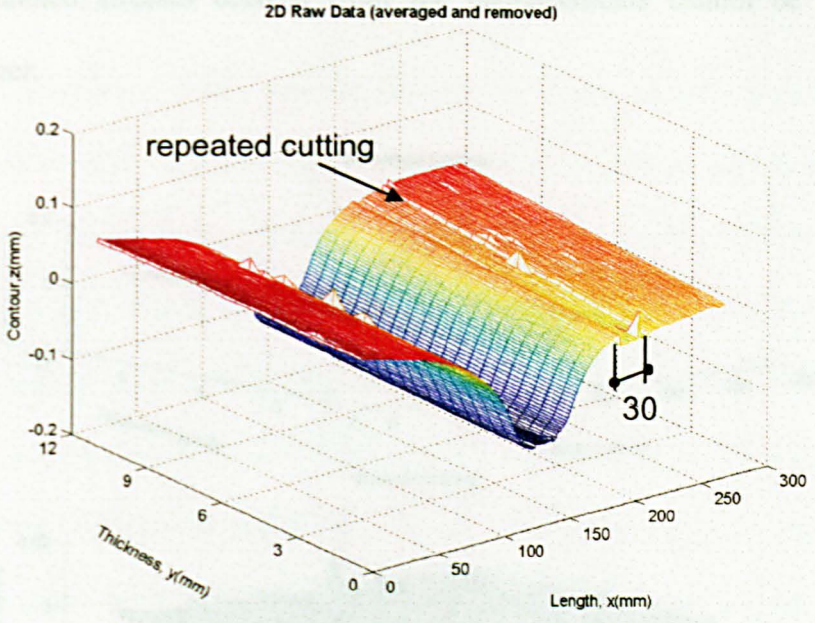

Figure 7-19 Averaged, removed and measured data: the repeated cutting can be clearly viewed from the shallow area 30 mm long

Data smoothing was performed on the valid data after the removal of the obviously false data. The running average was employed to smooth the measured data, in which the middle value is replaced by the average of three adjacent data including the middle value, as used in Chapter 6. The running average used in this case is slightly different from the smooth technique employed in the MIG weld where the measured data have abrupt changes. Extrapolation of the removed data was conducted using a spline function. The averaged and smoothed data together with smoothed error are displayed in Fig. 7-20. The standard deviation of the data smoothing was 0.70 μm. It can be seen from the error plot in Fig. 7-20 (bottom) that the error distributes randomly around zero and has no specific pattern except where the uncut and repeated cut occur. The measurement error was 3.26 μm. Finally, the averaged, smoothed and extrapolated data are illustrated in Fig. 7-21. The area of the repeated cutting still can be observed though it becomes less significant after smoothing. So use of the running average cannot completely get rid of the adverse influence arising from the cutting faults. However, the displacements around that area are not correct and

thus the calculated stresses derived from the displacements cannot be relied on, as discussed earlier.

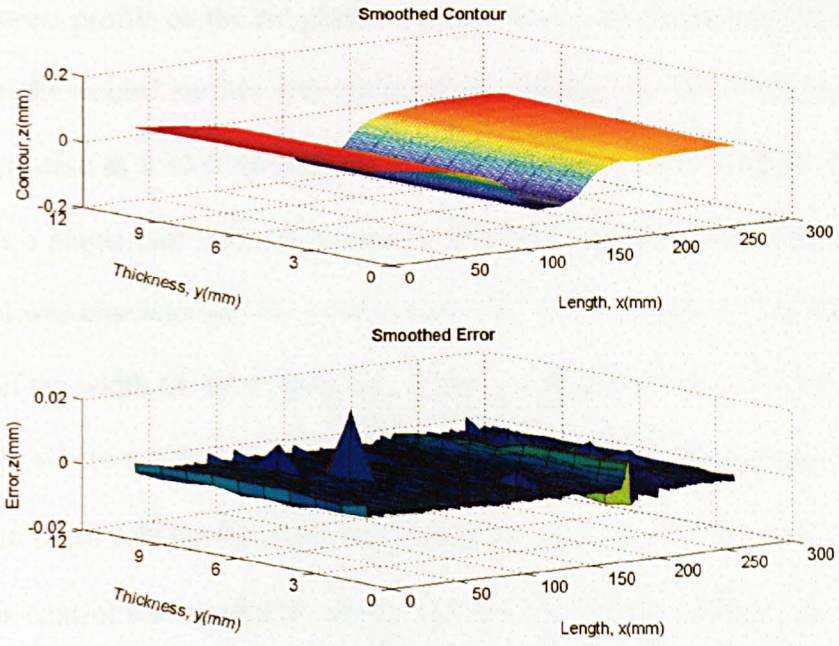

Figure 7-20 Smoothed contour (top) and smoothed error (bottom)

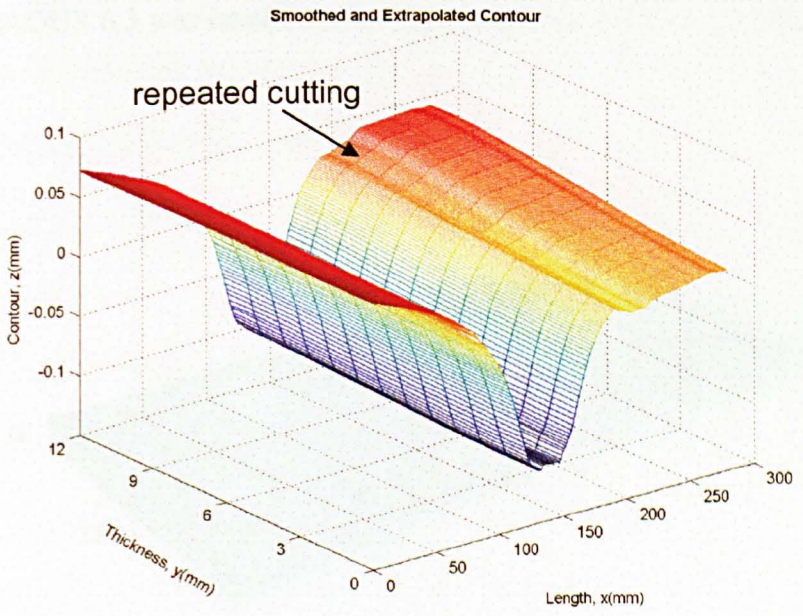

Figure 7-21 Averaged, extrapolated and smoothed contour: the repeated cutting still can be observed.

7.3.4 Finite element analysis and results

One of the two cut pieces, which was half the original specimen, was modelled to analyze the residual stress profile on the cut plane of interest based on the measured deformation. A perfectly straight welded surface was assumed. In addition, the lip of the weld seam was ignored in this case as it took up only 0.5% of the total area to be studied. The weld was considered as a single part with homogenous, isotropic, elastic material throughout. The 3D FE model was characterised by a thickness of 12 mm, a length of 278 mm, a width of 120 mm (half the width of the original specimen), as shown in Fig. 7-22. The plane on the XY-axis plane where $z = 0$, which represented the cut surface, was assumed to be flat. A 1 mm × 1 mm mesh scheme having 8-node brick elements along with reduced integration and hourglass control was applied to the model. The averaged, extrapolated and smoothed deformation, regarded as displacement boundary conditions, were carefully arranged to fit the meshed nodes of the cut plane on the FE model. The elastic constants of the Al2024-T351 material were 72.4 GPa for Young's modulus and 0.33 for Poisson's ratio as given in Table 7-2. ABAQUS 6.3 was employed to conduct the geometry modelling and the linear FE solution.

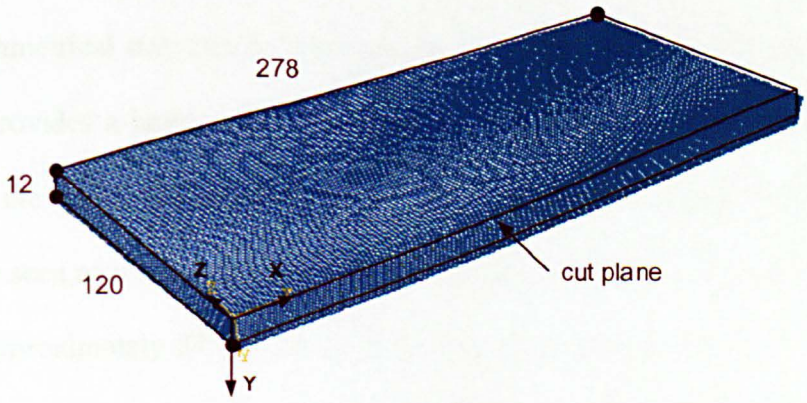

Figure 7-22 Meshed FE model of VPPA 2024 weld

A longitudinal residual stress through the thickness of the VPPA 2024-T351 aluminium alloy welded plate was obtained using the contour method as shown in Fig. 7-23, in which the thickness of the plate is magnified by 2 for clarity. A typical stress distribution for the weld is illustrated. Tensile stresses are in the middle portion of the weld, where the heat affected zone and fusion zone are dominant, and further away from the middle are compressive stresses. The maximum tensile stress reaches 193 MPa and the highest compressive stress is 135 MPa. The stress field varies significantly along the length of the plate and much less significantly through the thickness of the plate. A line plot of the longitudinal residual stresses at multiple specified thickness locations in the weld is depicted in Fig. 7-24 and offers more detail.

As can be seen in Fig. 7-24, the overall profile of the longitudinal residual stress across the thickness of the weld is similar to the stress distribution in the MIG weld displayed in Fig. 7-12. It should be noted that the stress profile on the far right of the weld 192 mm from the cut start or 53 mm from the weld centre onwards cannot be relied on due to the cutting error, shown in the shading area. It is found from Fig. 7-24 that the longitudinal stress profile keeps almost uniform through-thickness. On the contrary, the stress along the length of the weld changes substantially, and presents a mult-peaked stress profile. A slightly unsymmetrical stress distribution around the weld centre is indicated. The left half of the weld provides a larger area of tension but a smaller area of compression than the right half of the weld. Overall balance between tension and compression through the section can be seen as it is the consequence of the FE modelling. The tensile stresses are in the middle, approximately 27 mm away from the weld centre, and vary sharply. Further away from the middle area, at about 54 mm width, are the compressive stresses that gradually approach zero in the vicinity of both edges. The details of the variation in the tensile longitudinal stress around the weld centre are plotted in Fig. 7-25. It is found that

the tensile stress in the weld centre, which is the fusion zone of the welding, is slightly lower than the tensile stress away from the centre.

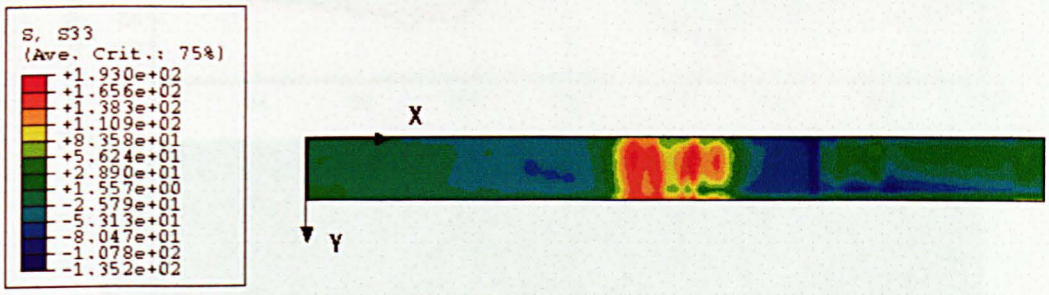

Figure 7-23 2D longitudinal stress map of VPPA weld (x = 278 mm, y = 12 mm)

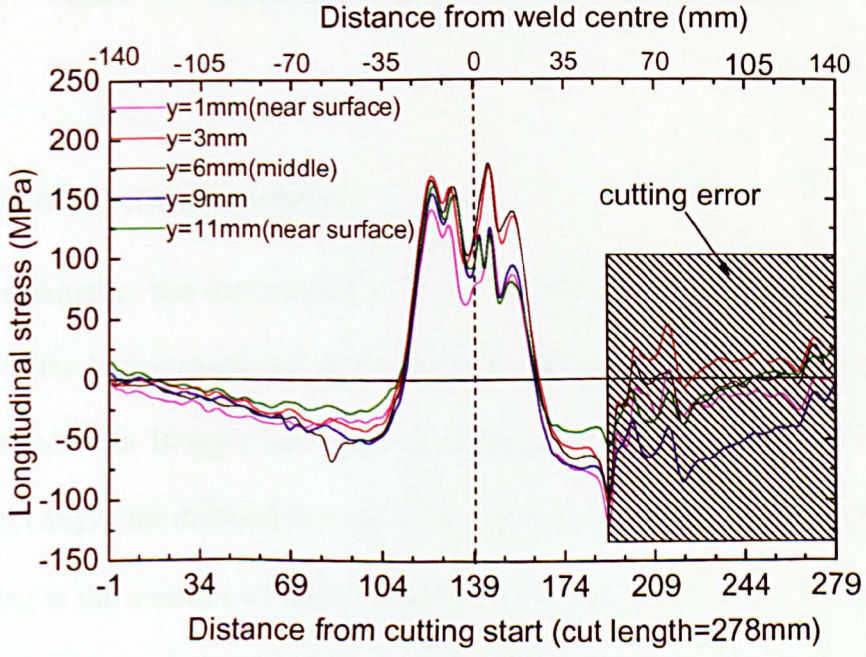

Figure 7-24 Line plot of longitudinal residual stress profile at specified thicknesses through the VPPA weld

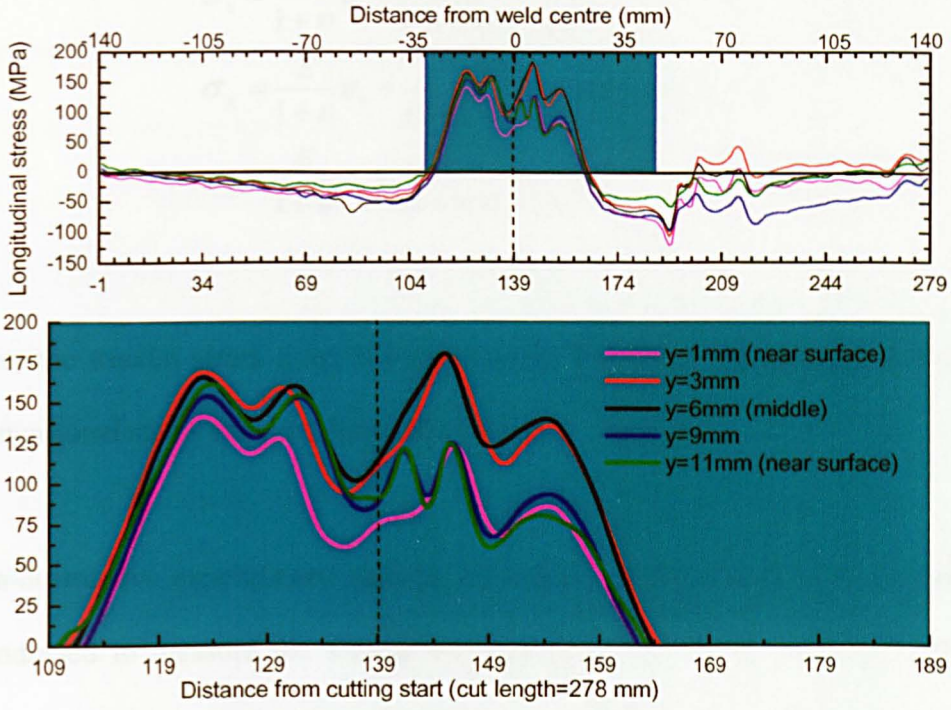

Figure 7-25 Detail of stress profile around the weld centre

7.3.5 Diffraction measurement

Diffraction techniques use the crystalline lattice of material as a strain gauge, and detect the change of the lattice spacing (d) of a particular diffraction plane. The residual elastic strain is derived from Bragg's law where the change in the lattice spacing is associated with the shift ($\Delta\theta$) of the diffraction peak. It is a widely accepted fact that the change of the lattice spacing is the measure of the residual elastic strain, rather than the total strain that may contain the plastic strain, and the plastic strain does not contribute any change in the lattice spacing. It had been demonstrated that the residual elastic strain is uniquely related to the residual stress independent of the residual plastic strain (Hills, 2002). The residual stress is then inferred from the measured elastic strain through Hooke's law as follows:

$$\sigma_x = \frac{E}{1+\upsilon}\varepsilon_x + \frac{\upsilon E}{(1+\upsilon)(1-2\upsilon)}(\varepsilon_x + \varepsilon_y + \varepsilon_z)$$
$$\sigma_y = \frac{E}{1+\upsilon}\varepsilon_y + \frac{\upsilon E}{(1+\upsilon)(1-2\upsilon)}(\varepsilon_x + \varepsilon_y + \varepsilon_z) \qquad (7.1)$$
$$\sigma_z = \frac{E}{1+\upsilon}\varepsilon_z + \frac{\upsilon E}{(1+\upsilon)(1-2\upsilon)}(\varepsilon_x + \varepsilon_y + \varepsilon_z)$$

Therefore, the triaxial stress state in materials can be readily determined as long as the three-dimensional stains are experimentally available.

Two non-destructive experiments, neutron diffraction and synchrotron X-ray diffraction, were conducted to measure the triaxial residual stress profile in the VPPA 2024-T351 aluminium alloy weld at the ILL (Institut Laue-Langevin), and the ESRF (European Synchrotron Radiation Facility), Grenoble, France, respectively.

Neutron diffraction

The neutron diffraction measurement, with a wavelength of 1.911 Å, was conducted to obtain the triaxial residual stress profile in the VPPA 2024 weld at the ILL, Grenoble, France. The lattice spacing of the {311} plane at a diffraction angle 103° (2θ) was measured for both the weld specimen and a reference comb sample since the {311} family of planes is most representative of the bulk material (Daymond et al., 1997). The triaxial strains were calculated from the lattice spacings measured in three directions after correction according to the measurements on the stress free comb sample. The triaxial stresses were then inferred from the measured triaxial strains based on the Hooke's law in Equation (7.1). The detailed measurement and data analysis are referred to elsewhere (Edwards et al., 2003a), as they are out of the scope of the present work.

Synchrotron X-ray diffraction measurement

Synchrotron X-ray diffraction has been gaining rapid development and application as a cost-effective method due to its quick acquisition of data. The use of intense beams of high energy X-rays permits penetration depths approaching centimetres in vast majority of engineering materials (Withers et al., 2002). However, difficulty in the measurement of strains normal to the plate surface arises due to the low scattering angles (≤14°) as a consequence of the use of high energy synchrotron X-rays (Stelmukh et al., 2002; Withers et al., 2002). As a result, strains were measured along longitudinal and transverse directions only of the welded specimen. The experiment, with a wavelength of 0.275 Å (45 KeV), was conducted on the VPPA 2024 weld using the BM16 diffractometer at the ESRF, Grenoble, France. The same specimen was also measured using the pulsed neutron source at ISIS, Didcot, UK, for the transverse and normal strain directions. The transverse strain measured by pulsed neutrons was in good agreement with the result measured by synchrotron X-rays despite the difference in the gauge volume and reflection geometry. Finally, the triaxial stresses were inferred from the longitudinal and transverse strains measured at ESRF and the normal strain measured at ISIS based on the Hooke's law in Equation (7.1). The more detailed measurement and data analysis should be referred to the technique report elsewhere (Edwards et al., 2003b), as they are out of the scope of the present work.

7.3.6 Discussion

The longitudinal stress field obtained from the contour method is compared with the outcomes measured by neutron and synchrotron X-rays at three specified depths of thickness, as depicted from Fig. 26 through to Fig. 31. As the contour method is substantially different in principle from the diffraction method, it is interesting to know how close or different the results that they measure are. The comparison is obviously

useful for validation of the contour method. In turn, the contour method offers an additional opportunity for confirmation of the results, particularly in welds that continuously challenge the reliability and accuracy of the diffraction measurement techniques due to the difficulties commonly present in welds such as large grain size, composition inhomogeneity and texture preference.

The three techniques sample the stress field on different scales. The contour method calculates the stress field in accordance with the mesh of $1 \times 1 \times 1$ mm^3 applied in the FE model. The neutron diffraction measurements average over $2 \times 2 \times 1$ mm^3 for the longitudinal strain, and over $2 \times 10 \times 1$ mm^3 for the normal and transverse strains. The synchrotron X-ray average the measurements over $0.5 \times 2 \times 3.8$ mm^3 for each direction. Moreover, the three techniques offer results in different detail. The contour method provides complete 2D information across entire surface of the thickness (12 mm thick × 278 mm long). By contrast, the neutron and the synchrotron X-ray methods offer data only at a specified depth of thickness (3 mm, 6 mm and 9 mm) within a limited length (100 mm long) as the exceedingly high cost of beam time needed makes measurement of the whole surface impractical. On the other hand, the neutron and synchrotron X-ray diffraction methods are able to measure triaxial stresses, while the contour method normally determines one-direction stress with one cut.

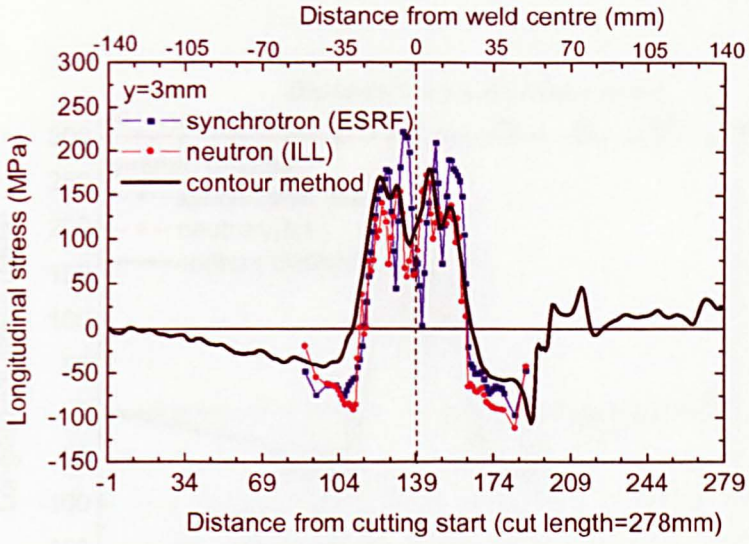

Figure 7-26 Comparison among the three techniques at y = 3 mm

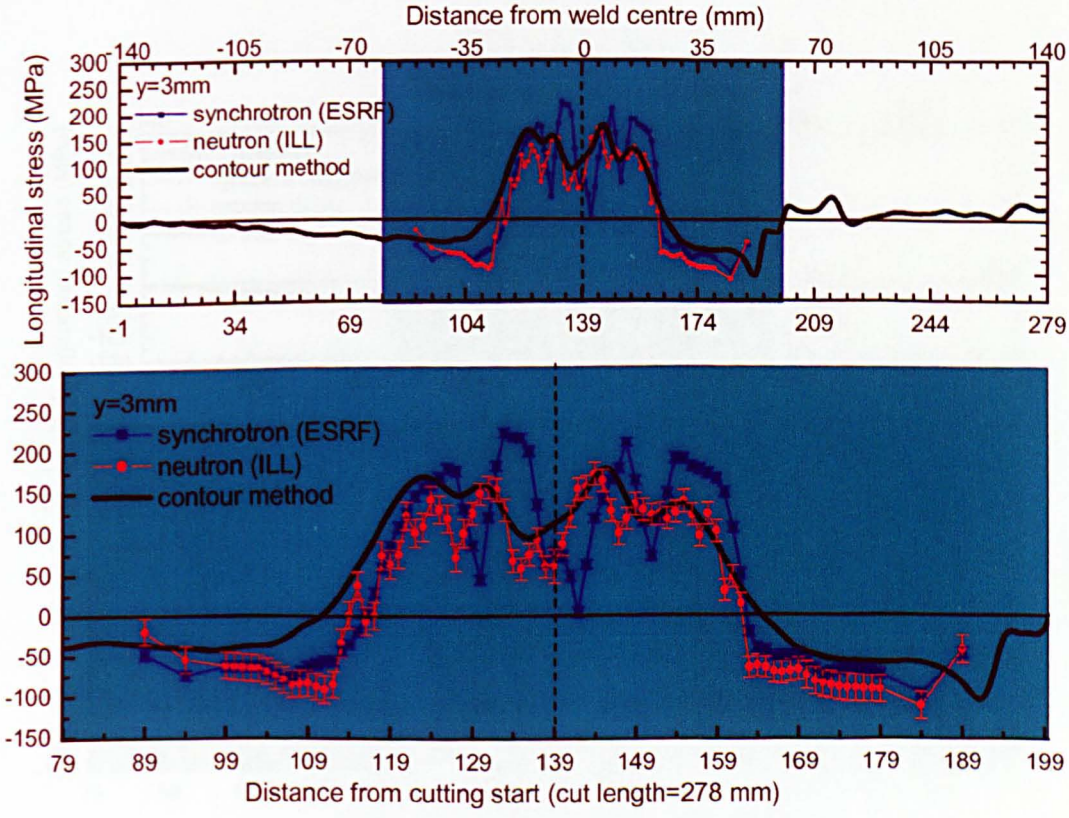

Figure 7-27 Detail of comparison at y = 3 mm

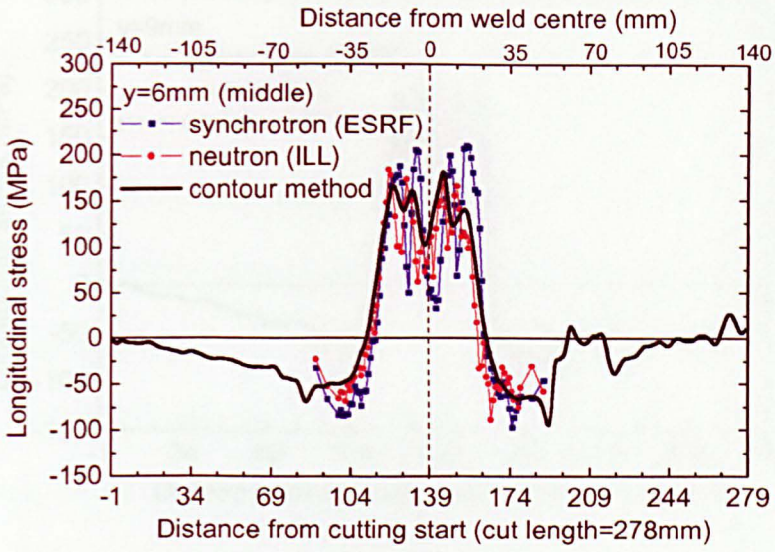

Figure 7-28 Comparison among the three techniques at y = 6 mm in the middle thickness

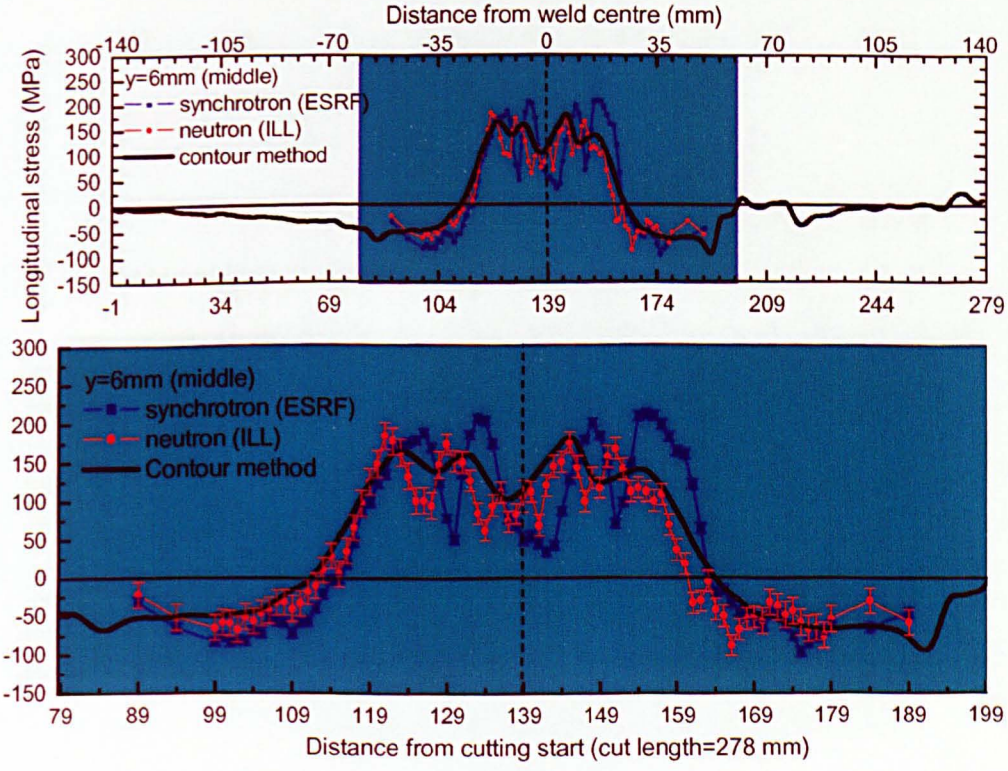

Figure 7-29 Detail of comparison at y = 6 mm in the middle thickness

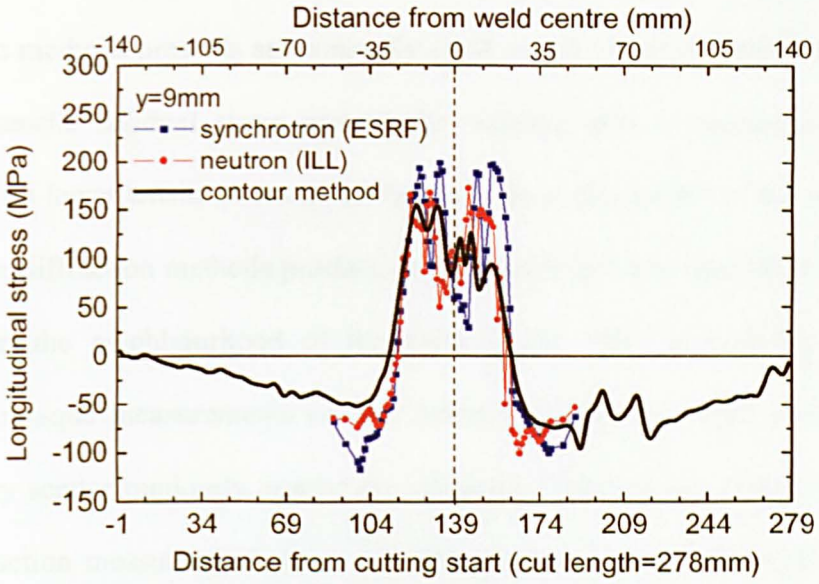

Figure 7-30 Comparison among the three techniques at y = 9 mm

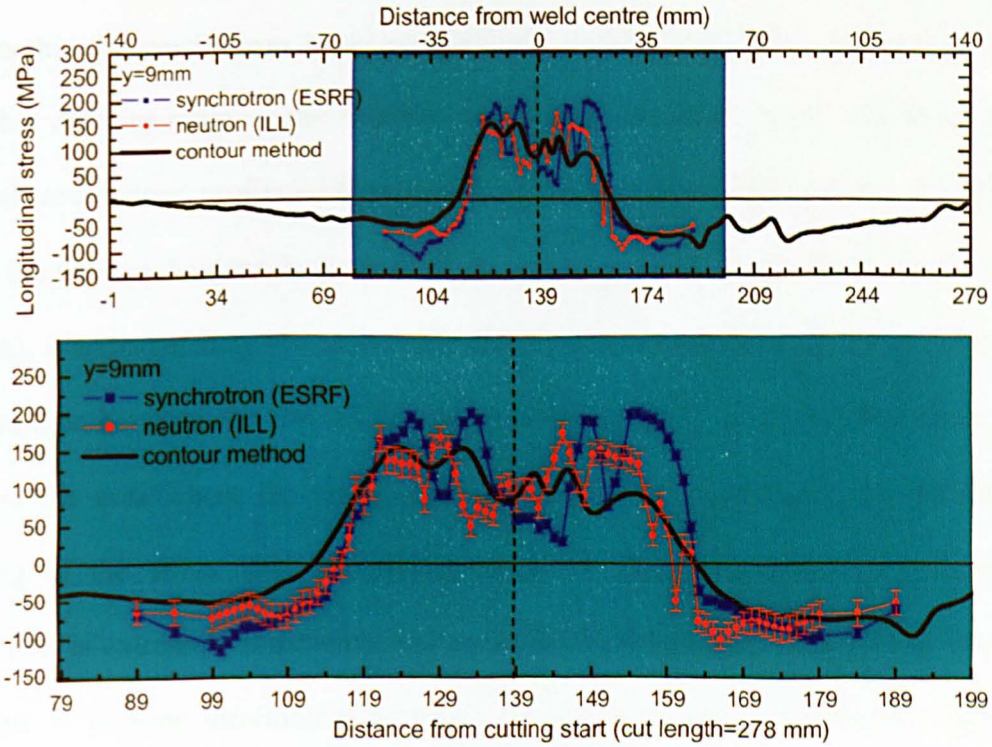

Figure 7-31 Detail of comparison at y = 9 mm

As can be seen in Fig. 7-26 through to Fig. 7-31, the comparison of the results measured from the three methods presents an extremely good match. A multi-peaked distribution of longitudinal tensile residual stress around the welding area is measured by all three techniques, with lower tensile stress in the fusion zone at the middle of the weld. It is also shown that the diffraction methods produce more scattered results than the contour method particularly in the neighbourhood of the weld centre. This is probably because the diffraction technique measurements contain interplanar stresses which add to the noise. However, they scatter randomly around the contour-method measurement. The averaged error of diffraction measurements was ~15 MPa (Edwards et al., 2003a; Edwards et al., 2003b) ; whereas the cutting-induced error of the VPPA weld was ~20 MPa in the contour method based on the 1 mm slice cut from the free edge of the specimen. In compassion to the contour-method measured data, neutron diffraction underestimates the stress about 22 MPa with a standard deviation of about 30 MPa; whereas synchrotron X-ray diffraction overestimates it by around 10 MPa with a standard deviation of 49 MPa. The analysis also suggests that the synchrotron X-ray measurement is slightly closer to the contour-method result, but contains more scatter than the neutron measurement. In the middle area of the weld, where the stress profile is of greatest engineering interest, for example, the difference among the three techniques in the area of 40 mm in the weld centre (between 119 mm to 159 mm), is approximately 9% on average, and the contour-method measurement is almost in the middle between the two diffraction measurements. In addition, divergence is also found in the area where the compressive stresses exist. Apparently, the difference in sampling of the stress field contributes partly to this divergence. Nevertheless, the comparison is extremely impressive and indicates that the contour method is a powerful technique to provide information accurate enough to be used reliably for engineering analysis.

7.4 Conclusion

The potential of the contour method had been demonstrated on two welded plates to determine a full 2D map of longitudinal stress profile across thickness. The result of the VPPA weld is compared with measurements from both neutron and synchrotron X-ray diffraction methods. The following major conclusions can be drawn on the basis of the investigations presented above.

- Complete 2D cross-sectional longitudinal stress profiles were obtained for the MIG 2024 weld and VPPA 2024 weld using the contour method and the results show some features in common. Tensile stress is measured in the vicinity of the welding centre, and compressive stress further away from the heat affected zone, gradually approaching zero at the edges. A generally symmetrical stress distribution is found, although a slight asymmetry is present. The peak tensile stress is situated away from the weld centre in the fusion zone and the most compressive stress is located in the heat affected area of the weld.
- The smoothing error was ~ 0.7 μm and the measurement error was ~3 μm. The cutting flatness was ~3 μm, which gave an error of approximately 20 MPa in stress for the 12 mm thick 2024-T351 aluminium alloy welds.
- The comparison of the contour-method result with the neutron and synchrotron X-ray diffraction measurements shows an excellent agreement. The deviation is found to be approximately 9% in the most interesting area at the middle of the weld. The stress profile obtained from the contour method varies almost in-between the two diffraction measured results, although slight divergence is found for the compressive stress.
- The determination of a suitable stress free lattice parameter often presents a big challenge for diffraction techniques and this is particularly true for welds due to the compositional gradient present in the fusion zone and the heat affected zone (Dutta,

1999). The contour method, having fewer assumptions in theory, offers a great opportunity to validate the results measured by diffraction techniques, especially for welds, as have been proved in this chapter.

The study indeed shows the potential of the novel technique of the contour method with the successful application to the two welds. It is also evident that the contour method is a reliable technique to provide a full cross-sectional map of longitudinal stress in welds with high accuracy.

7.5 References

[1] ASM (1979). Properties and selection: Nonferrous alloys and pure metals, Metals Handbook, Nine edition ,Volume 2. Ohio, USA, American Society for Metals.

[2] Daymond, M. R., Bourke, M. A. M. and Von Dreele, R. B. (1997). Use of Rietveld refinement for elastic macrostrain determination and for evaluation of plastic strain history from diffraction spectra. Journal of Applied Physics, Vol. 82 (4), pp. 1554-1562.

[3] Dutta, M. (1999). Residual stress measurement in engineering materials and structures using neutron diffraction. PhD thesis, Department of Materials Engineering. Milton Keynes, UK, The Open University.

[4] Edwards, L., Ganguly, S. and Bacon, D. (2003a). Durability of welded aircraft assembly - residual stress measurement in variable polarity plasma arc (VPPA) welded Al 2024-T351 alloy. Experimental number: 7-01-114/D1A STR, Grenoble, France, ILL.

[5] Edwards, L., Ganguly, S., Stelmukh, V. and Nadri, B. (2003b). Design and durability of welded aircraft: measurement of residual strains in a 2024 VPPA weld. Experiment number: ME-516, Grenoble, France, ESRF.

[6] Hills, D. A. (2002). The connection between the elastic and plastic components of residual strain and residual stress. Journal of Strain Analysis, Vol. 37 (4), pp. 371-372.

[7] Mendez, P. F. (2000). New trends in welding in the aeronautic industry. Proceedings of New Trends for the Manufacturing in the Aeronautic Industry, 24-25 May, Spain, pp. 21-38.

[8] Prime, M. B., Hill, M. R., Dewald, A. T., Sebring, R. J., Dave, V. R. and Cola, M. J. (2002). Residual Stress Mapping in Welds Using the Contour Method. Proceedings of the 6th International Conference: Trends in Welding Research, 15-19 April, Pine Mountain, Georgia, pp. 891-896.

[9] Stelmukh, V., Edwards, L., Santisteban, J. R., Ganguly, S. and Fitzpatrick, M. E. (2002). Weld stress mapping using neutron and synchrotron X-ray diffraction. Materials Science Forum, Vol. 404-407, pp. 599-604.

[10] Withers, P. J., Preuss, M., Webster, P. J., Hughes, D. J. and Korsunsky, A. M. (2002). Residual strain measurement by synchrotron diffraction. Materials Science Forum, Vol. 404-407, pp. 1-12.

8 Discussion of errors in the contour method

Quantitative estimation of errors is crucial to all measurement techniques and the contour method is no exception. Although some knowledge on the error study has been gained for each specific case, some issues in the estimation of the errors for the contour method should be clarified. This work is not trivial as it requires thorough knowledge of all steps involved in the use of the contour method. As described earlier, the procedure in applying the contour method primarily consists of four steps: cutting, contour measurement, data reduction and finite element modelling, which will be briefly discussed in the following context.

8.1 Cutting

Cutting is the first step in performing the contour method and the importance of this step is obvious. The cutting-induced error is directly associated with the cutting flatness, which can be evaluated from the stress-free specimen that should be cut under the exactly same conditions as the formal specimen to be measured. This cutting error in stress can be calculated by inputting the contour measured on the stress-free specimen into the finite element model as displacement boundary conditions in the same way as it is performed in the contour method. Alternatively, if a stress-free specimen is not available, a thin slice sectioned from the free edge of the actual specimen can be used, as it was done in the present thesis. Of course, the cutting-induced error can be substantially minimized by correction of the contour measured on the specimen after subtracting the contour measured on the stress-free specimen. It should be emphasized again that both specimens must be cut in the same fashion. Surely, no cutting-induced error is present if purely flat cutting could be achieved. However, this ideal situation is almost unlikely in practice. The factors

relevant to cutting flatness are complex and various, depending on the machine to be employed for cutting, the type of the material to be cut, the geometry of the specimen, the way of specimen clamping, etc. For instance, the surface flatness of the 2024 aluminium alloy with 12 mm thickness was approximately 3 μm, based on the contour measurement on the surface after a 1mm slice was sectioned from the free edge of the specimen by ϕ0.1 brass wire EDM, performed in our department workshop. This measured contour, applied to a finite element model as displacement boundary conditions, resulted in an about 20 MPa error in stress. Correction is suggested if the resulting stress error is unacceptable.

8.2 Contour measurement

The error in contour measurement, denoted by E_m, is largely dominated by the measurement instrument used. As an example, the linear measuring accuracy of Mitutoyo Crystal Plus 574 CMM is given in Equation 3.1; the volumetric accuracy is described in Equation 3.2; its resolution is 0.1 μm, as stated in Chapter 3. In addition, attention should be paid to proper arrangement of the two cut parts to secure the two corresponding points to be averaged ideally at the mirror location. Further, the measurement resolution should be high enough to capture all the features of the deformation relaxed following a cut.

8.3 Data reduction

On the basis of present investigation, it is found that the error stemming from data reduction, denoted by E_r, is generally less than the cutting-induced error. As an example in our study, the smoothing error using the running average was ~ 0.7 μm whereas a typical cutting flatness is up to 3 μm, for the case of the MIG weld, as presented in Chapter 7. It is believed that E_r is dependent on the smoothing techniques used and the level of the smoothness chosen. The trade-off between the smoothing accuracy and the roughness

plays a critical role, as discussed in Chapter 2. It has to been claimed that it is almost impossible to estimate the error due to the extrapolation of the deleted data in data reduction. Consequently, the stress evaluated based on the extrapolated data is not reliable, and probably it is better not to present in the final stress.

8.4 Finite element modelling

In the contour method, the stress is calculated using the finite element method, in which the half the cut specimen is geometrically modelled, and the smoothed and measured contour is then applied to the model. In this solution, the stress is mainly relevant to the Young's modulus of the material, Poisson's ratio, density of the meshed model and the element chosen. The accuracy of the model also requires trade-off between the mesh density and the computation time/cost. The error caused by the assumption of the flat surface in the finite element model instead of an actually curved surface is negligible, as demonstrated in Section 3.2.

8.5 Errors in the resulting stress

As discussed above, each step in performing the contour method will generate a certain amount of error, and the error resulting from each step is different.

Firstly, the cutting-induced error in stress can be directly estimated from the contour measurement on the stress-free sample by the finite element method. However, it has been pointed out that this estimation is very rough as it excludes the variations from the contour measurement, data reduction and finite element modelling. It would be better to make correction using the stress-free sample to minimize the cutting-induced error.

Secondly, the errors in the contour measurement and the data reduction can be combined into one error, termed as a data error, E_{mr}, by the following equation:

$$E_{mr} = \sqrt{E_m^2 + E_r^2} \,. \tag{8.1}$$

The error in stress can be roughly evaluated by inputting E_{mr} into the finite element model as a constant displacement. However, a question arises that what E_m in the contour measurement should be utilized to correctly evaluate the error in stress in the contour method. The use of the measuring accuracy of the instrument seems to overestimate the error in stress. The repeatability, which is generally less than the measuring accuracy, is reasonable to replace E_m as an estimation of the error in the resulting stress. However, this is just a tentative idea that needs confirming and further investigation, which will be regarded as future work. Gladly, a similar issue was successfully dealt with by the latest publication, in which the level of the data smoothing was determined by minimizing the uncertainty in stress (Prime et al., 2004). Therefore, the error in the resulting stress can be estimated through multiple FE solutions for different levels of data smoothness. It is opposite to the methodology used in this thesis, in which the data reduction was performed by the optimization of the smoothing accuracy and the smoothness/roughness only without considering the error in the resulting stress.

Lastly, it is generally thought that the error in the finite element modelling is least important in the contour method. In most cases, this error does not need to be reported.

8.6 Summary

A brief discussion of the error sources and their estimation in determination of the residual stress using the contour method is presented. It is felt that this work is still preliminary and requires continuing and comprehensive study.

8.7 Reference

[1] Prime, M. B., Sebring, R. J., Hughes, D. J. and Webster, P. J. (2004). Laser surface-contouring and spline data-smoothing for residual stress measurement. Experimental Mechanics, Vol. 44 (2), pp. 176-184.

9 Overall conclusions and suggestions for future work

9.1 Overall conclusions

The major objective of this project was to investigate the potential of a newly-invented residual stress measurement technique — the contour method. The principal of the contour method was simulated two-dimensionally and three-dimensionally using the finite element method and this was detailed in Chapter 4. The application of the contour method was demonstrated on a number of typical specimens such as hole cold expansion plates and welds. Detailed conclusions for each application can be found in Chapter 5 for a hole cold expanded EN8 medium carbon steel plate, Chapter 6 for a hole cold expanded 7475-T7351 aluminium alloy plate, and Chapter 7 for a MIG 2024-T351 aluminium alloy welded plate and a VPPA 2024-T351 aluminium alloy welded plate. The overall conclusions based on the work presented earlier are generalised as follows.

- This work shows that the contour method indeed has the potential capability to determine a full cross-sectional map of residual stress fields normal to a surface of interest by one straight cut only.
- The correct stress field can be obtained by measuring the deformation profiles of both cut surfaces following a flat cut, and then properly averaging them.
- Use of an originally flat surface in a finite element model to represent the deformed plane is fairly reasonable to produce a correct stress profile with a negligible error.
- The contour method can achieve a sufficiently high resolution of residual stress measurement, as necessarily required for most engineering applications. The resolution of stress evaluation using the contour method physically depends on the resolution of the CMM used in the contour measurement and the mesh density applied in the finite element model, largely controlled by the computer memory available. A modern CMM

can achieve a resolution as accurate as 0.1 μm and sufficiently fine mesh of the FE model can be realised by modern computation capability.

- Experimental minimisation of the cutting gap as much as possible will effectively reduce the error a great deal in stress evaluation. This is particularly true for surfaces at issue with high stress gradients.
- Appropriate extrapolation of missed or removed data is of importance to minimise the error in contour-method measurement, although the influence of the extrapolated data is generally local. Nevertheless, use of as many measured data as possible is strongly suggested.
- Disagreement in the reference planes used for cutting and contour measuring does not introduce errors. However, minimisation of the disagreement is desirable.
- Specimen cutting is the first step in the use of the contour method. The importance of this step goes without saying because the subsequent experiment and analysis rely on the quality of the cutting. It is found that the cutting error often occurs at the start and the end of the cutting, also at discontinuous locations such as holes if the cutting has to pass them occasionally. Our experiments indicate that bigger cutting errors arise within an area approximately 3 mm inward from any edge including hole edges. This excludes the case where the cutting goes through the hole all the way.
- The error induced by cutting is generally bigger than the error arising from data smoothing. Typically, the smoothing error is normally less than 1 μm whereas the cutting flatness is approximately 3 μm. Surely, the magnitude of the cutting-induced error is case-dependent and it primarily depends on, for instance, the geometry of a plane to be cut, properties of material, cutting machine and specimen clamping.
- The determination of a suitable stress free lattice parameter frequently presents a big challenge for diffraction techniques and this is particularly true for welds due to the compositional gradient present in the fusion zone and the heat affected zone (Dutta,

1999). By contrast, the contour method is subjected to only small influence by the welding in the change of macroscopic elastic properties which are utilised to evaluate the stress field (Prime, 2001). Therefore, the contour method offers a reliable technique to validate the results measured by the diffraction techniques, especially for welds.

- The analytical model for hole cold expansion presented in Chapter 4 can be used for most metallic plates, and is particularly well suited to comparatively thin plates with limited dimensions where the effect of boundary conditions is at issue. It provides a cheap and reasonably accurate solution with the advantages of ease of parametric study and quick generation of results for assessment of residual stress fields in hole cold expansion plates.

This study shows that the contour method has the proven ability to provide engineers, scientists and researchers a powerful alterative to current residual stress measurement methods. It is also evident that the contour method can be regarded as a reliable technique to assess the residual stress field in many engineering components with high accuracy.

9.2 Suggestions for future work

Although many aspects of interesting topics on the contour method have been investigated, some important issues remain incomplete and need to be studied further. Furthermore, the technique of the contour method is still new and there are a large number of virgin areas of research that are attractive and worth exploring.

As discussed earlier, the cutting is the first procedure in performing the contour method and the cutting quality affects each of the subsequent procedures. Minimisation of the cutting-induced error is vital to achieve accurate stress evaluation in the contour method, although a certain correction can be made using the stress-free specimen. The cutting

flatness is the most important criterion for the cutting-induced error. However, the factors relevant to flat cutting can be complex and various. The choice of operation parameters for wire EDM may be associated with the geometry of the specimen and the type of the material. However, it would be useful to systematically investigate these effects and eventually to optimise the cutting parameter for a particular application. In addition, further investigation of minimising the edge effect arising from cutting is also beneficial particularly for hole cold expansion specimens. It should be aware that those processes may involve tedious trials and experiments, which can be very time-consuming. Nevertheless, once optimisation of wire EDM parameters has been well established, it will be extremely rewarding.

The error stemming from data reduction is generally less than a cutting-induced error. In this work, choice of the level of smoothing was based on measured contours only without considering the outcome of calculated stresses. As mentioned in Chapter 8, the measuring repeatability potentially contributes the error in stress. It is of paramount importance to investigate factors in the data reduction and the contour measurement that lead to the error in the final resulting stress and how to evaluate the error properly.

Nowadays, the software available are able to offer a wide range of choices in univariate data smoothers, which are utilised for uniform stress field evaluation only, but are limited in bivariate data smooth and bivariate extrapolation, which are used in the 2D stress evaluation. Although advancements have been made to use suitable data smoothing techniques such as the parametric smooth method of bivariate Fourier fitting and the non-parametric smooth method of bivariate running average, there is still a need to develop new smoothing techniques to cater for a variety of contour shapes. It would be more useful if a universal smooth method can be generated to suit all kinds of cases. The bivariate running average employed in this thesis appears to be universally suitable for most

situations and can be smoothed as many times as necessary. However, this method is not efficient in removing abrupt data in measurements, and an increase of the smooth times to minimise the effect arising from the abrupt values may lead to filtering of 'real' peaks elsewhere. It would be ideal to generate a smoothing approach combining the characteristics of universality and efficiency to filter out outliers. It is also critical to establish a reliable method to extrapolate data bivariately. Certainly, it is better to find out existing software capable of performing these tasks.

The CMM contour measurement is accurate enough in terms of the surface quality that the EDM produces. It is felt that with the CMM it is easy to measure a simple specimen with a regular shape, but difficult to measure more complex surfaces. Laser measurement has advantages not only with higher measurement accuracy, but more importantly capable of measuring complex geometries with ease. Introduction of laser measurement undoubtedly opens up the possibility of a wide range of applications especially with irregular cross-sections difficult to measure by other techniques. In terms of this point, a laser measurement instrument might be worth investing.

As we know, the contour method enables only one-direction stress to be evaluated with one cut. So, it would be attractive to extend the uniaxial stress measurement to triaxial stress evaluation by combining laboratory X-ray diffraction measurement that enables the stresses in the other two directions on the surface to be measured (Prime, 2001). This should be one of most exciting scopes worth exploring.

Confidence has been increasingly gained in the course of investigation of the contour method and we believe that this novel technique has enormous prospects and great potential in many other application areas.

9.3 References

[1] Dutta, M. (1999). Residual stress measurement in engineering materials and structures using neutron diffraction. PhD thesis, Department of Materials Engineering. Milton Keynes, UK, The Open University.

[2] Prime, M. B. (2001). Cross-sectional mapping of residual stresses by measuring the surface contour after a cut. Journal of Engineering Materials and Technology, Vol. 123, pp. 162-168.